Université Libre de Bruxelles
Faculté des Sciences

Contribution to the study of the central tracking system of the CMS detector at the LHC collider and to the elaboration of its online triggering system

Dissertation présentée en vue
de l'obtention du titre
de Docteur en Sciences

Gilles DE LENTDECKER

Décembre 2002

Cette thèse de doctorat a été réalisée avec le soutien du Fonds pour la Formation à la Recherche dans l'Industrie et l'Agriculture (F.R.I.A.).

Contents

Chapter 1

Introduction

In 2007, the new proton-proton collider, the LHC, will enter in function. This machine should provide proton-proton collisions at an unprecedented energy of 14 TeV in the centre of mass. The LHC should allow to answer to different questions, still open to date, concerning the fundamental constituents of matter and their interactions: what is the origin of the particle mass, why are the fermion masses so different, are there other forms of matter besides the known quarks and leptons, do all the interactions unify at very high energies, etc. They are arguments suggesting that new physics may be discovered at very high collision energies, evolving new particles.

The probability of occurrence of these interesting phenomena is very small per proton collision. Therefore the highest luminosity is required in order to accumulate a significant statistics of interesting processes in a reasonable time. At LHC, proton bunches will cross every 25 ns, with on average 17 interactions producing up to 1,000 charged particles at every crossing. This high flux of particles put stringent constraints on the detectors that will be used at LHC and on the data acquisition system. In particular an extremely elaborated selective trigger of the data acquisition is required to minimize the loss of a large fraction of interesting events and to minimize the dead time.

The Compact Muon Solenoid (CMS) is one of the two general purpose experiments being installed at LHC. This apparatus has been designed to work with the highest LHC luminosity and to provide an efficient detection of muons. Indeed most of the new physics should show up by the presence of muons in the final state. The muon identification is provided by dedicated detectors located in the outermost part of the CMS apparatus. A very high precision measurement of their transverse momentum can be obtained by combining the measurements of these muon chambers with those of the inner tracker counters.

This thesis is a contribution to the research and development program that preceded the construction of the CMS inner tracker and to the elaboration of the high level muon trigger of the experiment. The innermost part of a tracker at a high energy hadron collider requires high granularity and high spatial resolution detectors for which only silicon detectors can presently be envisaged. For the outermost part of the CMS tracker, for which the granularity and spatial resolution constraints can be somewhat relaxed, it was initially foreseen to use cheaper detectors, the Micro-Strip Gas Counters (MSGC). The MSGC is built with microscopic electrodes printed on a glass substrate, which permits to produce small detection cells, allowing to cope with the particle rates expected in the

CMS tracker. Since its introduction in 1988, extensive researches have been performed in order to optimize the MSGC performance with respect to its use in a high rate experiment like CMS. These studies have demonstrated that the MSGC fulfills almost all the requirements to equip the CMS tracker. However several groups observed irreversible damages to the delicate MSGC electrodes due to discharges induced by heavily ionizing particles (HIP). To suppress the discharges in MSGC's, the advanced passivation technique was proposed. This technique consists in covering the edges of the cathode strips by a thin layer of insulator in order to suppress the electric field at the cathode edges. Although it has been shown that with this protection MSGC's can sustain a high rate of HIP's, this technique is relatively delicate and makes the MSGC substrate more expensive. Consequently alternatives to the MSGC have been investigated. Among them, devices with two amplification stages are of particular interest since it has been demonstrated that they allow to reach higher gas gains before discharges appear.

In this work we have studied two alternatives to the MSGC for the CMS tracker, the MICROMEGEM and the MSGC+GEM detectors. Both detectors are two amplifications devices equipped with a Gas Electron Multiplier (GEM) which provides the first amplification. The GEM consists in a kapton foil, 50 μm thick, copper cladded on both sides and perforated by a regular matrix of holes of typically 140 μm spacing. In the MICROMEGEM counter, the GEM foil is sustained 50 μm above an array of pick-up strips; the second amplification is provided by applying an intense electric field between the GEM and the pick-up strips. In the MSGC+GEM, the GEM foil is located 2 mm above an MSGC substrate which provides the second amplification. The performance of both counters in terms of gain, energy resolution, rate capability has been studied with X-ray sources in different gas mixtures and compared with those of the MSGC.

To investigate the robustness of these detectors under sustained irradiation, at LHC rates, in presence of heavily ionizing particles, they have been exposed to a high intensity pion beam at the Paul Scherrer Institute (PSI), in Villigen (Switzerland). For the MSGC+GEM detectors that were considered for the endcap part of the CMS tracker, the CMS collaboration performed a large scale test with eighteen MSGC+GEM modules in such a beam during five weeks. We have investigated the uniformity of the response with time and scrutinized the possible damages to the strips, due to discharges.

In order to ensure a high detection efficiency and a good energy resolution, the probability of transfer of the primary electrons through the GEM holes must be as high as possible. This probability is called the GEM transparency. We have investigated the influence of the electric field configuration, of the gas mixture, of the readout electronics and of the geometry of the GEM foil on the GEM transparency, for the MICROMEGEM and the MSGC+GEM detectors. The results of these measurements were then reproduced and studied further by means of a Monte Carlo simulation using a three-dimensional model of the GEM foil.

The second part of this thesis is dedicated to the study of the muon reconstruction and selection at the third level of the CMS muon trigger. The trigger is the first step of the physics event selection: the interesting phenomena have to be selected for further analysis while a maximum of background has to be rejected. At LHC, the event rate of 10^9 Hz has to be reduced to 100 Hz, the maximum rate which can be archived on tape for further offline analysis. The event selection in CMS will be performed with a staged trigger. It is composed of the level-1, hardware based, and the High Level Trigger (HLT), software based. The HLT is subdivided in three stages called level-2, level-3 and level-4.

The level-1 trigger system operates on a subset of the CMS data, including only the data from the calorimeters and of the muon system. The level-1 trigger output rate is limited to 100 kHz. The level-2 confirms the level-1 decision with the same subset of data using more complex algorithms than at level-1, reducing the rate by one order of magnitude. The level-3 is the first level which can also use the huge amount of data from the central tracker. Each HLT level should provide a reduction factor of the rate of about 10.

In this work we propose a new algorithm for the muon reconstruction at the level-3 of the muon trigger. This algorithm fully exploits the similarities and the common interface between the muon and the inner tracker systems. The algorithm, based on the Kalman filter method, performs a track fitting through both systems. We have studied the performance of this algorithm in terms of track finding efficiency and in terms of the accuracy on the track parameters estimation; this work was performed with a detailed simulation of the CMS experiment. Finally, we have studied the trigger rates at the different muon trigger levels and discussed the corresponding background rejection and signal acceptance.

The LHC project and the CMS experiment are presented in chapter 2. Chapter 3 introduces the principles of particle detection with gaseous detectors. In chapter 4, the MSGC working principle is described and the MSGC performance is discussed. In chapter 5 we present the study of the MICROMEGEM detector. The different operation modes of the MSGC+GEM detector are discussed in chapter 6 and the results of the large scale beam test are reported in chapter 7. In chapter 8, a new algorithm for the muon reconstruction for the level-3 muon trigger is presented and discussed. The conclusions on this work are summarized in chapter 9.

Chapter 2

The CMS detector at the Large Hadron Collider

2.1 Introduction

This work is a contribution to the study of the forward outer tracker of the Compact Muon Solenoid (CMS) at the Large Hadron Collider (LHC) and to the elaboration of its High Level Trigger. This chapter describes the LHC project and the CMS experiment as well as the physics that will be studied. A brief description of the LHC machine is given in section 2.2. Section 2.3 gives an overview of the physics performance expected with CMS whose various components are described in section 2.4. Finally section 2.5 describes the trigger and data acquisition systems of the CMS experiment.

2.2 The Large Hadron Collider

The Large Hadron Collider (LHC) [1] is presently under construction at CERN, the laboratory of the European Organization for Nuclear Research, near Geneva and should be operational in 2007. This accelerator will allow the study of proton collisions with an energy of 14 TeV in the centre of mass, about seven times higher than at the $p\overline{p}$ collider Tevatron, at Fermilab (USA). The partons, i.e. the quarks and the gluons inside the protons, carry only a fraction of the total proton momentum. Therefore, at LHC, they will interact at an energy up to 1 TeV. This is far beyond the reach of present accelerators.

The realization of this accelerator is based on the infrastructures already existing at CERN. On one hand it will be installed in the 27 km long tunnel of the Large Electron-Positron (LEP) collider. On the other hand, it will use the existing injection infrastructure system of CERN shown in figure 2.1. The protons are first accelerated in bunches in a linear accelerator (LINAC) and in a booster, before being injected at an energy of 1.4 GeV in the proton synchrotron (PS). The PS will accelerate the beams up to 25 GeV and will inject them into the Super Proton Synchrotron (SPS) where they reach an energy of 450 GeV. The beams are then injected in the LHC ring for the final acceleration up to 7 TeV per beam.

The performance of a collider can be characterized by two parameters: the energy available in the centre of mass and the luminosity $\mathcal{L}$. The luminosity relates the cross

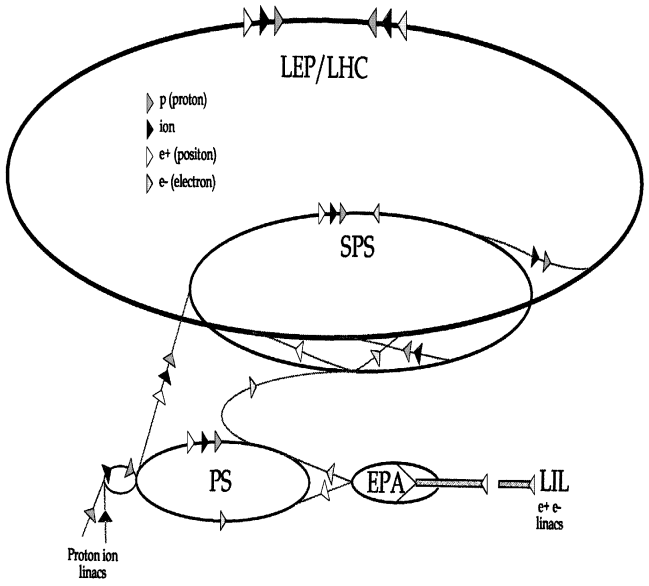

Figure 2.1: The CERN accelerator network as injection chain for the LHC.

section σ of a given process to its rate of occurrence r : $r = \mathcal{L}\sigma$. The luminosity depends on the number of particles per bunch in each beam (n_1, n_2), on the collision frequency of the bunches f and of the cross-sectional area of each particle bunch. If σ_x and σ_y are the standard deviations of the spatial distribution of the particle in the transverse directions in each bunch, we obtain:

$$\mathcal{L} = \frac{1}{4\pi} \frac{n_1 n_2 f}{\sigma_x \sigma_y} \tag{2.1}$$

The design parameters of the LHC at the nominal luminosity of 10^{34} cm^{-2}s^{-1} are given in table 2.1. However the LHC will not start with its nominal luminosity, but a low luminosity phase with $\mathcal{L} = 2 \times 10^{33}$ cm^{-2}s^{-1} will precede the high luminosity phase.

Luminosity	10^{34} cm^{-2}s^{-1}
Number of protons per bunch	1.05×10^{11}
Frequency	40 MHz
σ_x, σ_y	15 μm
Bunch crossing interval	25 ns
Interaction rate	$\sim 10^9$ Hz

Table 2.1: Nominal LHC parameters

Given the radius of the LHC ring, $\sim$ 4.3 km, a magnetic field of 8.4 Tesla is required in order to incurve the trajectory of the 7 TeV protons. This intense magnetic field will be provided by more than 10,000 superconducting coils cooled at 1.9 K with superfluid

helium. Since the two colliding beams have the same charge, they cannot be bent by the same magnet. The choice to have two proton beams, instead of one proton and one anti-proton beam, has the advantage to reduce a dead time of up to several hours, needed to accumulate the anti-protons, and to increase the luminosity. The solution adopted for the LHC to minimize the cost of the magnets is a single iron yoke and cryostat shared by two twin bore superconducting magnets. The beams cross at four points where the different LHC experiments will be located (see figure 2.2). ATLAS and CMS are the two general purpose detectors conceived for the physics studies at the highest LHC luminosity. ALICE and LHC-B are designed for the study of heavy ions collisions and for the study of B physics respectively.

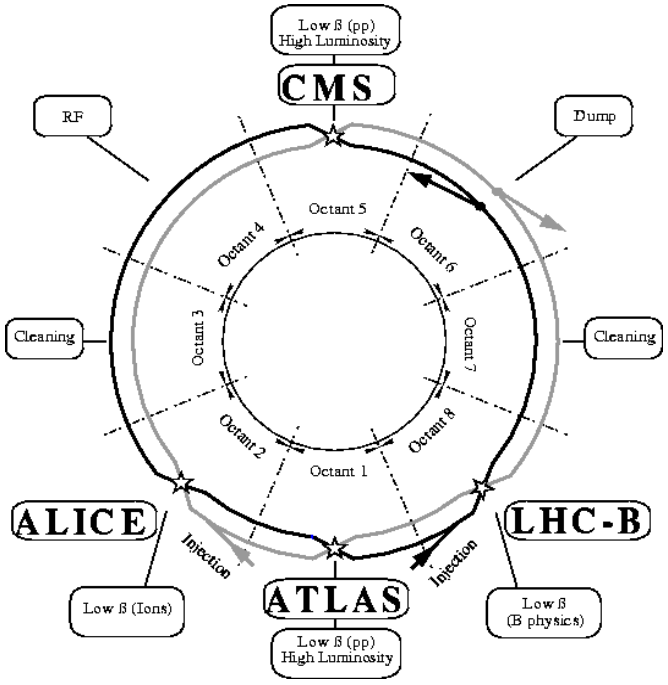

Figure 2.2: Schematic layout of the LHC. The figure shows the location of the different experiments, ATLAS, CMS, ALICE and LHC-B as well as the sections dedicated to the injection, the acceleration (RF), the cleaning and the dumping of the beam.

2.3 The CMS physics goals

The LHC will allow to study various physics signals. In this section we briefly overview some selected topics, particularly important since they represent the primary motivations for building the LHC. The most important topics are the searches for the Standard Model (SM) Higgs boson and for Minimum Supersymmetric Standard Model (MSSM) particles as well as for the CP-violation in the B sector and the study of the top quark.

Figure 2.3 shows the cross section of various processes as a function of the proton collision centre of mass energy at the nominal LHC luminosity of 10^{34} cm^{-2}s^{-1}. The cross sections estimated at a centre of mass energy of 14 TeV are Standard Model predictions extrapolated from data obtained with previous experiments. The cross-sections of the various processes cover a very broad range, from about 1 pb for the Higgs production if

the Higgs mass is around 500 GeV, up to 100 μb for $b\bar{b}$ pair production. The corresponding event rate at the nominal LHC luminosity is 10^{-2} Hz for the Higgs and more than 1 MHz for $b\bar{b}$ pair production. The total $p-p$ collision cross-section amounts to 100 mb, which will provide an event rate of about one gigahertz.

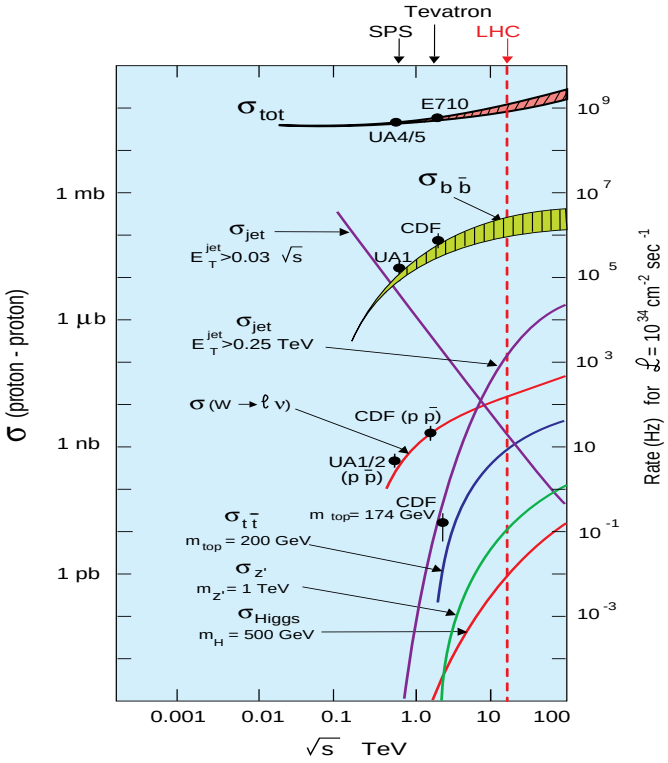

Figure 2.3: Cross-section and event rate of various processes at the LHC nominal luminosity of 10^{34} cm^{-2}s^{-1} as a function of the proton collision centre of mass energy [2].

The high luminosity of 10^{34} cm^{-2}s^{-1} is required to be able to observe very rare events like the production of the Higgs boson and of supersymmetric particles. The disadvantage is that on average 17 soft proton-proton interactions, called "minimum bias" events, will be superimposed on top of every hard event. These interactions will be distributed along the beam axis with a standard deviation of 5.3 cm. The high multiplicity of particles produced as well as the high collision frequency impose strong constraints to the triggering and data acquisition systems, as well as to the experiment detectors.

2.3.1 Search for the Standard Model Higgs

At the present time, the fundamental components of matter and their interactions are well described by the Standard Model. This theoretical framework is based on the Glashow-Salam-Weinberg model of the electroweak force, the quark model and the quantum chromodynamics (QCD). The predictions of the Standard Model have been verified with a very high precision by several experiments and no confirmed contradictions have been reported to date. In spite of the success of the Standard Model, the origin of the fermions mass and the spread of the measured fermion masses among several orders of magnitude are still to be solved.

The Standard Model is a quantum field theory which describes the interactions of pointlike spin 1/2 fermions (leptons and quarks), mediated by spin 1 gauge bosons. Originally all the particles have no mass in the Standard Model. The introduction of mass terms breaks the gauge invariance of the electroweak Lagrangian. In order to keep the gauge invariant theory, a theoretical solution has been introduced independently by F. Englert and R. Brout [3] and by P. Higgs in 1964 [4], the mechanism of spontaneous symmetry breaking. They postulate the existence of a new scalar field, the Higgs field. This mechanism associates to the Higgs field a neutral scalar boson, the Higgs boson. All matter particles and exchange bosons interact with this hypothetic particle. The intensity of the interaction between these particles and the Higgs determines the mass of the particle: the stronger the interaction, the heavier the particle. Up to now there is no experimental evidence for the existence of such a Higgs particle. Therefore it is one of the physics priorities of the LHC project.

The discovery of the Higgs boson is rendered difficult by the fact that the Standard Model does not predict the Higgs mass m_H. However the Standard Model describes extremely well the whole set of measurements obtained up to now and constraints the Higgs mass to be ≤ 212 GeV/c^2 at 95% confidence level. The experimental non observation of the Higgs at LEP excludes masses below 114.1 GeV/c^2 at 95% confidence level.

The diagrams of the dominant Higgs production mechanisms at a hadron collider are shown in figure 2.4. Since the coupling between the Higgs field and the elementary particles is proportional to their mass, the dominant production mechanisms will thus involve weak exchange bosons or top quarks, which are much heavier than the other quarks and leptons.

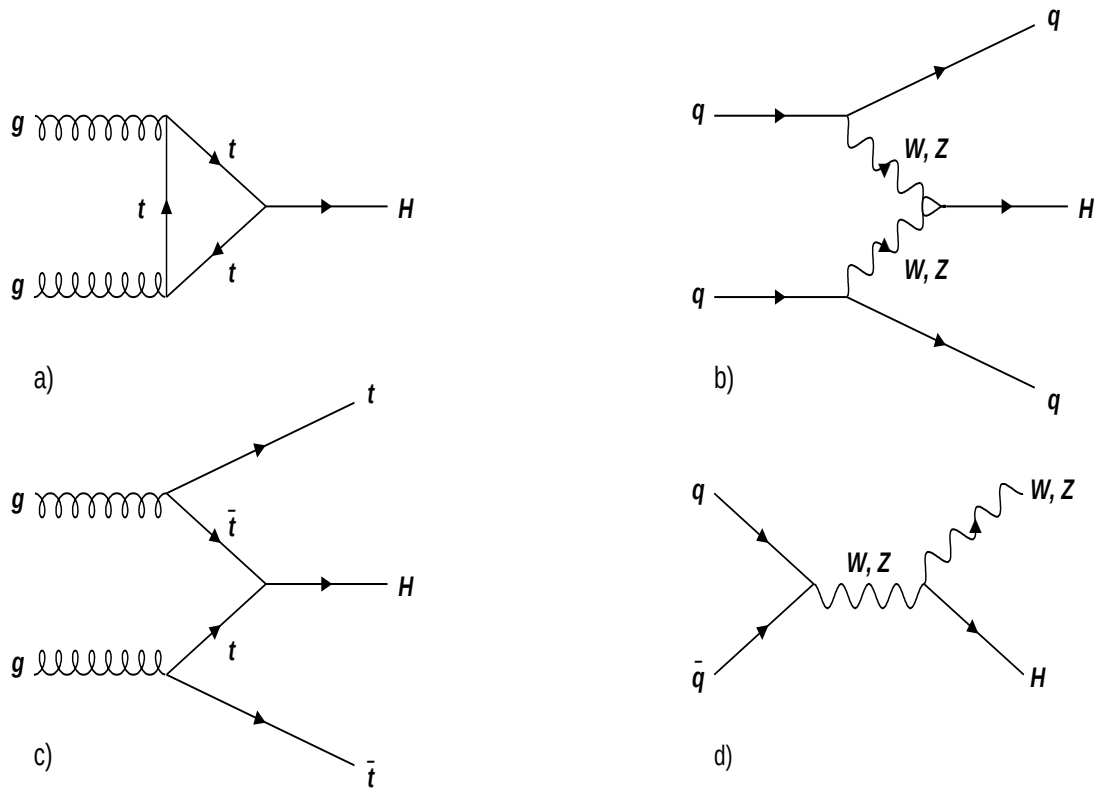

Figure 2.4: Feynman diagrams of the dominant Higgs production mechanisms at hadron colliders: gluon-gluon fusion (a), WW or ZZ fusion (b), $t\bar{t}$ fusion (c), W or Z bremsstrahlung.

The Higgs production rate expected at LHC is reasonably large, from 10^6 down to 10^4 events per year at high luminosity for Higgs masses ranging from 100 GeV/c^2 up to 1 TeV/c^2. Unfortunately the decay channels which provide the best experimental signature have small branching ratios, of the order of 10^{-3}. The branching ratios of the dominant Higgs decay modes are shown in figure 2.5. In the following we will overview some of these decay channels and briefly describe the search strategies to recognize the Higgs decay final states with respect to the background.

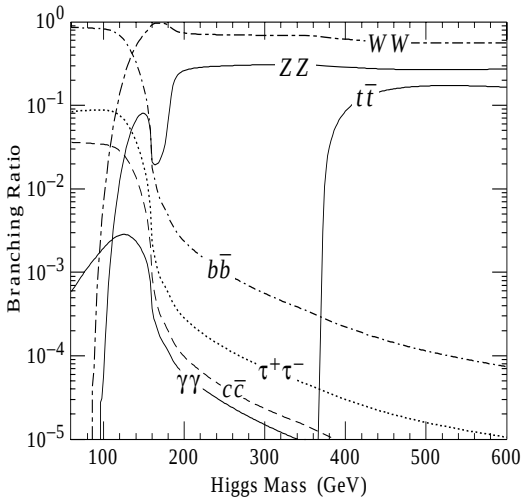

Figure 2.5: Branching ratios of the dominant decay channels of the Higgs boson as a function of the Higgs mass [5].

Below 130 GeV/c^2, the most important decay mode is $H \rightarrow b\bar{b}$, but it cannot be exploited experimentally since it is overwhelmed by the huge rate of direct $b\bar{b}$ pair production ($\sigma_{H\rightarrow b\bar{b}}/\sigma_{pp\rightarrow b\bar{b}} \sim \frac{20pb}{1mb} \sim 10^{-7}$). Consequently, the most favourable decay mode is $H \rightarrow \gamma\gamma$ resulting in two isolated energetic photons pointing to the same vertex. Although its branching ratio is as small as $\sim 10^{-3}$, this mode is interesting because of the low background. The main sources of background are:

- the prompt diphoton production during proton-proton collision, originating from quark annihilation, gluon fusion or bremsstrahlung. This background is irreducible.
- jets leaving a large amount of energy in the electromagnetic calorimeter. These deposits can be due to the decay of neutral hadrons inside the jets or to bremsstrahlung. This background can be reduced by the combination of an isolation criterion and the rejection of π^0. This can be achieved with a high calorimeter granularity, in order to separate the two photons coming from the π^0 decay.

In the mass range 120 GeV/c^2 $\leq m_H \leq 2\ m_Z$, the most favourable decay mode is $H \rightarrow ZZ^{(*)} \rightarrow 4l^{\pm}$, where l denotes an electron or a muon. One of the Z bosons may be virtual if the Higgs mass is smaller than 2 m_Z. The branching ratio of this channel is only about 1.2 10^{-3}, but it provides a clean signal by the presence of four energetic leptons. The main backgrounds come from the direct production of ZZ^* pairs, from $t\bar{t}$ pair production and $Zb\bar{b}$ events leading to a final state with four leptons. The first source is irreducible. The second source can be reduced by requiring that the reconstructed

mass of one pair of opposite sign leptons is compatible with the Z boson mass. Applying an isolation cut on the leptons and the identification of the b-jet can provide a further reduction of the $t\bar{t}$ and $Zb\bar{b}$ backgrounds.

Beyond $m_H = 2m_Z$, the two Z bosons can be on-shell. Consequently, an additional background rejection can be obtained by requiring that the reconstructed mass of two lepton pairs is compatible with the Z mass. Therefore this signature is almost background free and this channel is often called 'gold plated' channel. However the Higgs production cross section decreases rapidly at large values of m_H and the Higgs width increases. Consequently other decay processes with larger branching ratio have to be considered. For instance beyond $m_H = 600$ GeV/c^2 also the process $H \rightarrow ZZ \rightarrow 2l^{\pm}2\nu$ has to be considered. However the presence of two neutrinos in the final state excludes the possibility to reconstruct the Higgs mass.

In the Higgs mass range $120 \leq m_H \leq 2\, m_Z$, the decay process $H \rightarrow WW^{(*)} \rightarrow 2l^{\pm}2\nu$ has a branching ratio of one order of magnitude larger than the process $H \rightarrow ZZ^{(*)} \rightarrow 4l$ but this channel suffers from the presence of the neutrinos in the final state that prevent to reconstruct the Higgs mass. Beyond $m_H = 700$ GeV/c^2, one relies on the process $H \rightarrow W^+W^- \rightarrow l\nu jj$. A summary of the most favourable decay modes for the Higgs discovery and their corresponding mass ranges is given in table 2.2.

Final state	Mass interval
$H \rightarrow \gamma\gamma$	80 GeV/$c^2 \leq m_H \leq$ 150 GeV/c^2
$H \rightarrow ZZ^* \rightarrow 4l^{\pm}$	120 GeV/$c^2 \leq m_H \leq$ 180 GeV/c^2
$H \rightarrow ZZ \rightarrow 4l^{\pm}$	180 GeV/$c^2 \leq m_H \leq$ 650 GeV/c^2
$H \rightarrow ZZ \rightarrow 2l^{\pm}2\nu$	500 GeV/$c^2 \leq m_H \leq$ 1 TeV/c^2
$H \rightarrow W^+W^- \rightarrow l\nu jj$	$m_H \sim 1$ TeV/c^2
$H \rightarrow ZZ \rightarrow 2l^{\pm}2\nu$	

Table 2.2: Most favourable discovery channels of the Standard Model Higgs and corresponding mass intervals.

The reconstruction of the Higgs mass in the multilepton final state requires a large detector acceptance and a high track finding efficiency in order to reconstruct all the leptons. In particular a good lepton identification and precise energy or momentum measurement are needed to permit the use of a Z mass cut. In CMS a track reconstruction efficiency above 95% is required for isolated leptons.

2.3.2 Supersymmetry

Although it successfully describes the phenomenology of particle physics at the energies reached by the present experiments, the Standard Model is affected by conceptual problems due to the presence of a scalar boson in the model, and called the hierarchy problem. Indeed scalar fields are special in that the loop corrections to their squared masses are quadratically divergent. It is necessary then to bring down the Higgs mass by adjusting the counter-term to cancel the loop corrections. This adjustment, called fine-tuning, has to be done order by order and is not natural. In order to solve the problem, several possibilities exist which involve new physics at the scale of ~ 1 TeV. One of them is the introduction of an additional symmetry, the supersymmetry (SUSY), which naturally leads

to a cancellation of the divergences described above. SUSY postulates the existence, for all presently observed particles, of a superpartner, called s-particle, with a spin differing by 1/2. SUSY introduces then the bosonic superpartners of fermions (the squarks and sleptons) and the fermionic superpartners of bosons (gluinos and gauginos). Five Higgs bosons are also needed:

- 2 neutral scalar fields, denoted h and H;
- 1 neutral pseudoscalar field, denoted A;
- 2 charged vector bosons, $H^{\pm}$.

SUSY provides an elegant solution to the 'hierarchy problem': the corrections to the Higgs and other scalar masses become proportional to the SUSY mass scale of $\sim$ 1 TeV instead of the Planck scale at 10^{18} GeV.

Another motivation for SUSY is the unification of the gauge couplings. In the Standard Model, when extrapolated from their low energy measurements to large scales, the electromagnetic, weak and strong forces cannot be described by a unique symmetry. In supersymmetry, provided that the SUSY mass scale is of the order of 1 TeV, the gauge coupling constants unify at a mass scale of $\sim 10^{16}$ GeV. SUSY also provides a framework to include the gravity into the quantum theory of particle interactions and proposes a possible candidate for the cold dark matter, the lightest supersymmetric particle (LSP) which interacts weakly with matter.

If SUSY exists at the TeV scale, then its discovery at the LHC should be straightforward. The SUSY cross section is dominated by gluinos and squarks which are strongly produced. Gluinos and squarks then decay via a serie of steps into the LSP. These decay chains lead to a variety of signatures characterized by multi-jet, multi-lepton final state with missing transverse energy [6] The combination of a large production cross section and distinctive signatures makes it easy to separate the production of gluinos and squarks from the Standard Model background. The main challenge is then to measure the masses and other properties of SUSY particles. The lepton reconstruction is an important issue in order to reconstruct most of the sparticle spectrum.

2.3.3 The Top quark

The top quark, with a mass of $\sim$ 175 GeV/c^2, is the heaviest quark of the Standard Model; its mass is about 40 times larger than the next lighter quark, the b-quark. Because of its high mass, the top quark is strongly coupled to the electroweak symmetry breaking mechanism (see section 2.3.1). The top quark is also unique in that it decays prior to hadronize. It decays almost exclusively to a real W boson and a b-quark. A program to characterize the properties of this unconventional fermion is an obvious scientific priority.

The top quark has been discovered in 1994 by the CDF experiment at the Tevatron collider [7]. The CDF experiment has brought the first direct measurements of its mass m_t and cross section as well as valuable first experience in top quark physics [8]. With its large energy and high luminosity, the LHC is an excellent place to study the top quark. Despite the large mass of the top quark, it will be produced copiously at the LHC. Large

statistics are needed to measure the rate of Standard Model decays of the top quark, and thus determine indirectly if this quark decays to other new particles.

At LHC, the top quark will be produced in pairs ($t\bar{t}$). A clear signature of the $t\bar{t}$ pair production is the so-called dilepton mode, in which both decay to a b-quark and a W decaying leptonically ($W \rightarrow l\nu$). The nominal signature of this channel is two high p_T leptons (electrons or muons), missing transverse energy (from the two ν's) and two jets from the b-quarks. Unfortunately the branching ratio of this channel is small because of the small branching ratio of both W's decaying leptonically ($\sim 5\%$). The ratio of the $t\bar{t}$ cross section measured using dilepton events to that measured using lepton + jets events, in which one W decays leptonically and the other hadronically, is a test for non-Standard Model decay modes of the top. Since the cross section in each case assumes that each top decays into W bosons, a ratio different from 1.0 would indicate decays without a W-boson, such as charged Higgs ($t \rightarrow H^+ b$) or light supersymmetric top (stop).

2.3.4 B-Physics

At the LHC start-up, the luminosity should be equal to 2×10^{33} cm^{-2}s^{-1}, a factor five lower than the nominal value. The main topic of this low luminosity phase is to study beauty hadrons, which contain the bottom quark. Measurements with b hadrons can in principle be used to extract information on 5 of the 9 elements of the Cabbibo-Kobayashi-Maskawa quark mixing matrix ($V_{\rm CKM}$), which relates the weak-interaction and mass eigenstates of quarks. The CKM matrix can be written as:

$$V_{\rm CKM} = \begin{pmatrix} V_{ud} & V_{us} & V_{ub} \\ V_{cd} & V_{cs} & V_{cb} \\ V_{td} & V_{ts} & V_{tb} \end{pmatrix} \tag{2.2}$$

or in the Wolfenstein parametrization [9] :

$$V_{CKM} = \begin{pmatrix} 1 - \frac{\lambda^2}{2} & \lambda & A\lambda^3 r e^{i\delta} \\ -\lambda & 1 - \frac{\lambda^2}{2} & A\lambda^2 \\ A\lambda^3(1 - re^{i\delta}) & -A\lambda^2 & 1 \end{pmatrix} + \mathcal{O}(\lambda^4), \tag{2.3}$$

where the parameters λ, A, r and δ are real. The measured values of λ and A are 0.22 and 0.8 ± 0.04 [28]. A non-zero value of the phase δ leads to the violation of the CP symmetry in weak interactions. C and P are transformations of the particle wave function under the exchange of the particles by their anti-particles (Charge conjugaison) and by the reversal of the space coordinates (Parity) respectively. CP violation in weak interactions has been observed more than 30 years ago in the decay of neutral kaons and it was expected to occur in the B^0-$\bar{B}^0$ system. Recently, Babar [10] and Belle [11] experiments presented measurements showing that CP is definitely violated in decays of B mesons, beginning new era. The next step is to acquire sufficient statistics to make precision measurements that fully constraint the CKM matrix. Then by making further measurements, it will be possible to explore whether the Standard Model can fully explain CP violation in the B sector or whether there are indications of new sources of CP violation.

A possible procedure to select events involving beauty hadrons could rely on the large transverse momentum of the beauty hadron decay products. Semi-leptonic decay chains

lead to a high momentum lepton in the final state, a clear signature in an environment dominated by QCD processes. One of the most appropriate channel to measure the CP violation parameters is the decay $B_d^0 \to J/\psi K_s$, with $J/\psi \to \mu^+\mu^-$. At LHC, ~ 5500 of such events are expected for an integrated luminosity of 10^4 pb^{-1}, with a threshold of 5 GeV on the muon transverse momentum [12].

2.4 The CMS (Compact Muon Solenoid) detector

The Compact Muon Solenoid (CMS) detector [12] is designed to run at the highest LHC luminosity but is also adapted for physics studies during the low luminosity phase. The physics objectives at LHC together with the harsh radiation environment dictate the experiment design. The CMS detector must fulfill the following requirements:

- a very good muon identification and momentum measurement;
- a very good resolution on the photon and electron measured in the electromagnetic calorimeter;
- an efficient inner tracking system able to reconstruct charged particle trajectories with a precise measurement of their momentum;
- a large detector acceptance;
- fast and radiation hard detectors.

Like most of the modern collider experiments, CMS is composed of several subdetectors with complementary functions: muon chambers, calorimeters and tracking system. Figure 2.6 shows a three dimensional view of the CMS detector. The detector, of cylindrical shape, is 21.6 m long with a diameter of 15 m. The reference system used in CMS is a right-handed system in which the x-axis is oriented towards the collider centre and the y-axis upwards. The z-axis is oriented along the beam line. A spherical coordinate system is also commonly used. The coordinates are the radius r, the azimuthal angle ϕ with respect to the y-axis and θ the polar angle with respect to the z-axis. Instead of the polar angle, often called rapidity, we use the pseudo-rapidity, η defined as:

$$\eta = \frac{1}{2} \ln \frac{p + p_z}{p - p_z} = -\ln \tan \frac{\theta}{2}. \tag{2.4}$$

Here θ is the angle of emission of a particle of momentum p and $p_z = p \cos\theta$ is the z-component of the particle momentum. It has been shown that the distribution of the number of particles $dN/d\eta$ is roughly constant with the pseudo-rapidity [13].

To achieve the above mentioned requirements, CMS has chosen to have a superconducting solenoid generating a uniform magnetic field of 4 Tesla inside the coil. The magnetic field is returned outside the magnet through a thick saturated iron yoke instrumented with muon chambers. The large dimensions of the solenoid, 6 m in diameter and 13 m in length, allow to place the tracking and calorimetry systems inside the magnet. This layout prevents the calorimeter performance to be affected by the coil material, ensuring a high precision energy measurement which is required for the discovery of the Higgs in the two photons channel. In addition the high magnetic field will enable a good momentum measurement in the central tracker and will reduce the number of low momentum charged particles in the calorimeters.

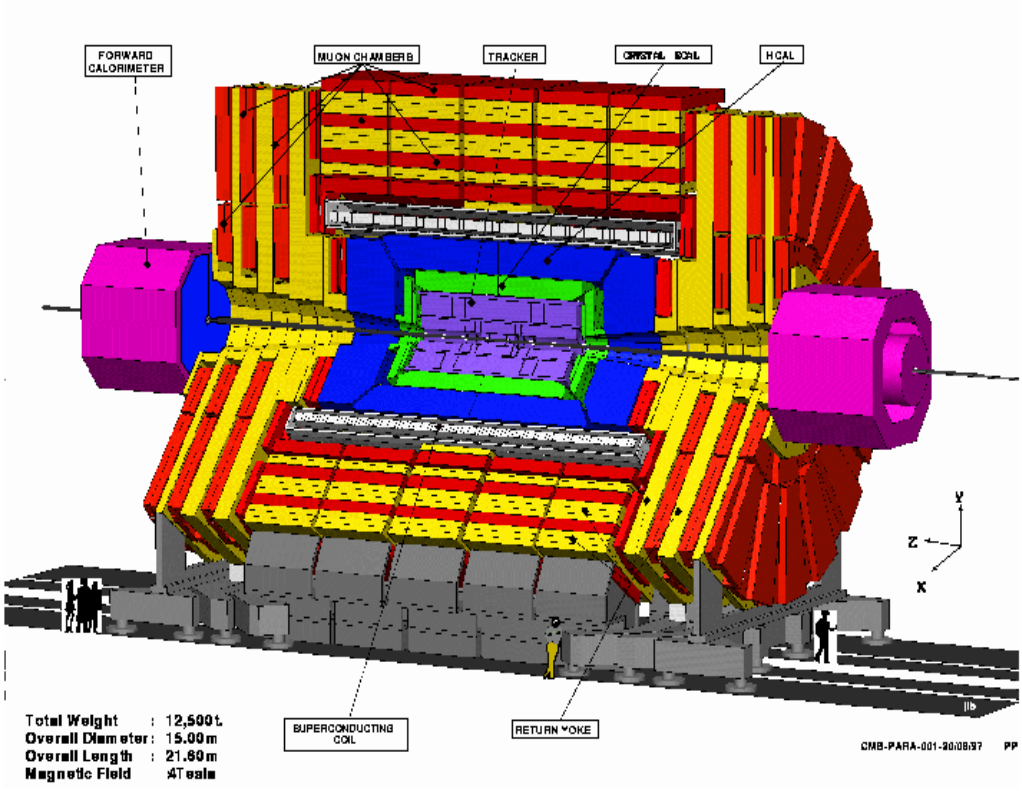

Figure 2.6: Three dimensional view of the CMS detector.

2.4.1 The muons detector

The signature of various interesting physics processes at LHC involves muons in the final state (see table 2.2). The muon system [14] should therefore fulfill three basic tasks: muon identification, momentum measurement and trigger. The muon identification relies on the fact that in contrast with other charged particles, muons do not interact much with matter. Therefore the muon system, composed of four muon stations interleaved with the flux return yoke plates, is placed after the other subdetector systems and outside the magnet coil. Moreover the thickness of absorber before the last muon chamber amounts to 16 interaction lengths which ensures that only muons can reach it. The muon system should measure the muon momentum with an accuracy ranging from 8% to 40% for muons with a transverse momentum of 10 GeV/c and 1 TeV/c respectively. This can be achieved by using detectors providing a spatial resolution of the order of 200 μm. For this purpose the muon system is equipped with Drift Tubes in the barrel region ($|\eta| < 1.2$) and with Cathode Strip Chambers in the forward region ($0.9 < |\eta| < 2.4$). In addition, to participate in the CMS trigger system, the muon system has to be able to react in less than 25 ns, the time between two bunch crossings. To achieve this objective, the muon system is equipped with Resistive Plate Chambers in the range $|\eta| < 2.1$ which are dedicated trigger detectors. We shall now briefly describe these different technologies.

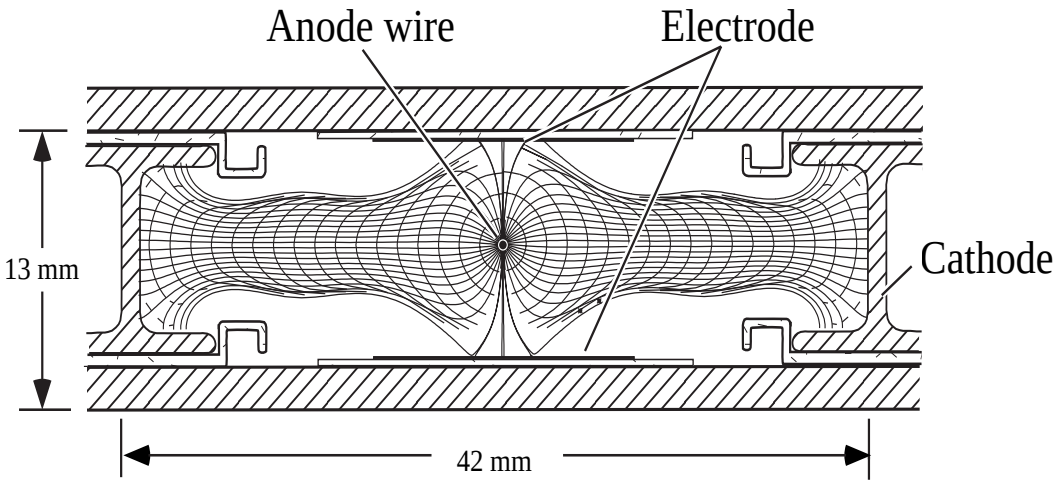

Figure 2.7: Transverse section of a CMS Drift Tube cell.

The Drift Tubes

The Drift Tubes (DT) are drift chambers with a detection cell of 42×13 mm^2 section filled with Ar/CO_2-80/20% gas mixture. Figure 2.7 shows the transverse section of a CMS Drift Tube. The use of DT's is limited to the barrel part of the muon spectrometer where the particle rate is expected to be of the order of 10 Hz/cm^2. The maximum drift time being $\sim$ 375 ns, the cell occupancy is below 1%. The cells are assembled in layers and four layers of 12 cells are assembled together, staggering the cells by half a cell, to form a super-layer. Each barrel station is composed of three super-layers. Two of them measure the coordinates of the muon crossing point in the (R,ϕ) plane and the third super-layer measures the coordinate along the beam. The spatial resolution of a single DT cell has been measured to be $\sim$ 180 μm. In addition each super-layer is able to provide a bunch crossing identification with an accuracy of 5 ns when averaging the drift time in the four layers of the super-layer.

The Cathode Strip Chambers

The endcap parts of the muon spectrometer is composed of Cathode Strip Chambers (CSC). The CSC is a multi-wire proportional chamber, as shown in figure 2.8, well suited to the conditions met in the endcap parts of the muon system: a particle rate up to 1 kHz/cm^2 and a large inhomogeneous magnetic field. The chambers have a trapezoidal shape and are composed of two cathode planes separated by a drift gap of 9.5 mm. The gap is filled with a Ar/CO_2/CF_4-30/50/20% gas mixture. One of the cathode plane is segmented in strips oriented radially. Anode wires are strung perpendicularly to the mid cathode strips. With this design, the CSC's are able to provide the $R\phi$ and R coordinates with a spatial resolution of 75 μm and 500 μm respectively.

The Resistive Plate Chambers

To participate in the trigger system, the muon system requires detectors able to react in less than one LHC bunch crossing that corresponds to 25 ns. This is achieved with

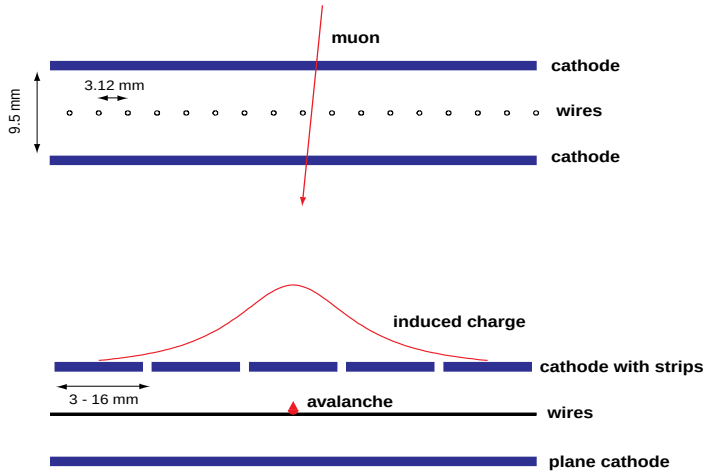

Figure 2.8: Layout of a Cathode Strip Chamber.

the Resistive Plate Chambers (RPC) which have a time resolution better than 3 ns. A RPC is composed of two Bakelite planes of high resistivity (10^{10}-10^{11} Ωcm), separated by a gas gap of a few millimeters filled with a gas mixture of $C_2H_2F_4$/i-C_4H_{10}-95/5%. The signal produced by the ionizing particle is read-out by Aluminium strips printed on the external side of one of the two Bakelite planes. The RPC's cover the pseudo-rapidity range $|\eta| < 2.1$. In the barrel part of the muon system two layers of RPC's are placed around the DT super-layers in the first two stations, and one layer per station for the two outer stations. In the endcap part of the muon system one layer of RPC is foreseen for each station.

2.4.2 The electromagnetic calorimeter

The main goal of the electromagnetic calorimeter (ECAL) [15] is to measure the energy and the position of the electromagnetic showers produced by electrons or photons. The ECAL can play an important role in the discovery of the Higgs boson, in particular in the decay modes in two photons or in four leptons, or in the observation of leptonic signatures of supersymmetric particles. To achieve these goals the calorimeter should have a very good energy resolution and a high granularity as well as a fast response in order to participate in the trigger.

To reach a good energy resolution CMS has chosen to build an homogeneous calorimeter made of 61,200 crystals of lead tungstate ($PbWO_4$) as active material. Indeed the energy resolution of a calorimeter can be parametrized as follows:

$$\left(\frac{\sigma}{E}\right)^2 = \left(\frac{a}{\sqrt{E}}\right)^2 + \left(\frac{\sigma_n}{E}\right)^2 + c^2, \tag{2.5}$$

where $a/\sqrt{E}$, σ_n/E and c are the stochastic, noise and constant terms. The stochastic term corresponds to statistical fluctuations in the number of primary processes that generate the signal. The noise term includes mainly the electronic noise and the pile-up. The constant c accounts for other contributions as the calorimeter non-uniformity. For the

CMS barrel ECAL, the contributions of the different terms are expected to be $a \simeq 2\%$, compared to 10% for a sampling calorimeter, $\sigma_n = 210$ MeV and $c = 0.55\%$, at high luminosity. The use of $PbWO_4$ crystals provides a short radiation length of 0.89 cm and a small Molière radius of 2.19 cm. On one hand, a small radiation length is required to limit the crystal thickness and to be able to place the whole calorimeter inside the superconducting coil. On the other hand a small Molière radius results in fewer crystals needed to contain the electromagnetic showers laterally, improving the shower isolation efficiency and reducing the pile-up. Note also that 60% of the crystal light is emitted within 15 ns matching the bunch crossing time of 25 ns.

The ECAL is divided into a barrel part, which covers the region $|\eta| < 1.48$, and two endcaps parts, which cover the region $1.48 < |\eta| < 3$. In the endcaps, over the range $1.65 < |\eta| < 2.61$, the granularity of the ECAL is not sufficient to distinguish a single photon from two photons coming from a π^0 decay. To improve the π^0/γ separation, a so-called preshower detector will be placed in front of the endcaps. It is made out of two lead plates separated by silicon strip detectors having a pitch of 2 mm. A π^0 rejection factor of 2 to 3 can be achieved with this set-up. It is also foreseen to install a similar set-up in the barrel, at $|\eta| < 0.9$, for the high luminosity phase.

2.4.3 The hadronic calorimeter

The signatures for the discovery of high mass Higgs include jets and missing energy. For example in the process $H \rightarrow W^+W^- \rightarrow l\nu + 2$jets, a fine segmentation is needed to separate the nearby jets and to measure the jet direction with sufficient precision. Moreover since missing energy, together with b-jets, is one of the clearest signature of supersymmetry, a good hermiticity is required.

The CMS hadronic calorimeter (HCAL) [16] is a sampling calorimeter made of sheets of active plastic scintillator layers interleaved with copper plates. It covers the pseudo-rapidity range $|\eta| < 3$. A quartz fiber calorimeter, placed in the very forward and backward parts, ensures the covering of $3 < |\eta| < 5$. The absorber thickness varies from 7.5 to 13 interaction lengths, so that the hadronic showers are nearly entirely contained in the calorimeter volume. The transverse granularity is $\Delta\eta \times \Delta\phi = 0.087 \times 0.087$, which should permit a good separation of two jets from the same event. Beam test results and simulations show that the CMS hadronic calorimeter can reconstruct isolated hadrons, in a range of 30 GeV/c to 1 TeV/c, with an energy resolution of square root of $(100\%/\sqrt{E})^2 + (4.5)^2$.

2.4.4 The CMS tracker

The goals of the central tracking system is to reconstruct the trajectory of charged particles with a high efficiency (above 95% for isolated tracks) and to measure the momentum and direction of the particles at their production vertex. In a uniform magnetic field B, charged particles describe a helicoidal trajectory around the field axis. The curvature of the track is directly related to the component of the momentum in the plane transverse to the field:

$$p_T = qBR_c, \tag{2.6}$$

where q is the particle charge and R_c is the radius of curvature. In a practical unit system Eq. 2.6 becomes:

$$p_T[\mathrm{GeV/c}] = 0.3\ B[\mathrm{T}]\ R_c[\mathrm{m}]. \tag{2.7}$$

The transverse momentum can be determined by measuring the coordinates (x, y) or (R, ϕ) of a set of points along the particle trajectory in the plane transverse to the magnetic field and by fitting a circle through these points. The particle momentum is then given by

$$p = p_T \sin\theta, \tag{2.8}$$

where θ is the angle of the particle direction with respect to the magnetic field axis. It is calculated from the z-coordinates of the measured points. The above formulas show that the momentum resolution has contributions from the errors on the track curvature and on the polar angle θ. In addition the momentum resolution suffers also from multiple Coulomb scattering in the material traversed by the particle. Consequently the momentum resolution can be written as follows

$$\left(\frac{\Delta p}{p}\right)^2 = \left(\frac{\Delta p_T}{p_T}\right)^2 + \left(\frac{\cos\theta}{\sin\theta}\Delta\theta\right)^2 + \left(\frac{\Delta p}{p}\right)^2_{m.s}. \tag{2.9}$$

It can be shown that the contribution of the error on the polar angle is below 10^{-3} and can be therefore neglected as compared to the other contributions.

The error on p_T due to the spatial resolution of the detectors is referred to as the intrinsic momentum error and is given by [135] :

$$\left(\frac{\Delta p_T}{p_T}\right)_{R\phi} = \frac{a_n \sigma_{R\phi}}{0.3 B L_T^2} p_T, \tag{2.10}$$

where $\sigma_{R\phi}$ is the spatial resolution of the detector elements in the $R\phi$ coordinate and L_T is the length of the particle path projected onto the transverse plane. The factor a_n is given by

$$a_n \simeq \sqrt{\frac{720}{n+4}} \qquad \text{for } n > 10 \tag{2.11}$$

in case of n uniformly spaced measurement points. Formulas 2.10 and 2.11 show that the intrinsic momentum resolution degrades linearly with the transverse momentum but improves with the magnetic field and with the radial size of the tracker. In CMS, to achieve an intrinsic momentum resolution around $10^{-4} p_T$ (p_T in GeV/c), the tracker is embedded in a 4 T magnetic field and has a radius of 1.2 m. With an average number of 12 measurements along the particle trajectory, an average resolution on the $R\phi$ coordinate of 25 μm per point is required.

At low transverse momentum, the momentum resolution is limited by the multiple scattering. This limit can be expressed as a function of the thickness of material traversed by the particle:

$$\left(\frac{\Delta p}{p}\right)_{m.s} = \frac{0.06[\mathrm{Tm}]}{\beta B L_T} \sqrt{\frac{L}{X_0}}, \tag{2.12}$$

where L is the track length inside the tracker, X_0 is the average radiation length in the material traversed and $\beta = v/c$ is the particle velocity. Eq. 2.12 shows that the contribution of the multiple scattering to the momentum resolution is independent of the particle momentum since β is close to 1 for all particles of interest.

Consequently, the intrinsic momentum resolution is the dominant error for particles of high transverse momentum, while at low transverse momentum the tracker performance is spoiled by the multiple scattering. In the CMS tracker, the amount of material is relatively large, between 0.2 and 1 radiation lengths depending on η. The momentum resolution is thus limited to 0.5 - 1% for particles of p_T below 10 - 20 GeV/c. The intrinsic resolution dominates only at transverse momenta above 50 - 100 GeV/c.

Objectives and requirements

The CMS tracker must be able to reconstruct with high efficiency the track of charged particles down to the lowest transverse momentum possible that is 1 GeV/c at high luminosity. The required detection efficiency is 95% for isolated tracks and 90% for tracks inside jets over the pseudo-rapidity range $|\eta| < 2.5$. Simulation studies have shown that to reach these requirements, the tracker must be built with tracking elements with a spatial resolution of 25 μm on average and a detection efficiency close to 100%.

Given the particle flux at the LHC, the detectors need:

- a fast response time, smaller than 50 ns, to keep the number of superimposed events at two;
- a small detection cell size in order to keep the occupancy of a single readout channel below a few percent;
- to be radiation resistant.

In addition the amount of material inside the tracker should be as small as possible. Indeed the presence of any absorber in front of the electromagnetic calorimeter causes bremsstrahlung and photon conversions which spoil the energy measurement of electrons and photons in the calorimeter. Moreover a light tracker reduces the multiple scattering.

Tracker equipped with Micro-Strip Gas Counters

Initially three detector technologies have been chosen to build the central tracker [17]. Silicon pixel detectors are located at less than 20 cm from the beam pipe, silicon strip detectors are placed at radii between 20 and 60 cm, and micro-strip gas counters at radii between 60 and 120 cm. This layout is shown in figures 2.9.

Solid state technologies have been chosen for the innermost layers of the tracker as they permit small cell sizes coping with the high rate of particles close to the interaction point and high spatial resolution for precise vertex reconstruction. Since the constraints on the particle flux and on the spatial resolution are slightly less stringent for the outer part of the tracker, the lower cost Micro-Strip Gas Counters (MSGC) were preferred.

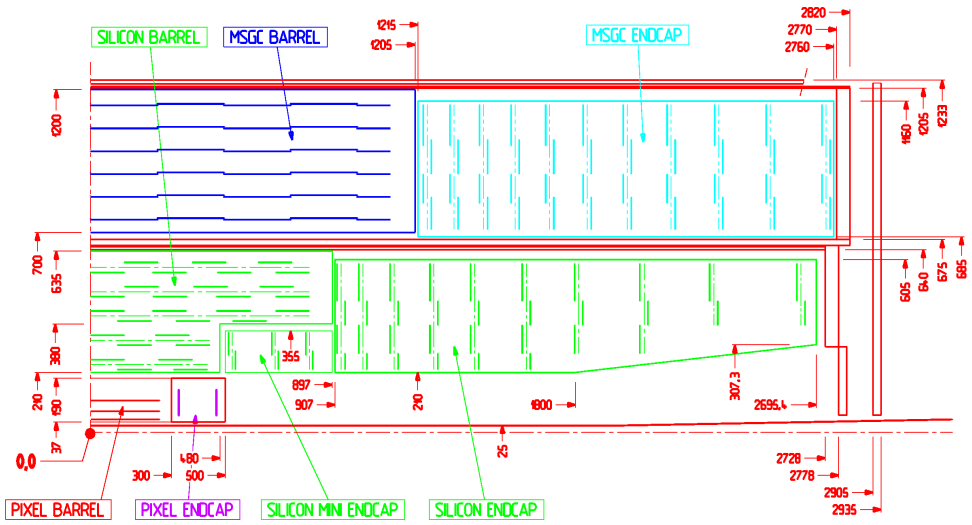

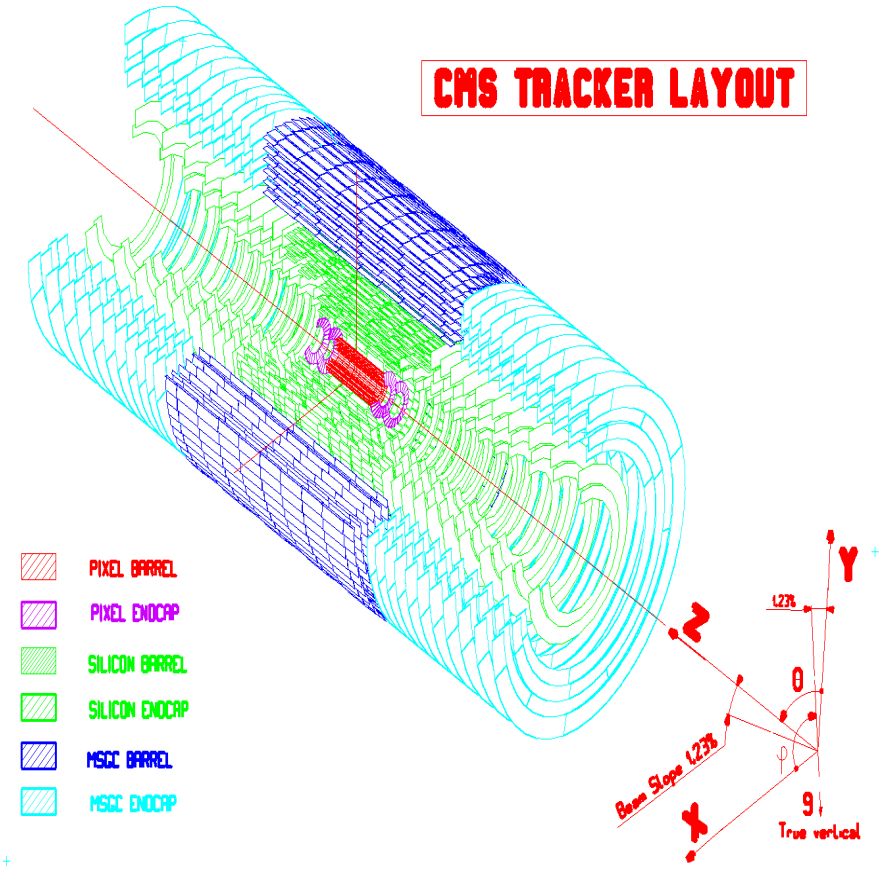

Figure 2.9: Longitudinal and three dimensional views of the CMS central tracker equipped with MSGC's in the outer part.

Each subdetector is divided in a barrel part, composed of cylindrical detection layers, and two endcap parts composed of disk shaped detection layers. In the barrel, the detectors measure the $R\phi$ and z-coordinates of the particle crossing points while the R-coordinate is given by the radius of the corresponding detection layer. In the endcaps, the detectors provide the $R\phi$ and R-coordinates and the position of the disk along the beam pipe provides the z-coordinate.

The pixel counters are squares of size 150 μm $\times$ 150 μm in the barrel region, with a thickness of 250 μm. The pixel system is composed of two barrel layers and two endcap layers on each side. Its main goal is to allow vertex reconstruction in three dimensions thanks to its good spatial resolution in two dimensions. Indeed the sharing of the charge deposited by an ionizing particle on several pixels will provide a resolution of 15 μm for the $R\phi$ and z-coordinates, in the barrel. In the forward, the spatial resolution amounts to 15 and 90 μm for the $R\phi$ and R-coordinates respectively. The silicon strip tracker is composed of five barrel layers and ten disks in each endcap. It extends up to 2.65 m along the beam line in order to provide precise $R\phi$ measurements up to $|\eta| = 2.2$. The barrel counters are inclined by an angle of 9^o with respect to the radial direction in order to compensate the effect of the magnetic field on the drift direction of the charge carriers. To provide the readout of the second coordinate, half the detection layers are double sided. In the single sided detectors, the strip are parallel to the beam line in the barrel and radial in the endcap. They provide a resolution on the $R\phi$-coordinate of 15 μm. In double sided counters, the strips of the second readout side are tilted by an angle of 100 mrad with respect to the strips of the first readout side, allowing to measure the second coordinate with an accuracy of less than 1 mm.

For the outermost part of the CMS tracker, the MSGC were envisaged. These detectors, cheaper than the silicon detectors, have shown that they fulfill the requirements to equip large detection surfaces in high luminosity experiments. The MSGC tracker consists of six barrel layers and eleven disks on each side. The MSGC strip layout is similar to the one of the silicon strip detectors.

Some layers are double with a stereo angle of 50 mrad allowing to measure the second coordinate with a resolution better than 2 mm. The intrinsic resolution of the CMS MSGC's is 30-40 μm in $R\phi$ for particles with a transverse momentum above 10 GeV/c. In the barrel the detectors are tilted by 14^o to compensate the effect of the magnetic field on the drift path of the charge carriers.

A thermal shield will separate the silicon strip and pixel counters from the MSGC's. Indeed, in order to survive to several years of running, the CMS solid state detectors will be kept at low temperature, of the order of -10°C. The MSGC's will be operated at room temperature.

The Full Silicon Tracker

Although the qualities of the MSGC have been demonstrated in many respects, the observation of irreversible damages to the strips due to sparks induced by the presence of highly ionizing particles triggered extensive studies to solve that problem. In 1999 the MSGC community of CMS achieved its research program with a successful beam test performed with a large number of detectors of final design in radiation conditions close to the LHC ones. However at the end of 1999, considering the decreasing price of silicon,

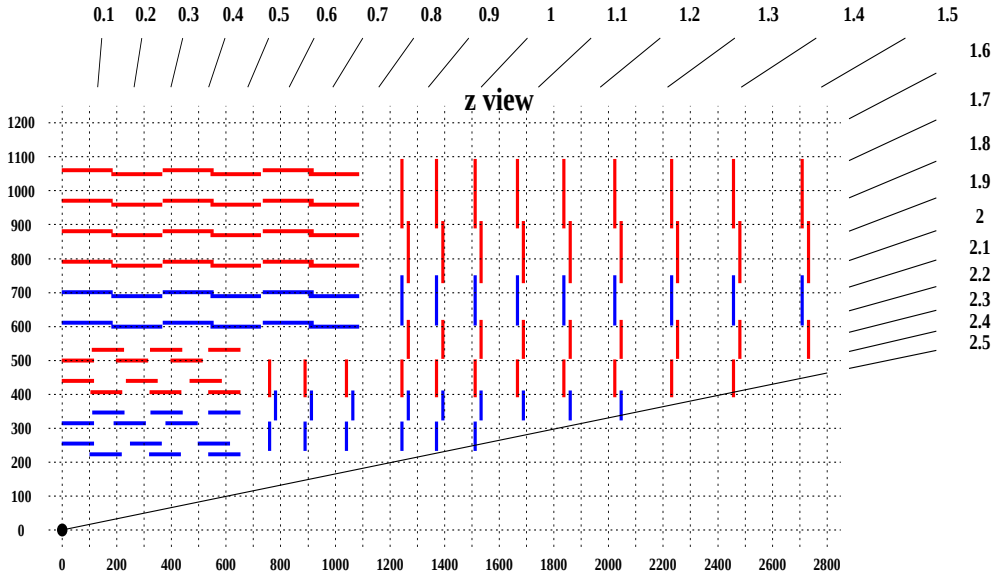

Figure 2.10: Layout of the new tracker entirely equipped with silicon detectors.

the CMS collaboration decided to abandon the MSGC technology and to build an entire silicon tracker hoping that the use of a single technology would render its construction and maintenance easier [18].

The proposed all silicon tracker has approximately the same number of readout channels, but it has somewhat less instrumented surface compared to the MSGC tracker. The all silicon tracker is divided into two parts, the pixel detector and the silicon strip tracker. The pixel detector consists of three barrel layers and two disks in each endcap part. The pixel cells are identical to those described for the MSGC tracker. The silicon strip tracker is divided in two parts, the inner and the outer silicon tracker, as seen in figure 2.10. The inner silicon tracker consists in 4 barrel layers and 3 mini disks in each endcap. In this part, the silicon strip detectors (11×12 cm^2) are made of single sided sensors with a thickness of 300 μm. The outer part has 6 barrel layers and 9 forward disks made of 500 μm thick single and double sided detectors. For this part, the detectors will have dimensions of approximately 11×16 cm^2. The increase of the strip length, 16 cm compared to 12 cm in the inner part of the tracker, is expected to increase the noise by 15%. This will be compensated by the use of thicker sensors which will yield to an increase of more than 30% of the charge created by an incident particle. The reduction in the number of layers was driven by budgetary constraints. As a result, the all silicon tracker is approximately cost neutral with respect to the previous design. Simulations show that the tracking performance in terms of efficiency and momentum resolution remains practically unchanged due to the faster time response and to the higher detection efficiency assumed to be 100% for the silicon detectors instead of 98% for the MSGC's. An important parameter to take also into account is the amount of material which has to be as small as possible to avoid bremsstrahlung of electrons and photon conversion in front of the electromagnetic calorimeter. Moreover, a larger amount of material increases also the multiple scattering. Figure 2.11 shows the amount of material inside the tracker, expressed in fractions of radiation length, as a function of the pseudo-rapidity for the all silicon tracker layout. The use of semi-conducting detectors instead of gaseous detectors increases the amount

of material by almost 50%. Consequently electrons emitted at $\eta = 2$ will on average lose 45% of their energy by bremsstrahlung before reaching the electromagnetic calorimeter. In the case of photons, the probability of conversion before the calorimeter at $\eta = 2$ is as high as 37%. Consequently the all silicon tracker will significantly affect the measurement of electrons and photons.

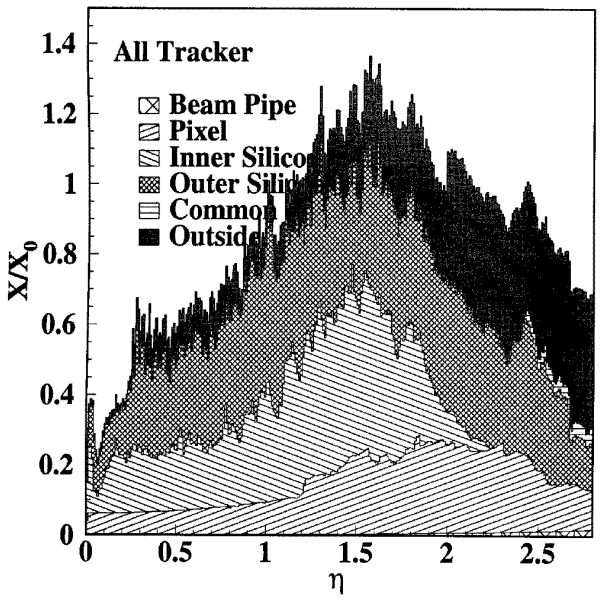

Figure 2.11: Thickness of the CMS tracker, expressed in fractions of radiation lengths as a function of the pseudo-rapidity for the all silicon tracker layout.

The radiation environment

The greatest challenge of the CMS tracker is the radiation hardness of its detector elements as well as the electronics; the tracking system must remain performant during several years at high luminosity. Two main sources contribute to the irradiation: the direct particle flux emerging from the interaction region and neutrons produced by nuclear interactions in the surrounding material. Figure 2.12 shows the expected radiation dose, the neutron and hadron fluences in the tracker as a function of z for several radii r in the tracker region. All values corresponds to an integrated luminosity of 5×10^5 pb^{-1}. The charged hadrons flux is almost independent of the z-coordinate and behaves roughly as $1/r^2$. It ranges from 10^{15} cm^{-2} at the innermost pixel layer to 3×10^{12} cm^{-2} at the outermost tracker layer. The neutron fluence rises with z, due to the intense source of albedo neutrons coming from the endcap part of the ECAL.

All silicon devices suffer from radiation damages and the most critical effect for the silicon counter is the change of doping concentration in the bulk of the substrate material. This results in an increase of the depletion voltage which can eventually exceed the breakdown limit of the material. With the full silicon tracker, the entire tracking system will therefore be operated at -10^{o}C.

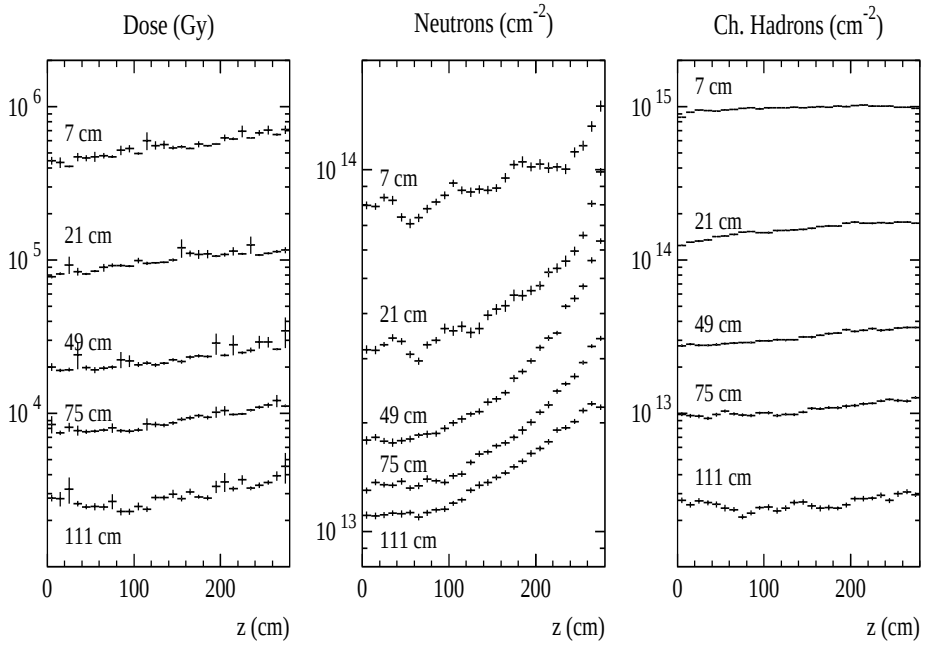

Figure 2.12: Radiation dose, neutron and charged hadron fluences, as a function of z-coordinate for different radii in the CMS tracker system. All values correspond to an integrated luminosity of 5×10^5 pb^{-1}.

2.5 The CMS trigger system

At LHC, the proton beams will cross each other at a frequency of 40 MHz. At the nominal luminosity of 10^{34} cm^{-2}s^{-1}, each crossing results on average in 17 $p-p$ inelastic events, generating a total of ~ 1 MB of data. Storing 1 MB of data at a rate of 40 MHz is several orders of magnitude larger than the current storing rates which are of the order of 100 Hz of events at a data rate of 100 MB/s. An online event selection, called trigger, is needed in order to inspect the detector data at the full crossing rate and to reduce it to a rate of 100 Hz, the maximum event rate that can be archived on disk. The rate reduction of at least a factor 10^5 is achieved with a multi-step trigger system selecting potentially interesting events with a clear signature like high p_T leptons and photons, high p_T jets and missing transverse energy. The CMS trigger system is subdivided in two separate steps, the level-1 trigger, based on the hardware, and the High Level Trigger (HLT), based on the software.

The level-1 trigger [19] has to absorb information from the CMS detector at the rate of 40 MHz. The time between successive beam crossings, 25 ns, and the wide geographical distribution of the electronic signals in the different CMS subdetectors render the processing of the complete detector data by fully programmable processing elements impossible. The time available in the level-1 trigger system is essentially dictated by the resources available in the front-end electronics to store the data during the level-1 decision-making process. Cost considerations dictate that the front-end electronics can store the data from 128 bunch crossings in pipelines, which provides 3.2 μs for the level-1 trigger decision. Therefore the level-1 trigger system operates on the front-end detector electronics using only coarsely segmented data from the muon system and from the calorimeters. The

level-1 trigger is designed to reduce the rate of events accepted for further processing to no more than 100 kHz.

The level-1 trigger is divided into three major subsystems as shown in figure 2.13: the level-1 muon trigger, the level-1 calorimeter trigger and the level-1 Global Trigger. The level-1 muon trigger uses the three muon subsystems: the Drift Tubes (DT), the Cathode Strip Chambers (CSC) and the Resistive Plate Chambers (RPC). Since each DT and CSC station is composed of several detection layers (see section 2.4.1), a first local trigger is performed in the front-end boards of the DT's and CSC's to build track segments. Afterwards regional tracking is performed to build muon track candidates from these segments. No local trigger is performed in the RPC's since they are arranged in single layers per muon station. The RPC trigger is based on a Pattern Comparator Trigger (PACT) which looks for RPC hits correlated in time and in space. The time coincidence also gives the bunch crossing identification to the muon candidate. Finally the candidates of the three subsystems are then delivered to the Global Muon Trigger which performs a matching according to the spatial coordinates and refines the track parameters p_T, η and ϕ.

The level-1 calorimeter trigger should be capable to select electrons, photons and jets over a large pseudo-rapidity range with high efficiency. Triggering on events with large missing energy is also required. The electron/photon trigger is based on the recognition of a large and isolated energy deposit in the electromagnetic calorimeter. In addition the energy deposit in the hadronic calorimeter behind the ECAL cluster should be small. The level-1 jet trigger sums the transverse energy computed in the ECAL and the HCAL. The four highest energy central and forward jets are selected. The missing transverse energy E_T is computed from all the calorimetry regions up to $|\eta| = 5$. The missing energy trigger is implemented with a number of thresholds. Some of these thresholds are used in combination with other triggers, namely jet triggers, in the search for SUSY events.

The Global Trigger accepts muon and calorimeter triggers information, synchronizes matching sub-system data arriving at different times and communicate the level-1 decision to the timing, trigger and control system to initiate the readout. The global trigger decision is made using logical combinations of the trigger data from the Global Muon Trigger and the Calorimeter Trigger. The CMS policy is to equally share the level-1 output rate between the four trigger streams: muons, electrons/photons, jets and mixed objects signatures. During the LHC running, the output rate attributed to each stream will probably be tuned with respect to the physics performance of the CMS experiment.

Given the output rate of 100 kHz for the level-1 trigger, the High Level Trigger will receive, on average, one event every 10 μs. This time is sufficiently long to allow the transfer of the data, through a network, from the front-end electronics into deep buffers which consist of commercial random-access memories. These buffers should permit to limit the dead-time of the data acquisition system to about 1%.

Experience with similar filtering processes in previous High Energy Physics experiments indicates that any further event selection has to be based on data that carry better granularity and resolution information than the corresponding data at level-1. Moreover, the algorithms employed must be almost as sophisticated as those utilized in the offline reconstruction of the events. This implies the use of fully programmable commercial processors for the execution of the HLT. The current estimate for the mean processing time per event is $\sim$ 50 ms for processors that will be available in 2007 [20].

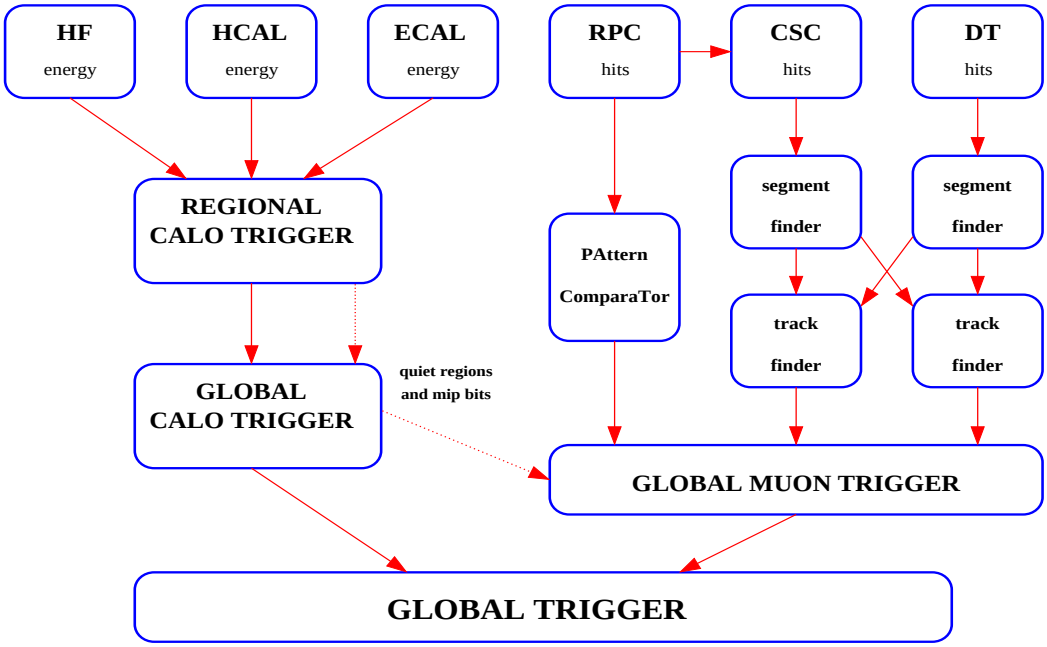

Figure 2.13: Layout of the CMS level-1 trigger.

The HLT is subdivided into three levels called level-2, level-3 and level-4. The main difference between these levels is the processing time. Given the performance of the current algorithms at each trigger level, it is expected that in 2007[1], the mean processing time at level-2 and at level-3 will be $\sim$ 40 ms and $\sim$ 60 ms respectively. The total HLT latency is one second. Assuming a factor 10 of rate reduction at each HLT step, we can estimate the number of CPU's needed for the HLT processing stage:

$$100\text{kHz} \times [(90\% \times 40\text{ms}) + (9\% \times 100\text{ms}) + (1\% \times 1\text{s})] \simeq 6000. \qquad (2.13)$$

This value is an indication and will probably change with the sophistication of the trigger algorithms used at the High Level Trigger and the evolution of the CPU processing power. A CPU farm containing up to 10,000 processors is considered manageable.

The time available for the decision puts constraints on the data that can be used at each level, as seen in table 2.3 which shows the rate, the processing time and the data available at each trigger level. Therefore the level-2 uses only the data from the calorimeters and the muon chambers. The data of the entire central tracker are only available from the level-3. The algorithms which have to run on the HLT processor farm must be fast and close to the algorithms that will be used for the offline analysis.

The most stringent requirement on the Data Acquisition (DAQ) system is the transfer of the data from the front-end modules to the commercial processors. On one hand the number of modules that store the various data of a CMS event after the acceptance of an event by the level-1 trigger amounts to roughly 700. This estimation takes into account the number of channels in the CMS subdetectors and the modularity of the various front-end electronics modules. On the other hand, several thousands of processors must be

[1]This estimation is based on Moore's Law, assuming that the CPU processing power increases by a factor 2 every 1.5 year.

	rate	processing time	data
level-1	100 kHz	3.2 μs	calo + μ (front-ends)
level-1 + safety factor	25 kHz 6 kHz/stream	3.2 μs	calo + μ (front-ends)
level-2	10 kHz 2.5 kHz/stream	40 ms on 2007 CPU	calo + μ (CPU farm)
level-3	1 kHz 250 Hz/stream	60 ms on 2007 CPU	calo + μ + tracker (CPU farm)
level-4	100 Hz 25 Hz/stream	900 ms on 2007 CPU	calo + μ + tracker (CPU farm)
HLT	100 Hz	1 s	(CPU farm)

Table 2.3: Rate, processing time and data available for the successive trigger levels.

employed for the HLT stage. The interconnection of such a large number of elements necessitates the introduction of a network. For this purpose, CMS has chosen to use a switching network with a sustained bandwidth of up to 10^5 Hz $\times$ 1 MB = 100 GB/s.

Chapter 3

Operation principles of gaseous detectors

The gaseous counters were the first electronic devices allowing precise tracking of ionizing particles. Their working principle is based on the ionization of gas molecules when a particle crosses the detector. The energy required to ionise is taken from the kinetic energy of the charged particle; this energy amounts typically to a few keV per centimetre of gas in normal conditions. The released electrons are drifted through the gas and amplified in avalanches inducing an electric signal on the electrodes which can be read-out.

In this chapter, we present various aspects of physics that are relevant to detect particles with gaseous counters. The basic principles of particle interaction with matter are given in section 3.1 and special emphasis is given to the electromagnetic interactions. Section 3.2 deals with the interaction of the photons with matter. In section 3.3 we report the drift and the diffusion of the charges inside the gas. In section 3.4 the avalanche process is described and the signal development in a proportional counter as well as its processing are discussed in section 3.5.

3.1 Particle interactions with matter

Two types of interactions must be considered for particle detection, i.e. the electromagnetic and the nuclear interactions. In gaseous detectors, the electromagnetic interaction is the most important in terms of energy loss and will therefore be described in detail. A fast charged particle traversing a gaseous or condensed medium will interact with the atomic electrons and the nuclei located along the particle trajectory through their electromagnetic field. Thanks to the highly probable Coulomb scattering a charged particle leaves a track even in thin samples of material, as for example a few millimeters of gas. Charged particles can undergo several processes:

- inelastic collisions with atomic electrons: the charged particle interacts with matter through Coulomb forces between its charge and the negative charge of the orbital electron, resulting in both excitation and ionization of the atoms of the absorber material;

- emission of bremsstrahlung photons in the Coulomb field of the nuclei and of the atomic electrons. The energy loss of this process depends on the ratio of the particle energy to its mass squared. Consequently, this process dominates the ionization loss for electrons at energies as low as 10 MeV but for muons and pions, the transition occurs at several hundreds of GeV;

- Elastic scattering on the nuclei and on the atomic electrons, leading to modifications in the particle direction;

- Electron-positron pair production.

Since the particle detection with gaseous counters relies mainly on the first of these processes, it is described here in detail. On the other hand, since the e^+e^- pair production occurs for ultra-relativistic particles (beyond several hundred of GeV for muons in rock [21]), this process will only be discussed in the case of the photon detection, in section 3.2.

3.1.1 Energy loss due to electromagnetic interactions

Relativistic charged particles heavier than the electron lose energy by collisions with atomic electrons creating excited atoms or electron-ion pairs. The quantum expression of the mean energy loss per unit length of traveled material, normalized to the medium density, is given by the Bethe-Bloch equation [22]:

$$-\frac{dE}{\rho dx} = \kappa z^2 \frac{Z}{A}\frac{1}{\beta^2}\left[\frac{1}{2}\ln\frac{2m_e c^2\beta^2\gamma^2 T_{max}}{I^2} - \beta^2 - \frac{\delta}{2}\right], \tag{3.1}$$

where ρ, A, Z, and I are respectively the density, the atomic weight, the atomic number, and the effective ionization potential of the material. z is the particle charge and $\beta = v/c$ is its velocity. The constant κ is equal to 0.307 MeV g^{-1} cm^2. In this equation, T_{max} represents the maximum energy transfer allowed in each single collision and it is given by

$$T_{max} = \frac{2m_e c^2\beta^2\gamma^2}{1 + 2\gamma\frac{m_e}{M} + \left(\frac{m_e}{M}\right)^2}, \tag{3.2}$$

where M is the mass of the incident particle. The Bethe-Bloch function is shown in figure 3.1 for various materials.

Inspection of Eq. (3.1) shows that the differential energy loss depends only on the velocity β of the incident particle and does not depend on its mass; the dependence on M introduced through T_{max} is negligible and becomes sizeable at high energy, about 100 GeV for pions. The energy loss is only slightly dependent on the chemical composition of the material; the ratio $\frac{Z}{A}$ drops slowly with increasing Z ($\leq$0.5 for most elements). The minimum energy loss in hydrogen is exceptionally large, because here, $\frac{Z}{A}$=1.

At low energy, the ionization loss falls with the $\frac{1}{\beta^2}$ term and reaches a broad minimum at $3 \leq \beta\gamma \leq 4$. For most materials, $\frac{dE}{dx}$ is equal to about 2 MeV g^{-1} cm^2 at the minimum. At relativistic velocities ($\gamma \gg 1$) Eq. (3.1) is dominated by the logarithmic term. This rise, called the logarithmic rise, results from two causes. First the transverse component of the particle electric field acquires a factor γ when transformed into the laboratory frame. Consequently the field of the particle extends to greater distances from the trajectory and

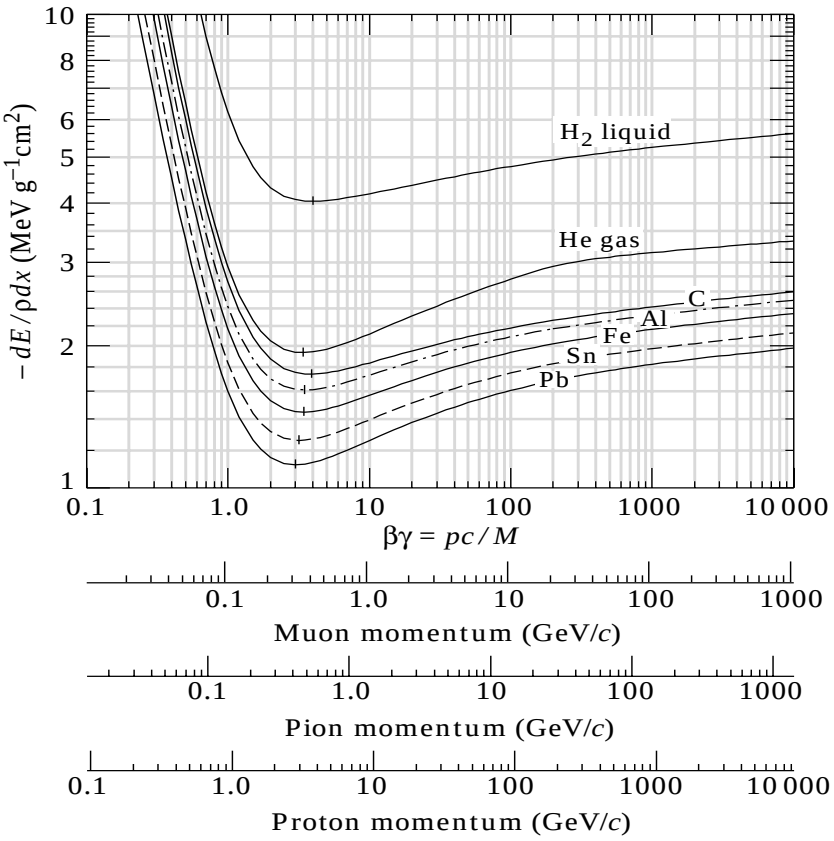

Figure 3.1: Energy loss of heavy charged particles as a function of the particle momentum for muons, pions and protons in various materials.

more collisions occur. Secondly the maximum transferable energy T_{max} rises as γ^2. At ultra-relativistic speeds, the energy loss reaches a plateau, called the Fermi plateau. The cancellation of the relativistic rise results from the medium polarization by the incident particle electric field. This shielding limits the extension of the field and reduces the influence of collisions with a large impact parameter.

In the present high energy physics experiments most of the particles produced have an energy close to the minimum and are therefore called minimum ionizing particles (MIP). In contrary the slow particles, undergoing a huge ionization, are called highly ionizing particles (HIP).

The total energy deposited by an ionizing particle in a thin gas volume results from a small number of interactions, each having a large range of possible energy transfers. Therefore the total energy fluctuates around the most probable value given by equation (3.1) with an asymmetric distribution, called Landau distribution, which can be approximated by [23]

$$f(\lambda) = \frac{1}{\sqrt{2\pi}} e^{-\frac{1}{2}(\lambda + e^{-\lambda})}, \tag{3.3}$$

where λ is a reduced variable representing the normalized deviation of the energy loss to the most probable energy loss, $\lambda = \frac{\Delta E - (\Delta E)_{mp}}{\xi}$; $\xi = \kappa z \frac{Z}{A} \frac{\rho}{\beta^2} x$ is a factor proportional to

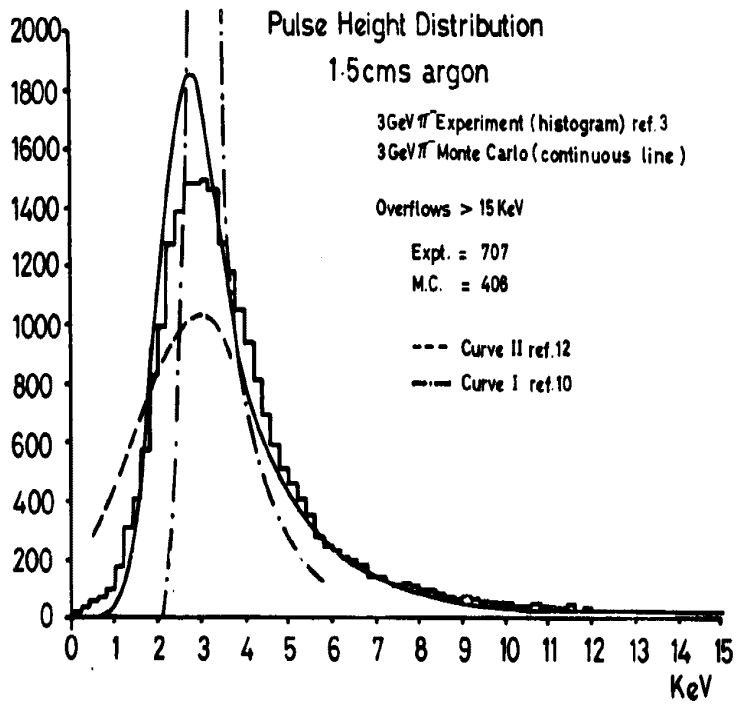

Figure 3.2: Experimental energy loss distribution for 3 GeV π^- in a thin proportional counter (1.5 cm) filled with argon. The solid curve represents the distribution computed from the model of Cobb et al. and the dashed dotted curve corresponds to the Landau's theory.

the length x of the absorber material. Landau was the first to calculate the fluctuations of the energy loss around the mean for thin absorbers [24]. He considered the electrons as free and the energy transferred to the electrons was supposed to be large compared to the electron binding energy. In the seventies several models have been introduced including the contribution of the low energy transfers. Figure 3.2 shows the energy loss distribution for 3 GeV π^- in 1.5 cm of argon at atmospheric pressure. The experimental curve is compared to a Landau distribution and to the model of Cobb et al. [25]. It shows that the model of Cobb et al. is closer to the experimental data.

3.1.2 Primary and secondary ionization

We have seen that a particle crossing the sensitive volume of a gaseous counter will create few pairs of electrons and ions. The emitted electrons have a kinetic energy equal to the energy lost by the incident particle minus the atomic binding energy. These electrons are called primary electrons or δ-rays. When these primary electrons have an energy greater than the ionizing potential of the medium, they can also ionize atoms A by the process

$$e^- + A \rightarrow e^- + A^+ + e^-, \tag{3.4}$$

Both contributions form the total ionization and generally the average number of electron-ion pairs created by unit length n_T is expressed by :

$$n_T = \frac{1}{W_i}\frac{dE}{dx}, \tag{3.5}$$

where $\frac{dE}{dx}$ represents the energy loss per unit length and W_i, the mean energy needed to create one ion-electron pair. Table 3.1 gives the W_i and n_T values for different gases as well as the primary electron density n_P and the ionization potential I. W_i is about twice the value of I because of the energy lost by excitation.

In the case of a mixture we use the following equations to determine the primary and the total ionizations:

$$n_P = \sum_{i=1}^{n} (n_P)_i p_i \tag{3.6}$$

$$n_T = \sum_{i=1}^{n} (n_T)_i p_i \tag{3.7}$$

where p_i represents the percentage of the ith-gas and $(n_P)_i$ and $(n_T)_i$ are respectively the average number of primary and secondary electrons produced in the ith-gas. The sum is performed on the different components of the mixture.

Gas	n_P (cm^{-1})	n_T (cm^{-1})	W_i (eV)	I (eV)
He	3.3	7.6	42.3	24.6
Ne	10.9	39.9	36.4	21.6
Ar	24.8	96.6	26.3	15.8
Kr	33.0	197.5	24.0	14.0
Xe	44.8	313.3	21.9	12.1
CO_2	33.6	100.0	32.8	13.8
CH_4	24.8	59.3	27.1	12.7
DME(CH_3-O-CH_3)	55	160.0*	23.9	10.0
iso-C_4H_{10}	83.6	232.8	23.2	10.5

Table 3.1: Properties of several gases commonly used in gaseous detectors. n_P and n_T are the primary and total ionization densities at standard temperature and pressure for minimum ionizing particles. W_i is the effective mean energy to produce one electron-ion pair and I is the ionization potential. (*)In the literature the total ionization density of DME varies from 160 to 200 cm^{-1}.

The number of primary ionizations follows a Poisson distribution and the probability to have k primary electrons after a distance x traversed by the incident particle is :

$$P(k) = \frac{(n_p x)^k}{k!} exp(-n_P x). \tag{3.8}$$

From this expression one can calculate the theoretical inefficiency of an ideal detector of thickness x which is equal to the probability of having no primary electron released by the incident particle inside the sensible volume, that is $P(0) = exp(-n_P x)$. In section 3.4 we will see that the amplitude of the detected signal is proportional to the number of electrons released in the gas volume and thus to the total ionization density (n_T). Therefore a gas with high primary and total ionization densities is required to obtain a high detection efficiency and large signals. Moreover it will be shown in section 3.4.2 that the energy resolution improves with n_T.

3.1.3 Bremsstrahlung

If a charged particle is decelerated in the Coulomb field of a nucleus, a fraction of its kinetic energy will be emitted in form of real photons called bremsstrahlung photons. The emission probability varies as the inverse square of the particle mass and the bremsstrahlung is thus essentially produced by electrons. For instance the radiation loss by muons (m = 106 MeV), the next lightest particle, is 40,000 times smaller than for electrons at the same energy; the radiation loss is negligible for heavier particles at the current energies of particle physics today. It is convenient to define the critical energy corresponding to the energy at which the losses due to ionization and bremsstrahlung are equal. In iron the critical energy is about 25 MeV and 960 GeV for electrons and muons respectively.

In an experiment like CMS, the bremsstrahlung may affect the detector performance. Because of the tracker material, high energy electrons suffer from bremsstrahlung before reaching the electromagnetic calorimeter. On one hand this increases the photon background in the electromagnetic calorimeter. On the other hand it renders difficult the reconstruction of the electron trajectories because of the discontinuities in the curvature at the photon emission points. Consequently it is crucial to limit the material amount of the Tracker located before the calorimeters. It is convenient to measure the thickness of the detector material in terms of the radiation length X_0 defined as the distance over which the electron energy is reduced by a factor 1/e due to radiation loss only. For instance, in the all silicon Tracker of CMS, each detection layer with its support structure and cabling has a thickness of about 7% of a radiation length.

3.1.4 Multiple Coulomb scattering

In addition to inelastic collisions with the atomic electrons, charged particles passing through matter also suffer repeated elastic Coulomb scatterings from nuclei. For small angle multiple scatterings, the cumulative effect is a net deflection from the original particle direction. The deflection angle distribution, projected onto a plane parallel to the direction of the incident particle, is Gaussian with a standard deviation given by [28]:

$$\theta_0 = \frac{13.6MeV}{\beta cp} z \sqrt{\frac{x}{X_0}} \left[1 + 0.038 \ln \frac{x}{X_0} \right] \tag{3.9}$$

where β, p and z are the velocity, the momentum and the charge of the incident particle, x and X_0 the material thickness and the radiation length respectively.

In the CMS tracker, multiple scattering will cause a deflection of 0.3 milliradians for 10 GeV particles at each detection layer. Consequently the uncertainty on the particle impact coordinates at the next detection layer will be of the order of 30 μm which is comparable to the detector resolution. This indicates that multiple scattering must be accounted for in track reconstruction. The multiple scattering also affects the efficiency to reconstruct a muon trajectory in the muon and the tracker systems. Combining the muon chambers and the inner tracker, a momentum resolution of less than 1.2% over the entire η range can be reached for muons with a momentum lower than 70 GeV [14]. This requires the matching of track segments in the muon system with the correct track in the central tracker in presence of several accompanying tracks. This matching efficiency is limited

for low transverse momentum muons ($p_T \leq 10$GeV) because of the multiple scattering in the calorimeters and the magnet. The error in the $R\phi$-coordinate, extrapolated from the innermost muon station towards the outermost tracker layer, increases from 0.2 cm at $p_T = 100$ GeV to ~ 3 cm at $p_T = 10$ GeV for η=0 [14].

3.2 Photon detection

As numerous measurements in this work have been carried-out with X-rays, the detection of photons will be described in detail in this section. The detection of photons is based on the electromagnetic interaction as for charged particles. The attenuation of a photon beam traversing a thickness x of a medium having N molecules per unit volume is given by

$$I = I_0 e^{-\sigma N x} = I_0 e^{-\mu X} \tag{3.10}$$

where σ is the total cross section of photon interactions, μ is the mass attenuation coefficient, expressed in cm^2 g^{-1} and $X = \rho x$ is the reduced thickness of the medium. The total cross section σ is the sum of the cross sections of three different mechanisms. At low energies, up to several keV, the dominant process is the photoelectric absorption. The Compton scattering dominates up to a few hundred of keV and at higher energies electron-positron pair production is the most probable process. The coherent scattering refers to the Compton scattering on strongly bound electrons. Figure 3.3 represents the absorption cross-section of each process and their sum, in argon, as a function of the γ-ray energy.

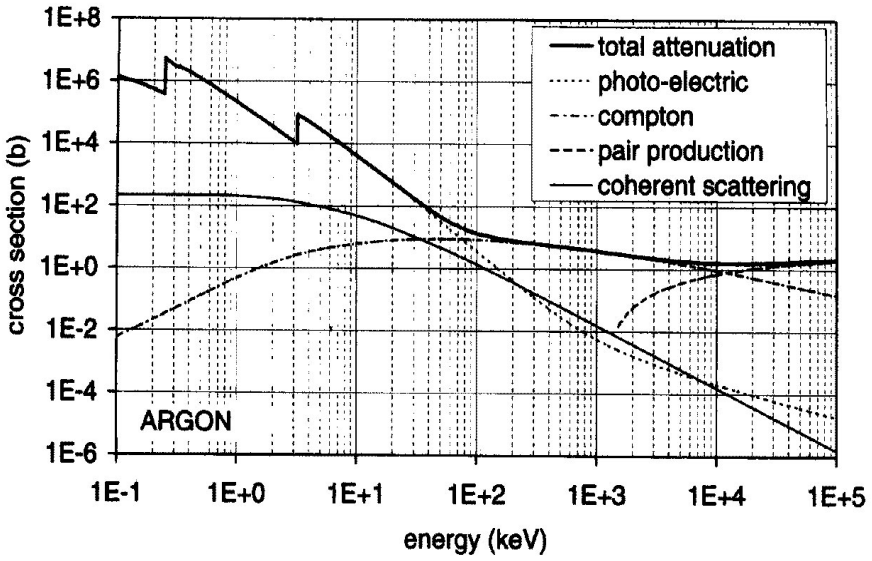

Figure 3.3: Absorption cross-sections in argon for γ-rays as a function of their energy.

3.2.1 Photoelectric absorption

The photoelectric absorption is an important process in the use of gaseous counters for two reasons. First it is common to use radioactive isotopes emitting low energy photons of

a few keV to test the gaseous detectors in the laboratory. Secondly, possible applications of micro-pattern gaseous counters are the detection of X-rays in medical radiography or in X-ray astronomy [29].

The photoelectric absorption is a quantum interaction between the incident photon and an atomic electron which is emitted with a kinetic energy $E_K \simeq E_\gamma - E_j$, where E_γ and E_j are the energy of the incident photon and the energy of the j^{th} electron shell, respectively. For energy-momentum conservation this mechanism can not occur on a free electron. During this process the photon is absorbed and gives up all its energy. For a given photon energy, the contribution of all shells having $E_j \leq E_\gamma$ add up. The photoelectric cross-section decreases rapidly with the photon energy and presents discontinuities at values corresponding to the different electron binding energies as seen in figure 3.4, which displays the photoelectric cross section as a function of the photon energy for different noble gases commonly used with proportional counters. For a given photon energy, the lightest elements have the smallest absorption coefficients. Especially the organic vapours used as quencher in gaseous counters have a very small photoelectric absorption coefficient since they are mainly composed of light elements.

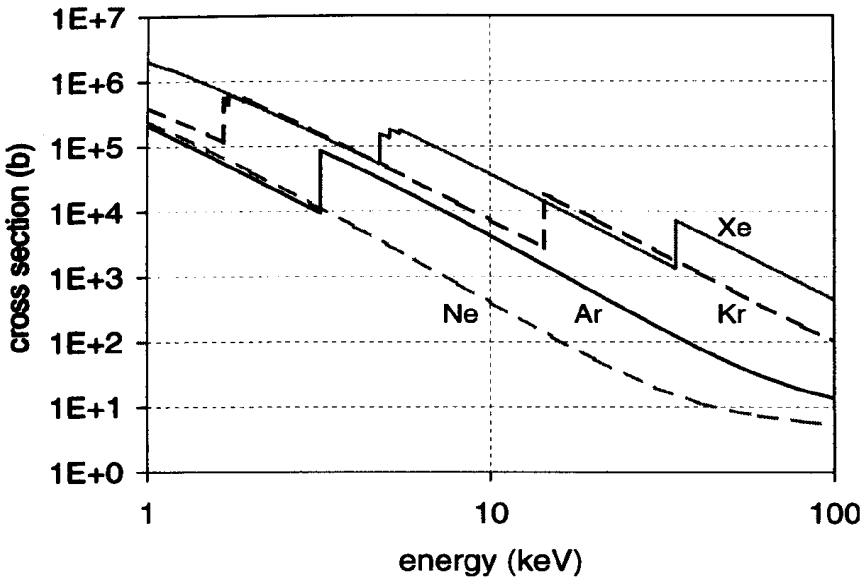

Figure 3.4: Cross sections for photoelectric effect as a function of the photon energy in several noble gases.

The excited molecule can return to its ground state by two different processes: fluorescence or radiationless transitions called Auger effect. The fluorescence occurs when the empty position left by the photo-electron is almost immediately (within $\sim 10^{-14}$s) filled by an electron from a shell of energy $E_i \leq E_j$. This transition is accompanied by the emission of a photon with an energy equal to $E_j - E_i$. The Auger effect occurs due to an internal rearrangement involving several electrons of the lowest energy shells accompanied by the emission of an additional electron of energy very close to E_j.

As an example, consider the absorption of 5.9 keV photons emitted by a ^{55}Fe source, in an argon-based gas mixture. The binding energy of the K shell is 3.2 keV for argon. Therefore a K shell emitted electron receive a kinetic energy of 5.9 keV - 3.2 keV = 2.7 keV. With argon almost the entire binding energy of 3.2 keV is picked-up by an Auger electron in 85% of the events. In the other 15% of the cases, a fluorescence X-ray is

emitted. This X-ray, having a typical energy of 3 keV, is likely to escape the gas volume. Therefore not all the initial 5.9 keV energy is deposited in the gas volume, but in this case only 2.7 keV, which causes a second peak, called escape peak, in the energy spectrum of fluorescent gas mixtures.

3.2.2 Compton scattering

At energies above a few tens of keV, the Compton scattering dominates the photon absorption mechanisms. The incident photon of energy $h\nu_i$ is scattered by a quasi-free electron by an angle θ and takes the energy $h\nu_f$. The energy of the hit electron becomes :

$$h\nu_i - h\nu_f = h\nu_i \frac{\gamma(1 - cos\theta)}{1 + \gamma(1 - cos\theta)} \tag{3.11}$$

Quantum-mechanical theory provides the differential cross sections for Compton scattering by a single electron. Figure 3.5 shows the computed absorption coefficient by Compton scattering as a function of the photon energy for different elements [30]. For an energy of 10 keV in argon, the absorption coefficient by Compton scattering is two orders of magnitude smaller than by photoelectric absorption (see figure 3.3). Therefore, in the following of this work, we will neglect the Compton scattering when we study the performance of gaseous counters using X-rays with an energy of 5.9 keV or 8.3 keV (see chapters 5 and 6).

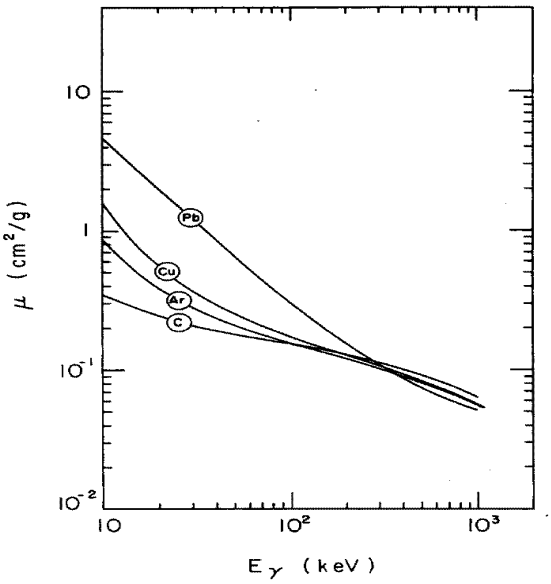

Figure 3.5: Absorption coefficient for Compton scattering as a function of the photon energy for several gases [30].

3.2.3 Electron-positron pair production

The electron-positron pair production takes place at photon energies above the threshold of 1.02 MeV corresponding to two times the electron mass. For energy-momentum conservation the pair production occurs in the electromagnetic field of a nucleus or of an

electron. It is convenient to define a quantity called conversion length λ_{pair}. It corresponds to the distance after which a photon beam is attenuated by a factor e by creation of pairs only.

In high energy physics experiments, the electron-positron pair production degrades the performance of the detectors especially the electromagnetic calorimeter since it renders the identification of photons difficult. In the CMS experiment 32% of the photons produced by H$\rightarrow\gamma\gamma$ convert in the Tracker. Consequently both photons reach the electromagnetic calorimeter in only 46% of these Higgs decays.

3.3 Drift and diffusion of electrons in gases

The performance of a gaseous detector depends on the drift and diffusion of the electrons and ions. The electron drift velocity determines the ionization collection time and therefore the speed of the detector response. The diffusion is responsible for the spread of the ionization cloud in the gas volume which affects the determination of the particle crossing point. Before discussing the influence of the drift velocity and the diffusion on the detector performance, we shall try first to get a general understanding of the phenomena at play.

3.3.1 Drift and diffusion from a macroscopic model

The motion of charged particles under the influence of electric and magnetic fields, $\mathbf{E}$ and $\mathbf{B}$, may be understood in terms of an equation of motion with friction:

$$m\frac{d\mathbf{u}}{dt} = e\mathbf{E} + e[\mathbf{u}\times\mathbf{B}] - K\mathbf{u}, \tag{3.12}$$

where m and e are the mass and the charge of the particle, $\mathbf{u}$ is its velocity and $K\mathbf{u}$ is a frictional force caused by the collisions of the particle with the gas molecules. $\tau = m/K$ has the dimension of a time, and depends on the gas through the parameter K. The drift velocity $u = |<\mathbf{u}>|$, which is the average of all drifting electrons, is also a solution of equation 3.12. For large t ($t >> \tau$) the increasing friction force compensates the accelerating electromagnetic force leading to a constant drift velocity u, solution of the steady state equation $d<\mathbf{u}>/dt = 0$:

$$\frac{<\mathbf{u}>}{\tau} = \frac{e}{m}(\mathbf{E} + <\mathbf{u}>\times\mathbf{B}). \tag{3.13}$$

In this equation, the right hand side corresponds to the acceleration of the electron between two collisions, due to the electromagnetic force, and therefore τ can be considered as the average time between two collisions. In the absence of a magnetic field, equation 3.13 gives the drift velocity:

$$u = \frac{e}{m}E\tau = \mu_e E, \tag{3.14}$$

where $\mu_e = \frac{e\tau}{m}$ is defined as the electron mobility.

Although the macroscopic treatment gives a global understanding of the electrons behaviour under an electric and magnetic field, it is not able to describe the diffusion of electrons nor the drift velocity dependence on the the electric field intensity as for electrons τ may depend on the electric field E. To have a deep understanding of these parameters, a microscopic treatment is mandatory.

3.3.2 Drift and diffusion from a microscopic model

A simple classical model relates the macroscopic transport parameters and the variables describing the microscopic motion of the drifting electron. This model provides a theoretical understanding of the behaviour of the electron drift velocity and diffusion in gas mixtures as a function of the electric field intensity.

Charge diffusion in the absence of electric field

In the absence of an electric field, the gas molecules are submitted to the thermal agitation described by the classic kinetic theory. The charges released by an ionizing particle behave in a similar way: the classic kinetic theory attributes to each particle having three degrees of freedom an average kinetic energy ϵ_T of $\frac{3}{2}kT \simeq 0.04$ eV in the normal conditions of temperature and pressure, where k is the Boltzmann's constant and T, the gas temperature. In absence of other forces, charges locally distributed diffuse by multiple scattering following the Gaussian law,

$$\frac{dN}{dx} = \frac{N_0}{\sqrt{4\pi Dt}} exp(-\frac{x^2}{4Dt}), \tag{3.15}$$

where N_0 is the total number of charges, D is the diffusion coefficient and $dN(x)$ represents the fraction of charges located in the element dx at the distance x from the initial point, at the time t. The standard deviation of the distribution in one dimension is given by

$$\sigma_x = \sqrt{2Dt}. \tag{3.16}$$

At three dimensions the standard deviation of the spherical distribution is given by

$$\sigma(r) = \sqrt{6Dt}, \tag{3.17}$$

where r is the radial distance. The diffusion coefficient is a parameter which can be calculated from the kinetic theory and it will be shown later to be related to the kinetic energy ϵ:

$$D = \frac{2}{3}\frac{\epsilon}{m}\tau = \frac{3}{2}kT\frac{2}{3}\frac{\tau}{m}, \tag{3.18}$$

where τ is the average time between collisions. Equation 3.18 shows that due to their smaller mass the diffusion coefficient of electrons is much larger than the coefficient of ions.

Electron drift velocity and diffusion in the presence of an electric field

In the presence of an external electric field, between the collision, the electrons and the ions are accelerated along the field lines towards the anode and the cathode respectively and the average kinetic energy increases :

$$\epsilon = \frac{1}{2}mv^2 = \epsilon_E + \frac{3}{2}kT, \tag{3.19}$$

where ϵ_E is the average energy acquired from the electric field. At drift field values commonly used in gaseous detectors, above a few hundred of V/cm, and in most gases, ϵ_E amounts up to a few electron-volts. Therefore the contribution of the thermal energy can be neglected.

drift velocity

Because of its small mass, an electron is scattered isotropically during a collision; immediately after the collision, the electron has no preferential direction. However in a time interval τ between two collisions, the electron has acquired an extra velocity u given by equation 3.14. This extra velocity appears macroscopically as the drift velocity ($u << v$).

At every collision, the electron loses a fraction λ of the energy ϵ_E acquired from the external field. Therefore there is a balance between the energy picked up and the collision losses. Over a distance x in the direction of the field, the number of collisions is equal to the drift time $\frac{x}{u}$ divided by τ and the energy balance can be written as :

$$\frac{x}{u\tau}\lambda\epsilon_E = eEx. \tag{3.20}$$

For drifting particles with an instantaneous drift velocity v, the average time τ between two consecutive collisions can be expressed as a function of the cross section σ and the molecular density N:

$$\frac{1}{\tau} = N\sigma v. \tag{3.21}$$

For electron drift in gaseous detectors, we can neglect the thermal motion, and equations 3.14, 3.19 and 3.20 combine to give the expressions of the equilibrium velocities:

$$u^2 = \frac{eE}{mN\sigma}\sqrt{\frac{\lambda}{2}}, \tag{3.22}$$

$$v^2 = \frac{eE}{mN\sigma}\sqrt{\frac{2}{\lambda}}. \tag{3.23}$$

These equations show that to understand the behaviour of the drift velocity, we have to look at the curves of the average kinetic energy or the characteristic energy $\epsilon_K = (2/3)\epsilon$ as a function of the electric field as well as at the dependence of the fractional energy loss λ and the collision cross section σ on the electron energy. These curves are shown for argon and CH_4 in figures 3.6 and 3.7 a) - b) respectively. In pure argon ϵ_K slowly increases from $\sim$ 3 to 10 eV for electric fields ranging from 100 to 2000 V/cm. At these energies, we observe in figures 3.7 a) and b) that the collision cross-section is close to its maximum of 10^{-15} cm^2 and that the fractional energy loss is constant and very small, around 2×10^{-5}. This small fractional energy loss value is due to the fact that in a noble gas like argon, the only possible collisions below the excitation threshold are elastic. Therefore expression 3.22 suggests that the drift velocity in argon is low as shown in figure 3.8 which displays the drift velocity in Ar-based gas mixtures as a function of the reduced electric field E/p.

Figure 3.8 also shows that the addition of a small amount of methane to argon drastically modifies the drift velocity due to the variations of σ and λ. Indeed the polyatomic molecules CH_4 have various rotation and vibration excitation levels which can be excited by collisions with low energy electrons; the excitation threshold for methane is 0.03 eV instead of 11.5 eV for argon. This results in a much larger value of λ in CH_4 as compared to Ar (see figure 3.7 b). Consequently adding a small amount of CH_4 to Ar will increase the drift velocity.

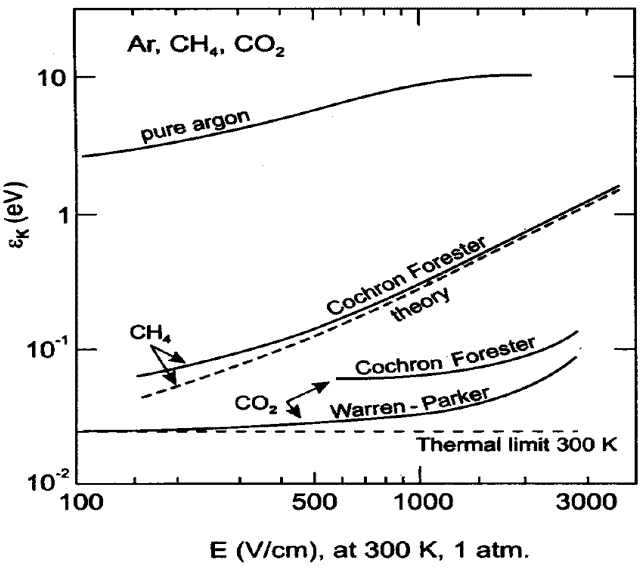

Figure 3.6: The electron characteristic energy ϵ_K as a function of the electric field in argon, CO_2 and CH_4.

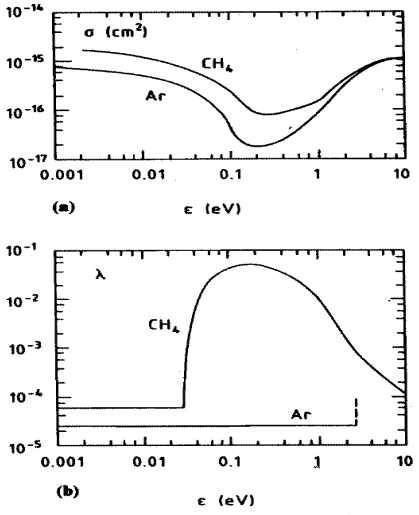

Figure 3.7: Collision cross section in argon and CH_4 (a) and fractional energy loss per collision as a function of the electron energy (b).

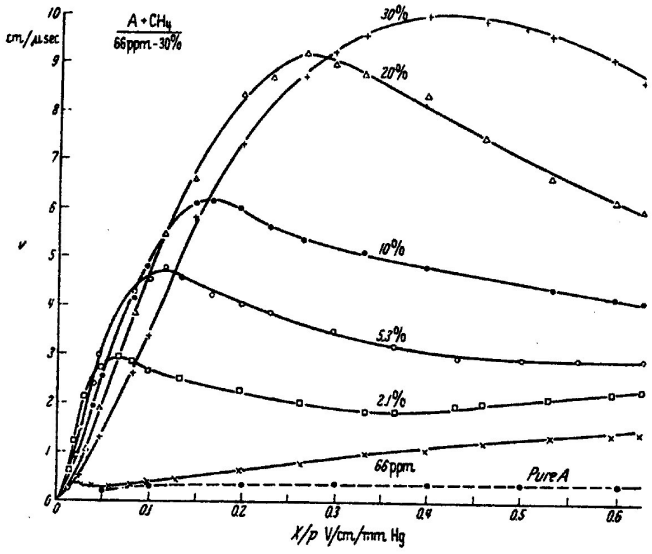

Figure 3.8: The electron drift velocity as a function of the reduced electric field E/P for different mixtures of Ar/CH_4.

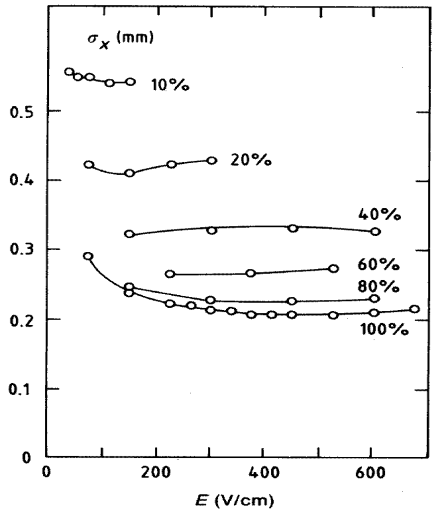

Figure 3.9: Width of the electron cloud after a drift of 1 cm for various mixtures of Ar/CH_4 at atmospheric pressure. The upper curve corresponds to the Ar/CH_4-90/10% gas mixture.

diffusion of the electrons

To express the diffusion coefficient in terms of the microscopic variables, let us consider the isotropic diffusion of the electron. After a time t at which a large number of collisions N have already occurred, the mean squared displacement in direction $\mathbf{x}$ is given by :

$$\sigma_x^2 = \sum_{i=1}^{N} x_i^2 = n < x^2 >, \tag{3.24}$$

where $< x^2 >$ denotes the mean squared displacement between two collisions. As the free path l between two collisions is distributed as a decreasing exponential we can write

$$< x^2 >= \int_0^{+\infty} \frac{dl}{l_o} \int_{-1}^{+1} (l cos\theta)^2 e^{-l/l_0} \frac{dcos\theta}{2} = \frac{2}{3} l_0^2, \tag{3.25}$$

where $l_0 = v\tau$ is the mean free path between two collisions. Replacing t by $n\tau$, equation 3.16 becomes:

$$D = \frac{2}{3}\frac{l_0}{2t} = \frac{2}{3}\frac{\epsilon}{m}\tau. \tag{3.26}$$

The diffusion is also very often expressed in centimeters per unit of drift distance z:

$$D' = \frac{\sigma_x}{\sqrt{z}}, \tag{3.27}$$

and so, the width of the electron cloud is proportional to the square root of the drift distance. Equation 3.26 shows that a small electron energy is required in order to have a small diffusion coefficient. Figure 3.6 shows that the characteristic energy in methane is one order of magnitude smaller than in argon. Therefore adding some percentage of CH4 to Ar will reduce the diffusion as observed in figure 3.9.

Several gases like Di-Methyl-Ether (DME) and CO_2 (see figure 3.6) have a constant kinetic energy around $(3/2)kT$ in a large electric field range, up to 1 kV/cm. Beyond this value, called the thermal limit, the electron energy rises slowly with increasing electric field. In this case the diffusion coefficient is very small ($\sim$ 70 μm/cm at 1000 V/cm) and constant. These gases are generally added to a noble gas to decrease the diffusion and to permit a better localization accuracy.

longitudinal diffusion

Since the experiment of Wagner at al. in 1967 [32], it has been observed that the value of the electron diffusion in the direction of the electric field can be quite different from that in the transverse direction. Therefore we introduce two diffusion coefficients D_L and D_T respectively for the longitudinal and the transverse direction with respect to the electric field. The electron diffusion anisotropy is theoretically explained by a difference in mobility for the electrons located in the leading edge and in the center of the electron cloud [31].

3.3.3 Electron attachment

During their drift in the gas the electrons may be absorbed by molecules to form negative ions. Although the noble gases and the organic molecules can form only stable negative ions at energies beyond several electron-volts, some molecules can attach the electron at much lower energies. Such molecules, called electronegative, are sometimes present in the gas mixture as impurities. The gases presenting the largest electron affinities are the halogenides, water and oxygen. Therefore a clean gas system is required to avoid any contamination due to air or water vapour. The basic process of electron attachment depends in first order on the electron energy. If the energy is close or above the threshold for molecular dissociation (4.6 eV for $O_2 \rightarrow O^- + O^+$ and 5.5 eV for $H_2O \rightarrow OH^- + H^+$) the free electrons get easily absorbed by the positive ion and we observe a rapid increase of the attachment cross section with increasing electric field. This situation can be met in modern micro-pattern gaseous counters which are operated with a high drift field, up to 10 kV/cm for MSGC's.

In 1935 Bloch and Bradbury [33] proposed a three-body process for electron attachment by oxygen molecules below the threshold for molecular dissociation. This mechanism can play a role in drift chambers where the drift field is typically of the order of 0.5 kV/cm and the mean electron energy mainly below 1 eV. This mechanism occurs in two steps. First, the electron encounters an electronegative molecule like O_2 and forms the excited and unstable state O_2^{*-}. Unless the excitation energy is carried away by a third body M, the O_2^{*-} ion will lose its electron which is then no longer attached. The attachment probability depends strongly on the nature of the M molecule; a complex molecule like isobutane has various vibration and rotation energy levels and is therefore more likely to absorb the excitation energy by the process

$$O_2^{*-} + M \rightarrow O_2^- + M^*. \tag{3.28}$$

Noble gases like argon have no vibration level and are inert from the view-point of electron attachment and therefore favour the reaction

$$O_2^{*-} + M \rightarrow O_2 + M + e^-. \tag{3.29}$$

The three body attachment coefficient with O_2 involving the methane molecule can be large enough to produce charge losses in large drift chambers were the methane is used as quencher. At 8.5 bar, a O_2 contamination of 1ppm will cause an absorption of $\sim 3\%$ per meter of drift at a velocity of 60 μm/ns.

3.3.4 Ion drift

Because of their large mass, comparable to the mass of the gas molecules, the behaviour of ions differs from that of electrons. In the same electric field the ions acquire on one mean free path an amount of energy which is similar to the energy picked-up by an electron in the same conditions. However a large fraction of this energy is lost at the next collision. Consequently their energy remains mostly thermal which results in a diffusion being two orders of magnitude smaller than for the electrons. This also implies that the ion mobility, μ_i, is constant and their drift velocity linearly increases with the electric field. Typically the ion mobility is 10^4 smaller than the electron mobility.

In a gas proportional counter, the particle detection is based on the read-out of electric signals induced by the motion of charges, created in the avalanche and drifting towards the electrodes. We will see in section 3.4.2 that most of the signal is due to the motion of the ions. Therefore, the ion drift speed determines the time development of the signal.

3.4 The avalanche process

The working principle of gaseous detectors is based on the process of ionizing collisions leading to an avalanche development. In an electric field of a few kV/cm, electrons acquire a sufficient energy between two consecutive collisions to produce inelastic phenomena as the excitation or the ionization of gas molecules. However all the gases behave differently depending on the complexity of the molecules. For instance, noble gases can only be excited by the absorption or the emission of a photon while hydrocarbures, generally composed of multiple atoms, also present rotational and vibrational excitation modes.

When the energy becomes larger than the ionization potential, ionization may occur and an electron-ion pair is created while the first electron continues to drift. The ionization mean free path is defined as the average distance between two ionizing collisions. The inverse of this mean free path α is called the first Townsend coefficient and represents the number of electron-ion pairs created per unit length.

Now consider one single electron released by an ionizing particle drifting in a gas volume with a high and uniform electric field. After an average distance α^{-1}, an ion-electron pair will be created and two electrons will continue their drift to generate after another α^{-1} two other pairs and so on. For a number of electrons N, at a given potential, after a path dx, the increase in the number of electrons is given by

$$dN = N\alpha dx. \tag{3.30}$$

The coefficient α is determined by the excitation and ionization cross sections and depends

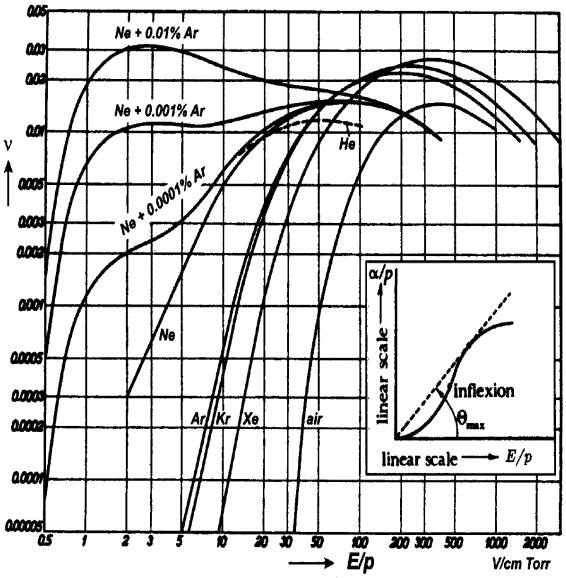

Figure 3.10: Amplification coefficient $\nu = \alpha/E$ in V^{-1} as a function of the reduced electric field in various noble gases, air and in mixtures of neon with argon.

in a complicated manner on the electron energy distribution. Therefore no fundamental expression of the Townsend coefficient exists and it must be measured for every gas and in a large range of electric fields. The total gain is obtained by integrating Eq. (3.30) along the electron path:

$$M = \frac{N}{N_0} = \exp \int_{x_1}^{x_2} \alpha(x) dx = \exp \int_{E_1}^{E_2} \frac{\alpha(E)}{\frac{dE}{dx}} dE, \tag{3.31}$$

where x_1 represents the point where the electric field is high enough to produce secondary electrons by ionization and x_2 the anode position. M is called the multiplication factor or gain. Figure 3.10 shows the behaviour of $\nu = \alpha/E$ for different noble gases as a function of the reduced field E/P. It can be seen that α rises steeply up to very high electric field, $\sim$ 100 kV/cm. Note also the large electric field range over which amplification occurs: $\alpha \simeq 10$ e$^-$/cm at a field of 10 kV/cm and $\alpha \simeq 2000$ e$^-$/cm at a field of 100 kV/cm in argon at atmospheric pressure. Therefore a given gas gain can either be obtained by an intense electric field in a small volume or with a moderate field in an extended region. We will see in chapter 5 how this principle is used in the MICROMEGEM counter.

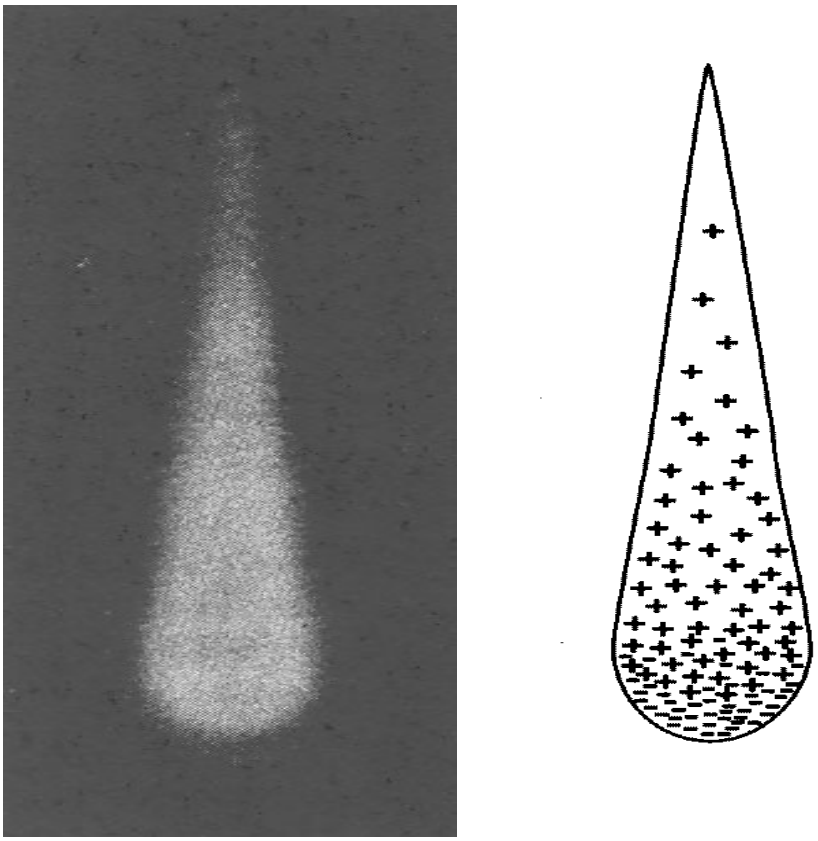

Figure 3.11: Picture of a single electron avalanche and sketch of its internal charge distribution.

Since the drift velocities of ions and electrons are very different, the multiplication process described above produces an avalanche with a drop-like shape as shown in figure 3.11. At a given instant, all the electrons should be located in the front of the charge

distribution with a long tail of positive ions behind. Half of the total number of ions are contained in the front part as they are produced in the last mean free path.

3.4.1 Gain limitation and breakdown mechanisms

The gain cannot be increased indefinitely. Indeed when the avalanche grows, the electric field produced by the charge distribution becomes important and may distort the external field in the neighborhood of the avalanche. Moreover secondary processes like photon emission induce avalanches spread all over the detector, eventually resulting in a spark breakdown. We describe here two important breakdown mechanisms which can occur in micro-pattern gaseous counters:

- Secondary emission of electrons: this process, also called photon feedback, results from the emission of electrons ejected from the cathodes. The electrons can be extracted through the photoelectric absorption of a photon emitted during the avalanche process. It also happens that the ions neutralizing at the cathode release their excitation energy by extracting another electron from the metal surface. Both processes may induce a permanent regime of discharge.

  The photon feedback is particularly present in high Z noble gases, like argon. Such gases are very attractive for use in a proportional counter as the avalanche multiplication occurs at much lower fields than in complex molecules. However they present low energy excitation levels which can return to the ground state only through a radiative process. The minimum energy of the emitted photon, 11.6 eV for argon, is well above the ionization potential of any cathode metal (7.7 eV for copper). To prevent photon feedback, it is therefore necessary to add a fraction of polyatomic vapour called quencher. The large amount of non-radiative excited states (rotational and vibrational) allows the absorption of the photons in a wide energy range.

  The main drawback resulting from the addition of polyatomic components is that they can form polymeric deposits on the electrodes. This phenomenon is called ageing. These deposits can substantially modify the operation of the counter. Indeed the accumulation of charges on the insulating layer covering the electrodes can modify the electric field strength and therefore the gain of the counter. Moreover at high radiation flux, $\sim 10^2 - 10^3 \frac{Hz}{cm^2}$, the production rate of ions can exceed their neutralizing rate on the cathode and very quickly a high density of charge develops across the thin polymeric layer. The dipole electric field can be so high as to extract electrons from the cathode. This phenomenon is called Malter effect. Even with a single inorganic quenching gas like CO_2 ageing can be observed due to a small amount of polluting agent released in the gas by the materials used to build the counter. A review of ageing properties of gases and construction materials commonly used in gaseous proportional counters can be found in Ref. [34].

- Streamer development: The second breakdown mechanism is the development of streamers between the electrodes. During the avalanche development, the total electric field is strongly enhanced in the front and in the back of the avalanche. In the avalanche, the dipole field created by the electron and ion charge distributions reduces the external field strength and recombinations can occur. Electrons that are released by photoionization at the tips of the avalanche are amplified in the high

electric field of the avalanche itself and produce quickly new avalanches merging with the primary one to form a streamer.

If the process evolves, it will create a conducting plasma between electrodes of opposite polarity leading to a discharge. In micro-pattern gaseous counters, streamer development should be avoided because the streamer current may be high enough to damage the electrodes or to destroy the readout electronics. In the case of MSGC's, the consequences of the discharges will be discussed in some detail in section 4.3.4.

3.4.2 Gain fluctuations and energy resolution

The total charge recorded from a proportional counter can be assumed to be the sum of the charges developed in each individual avalanche. There will be n_0 such avalanches, each triggered by a primary electron created by the incident radiation. If M_i represents the electron multiplication factor for the i$^{\text{th}}$ primary electron, we can write the average multiplication factor G for all avalanches produced by the incident radiation and contributing to the recorded charge Q:

$$G = \frac{1}{n_0} \sum_{i=1}^{n_0} M_i = \bar{M} \tag{3.32}$$

or

$$Q = n_0 \; e \; G. \tag{3.33}$$

Even in the case of a fixed energy deposition by the incident radiation, the total charge collected Q varies from one event to another because both n_0 and M fluctuate. Because these factors are independent and assuming each avalanche to be independent, the relative covariance of the total charge can be written as

$$\left(\frac{\sigma_Q}{Q}\right)^2 = \left(\frac{\sigma_{n_0}}{n_0}\right)^2 + \frac{1}{n_0}\left(\frac{\sigma_M}{M}\right)^2. \tag{3.34}$$

In the simplest model, the formation of each ion pair would be considered as a Poisson process and the total number of ion pairs created by an incident particle, n_0, should be subject to fluctuations with a standard deviation equal to the square root of the average number of ions produced. However careful measurements of the energy resolution performed with different detectors have shown that the achievable resolution can be better than the minimum predicted by the statistical assumption. These results suggest that the processes which produce the individual charge carriers are not independent and that the number of primary electrons cannot be described by a simple Poisson statistics. Consequently, the Fano factor is introduced in order to quantify the departure from pure Poisson statistics and is defined as

$$F = \frac{\text{observed variance in } n_0}{\text{Poisson predicted variance}} \tag{3.35}$$

For gaseous detectors, the Fano factor is empirically observed to be less than 1, ranging from 0.05 to 0.2. The fluctuations can be expressed by

$$\left(\frac{\sigma_{n_0}}{n_0}\right)^2 = \left(\frac{F}{n_0}\right). \tag{3.36}$$

The second term in eq. (3.34) represents the contribution of the fluctuations during the avalanche development from a single electron. Assuming that the probability of ionization by an electron depends only on the electric field strength and does not depend of its previous history, the distribution of the amplification factor M should have the exponential form

$$p\left(\frac{M}{\bar{M}}\right) = \frac{1}{\bar{M}} e^{-M/\bar{M}}. \tag{3.37}$$

However in strong electric fields, the avalanche size distribution tends to show a peaked shape, suggesting that the probability of ionization can no longer be considered as totally independent on its past history. In a model proposed by Byrne, the probability for ionization per unit path length depends on the total number of electrons already produced in the avalanche and the simple exponential distribution of eq. (3.37) is replaced by a Polya distribution

$$P(M) = \left(\frac{M(1+\theta)}{\bar{M}}\right)^{\theta} \exp\left(\frac{-M(1+\theta)}{\bar{M}}\right) \tag{3.38}$$

where θ is a parameter related to the fraction of electrons whose energy exceeds a threshold for ionization. It can be shown that the relative variance of the Polya distribution is equal to

$$\left(\frac{\sigma_M}{\bar{M}}\right)^2 = \frac{1}{1+\theta} \tag{3.39}$$

for large values of the amplification factor and is of the order of 0.5. In order to predict the relative variance of the total collected charge distribution, we replace in Eq. (3.34) the formulae (3.36) and (3.39)

$$\left(\frac{\sigma_Q}{Q}\right)^2 = \frac{1}{n_0}\left(F + \frac{1}{1+\theta}\right). \tag{3.40}$$

From the relative magnitude of F and $\frac{1}{1+\theta}$ we see that the gain fluctuations are dominated by the fluctuations in the avalanche size.

In practice, other factors than n_0, F and θ affect the energy resolution, like inhomogeneities in the electric field. It has been shown in reference [36] that the gain fluctuations in a uniform field are a decreasing function of the parameter $\kappa = \alpha(E)W_i/E = \nu(E)W_i$ where W_i is the energy required to create an electron-ion pair (see table 3.1). As $\nu(E)$ rises with E in a large range of electric fields (see figure 3.10), small gain fluctuations are reached when operating at high fields. The argument can be generalized to non-uniform fields: the total amplification can be considered as a succession of small avalanches in constant fields. Therefore, for the same total gain, smaller gain fluctuations will be observed when the avalanche develops in a small region with an intense electric field compared to configurations with a small electric field gradient. This effect is illustrated in figure 3.12 showing the normalized gain distribution for three types of gaseous counters of increasing electric field confinement: the proportional counter, the micro-strip gas chamber and the micro-gap chamber. Each distribution is calculated with a Monte Carlo simulation of the avalanche development and Polya distributions of parameter $1+\theta = 1.5$, 2 and 2.5 respectively are fitted [38].

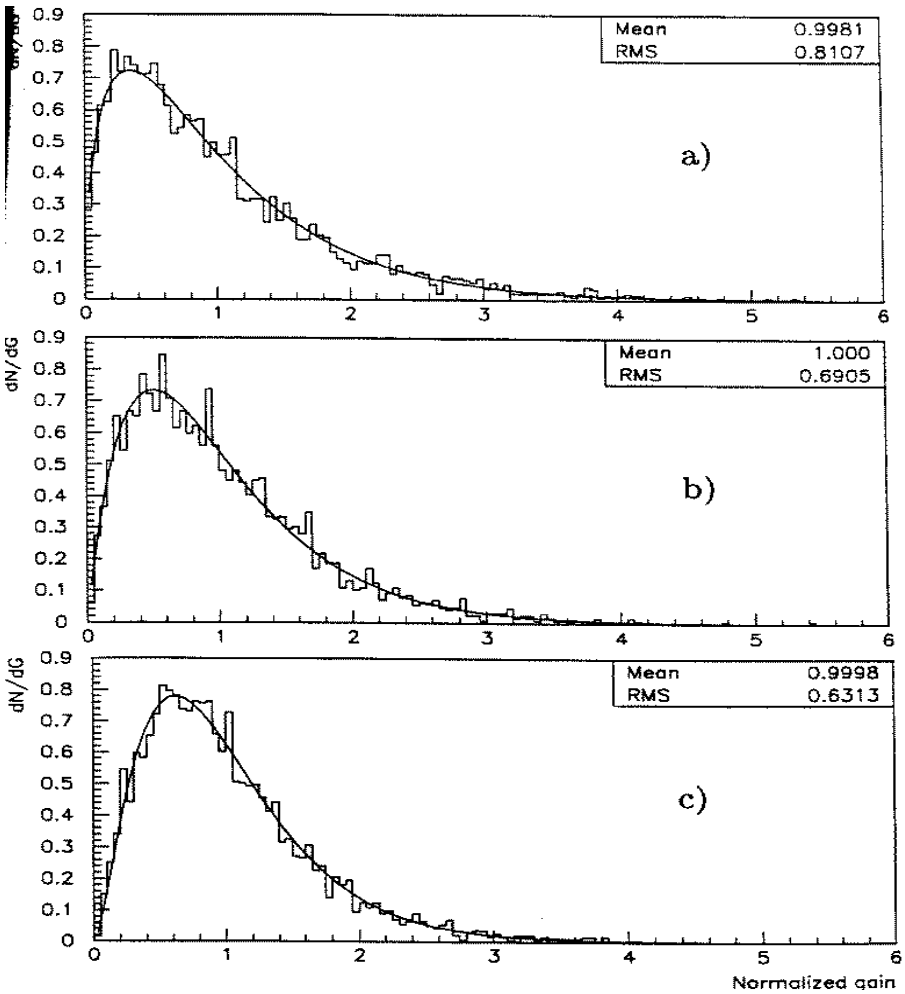

Figure 3.12: Size distribution of avalanche (normalized to the average gain) for a) a cylindrical proportional counter, b) an MSGC and c) a Micro Gap Chamber (MGC). The distributions have been computed by a Monte Carlo simulation of the avalanche development. The curves represent Polya distributions of parameters $1 + \theta = 1.5$, 2 and 2.5 respectively [38].

3.5 Signal development and processing

The charges created in the avalanche drifting towards the electrodes of a gaseous counters give rise to electrical currents that can be picked-up by amplifiers connected to the electrodes. In the presence of several electrodes the situation is more complicated because of the capacitive coupling between the electrodes. Therefore we will describe the signal generation on the anode of a cylindrical counter as shown in figure 3.13.

3.5.1 Signal generation

The counter consists of a gas filled cylindrical volume with a thin wire in its middle. The wire of radius a is set to a high positive voltage V_0 with respect to the grounded tube of radius b. The electric field rises as the inverse of the distance to the counter axis, and the avalanche process begins at a distance corresponding to a few wire radii, ~ 50 μm.

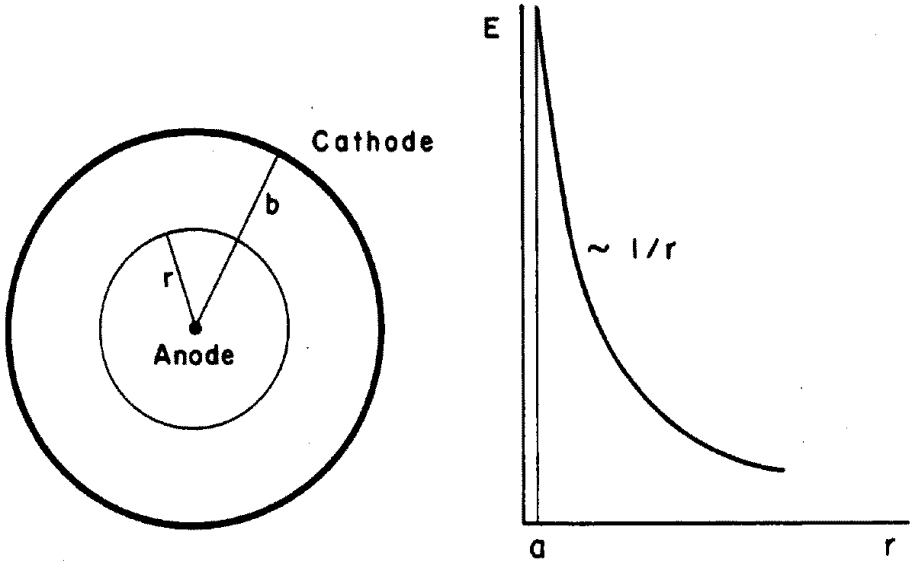

Figure 3.13: Transverse section of a cylindrical counter and its electric field as a function of the distance from the anode wire.

Taking a typical electron drift velocity value of 50 μm/ns, the avalanche lasts only a few nanoseconds. Afterwards the electrons are collected at the anode wire and the ions travel in the opposite direction towards the cathode with a drift velocity typically 1000 times smaller. In such geometry, the electric field and potential can be expressed as:

$$E(r) = \frac{CV_0}{2\pi\epsilon_0}\frac{1}{r}, \tag{3.41}$$

$$V(r) = -\frac{CV_0}{2\pi\epsilon_0}\ln\frac{r}{a}, \tag{3.42}$$

where C, the capacitance per unit length of the tube is equal to $\frac{2\pi\epsilon_0}{\ln b/a}$. Considering a small charge q traveling by a distance dr in a cylindrical counter of length l, the potential variation induced can be written as:

$$dv = \frac{q}{lCV_0}\frac{dV}{dr}dr. \tag{3.43}$$

Assuming that all charges are produced at a distance d from the wire the electron and ion contributions are:

$$v_e = -\frac{q}{lCV_0}\int_{a+d}^{a}\frac{dV}{dr}dr = -\frac{q}{2\pi\epsilon_0 l}\ln\frac{a+d}{a}, \tag{3.44}$$

$$v_{ion} = \frac{q}{lCV_0}\int_{a+d}^{b}\frac{dV}{dr}dr = -\frac{q}{2\pi\epsilon_0 l}\ln\frac{b}{a+d}, \tag{3.45}$$

The total maximum signal induced on the anode is given by the sum of these contributions, $v = v_e + v_{ion} = -q/lC$, and their ratio is:

$$\frac{v_e}{v_{ion}} = \frac{\ln\frac{a+d}{a}}{\ln\frac{b}{a+d}}. \tag{3.46}$$

As an illustration, taking some typical values: $a = 10$ μm, $b = 10$ mm and $d = 1$ μm, it turns out that the electron contribution to the signal is of the order of 1% of the total. The induced signal is therefore almost due to the motion of the ions. For simplification we will now calculate the time development of the ion pulse, assuming that all the ions leave the wire surface with a constant mobility. Integration of the equation 3.45 gives:

$$v(t) = \int_0^t dv = -\frac{q}{2\pi\epsilon_0 l} \ln \frac{r(t)}{a}. \tag{3.47}$$

Using the definition of the mobility $\mu = u/E$ (see Eq. 3.14) we can show that

$$r(t) = \sqrt{\frac{\mu C V_0 t}{\pi \epsilon P} + a^2}, \tag{3.48}$$

and substituting in equation 3.47 we obtain

$$v(t) = \frac{-q}{4\pi\epsilon_0 l} \ln \left(1 + \frac{\mu C V_0 t}{\pi \epsilon P a^2}\right). \tag{3.49}$$

This function is shown in figure 3.14 for a typical cylindrical counter. The very fast rise is generally exploited by passing through a simple RC differentiation filter. In this manner the length of the output can be strongly reduced without much loss in the rise time and the amplitude. Figure 3.14 shows also some examples of pulse shapes obtained with several differentiation constants τ_f.

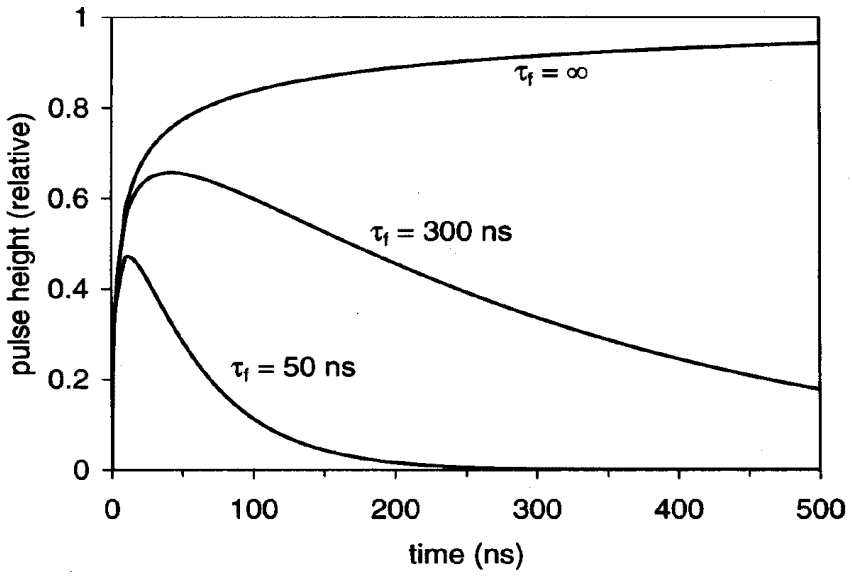

Figure 3.14: Relative pulse height from a proportional counter as a function of time for different RC differentiation filters τ_f.

In the case of multiple electrodes, the treatment is different and more delicate. The most general way to calculate signal currents induced in electrodes is provided by Ramo's theorem. This theorem considers the case where each electrode is perfectly conductive and connected to an infinite reservoir of charges. In practice this occurs when the impedances of the electrode and of the power supply are small, such that the RC time constants are

much smaller than the signal rise time. The Ramo's theorem states that the current I that flows into one particular electrode i under the influence of a moving charge q at some point d with the velocity v is given by

$$I_i = qv\frac{E_i(d)}{V_i}, \tag{3.50}$$

where E_i is the electric field created by raising this electrode to the potential V_i and grounding all the others in the absence of the charge q. A complete derivation of this theorem can be found in reference [39].

3.5.2 Signal processing

Gaseous counters are commonly equipped with charge preamplifiers similar to the circuit shown in figure 3.15. The basic idea is to integrate the charge carried by the incoming pulse on the feedback capacitor C_f. If the amplifier gain is large enough ($> 10^4$) it can be shown that the output voltage is proportional to the input charge Q as:

$$V_{out} = \frac{-Q}{C_f}. \tag{3.51}$$

This equation shows that the output amplitude does not depend on the detector capacitance. This explain the reason for which these amplifiers have been developed for silicon detectors where the capacitance varies with the temperature; but they are also suited for micro-pattern gaseous counters having similar signal amplitude and detector capacitance.

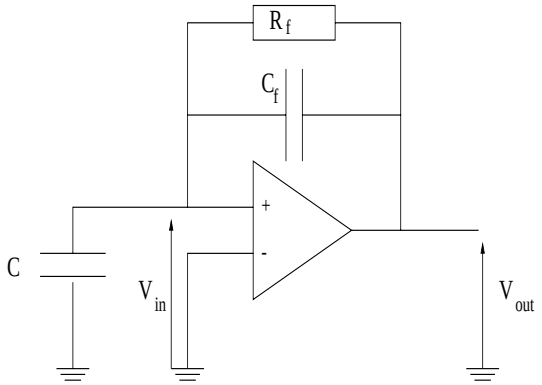

Figure 3.15: Schematic view of a charge preamplifier. V_{in} and V_{out} are the input and output voltages of the amplifier respectively, C represents the detector capacitance, R_f and C_f are the feedback resistor and capacitor.

The feedback network also contains a resistor R_f which serves to reset the amplifier and to shape the signal. Although a small $\tau_f = R_f C_f$ time constant is required to avoid that a second pulse rides on the tail of the first (pile-up effect), a time constant longer than the signal rise time is preferable. Indeed if the shaping time $R_f C_f$ is of the same magnitude or smaller than the rise time, the amplifier feedback capacitor starts to discharge before the whole charge has been amplified. This results in a decrease of the output signal, called ballistic deficit. This effect can be observed in figure 3.14.

In the CMS experiment, radiation hard amplifiers of the type APV have been envisaged to equip the silicon strip and the micro-strip gas counters in the Tracker. The APV chip consists of 128 amplifiers, each composed of a charge preamplifier and a shaper with a 45 ns shaping time. Because of a longer collection time, typically 50 ns instead of few nanoseconds in solid state detectors, MSGC's suffer from a ballistic deficit of the order of 0.3.

Chapter 4

Micro-pattern gaseous detectors

In 1968, G. Charpak introduced an electronic gaseous tracking device providing the possibility of direct position measurement of an incoming particle: the Multi-Wire Proportional Chamber (MWPC) [40]. As the Micro-Strip Gas Counter (MSGC) is the modern version of the Multi-Wire Proportional Chamber, the MWPC will be described first in section 4.1. Both detectors work following the detection principles discussed in the previous chapter.

The MSGC, described in detail in section 4.2, is a relatively recent gaseous detector built with the microelectronics technology. In the last ten years, a wide effort has been undertaken to improve this device and in particular to meet the high rate requirements of an experiment as CMS. Section 4.3 gives an overview of the performance and of the optimization studies of MSGC's for high rate experiments. However, some problems persist, like the damages produced by discharges induced by heavily ionizing particles. The occurrence of discharges put severe limitations on the safety margin in gain before breakdowns occur in MSGC's. Therefore new types of micro-pattern gaseous detectors have been introduced in the last few years as alternative to the MSGC's. Section 4.4 describes two of these alternatives, the MICROMEGAS detector and the GEM. These structures are of particular interest for the following as their working principles govern the operation modes of the MICROMEGEM and MSGC+GEM detectors studied in chapter 5 and chapter 6 respectively. Finally the softwares used to simulate the micro-pattern gaseous counters are presented in section 4.5.

4.1 The Multi-Wire Proportional Chamber

The MWPC consists of a plane of equally spaced thin wires of typically 20 to 70 μm diameter strung in a gas volume between two conducting planes as shown in figure 4.1 a). Each individual wire acts as an independent proportional counter. The anode wires are set to a positive voltage of a few thousand volts while the cathode planes are on a negative voltage, leading to an electric filed configuration as shown in figure 4.1 b). The electrons released by an ionizing particle move towards the nearest anode wire and the positive ions to the cathode planes. In the neighborhood of the anode wires, the electrons are accelerated and amplified through the avalanche process. The electric signal recorded on the electrodes determines the particle crossing point.

Until recently, the MWPC's have been used in many high energy physics experiments. However confronted to the increasingly demanding requirements of the next generation of

experiments, the MWPC's have met two major limitations. First, the distance between adjacent wires cannot be made much smaller than 1 mm because of the electrostatic and mechanical instabilities. The granularity, i.e. the number of detection cells per surface unit, is therefore limited. Secondly, the ions produced during the avalanche process are slowly collected by the cathode planes, which develops a space charge near the anodes that modifies the electric field. Consequently, the gain drops quickly if the particle rate exceeds 10^2 - 10^3 Hz/mm^2, which prevents to use MWPC's in the inner tracking system of a high rate experiment like CMS (see section 2.4).

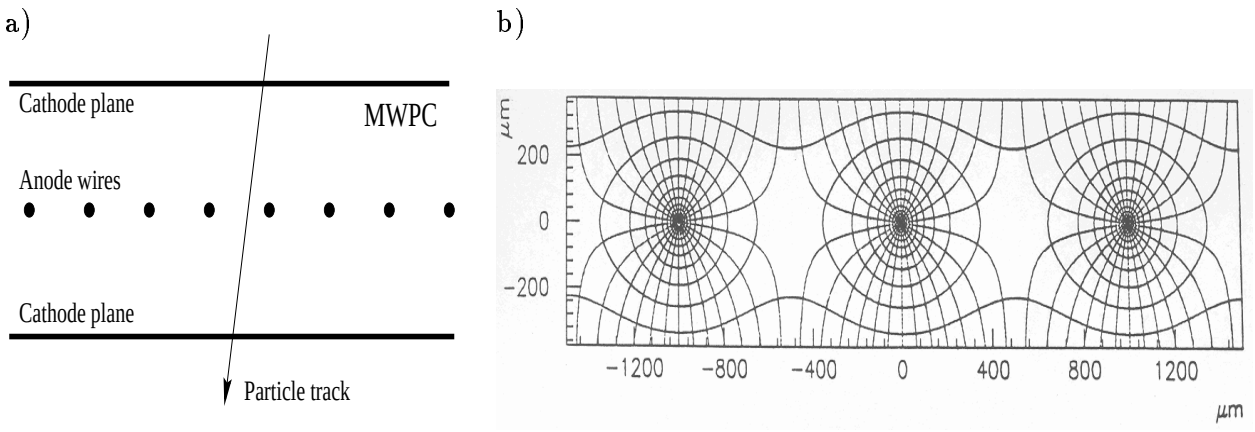

Figure 4.1: Schematic view of a Multi-Wire Proportional Chamber (MWPC) (a) and the corresponding electric field configuration in the neighbouring of the anodes (b).

4.2 The Micro-Strip Gas Counter

In 1988, A.Oed [41] introduced the Micro-Strip Gas Counter (MSGC) from the attempt to build high granular gaseous detectors. In the MSGC the wires have been replaced by conducting strips printed on an insulating substrate by a photolithographic process as the one used in micro-electronics. This technique permits to reduce the detection cell down to 200 μm, typically, which increases the accuracy on the measurement of the particle crossing point. The use of strips fixed on an insulating substrate also prevents the breaking of an electrode. In addition the alternance of anode and cathode strips on the substrate allows a fast ion collection which increases the rate capability.

The Micro-Strip Gas Counter, schematically drawn in figure 4.2, consists of an insulating glass plate, 300 μm thick, on which narrow anode strips are interleaved with larger cathode strips. The inter-anode distance is 200 μm and typically the anodes and cathodes are 10 μm and 100 μm wide respectively. The substrate is placed in a gas volume closed on top with a cathode drift plate located 3 mm above the substrate. Typical voltages applied to the cathode strips and to the drift plane are - 600 V and - 3000 V respectively; the anodes are grounded through the readout electronics.

Charged particles passing through the active volume ionize gas molecules and the liberated electrons are pushed towards the substrate by the uniform drift field (up to 10 kV/cm). There the potential difference between cathodes and anodes develops an

intense electric field, up to 100 kV/cm, around the anodes where the avalanche multiplication takes place over a small distance, less than 50 μm from the anodes. This field configuration which is drawn in figure 4.3 allows to obtain gas gains of the order of 10^3 - 10^4 [42].

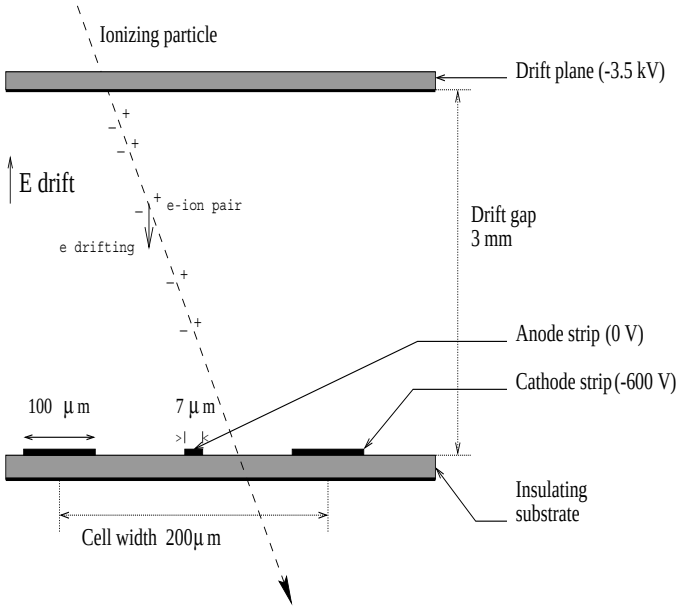

Figure 4.2: Cross section of an MSGC with typical dimensions

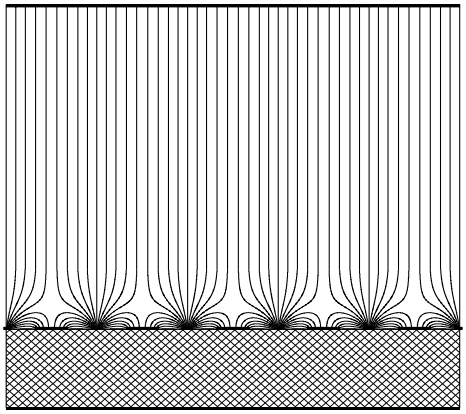

Figure 4.3: Electric field lines in an MSGC.

The use of micro-strips provides multiple advantages with respect to the wire chamber. First it allows to reduce the distance between the anodes up to 200 μm which increases the detector granularity. Moreover the proximity of the cathode strips allows the fast remove of most of the ions created during the avalanche from the region of high electric field around the anodes. As 90 % of the signal induced on the anode is provided by the ion motion [38], the signal formation is faster in MSGC's than in MWPC's. This is illustrated in figure 4.4 where the fraction of charge induced on the anodes of an MWPC (a) and of an MSGC (b) is shown as a function of time. The fraction of charge induced on the two adjacent cathodes is also shown for the MSGC (dashed curve). After 50 ns more than 70% of the charge is already collected in the MSGC instead of only 25% in an MWPC. It is important to note that the cathode signal is clearly less than the anode one, which shows the advantage of the anode readout for MSGC's.

The high granularity and the fast response result in a high rate capability; the MSGC can be operated at particle fluxes above 10^4 Hz/mm^2 [43]. The small detection cell of the MSGC, 200 μm, also increases the precision on the determination of the particle impact point. The spatial resolution can be as good as 40 μm for particles of normal incidence with respect to the substrate, when calculating the barycentre of the charge collected by the hit strips [44]. The intense electric field around the thin anodes ($\geq$ 10 kV/cm) provides high gains, beyond 10^4, which corresponds to signals of a few times 10,000 electrons for minimum ionizing particles [42]. These high gains allow to obtain a detection efficiency for minimum ionizing particles close to a 100%. In addition, the field configuration with an intense electric field concentrated around the anodes reduces the gain fluctuations (see

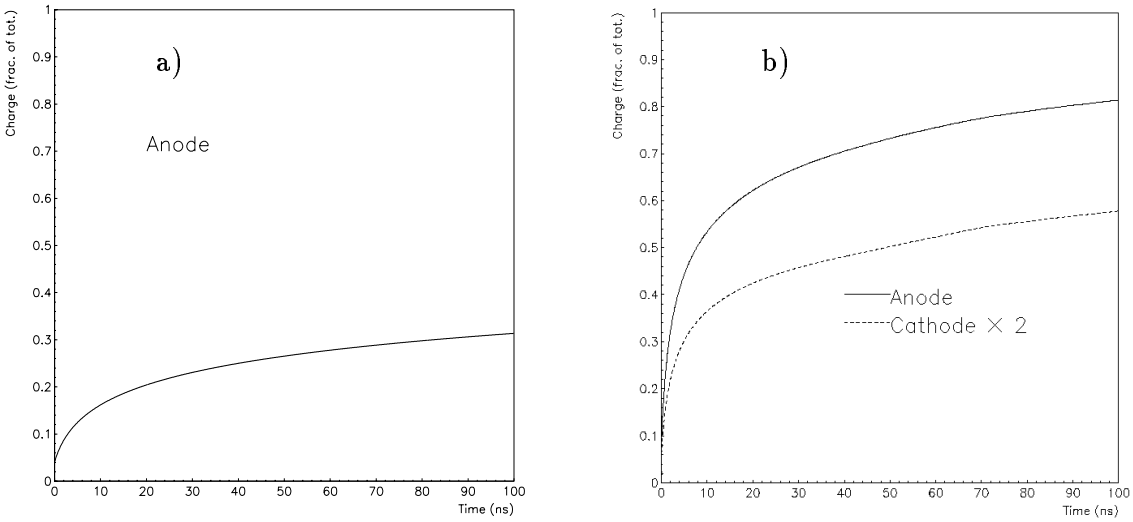

Figure 4.4: Fraction of the induced charge as a function of time for an MWPC (a) and for an MSGC (b).

section 3.4). An energy resolution of 12% has been obtained with 5.9 keV photons [45]. It has also been shown that MSGC's can sustain high radiation doses, up to 100 mC of accumulated charge per strip, which corresponds to more than the charge collected by the anodes in 10 years of the LHC operation at 50 cm from the beam pipe [46].

The main drawbacks of the MSGC are related to its high resistive insulating substrate which carries the strips. The accumulation of ions on the insulating substrate causes the charging-up of the substrate which modifies the electric field configuration and therefore the gain of the counter. The charging-up can be reduced by the use of substrates with a moderate resistivity. Care has also to be taken in the choice of the material since some reactions between the insulating surface and gas pollutants may lead to a fast deterioration of the gas gain when exposing the detector to a high particle rate.

Due to their good features, the MSGC's are an adequate device for tracking at high luminosity and are already used in several experiments. In the HERMES experiment at HERA, 12 MSGC's of large active area, up to 15 $\times$ 20 cm^2, constitute the vertex detector [47]. In the NA12 experiment at CERN, 8 MSGC plates have been used as an upgrade of the beam magnetic spectrometer previously equipped with MWPC's [48]. Thanks to the better spatial resolution of the MSGC, the accuracy of the momentum measurement of the 450 GeV/c proton beam was improved from 7.0 GeV/c to 1.2 GeV/c. Moreover 16 MSGC's of 10 $\times$ 10 cm ^{2} have also been successfully used at the fixed target experiment SMC at CERN [49]. All these applications have proven the feasibility of using MSGC's as tracking detectors.

4.3 Design optimizations and performance of the MSGC

Since the introduction of the MSGC, a large number of studies have been dedicated to the performance of this detector. The most complete program has been performed by the RD-28 collaboration [50] which coordinated between 1992 and 1996 the research performed

in several laboratories. We shall review some of the main results concentrating on LHC-related topics, but also on generic developments as they strongly influence the studies of the other micro-pattern gaseous detectors.

4.3.1 detector geometry

For an application at a high luminosity collider like the LHC, the tracking detectors are required to have a high detection efficiency (above 95 %), a high gain (several thousands), a good spatial resolution better than 40 μm, a fast signal development ($\sim$ 50 ns) and a strip occupancy of the order of a few percent per channel.

The theoretical detection efficiency directly determines the minimum thickness of the drift gap. We know from table 3.1 that for the gas mixtures commonly used in proportional counters the average number of primary electrons released in 1 mm of gas is between 3 and 5 at atmospheric pressure. As the number of primary electrons released by a charged particle is Poisson distributed (see section 3.1.2), we can see that the probability of releasing at least one electron is between 95% and 99%. Therefore the minimal thickness of the drift gap is 1 mm. On the other hand, the maximal thickness is determined by the electron drift velocity. In commonly used gas mixtures the drift speed is limited to about 60 - 70 μm/ns which limits the drift path to 3 mm in order to collect all the primary ionization within 2 LHC bunch-crossings.

The spatial resolution also can be affected by the drift gap thickness since we have seen in section 3.3 that the width of the electron cloud is proportional to the square root of the drift distance. Monte Carlo simulations made by J. Schmitz [51] have shown that for ionizing particles crossing the detector at normal incidence, the RMS of the spatial distribution, on the substrate, of the electrons created by ionization along the incident particle path is approximately given by

$$\Delta x \simeq \frac{1}{2}\sigma_T\sqrt{L}, \tag{4.1}$$

where σ_T is the transverse diffusion coefficient and L is the thickness of the gas volume. Measuring with an infinite precision the position of each of the N electrons, homogeneously distributed along the track of the particle, the RMS of the distribution of these N electrons on the substrate can be written as

$$\Delta x_N \simeq \frac{1}{2\sqrt{N}}\sigma_T\sqrt{L} = \frac{\sigma_T}{2\sqrt{n_T}}, \tag{4.2}$$

where $n_T = N/L$ represents the total ionization density. This means that if the gap is increased, the cloud width becomes larger but the larger electron statistics compensates the larger dispersion. This formula shows that for normal incidence tracks, the ultimate spatial resolution depends only on the transverse diffusion coefficient and on the ionization density but not on the drift gap thickness. In practice, N varies statistically from event to event and the electrons are not homogeneously distributed; equation 4.2 is only valid for large value of N ($>$100), i.e. if L $\geq$5 mm. For smaller gap thickness, Δx is higher than equation 4.2 would suggest.

The anode pitch p also affects the spatial resolution; the optimal performance is obtained when the pitch is smaller than the electron spread. If p is much larger than Δx, all

the electrons are collected by one strip and the spatial resolution is given by $p/\sqrt{12}$. It has been shown experimentally [17] and with simulations [53] that an accuracy of 35 μm can be achieved for normal incident tracks with 3 mm thick counters filled with a Ne/DME - 50/50% gas mixture and with an anode pitch of 200 μm. In this case the spatial resolution is almost 50% better than the spatial resolution obtained if all the charge is collected by only one strip (200 $\mu m/\sqrt{12} \simeq 58$ μm). However the spatial resolution degrades with the incident angle of the particle and this deterioration is faster for thicker gas gap [51]. Indeed for inclined tracks, the charge starts to be collected by several strips. Because of large fluctuations in the individual strip signals within the cluster, the cluster position also fluctuates. Moreover as particle tracks crossing the counter with a certain angle generate signals on a larger number of anodes, the number of hit strips and the strip occupancy will therefore increase for inclined incident particles with the gas thickness. Thus the smallest gap providing sufficient detection efficiency should be preferred.

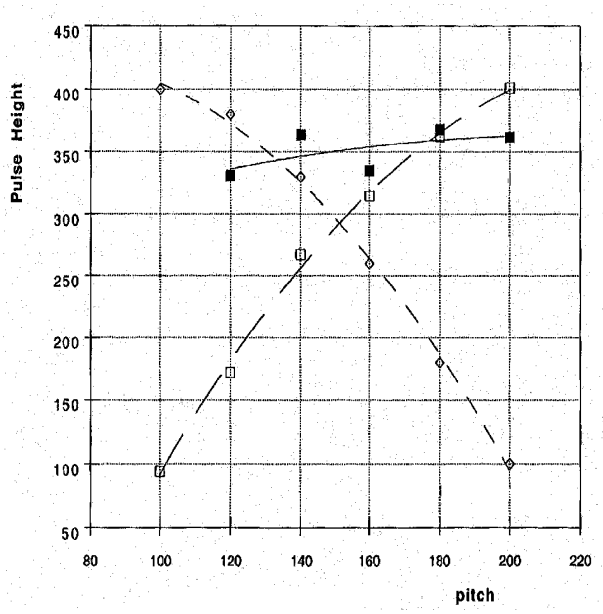

Figure 4.5: Pulse height as a function of the anode - cathode pitch for three different strip configurations. The open diamonds correspond to fixed anode and cathode widths. The open squares correspond to the configuration in which the anode width and the anode-cathode gap is fixed. The closed squares represent the case where both the gap and the cathode width vary according to the NIKHEF rule (Eq.4.3).

The anode pitch also influences the gain as observed in figure 4.5 which displays the pulse height as a function of the anode - cathode pitch for three different strip configurations. On one hand, for fixed anode and cathode widths, the gain decreases with a larger pitch as the electric field strength is reduced in the gap (open diamonds). On the other hand, if the anode width and the anode-cathode gap are fixed, the gain increases with the pitch, as shown by the open squares. In this case, a larger number of field lines are collected by the anode, which results in an increase of the amplification. Both effects can thus be compensated by varying in the same time the anode-cathode gap and the cathode width (closed squares). It has been shown experimentally [54] and by extensive simulations [55] that one is able to construct MSGC counters with varying pitch and constant

gain (closed squares) following the so-called NIKHEF rule [56]

$$g = \frac{p}{8} + 20\mu\text{m}, \tag{4.3}$$

where g represents the anode-cathode gap and p is the pitch.

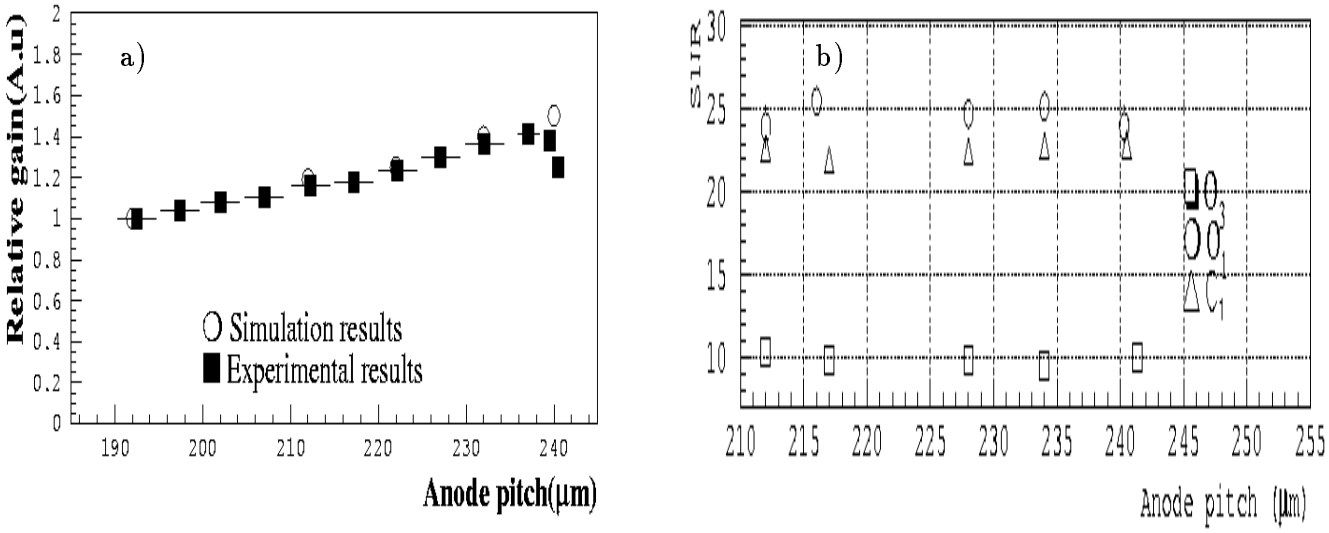

Figure 4.6: (a) Measured and simulated relative gain as a function of the anode pitch for an MSGC which is not designed according to the NIKHEF rule (Eq. 4.3). (b) Signal to noise ratio as a function of the anode strips for three different counters following the homothetic rule (Eq. 4.3)[55].

Monte Carlo simulations performed by O. Bouhali [55] have shown that the above rule is valid only over a limited range of anode pitches called the uniformity plateau. The limits of this plateau depend on the cathode width which leads to two constraints:

$$0.8 \times a + 38\mu\text{m} \leq g = \frac{p}{8} + 20\mu\text{m} \leq 1.4 \times a + 45\mu\text{m}, \tag{4.4}$$

where a represents the anode width.

This law is used to construct trapezoidal MSGC counters as those which have been foreseen for the forward part of the CMS tracker, having their strips radially pointing to the beam pipe. Figure 4.6 a) shows the relative gain variation as a function of the anode pitch for an MSGC which is not designed according to the NIKHEF rule (Eq. 4.3). The simulations are in good agreement with the data and both show gain variations up to 47%. The signal-to-noise ratio variations are less than 10% in counters built according to this law, as observed in figure 4.6 b) showing the signal-to-noise ratio (SNR) as a function of the anode pitch.

Once the anode pitch of a MSGC counter is fixed, the strip length has to be defined in order to maintain the hit occupancy to the level of 1%. In CMS, this length is equal to 12.5 cm in the barrel part of the tracker for the four innermost MSGC layers. For the forward region, the strip length varies from 8 cm to 14 cm to cope with the increase of particle rate with the pseudo-rapidity (see section 2.4).

4.3.2 Choice of the gas mixture

The required detector performance also determines the choice of the gas mixture. For tracking in a high energy physics experiment like CMS, the gas shall ensure a high gain (several thousands), a good spatial resolution (< 50 μm), a good detection efficiency ($> 98\%$), a fast response (≤ 50 ns) and also good aging properties. To reach a high efficiency at a moderate gain, a gas mixture with a large primary ionization is preferable. This restricts the choice to mixtures with a large content of noble gases, organic components like CH_4 or i-butane, CO_2 or DME (see table 3.1). Because of photon feedback, high Z noble gases like Xe or Kr are not considered except in combination with good quenchers. The use of organic compounds like isobutane or methane is also to be avoided as they lead to a fast degradation of the detector performance due to polymeric deposition on the strips [57] [58] while long term tests have been successfully carried out with DME-based gas mixtures [59] [60]. Finally, because of the lower primary ionization density and the poorer quenching properties of CO_2, the use of DME as the main compound of the gas mixture is a natural choice.

The main drawback with pure DME is its low electron drift velocity. Indeed the drift velocity levels off at a relative low value of 50 μm/ns at a high drift field of 10 kV/cm as shown in figure 4.7. This value is just sufficient to meet the requirements of CMS to collect the signal in less than 2 bunch-crossings. A second disadvantage of pure DME is that a high cathode voltage is required to get gas amplification which increases the probability of breakdowns as well as the risk of damages since the energy which can be released in case of discharges is increased at higher voltages.

In order to overcome these limitations, mixtures of DME have been extensively studied. Among the best candidates, mixtures of DME and CO_2 provide high drift velocity, $\sim$ 70 μm/ns with DME-CO_2-60-40% at E_{drift} = 10 kV/cm with a low diffusion, $\sim 120\ \mu m/\sqrt{cm}$, which provides a good position accuracy [55]. However CO_2 is a quencher and its combination with DME also requires high voltages to reach gas amplification.

In 1995 the group of R. Bellazzini [61] observed very large gains, up to 2×10^4 with the Ne/DME-70/30% gas mixture. The MIP detection efficiency of Ne/DME mixtures was for the first time intensively studied in Brussels using a cosmic hodoscope [53]. Although the primary ionization of Ne is slightly lower than DME, the advantage of adding an amount of this noble gas to DME is that the 98% detection efficiency plateau is reached at a lower strip voltage, 95 V less with Ne-DME 50/50% than with CO_2-DME/40-60%. Moreover the 70 V length of the efficiency plateau provides a good safety margin for long term applications as a gain drop of a few percent can be safely compensated by an increase of a few volts in the cathode voltage. However drift velocity studies [65] have shown that the drift velocity is still limited to 55 μm/ns for Ne-DME based gas mixtures, as seen in figure 4.7 a). Therefore triple gas mixtures of Ne/DME/CO_2 have been tested. Adding 20% of CO_2 to a mixture of equal parts of Ne and DME leads to an increase of the drift velocity up to 65 μm/ns at a drift field of 10 kV/cm (see figure 4.7 b). Since CO_2 is also a quencher, the efficiency plateau is shifted by 10 V towards higher cathode voltages but becomes 20 V longer.

Finally one has to take care of the choice of the materials used to build the detector and the gas alimentation system since DME is a solvent. For instance DME can react with Teflon which results in the release of electronegative elements leading to a significant decrease of the signal [63]. Extensive researches have been carried out on this subject

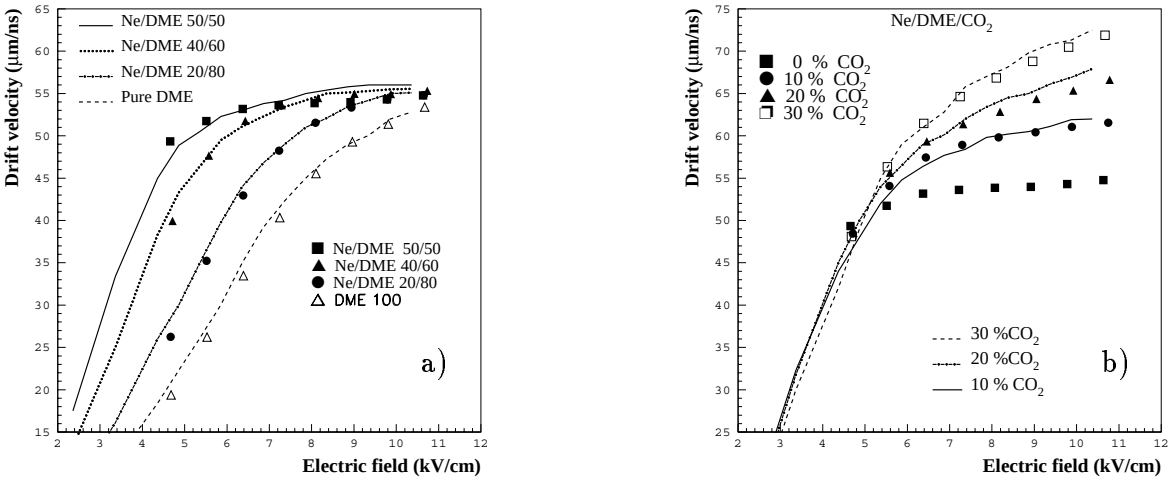

Figure 4.7: Measured (points) [65] and calculated (lines) [55] drift velocity as a function of the electric field for various Ne/DME gas mixtures (a) and for several gas mixtures with equal amounts of neon and DME with increasing CO_2 content (b).

and a compilation of recommended as well as incompatible materials can be found in references [62] and [64].

4.3.3 Rate capability and ageing of MSGC's

Almost any insulator with high dielectric strength and adequate surface quality for photolithography can be used to make the MSGC substrate. One of the most commonly used material is the DESAG D-263 glass with a high resistivity of 10^{15} Ωcm, having a good surface flatness and good mechanical strength. However several groups have reported important performance degradation after an accumulated charge of 100 mC per centimeter of strip [66] [67] [68]. This phenomenon, called ageing, is not well understood and can be caused by several factors as polymeric deposit during the avalanche process, pollutant in the gas or outgasing of the building material.

In addition detectors built with high resistivity substrates suffer from the accumulation of charge on the strip support. This phenomenon is called charging-up. The space charge field may distort the amplification field and reduce the gas gain. At switching on, the gain changes rapidly, then reaches a plateau as the substrate is charged-up. The equilibrium is reached when the deposition of charge is balanced by the charge conduction on the surface. The gain at equilibrium depends on the radiation rate as illustrated in figure 4.8 a) showing the gain as a function of time for various irradiation rates with 5.9 keV X-rays for plastic substrates [70].

The charging-up effect can be reduced by the use of substrates with a moderate resistivity ($10^9 - 10^{12}$ Ωcm). Systematic studies have shown that a lower resistivity results in a higher rate capability (see Ref. [43, 69]). MSGC's equipped with a low resistivity

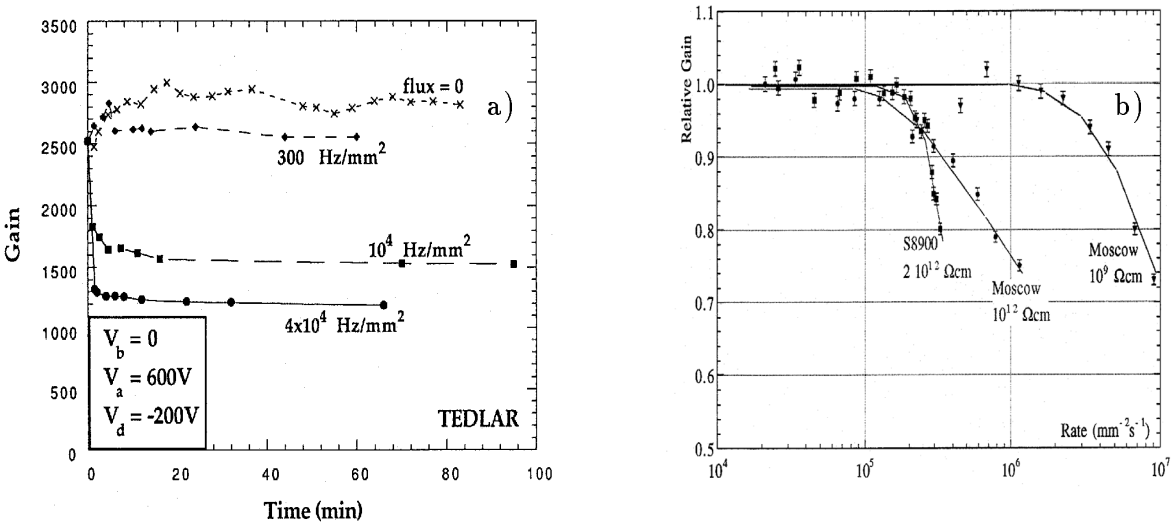

Figure 4.8: Gain as a function of time for different 5.9 keV X-rays rates for an MSGC equipped with a plastic substrate (a) [70]. Relative gain as a function of the irradiation rate for MSGC's equipped with semi-conducting substrates having a bulk resistivity between 10^9 and 10^{12} Ωcm (b) [59].

substrate, like Moscow[1], Pestov or Schott S-8900[2] glasses show much better high rate behaviour, without significant gain drop up to 2×10^5 Hz/mm^2 and even up to 10^6 Hz/mm^2 for a substrate resistivity of 10^{12} and 10^9 Ωcm respectively (see figure 4.8 b) [59]). It should be noted that with a DESAG D-263 glass substrate, the rate capability is reduced to 10^4 Hz/mm^2 [17]; this value is comparable to the LHC particle flux at 50 cm from the interaction point.

In addition to high rate capability its has been shown experimentally that substrates with a moderate resistivity also present good ageing properties. As an example, figure 4.9 a) shows the relative gain and the energy resolution as a function of the accumulated charge per centimeter of strip for an MSGC made of a S-8900 glass substrate. No gain drop or energy resolution degradation have been observed up to an accumulated dose of 100 mC per centimeter of strip [59]. Although the MSGC's built with custom-made or commercial glass (Moscow, Pestov or Schott S-8900) have shown very promising ageing properties, they are not adequate for tracking because these materials contain high Z elements increasing the multiple scattering and they are often too fragile to be produced in layers thinner than 200 μm over a large area of 10×10 cm^2. Consequently several techniques have been tried in order to grow thin slightly conductive layers on the substrate. One approach is to use plasma deposition of diamond-like carbon (DLC) [71]. Initially MSGC's made with diamond-like coated substrates demonstrated very good ageing performance [72], as illustrated in figure 4.9 b), showing no degradation up to 80 mC per centimeter of strips [60]. However later tests showed that these detectors suffer from discharges in high rate hadron beams, making such solution not suitable for LHC applications. An alternative is the sputtering onto a standard 300 μm thick DESAG D-263 glass

[1]SSPC NIIES, Moscow, Russia

[2]Schott Glass Technologies, Duryea, USA

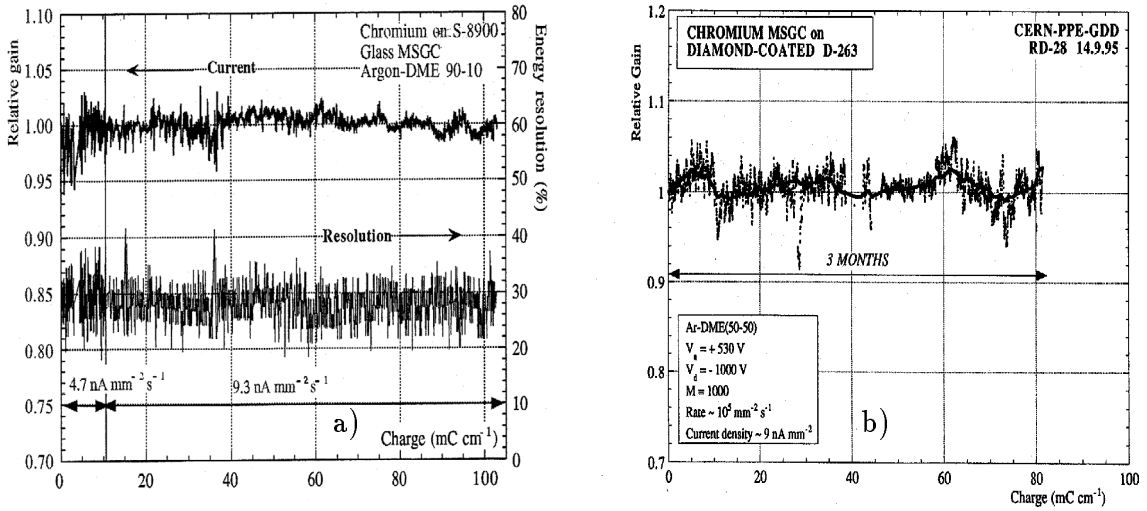

Figure 4.9: (a) Gain and energy resolution as a function of the accumulated charge for an MSGC equipped with a S-8900 glass substrate [59]. (b) Relative gain as a function of the accumulated charge for a diamond-coated MSGC detector [60].

substrate of a thin layer ($\sim$ 1 μm) of low resistivity glass. This technique provides better control of the surface smoothness than diamond-like coatings, allowing better quality of the strip metallization. As good ageing performance as with S-8900 substrate was observed with a 800 nm thick S-8900 layer deposited on top of a high resistivity glass [66]. Moreover this technique increases by more than one order of magnitude the rate capability, beyond 10^6 Hz/mm^2, as shown in figure 4.10 a) which displays the relative gain as a function of the irradiation rate for an uncoated DESAG D-263 MSGC and for an MSGC's coated with a thin film of Pestov glass having two different bulk resistivities [73].

The main drawbacks of using low resistivity substrate are that a higher voltage must be applied on the cathode strips in order to reach the equivalent gain as with an insulating substrate and that the probability of streamer development is increased. This effect is due to the reduced field strength around the anodes as shown in figure 4.10 b) showing the computed electric field strength parallel to the substrate as a function of the distance from the anode on the dielectric surface, with and without a conductive layer [74]. The field was computed at strip voltage values adjusted to give the same gas gain in both cases. We observe that the peak value is reduced by a factor 3 when the surface is coated. On the other hand it is important to note that a high uniform electric field of $\sim$ 80 kV/cm is created in the anode-cathode gap. This field configuration is unsafe as it can favor the development of unquenched streamers between the electrodes [75].

4.3.4 Breakdowns in MSGC's

The appearance of discharges beyond some critical amplification factor is a common feature of gaseous proportional counters (see section 3.4.1) and has been systematically studied for many years [76] [77]. With MSGC's, streamers and discharges have to be avoided as they can destroy the delicate detector structure. Indeed, the energy released

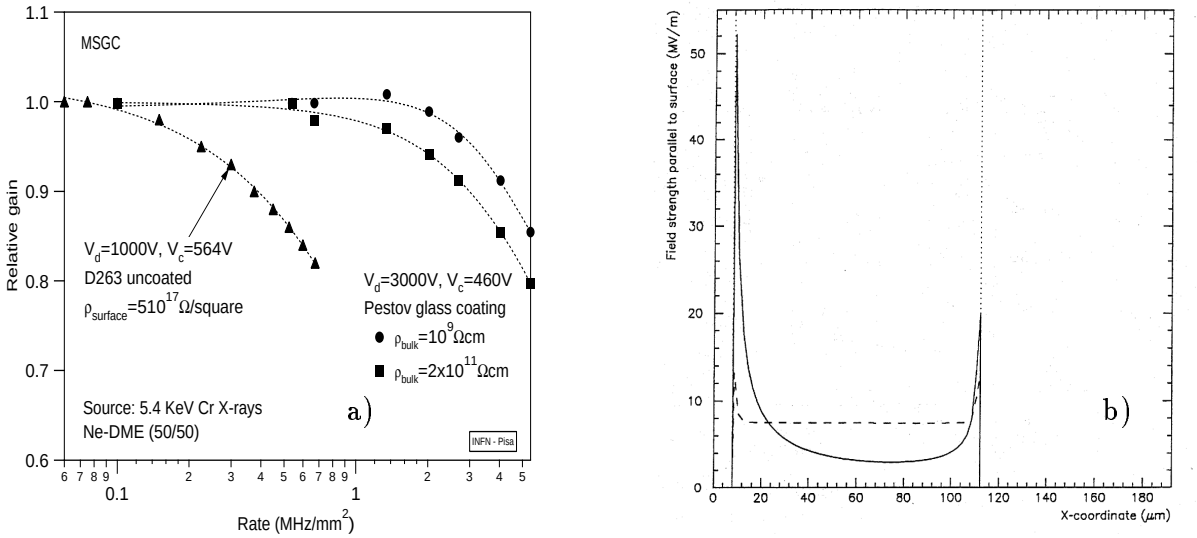

Figure 4.10: (a) Relative gain as a function of X-ray rate for an uncoated D263 MSGC and for two MSGC's coated with a thin film of Pestov glass having two different bulk resistivities [73]. (b) Electric field strength parallel to the surface as a function of the distance from the anode for an uncoated substrate (solid line) and for a substrate coated with a 4 μm thick conductive layer on top (dashed line). The vertical lines corresponds to the electrode edges [74].

during a discharge can be sufficient to melt the gold which the thin anodes are made of, as illustrated in figure 4.11.

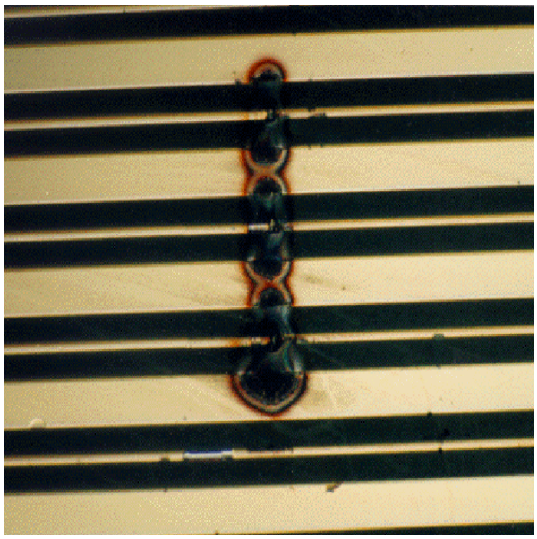

Figure 4.11: Strip pattern damages in an MSGC after repeated discharges.

MSGC's exposed to X-rays or MIP's can be stably operated without discharges at gas gains up to 10,000. However in a high energy physics experiment like CMS, the MSGC's

have to detect not only the high rate of 10^4 Hz/mm^2 of MIP's but also a superimposed low rate of HIP's produced through the strong interactions between hadrons and the detector material. The energy deposited in the gas by HIP's can release a charge up to 100 times the ionization deposited by MIP's. Consequently streamers can be produced by the space charge of such large avalanches. At the LHC, the neutron fluence at 50 cm from the beam intersect will be about 10^3-10^4 Hz/mm^2, which generates a rate of HIP's estimated to 0.1-1 Hz/cm^2 in the detectors [17]. Given the large avalanche size, streamers induced by HIP's may occur even at moderate gas gain of a few thousands. This behaviour has been observed by several groups by exposing MSGC's to α-particles emitted from ^{220}Rn [79]. In presence of such particles the maximum gain that can be reached is reduced to 3500, less than a factor 2 above the gain required for efficient MIP detection. In presence of HIP's the safety margin between the voltage required for detection efficiency and the appearance of discharges is small and not sufficient for long term operation of a large MSGC system at the LHC.

These observations have triggered studies of different approaches to avoid the onset of discharges and to extend the counter lifetime. The most critical parts of the MSGC's are the electrode ends where the electric field is strongly enhanced [80] which favors the extraction of electrons from the electrode metal. The group of R. Bellazzini [81] introduced the 'advanced passivation' method, illustrated in figure 4.12 a). It consists in covering the cathode edges by a narrow dielectric strips; the rounded electrode extermities are also passivated . Figure 4.12 b) shows the gas gain an the discharge rate for diamond coated MSGC's with and without advanced passivation. With this protection, the MSGC can be operated at gains up to 20,000 instead of a few thousands without passivation.

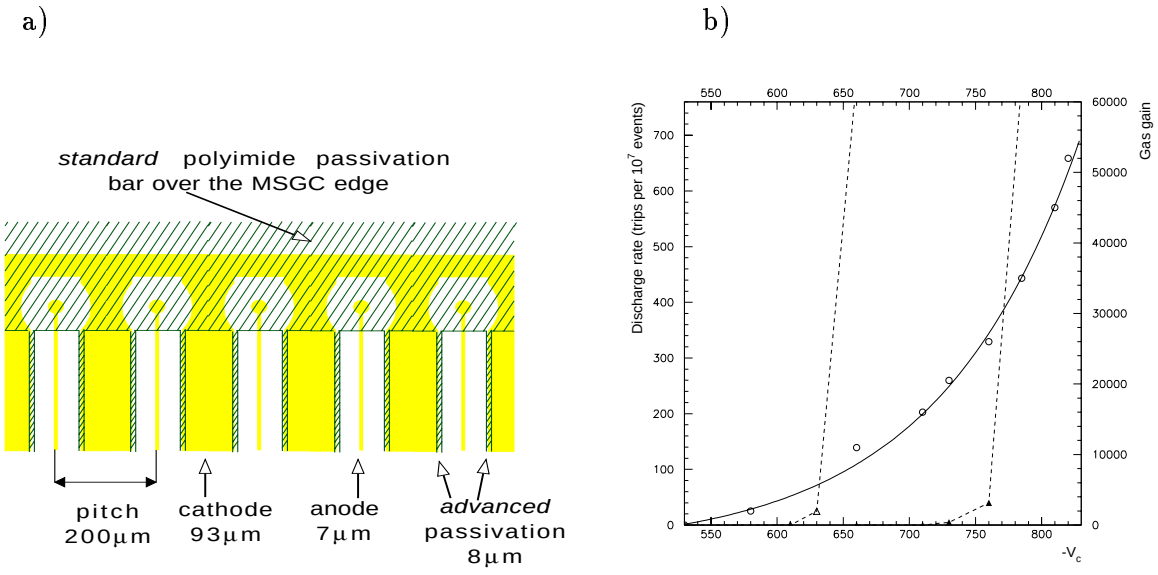

Figure 4.12: (a) Scheme of the advanced passivation technique. (b) Discharge rate as a function of the cathode voltage for diamond-like coated MSGC's with and without advanced passivation (closed and open triangles respectively). The gain dependence is also shown [81].

In 1999, the MSGC group of CMS has carried out a large scale test with 32 passivated MSGC's in a high intensity (6 kHz/mm^2) hadron beam in presence of HIP's for

an integrated time of 493 hours [82]. During this test all the chambers were operated with a signal-to-noise ratio corresponding to 98% detection efficiency with the final CMS electronics. No indication of any gain instabilities or ageing effect were observed during the entire period. The spark rate of the detectors was very low, of the order of 1 spark per chamber per day and three strips among the 16384 anodes exposed were damaged, this corresponds to 1% of strip loss when extrapolated to 10 years of LHC running.

4.4 Recent micro-pattern gaseous detectors

Since the introduction of the MSGC, a new class of micro-pattern gaseous detectors has emerged. Among the recent developments, the Gas Electron Multiplier (GEM) and the MICROMEGAS detector are of particular interest for high energy physics experiments and have been envisaged as possible alternative to MSGC's for the CMS outer tracker. These detectors have been shown to yield comparable performances as MSGC's in terms of spatial resolution, detection efficiency and counting rate. Moreover the working principles of these detectors directly govern the operation mode of the MICROMEGEM and the MSGC+GEM detectors studied in this work.

4.4.1 The Gas Electron Multiplier

The Gas Electron Multiplier (GEM) has been introduced by F. Sauli at CERN in 1996 [83]. It consists of a thin polymer foil, 50 μm thick, metal coated on each side, and regularly perforated by a pattern of holes as shown in figure 4.13 a). The holes have a diameter in the metal layers of $\sim$ 75 μm and the hole pitch is of the order of 140 μm. Applying a potential difference of a few hundreds volts between the two metal layers creates an intense electric dipole field in the holes.

Inserting the GEM foil in a gas volume, one can amplify the electrons released by the ionizing particle above the GEM and pass them below the GEM where the electrons may be collected by any strip pattern printed on a substrate or a micro-pattern gaseous counter like the MSGC.

The combination of a GEM with an MSGC has attracted a lot of interest. It equips the tracker of the HERA-B experiment [52, 84] and has been envisaged for the Endcap outer Tracker of CMS. Indeed the preamplification provided by the GEM foil allows to reduce the cathode strip voltage by up to 200 V to reach the same overall gain. This is extremely important since it increases the safety margin before the onset of discharges on the substrate. Indeed, the additional spread of the charge cloud due to diffusion in the double amplification stage devices reduce the charge density in the avalanche. Moreover, the lower working voltage applied between the MSGC electrodes reduces the risk of damages in case of sparks due to the lower released energy.

Gains up to several hundred were achieved in the early GEM's, necessitating a second amplification element for detection [85]. Recent advances in the GEM manufacturing technology together with the geometry optimization have permitted to reach gains up to 10^4, sufficient for detection using as second element a simple printed circuit board (PCB) with pick-up strips, without any further amplification [86]. This mode of operation is intrinsically fast since the signal is entirely produced by electrons; no ions are produced

a) b)

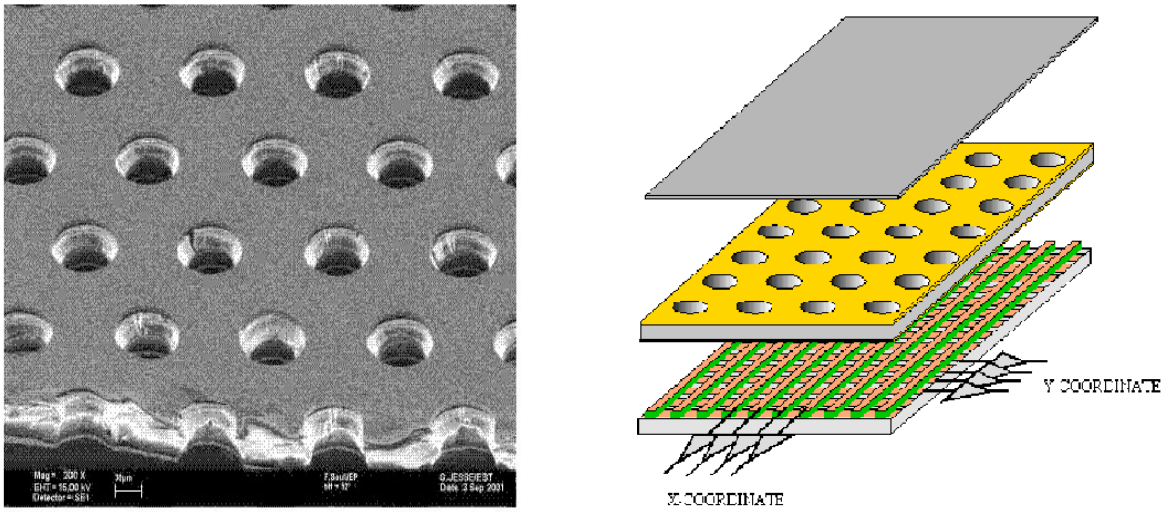

Figure 4.13: (a) Picture of a GEM foil (200 $\times$ magnification). (b) Schematic view of the combination of a GEM foil and a PCB substrate with two dimensional readout.

in the gap below the GEM. It is also safe since a moderate field of a few kV/cm prevents the propagation of streamers or discharges from the GEM towards the readout strips and the sensitive electronics. This new combination is expected to provide similar performance as the MSGC in terms of spatial resolution and detection efficiency. Beam tests performed at CERN with a GEM+PCB detector [87] have shown that 98% detection efficiency is reached at a signal-to-noise ratio of 20 with a potential difference across the GEM of 530 V. The efficiency plateau length is around 50 V. On the efficiency plateau the spatial resolution for normal incident particles is $\sim$ 45 μm.

Exploiting the kapton etching technology developed for making GEM electrodes, other promising multiplying structures have been recently developed: the Micro-Groove Detector (MGD) [102], the WELL Detector [103] and the micro-wire detector [90]. First results obtained with these counters suggest that although the size of the smallest electrode structure is almost ten times larger than those obtained with micro-electronics techniques, the results on gain, energy resolution, counting rate, etc., compete well with the performance of the MSGC. All devices permit to reach gains as high as 10,000 when they are exposed to X-rays and MIP's but their maximum sustainable gain is reduced in presence of highly ionizing particles. The limitation of these one stage-amplification devices and the good performance of the combination of a GEM with an MSGC triggered the development of multi-amplification devices where the total gain is shared between several cascaded amplifying structures. In these devices each element is operated at much reduced voltage which should increase the operational margin. In this work we have studied two detectors working on this principle: the MICROMEGEM (see chapter 5) and the MSGC+GEM detector (see chapters 6 and 7).

Finally, it is important to note that the use of the printed circuit board technology instead of the micro-electronics technology to produce the substrate and the strip pattern allows to build easily a two dimensional readout. Indeed, with a metal coated kapton foil, we can produce strips on each coated side, with a certain angle, for instance 90^o as shown

in figure 4.13 b). The etching procedure allow to remove the kapton except at the strip intersections to avoid any contact. One of the metal side of the foil is then glued on a another kapton substrate, which ensures the mechanical robustness of the structure. The use of PCB technology is also very attractive as it allows to produce more robust and cheaper detectors than the MSGC.

4.4.2 The MICROMEGAS detector

The MICROMEGAS (MICRO-MEsh GAseous Structure) detector has been introduced in 1995 at Saclay [91]. A schematic view of this detector is shown in figure 4.14. The device operates as a parallel-plate avalanche chamber with two asymmetric volumes. A microscopic mesh separates the conversion gap (also called drift gap), 3 mm thick, from a small amplification gap, 100 μm thick. The mesh is a metallic grid, 3 μm thick, with a cell size of 25 μm, produced by an electroforming technique. The mesh is supported by regularly located insulating spacers glued on a printed circuit board, 300 μm thick, on which gold coated anode strips, 150 μm large, are printed with a pitch of 200 μm. The drift gap is closed by a cathode drift plane made of an Aluminium foil glued on an epoxy frame.

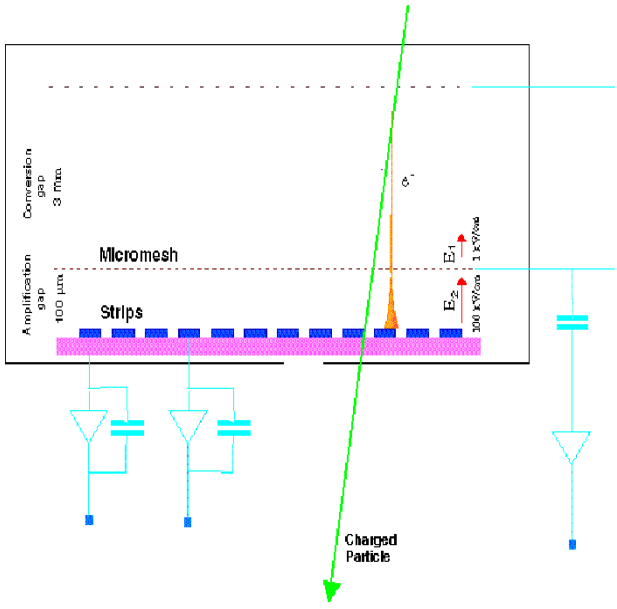

Figure 4.14: Schematic view of the MICROMEGAS detector [91].

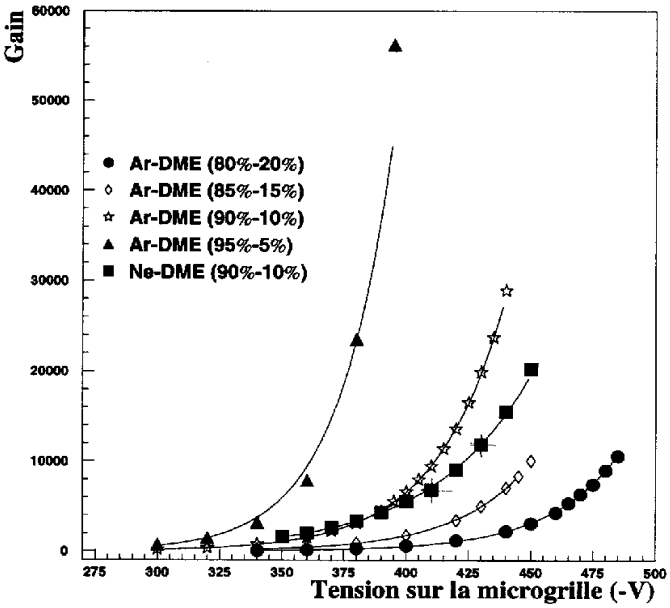

Figure 4.15: Gain of the MICROMEGAS detector as a function of the micromesh voltage for different gas mixtures [92].

Applying suitable voltages on the mesh and on the cathode drift plane, typically -500 V and - 1000 V respectively, one creates a very high electric field, $\sim$ 50 kV/cm, in the small amplification gap and a relatively low electric field, a few kV/cm, in the drift gap. The electrons released by an incident particle in the drift gap will drift towards the mesh because of the drift field and will be amplified over a distance of 100 μm due to the high uniform electric field below the mesh. Most of the ions produced in the avalanche are quickly collected onto the mesh, which prevents space charge build-up in the drift gap

as well as a fast signal. Generally, the signal is read-out by the anode strips at ground potential. This structure allows to reach gains well above 10^4 in various gas mixtures (see figure 4.15), a signal rise time of less than 100 ns and counting rates up to 10^6 Hz/mm^2.

The fabrication of the microscopic meshes seems less delicate than the production of a microscopic pattern. Moreover the absence of cathodes on the substrate allows to use wide anode strips, up to 150 μm and a simple and robust printed circuit board can be used as readout plane. Finally, the absence of insulator between the anodes and the cathodes and the use of larger anodes should improve the long term stability. These promising results make of the MICROMEGAS an alternative to the MSGC for high rate experiments. However systematic laboratory tests carried-out with α-particles [78] as well as beam tests [92] have shown that in presence of heavily ionizing particles the MICROMEGAS gain is limited to a few thousands because of breakdowns. Note that despite the frequent discharges, the detectors have been demonstrated not to suffer from permanent damages [92] [93].

4.5 Software used to simulate micro-pattern detectors

Together with the introduction of new micro-pattern gaseous detectors the simulation of their performance has been intensively developed during the last decade. To study the structure of the electric field in various geometries and to understand the detector response, we have used two programs available at CERN, MAXWELL [94] and GARFIELD [95]. MAXWELL is a commercial software package including 2D and 3D electrostatic and magnetostatic field calculators which allow to generate the electric field maps of various micro-pattern gaseous counters using the finite element method. After the calculation of the electrostatic solution, the field map can be easily imported into GARFIELD, originally written to simulate in two dimensions the detector response of drift chambers. GARFIELD is also interfaced with MAGBOLTZ [96] which computes the transport properties for electrons in various gases, i.e. the drift velocity, the longitudinal and transverse diffusion coefficients as well as the Townsend and attachment coefficients using a multiterm Boltzmann expansion. The Boltzmann transport equation expresses the conservation of the number of electrons. If f($\mathbf{r}$,$\mathbf{v}$,t) is the distribution of electrons at the point $\mathbf{r}$, $\mathbf{v}$ of the phase space at time t, this equation reads [97]:

$$\frac{\partial f}{\partial t} + \frac{\partial f}{\partial \mathbf{r}}\frac{\partial \mathbf{r}}{\partial t} + \frac{\partial f}{\partial \mathbf{v}}\frac{\partial \mathbf{v}}{\partial t} - \frac{\partial f}{\partial t}|_{collision} = 0 \qquad (4.5)$$

Here $\partial f/\partial t$ represents the time evolution of f($\mathbf{r}$,$\mathbf{v}$,t), $(\partial f/\partial \mathbf{r})(\partial \mathbf{r}/\partial t)$ represents the loss of electrons in interval $d\mathbf{r}$ due to diffusion, $(\partial f/\partial \mathbf{v})(\partial \mathbf{v}/\partial t)$ represents the modification of the electrons density due to the acceleration by the electric field E and $\partial f/\partial t|_{collision}$ is the change of the electrons density, due to collisions with gas molecules, which should contain the full dynamics of the elastic and inleastic processes that could take place. To solve equation 4.5, this function is expanded in Legendre polynomials. MAGBOLTZ performs the calculation up to the second order. The higher terms of the expansion contribute to less than 1% and can be neglected, giving a set of two coupled differential equations which can be exactly solved.

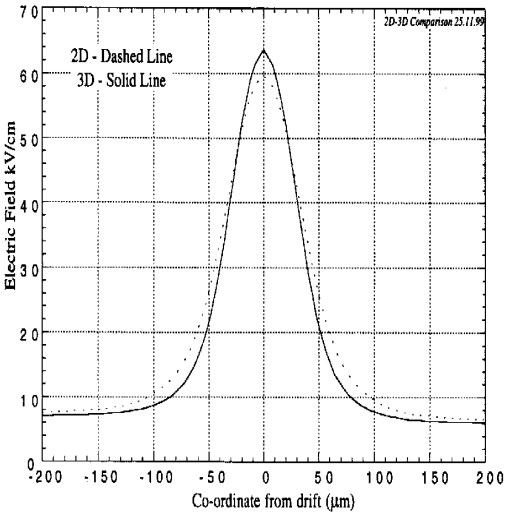

Figure 4.16: Electric field strength through a GEM hole calculated with a two- (dashed line) and a three-dimensional (solid line) field simulator as a function of the position along a line passing through the hole axis.

Although the programs are intrinsically three-dimensional, the simpler two-dimensional models are commonly used to simulate micro-pattern gaseous detectors like the MSGC or the MICROMEGAS where the simulation of the electric field in a plane perpendicular to the strips is sufficient (see figure 4.10). However this approach is not suitable to simulate the electric field through GEM holes etched in staggered arrays (see figure 4.13). Indeed, calculating the electric field in a plane containing the holes does not represent the behaviour along diagonal lines. Figure 4.16 shows the electric field strength in a single GEM hole with a two- (dashed line) and three-dimensional (solid line) model as a function of the position along a line passing through the hole axis. The 10% increase of the field strength in the centre of the GEM hole is due to the contribution of the regions equidistant from a set of three holes. These contributions are not taken into account in the two-dimensional model. In addition the probability that a primary electron hit the upper copper surface in these regions is also higher.

To quantitatively study the response of gaseous detectors equipped with GEM foils, we have modeled with the MAXWELL 3D field simulator a three dimensional GEM geometry has shown in figure 4.17.

Since the field is computed by the Finite Element Method, we have to reduce the size of the model by exploiting the inherent periodicity of the structure in order to avoid too long computing time and to obtain a solution with a good accuracy in the region of interest, the GEM hole. The volume of the model shown in figure 4.17 is $121 \times 70 \times 500$ μm^3.

It computes the static electric field that exists in a structure, given a set of voltages and a distribution of static charges. This is based on the Gauss's law which indicates that the net electric flux passing through any closed surface is equal to the net positive charge enclosed by that surface. In differential form, this law reads:

$$\nabla . \mathbf{D} = \rho \tag{4.6}$$

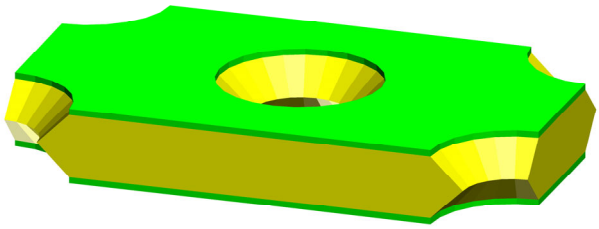

Figure 4.17: GEM detector model used to compute the electric field in a GEM hole.

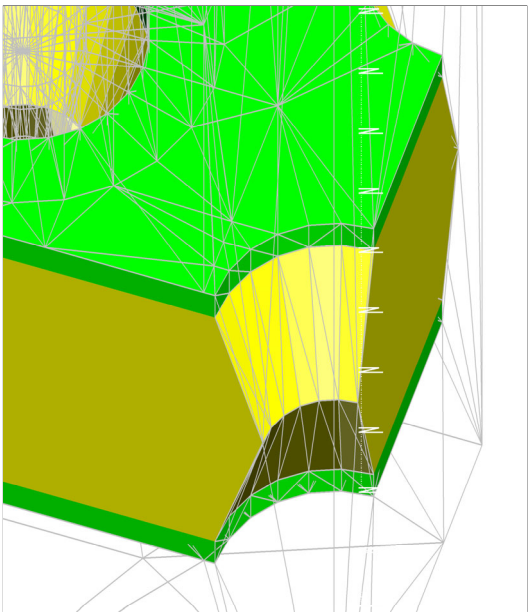

Figure 4.18: Tetrahedra used by the electrostatic solver to compute the electrostatic field in the 3D GEM model.

where $\mathbf{D}(x,y,z)$ is the electric flux density and $\rho(x,y,z)$ is the charge density. The electric flux density is related to the electric field $\mathbf{E}$ by:

$$\mathbf{D} = \varepsilon_r \varepsilon_0 \mathbf{E} \tag{4.7}$$

where ε_r is the material relative permittivity and ε_0 is the permittivity of free space. Equation (4.6) becomes then:

$$\nabla.(\varepsilon_r \varepsilon_0 \mathbf{E}(x,y,z)) = \rho \tag{4.8}$$

Since in a static field:

$$\mathbf{E} = -\nabla\phi \tag{4.9}$$

where $\phi(x,y,z)$ is the electric potential, equation (4.8) becomes:

$$\nabla.(\varepsilon_r \varepsilon_0 \nabla\phi(x,y,z)) = -\rho \tag{4.10}$$

The electrostatic solver solves this equation, for the electrostatic potential, using the finite element analysis. The program calculates the electric field in an iterative way, dividing the volume of the model in tetrahedra. Figure 4.18 shows several tetrahedra used to compute the electric field in the 3D GEM model. The density of tetrahedra increases in the regions of more complex geometry, like in the centre of the GEM hole. The electrostatic field solver stores the value of the electric potential at each tetrahedron node and at the midpoint of all edges. The potential field inside each tetrahedron is then interpolated from these nodal values. In our model, the final field is computed by more than 47,000 tetrahedra after 12 iterations. Note that GARFIELD can support field maps with up to 50,000 tetrahedra. Once the solution of the potential is generated, the program computes the electric field and the electric flux density using respectively relations (4.9) and (4.7).

The field map generated by MAXWELL is then imported into GARFIELD. Using the electron transport properties calculated by MAGBOLTZ, GARFIELD can compute the drift path of the electrons by Monte Carlo. The program proceeds in an iterative way. The electron drift velocity as well as the transverse and longitudinal diffusion coefficients are computed at a given starting point in the detector cell according to the electric field strength at that point. The program then computes a drift step, with one longitudinal component in the direction of the drift and two transverse components, according to three uncorrelated Gaussian distributions. The location of the electron is updated by adding the step due to the velocity and the random step due to the diffusion. The iteration ends when the electron reaches an electrode or a dielectric. The gas gain can be computed by integrating the first Townsend coefficient along the drift path (see equation 3.31).

The validation of the MAXWELL and GARFIELD programs has already been demonstrated in many respects in two dimensions (see references [95, 55]). To validate the three-dimensional model, the gain of a GEM has been simulated. The results shown in figure 4.19 are in good agreement with the data, at the level of 20%. The difference are attributed to large uncertainties on the first Townsend coefficient [96]. This three dimensional model will be extensively used in order to simulate the response of the different detectors studied in this work, all equipped with a GEM foil.

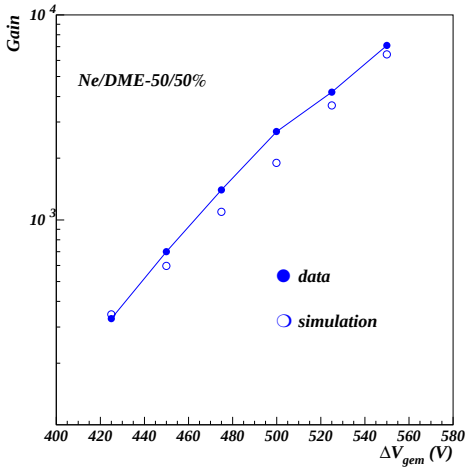

Figure 4.19: Simulated (open markers) and measured (closed markers) gain as a function of the GEM potential difference with Ne/DME-50/50% gas mixture. The simulation has been performed with GARFIELD [95] and MAXWELL [94].

4.6 Conclusions

The introduction of the micro-strip gas counter has triggered the development of a new class of detectors, the micro-pattern gaseous counters, which has opened a new range of applications for gaseous detectors. The MSGC has been subject to extensive studies for more than 10 years and has reached a high level of maturity which makes it an adequate

detector for high rate experiments like at the LHC. However it suffers from three weak points: its mechanical fragility, the occurrence of sparks in presence of highly ionizing particles and the loss of performance at large irradiation dose. Motivated by these problems, a large effort has been invested to find improvements. The main improvement to the MSGC is the introduction of the advanced passivation. It has been shown that passivated MSGC's can reach high gains, well above 10,000 before the onset of discharges. However alternatives to the MSGC's have been investigated. Among them we have described the MICROMEGAS detector and the Gas Electron Multiplier.

The MICROMEGAS detector exploits the parallel plate multiplication in a thin gap between a microscopic mesh and large anode strips. This geometry makes the detector more robust face to the sparks but they appear almost at the same gain value than for the MSGC. The Gas Electron Multiplier is another innovative amplifying structure. The GEM foils, perforated with microscopic holes, are produced by the Printed Circuit Board technology which makes it more robust and cheaper than the MSGC's with advanced passivation. This amplifying structure can be added in the gas volume of an MSGC to provide a first amplification. This combination allows to reduce the cathode voltage and therefore to reduce the spark probability. The PCB technology has been exploited to develop new micro-pattern detectors like the Micro-Groove, the WELL, and the micro-wire detector. Although these devices have shown promising performance during laboratory tests, their reliability in high and harsh particle environment is still to be proven.

In chapter 5 we shall describe the extensive studies of a new device, the MICROMEGEM, built with the PCB technology and equipped with a GEM. We shall first discuss the performance in terms of gain, energy resolution and rate capability. Then we shall study the behaviour in presence of heavily ionizing particles. In chapter 6 we will present the study of the performance of the MSGC+GEM detector, envisaged as alternative of the MSGC in the endcap tracker of CMS. Finally in chapter 7 we report on the large scale test performed with 18 MSGC+GEM detectors in a high intensity hadron beam, in irradiation conditions close to those of the LHC operation.

Chapter 5

Experimental study of the MICROMEGEM detector

The MICROMEGEM detector is a new position sensitive particle detector produced using advanced Printed Circuit Board (PCB) technology. It has been developed at the IIHE during the summer 1998 in the framework of the CMS experiment as alternative to the MSGC's (see section 4.2). The detector is equipped with a Gas Electron Multiplier (GEM) placed 50 μm above a plane of pick-up strips. The GEM foil produces a first gas amplification which can be extended afterwards by applying an intense electric field between the strips and the bottom GEM electrode.

The MICROMEGEM counter has been designed following two important observations concerning gaseous detectors. First, systematic studies carried out with gaseous proportional counters [78] have shown that sharing the gas amplification between several cascaded stages may improve the safety margin in presence of heavily ionizing particles. Secondly, it has been shown that it is possible to use advanced PCB techniques to fabricate new devices, avoiding delicate and expensive micro-electronics based procedures used in the production of the MSGC. Examples of detectors using advanced PCB technology are the Micro-Groove Detector (MGD) [102] and the WELL Detector [103] (see section 4.4).

We first describe the MICROMEGEM detector in section 5.1 and we present the electrostatic field computation in section 5.2. Section 5.3 is devoted to the study of the MICROMEGEM's performance on gain, energy resolution and rate capability, using X-ray sources. We discuss the behaviour of the detector in an intense hadron beam in section 5.4, before drawing the conclusions in section 5.5.

5.1 Description of the MICROMEGEM detector

We used several MICROMEGEM counters produced with the same layout. The detector whose construction is discussed below is schematically represented in figure 5.1. The counter uses a GEM (see section 4.4.1) as pre-amplifying structure, stretched 50 μm above a plane of pick-up strips. A cathode drift plane is mounted 3 mm above the GEM foil. The volume between the drift plane and the GEM is called the drift gap. The volume below the GEM is named the transfer gap. Typical voltages applied to the cathode drift

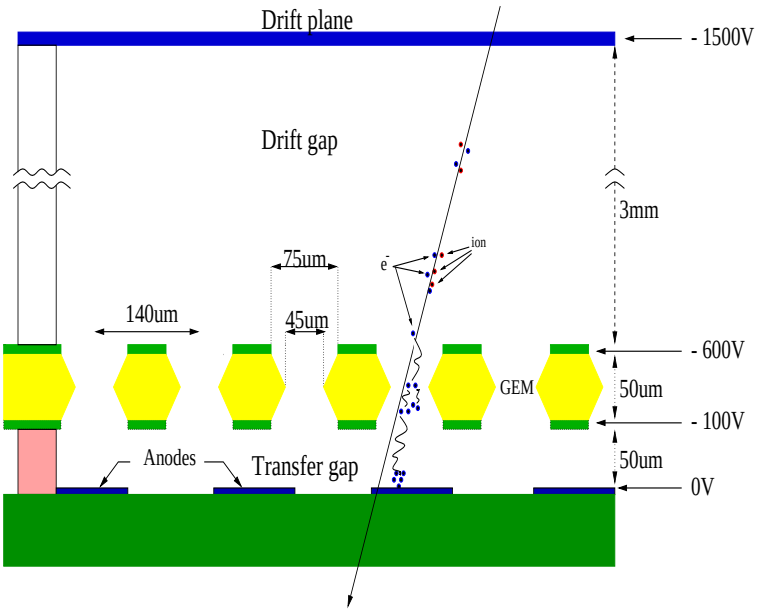

Figure 5.1: Schematic cross section of a MICROMEGEM detector.

plane, the upper and lower GEM electrodes are - 1500 V, - 600 V and - 100 V respectively. The pick-up strips are grounded through the readout electronics.

The primary electrons released by ionizing particles passing through the gas volume of the detector are pushed towards the GEM holes by the drift field of a few kV/cm. There the potential difference between the two copper layers of the GEM foil develops an intense electric field of several tens of kV/cm. The avalanche induced by this high field in the holes can be extended below the GEM grid by increasing the negative voltage on the lower GEM electrode as in the MICROMEGAS detector (see section 4.4.2). The electrons are finally collected by grounded pick-up strips.

The strip board and the GEM have been both manufactured by the CERN Surface Treatment Service[1] using advanced Printed Circuit Board Technology. They are produced from a kapton foil, 50 μm thick, copper-coated on both sides. For the strip board, the basic procedure is represented in figure 5.2 a). The foil is coated with a thin film of photo-sensible resin as a first step. A mask with the desired pattern, realized on a film by computer assisted laser photo composer, is placed on the foil afterwards. After exposure to UV light the exposed photoresist is etched in a Na_2CO_3 bath. The copper is removed from the desired pattern by a $FeCl_3$ bath and the strip side of the foil is then glued on a 200 μm thick vetronit plate. The strips are 80 μm large with a pitch of 200 μm. With the same procedure, the foil is etched again from above with a second mask to remove all the copper layer and all the kapton except small spacers. These kapton spacers, 50 μm thick, 120 μm large and 10 mm long, are located between two readout strips, with a pitch of 3 cm along the strips and 2.4 mm in the perpendicular direction. To ensure a uniform support to the GEM foil, the spacers are staggered.

The GEM foil is produced in the same way but both sides are etched simultaneously (figure 5.2 b). This explains the double conical profile of the GEM holes which are 75 μm and 45 μm in diameter, in the copper and in the middle of the kapton layer respectively (see figure 5.1). The cathode drift plane is composed of a thin aluminized mylar foil, a few microns thick. The GEM and the drift electrode are glued on a vetronit frame, 3 mm

[1] A. Gandi and R. De Oliveira, CERN-EST-MT

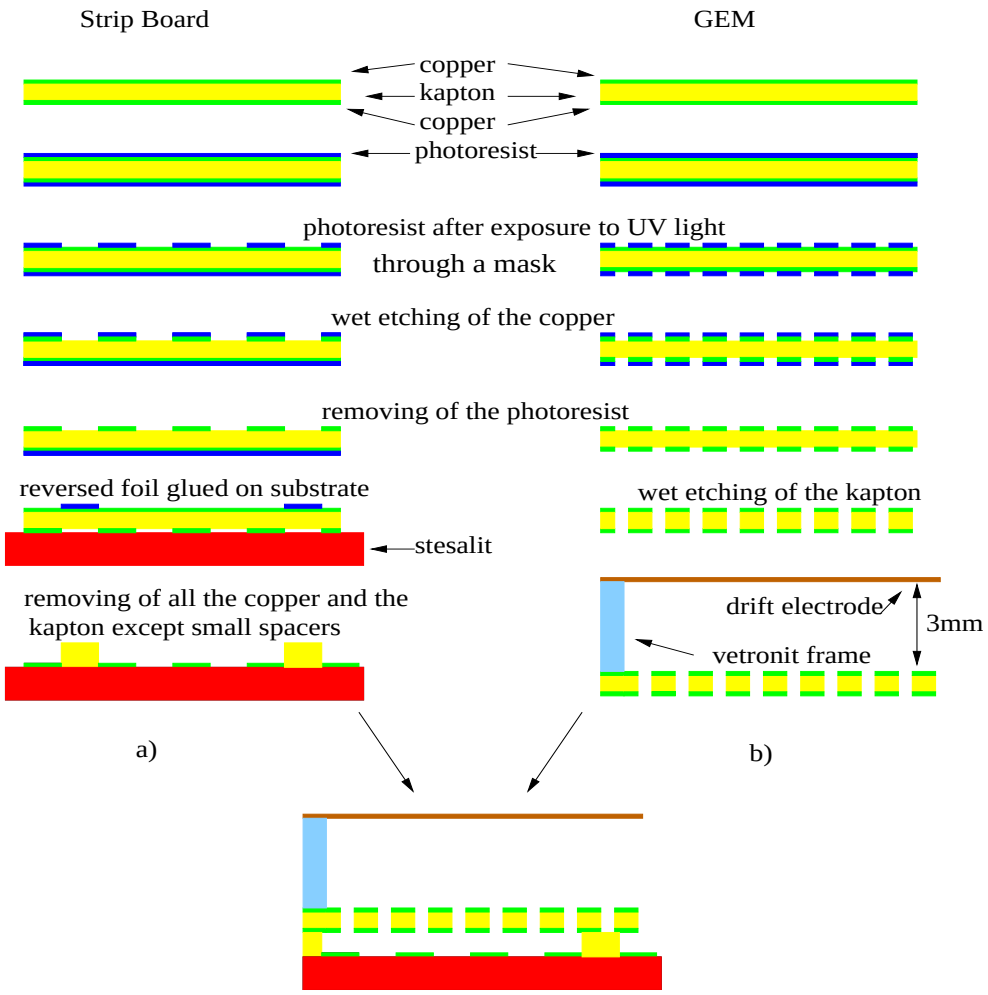

Figure 5.2: Manufacturing procedure to build the MICROMEGEM, from top to bottom. The basic procedure is similar for the substrate (a) and the GEM (b).

thick. This structure is then glued on the strip board where the small kapton spacers sustain the GEM foil 50 μm above the readout strips.

5.2 Electrostatic field simulation

In order to understand the behaviour of the MICROMEGEM detector, various simulations have been performed using two interfaced programs, MAXWELL [94] and GARFIELD [95], both described in more details in section 4.5. In the present section, the electrostatic field calculation aims to describe the working principle of the detector. In the following of this work the simulation of the detector response will be compared to the experimental data and will increase our understanding of the detector operation modes.

Figure 5.3 represents the electric field map, actually the drift lines of electrons and some equipotentials in a two dimensional cell of the MICROMEGEM detector. The cell corresponds to a plane perpendicular to the substrate, with a width equal to the GEM hole pitch of 140 μm. For the visibility of the figure, the drift gap has been limited to 190 μm. Note that at this distance from the GEM hole, the drift field is well uniform.

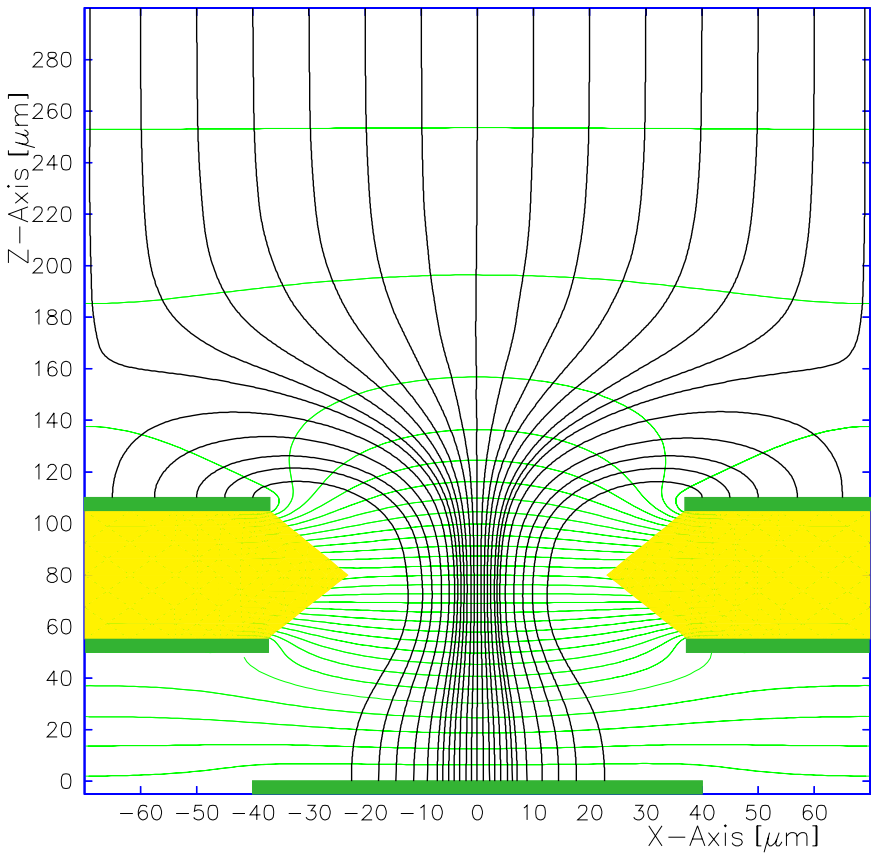

Figure 5.3: Field lines and equipotentials in one MICROMEGEM cell at V_{low} = - 100 V, ΔV_{gem} = 500 V and E_{drift} = 3 kV/cm.

The electric field has been calculated with a lower GEM electrode V_{low} of - 100 V, with a potential difference across the GEM ΔV_{gem} of 500 V and with a drift field E_{drift} fixed to 3 kV/cm. As all field lines from the drift region enter the GEM hole, we can assume that all the primary electrons released by the ionizing particle will reach the amplification region. However we will see in section 5.3.2 that a fraction of the primary charge can be lost on the upper GEM electrode, depending on the drift field and on the GEM potential difference.

Figure 5.4 a) shows the electric field strength in kV/cm as a function of the distance from the substrate, along a line passing through the axis of one GEM hole, with the voltage settings used to compute the field map shown in figure 5.3. With this configuration, the electric field is not symmetric with respect to the GEM. The field reaches a maximum value of 55 kV/cm in the centre of the GEM hole. In the drift gap, it rapidly decreases with the distance to reach the nominal drift field value of 3 kV/cm at a distance of $\sim$ 100 μm from the GEM foil. Below the GEM foil the transfer field decreases up to 30 kV/cm. With gas mixtures commonly used with GEM's, like Ar/CO_2, the avalanche multiplication starts at an electric field of $\sim$ 25 kV/cm. In the MICROMEGEM, this field value is reached at a distance of 120 μm from the substrate which corresponds to the entrance of the GEM hole.

The electrostatic field simulation shows also that the field is not homogeneous in the transfer gap even at a constant distance from the substrate as seen in figure 5.4 b) which represents the electric field calculated along a line parallel to the anodes at a distance of 10 μm from the substrate as a function of the distance from the GEM hole center. We observe that the transfer field located below the GEM hole is up to two times greater than the field calculated at a distance of 70 μm from the hole axis. This effect is due to asymmetric structure of the MICROMEGEM detector where the GEM foil is supported only 50 μm above the anode strips.

These field calculations suggest that due to the proximity between the anodes and the GEM, the electric fields in the transfer gap and in the GEM are not decoupled. Even with a moderate V_{low} value of - 100 V, the overlap between these fields seems to create one single amplification channel of 100 μm.

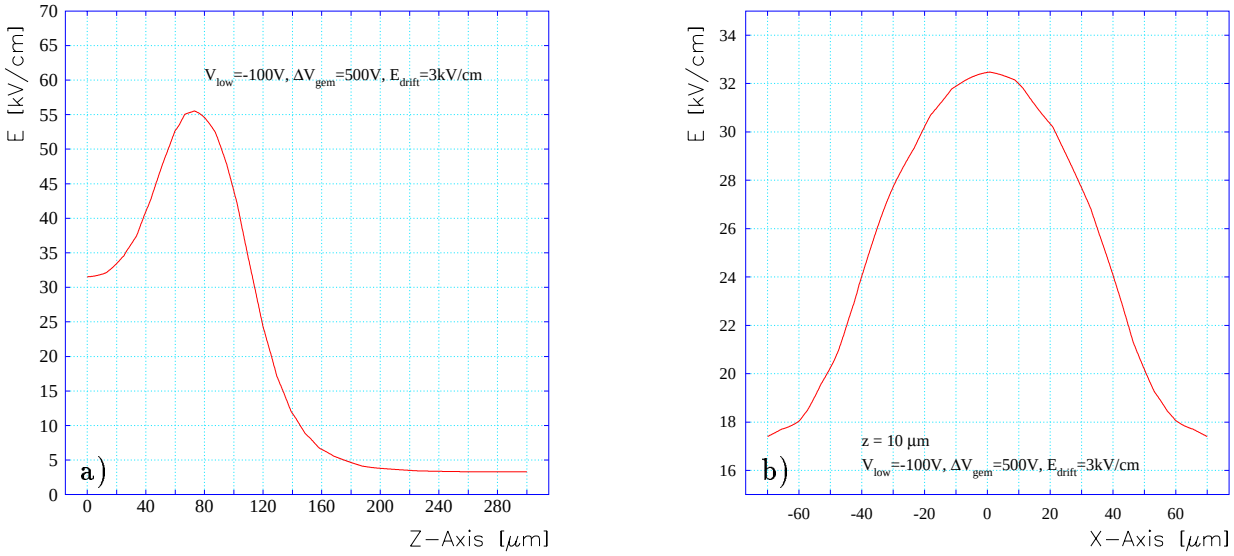

Figure 5.4: Electric field strength has a function of the distance from the substrate along a line passing through the center of the GEM hole (a). Electric field strength along one anode, 10 μm above the substrate, as a function of the distance from the GEM hole center (b).

5.3 Study of the MICROMEGEM using X-ray sources

The gain and the energy resolution are two important features of a gaseous detector. As discussed in chapter 2.4, the detectors foreseen for the CMS tracker should have a very good detection efficiency for minimum ionizing particles (MIP's), 98%, and a spatial resolution, better than 50 μm. To fulfill these requirements, the counters should sustain high gains, up to several thousands, to reach a high signal-to-noise ratio (SNR), which determines these parameters. A large electron statistics increases the detection efficiency and improves the position resolution when the position is determined by calculating the centre of gravity of the signals. Moreover, large gain fluctuations degrade the MIP's detection efficiency by increasing the overlap between the energy distribution (Landau) and the noise distribution.

Another parameter which influences the detection efficiency and the spatial resolution is the number of primary electrons released by the ionizing particle in the sensitive volume of the detector. The primary ionization density should be as high as possible. Therefore we have extensively studied the transfer of the primary electrons through the GEM holes, a property called the transparency. Finally, given the high fluxes of particles foreseen in the CMS tracker, the rate capability of the detector is another parameter to study.

The various experimental set-ups are described in section 5.3.1. The transparency of the GEM foil is defined and discussed in section 5.3.2. The study of the gain with different electric field configurations and for different gas mixtures is reported in section 5.3.3. The gain uniformity and the energy resolution are discussed in sections 5.3.4 and 5.3.5. The stability of the detector response in an intense photon beam is presented in section 5.3.6.

5.3.1 Experimental set-ups

Experimental set-up using a ^{55}Fe X-ray source

The experimental set-up, shown schematically in figure 5.5, is composed of two parts: the MICROMEGEM prototype, equipped with the gas system and the power supplies, and the data acquisition system. Unless mentioned otherwise, this set-up was used for the study of the gain and of the energy resolution.

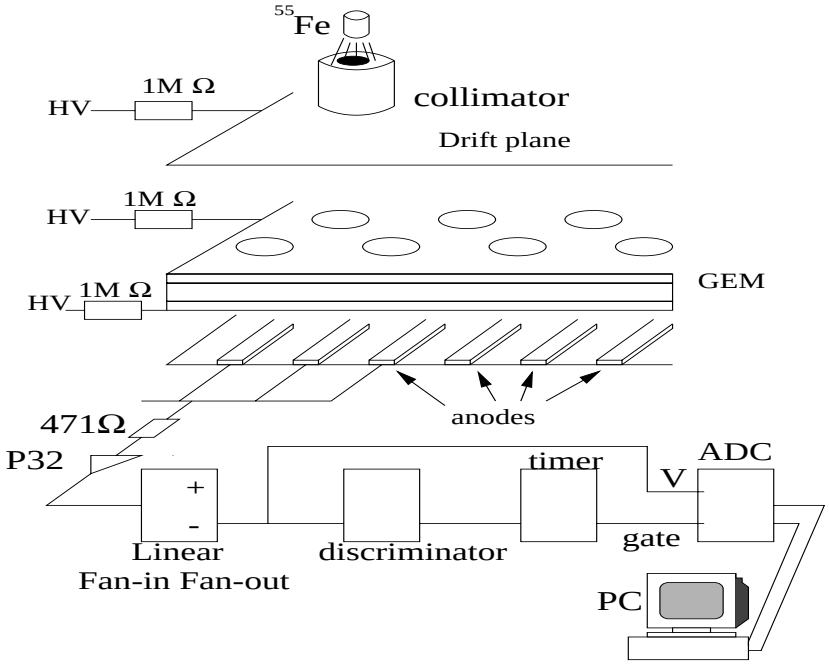

Figure 5.5: Layout of the experimental set-up used to study the gain and the energy resolution using a ^{55}Fe source.

Gas system During our measurements two gas mixtures have been used: Ar/CO_2-70/30% and Ne/CO_2-70/30%. The use of premixed bottles avoid the use of a gas mixer and therefore reduce the probability of gas pollution. However the mixture is flushed through a flowmeter, reducing the gas flow to 1 l/h which corresponds to 3.3 gas renewals per hour.

High voltage system A four channels programmable CAEN (Mod. N470A) power supply delivers negative voltages independently to the drift plane, the upper and the lower GEM electrodes, through 1 MΩ resistors. Typically the applied voltages are of the order of - 2 kV on the drift plane, around - 600 V on the upper GEM electrode and between - 50 V and - 350 V on the lower one. The pick-up strips are grounded through the readout electronics. In order to protect the electrodes from damages in case of sustained discharges, the high voltages are automatically switched off as soon as the electrode current exceeds a threshold set to 1 μA. When the counter is powered but not irradiated, the drawn current is of the order of few nA.

Photon source We use a ^{55}Fe source emitting 5.9 keV photons at a rate of $\sim$ 10 Hz/mm^2. The source irradiates the center of a group of 16 strips, using an Aluminum collimator, 5 mm thick, with an aperture of 1.5 mm. The source and the collimator are placed on top of the drift cathode plane.

Readout and Data acquisition To read out the pick-up strips, we mainly used the PreShape 32 chip [104] as front-end amplifier. This electronics is similar to the chip which will be used in the CMS tracker, the APVM [105]. The PreShape chip contains 32 channels. A functional schematic of a single channel is shown in figure 5.6. Each channel consists of a charge amplifier followed by a shaping amplifier which can be adjusted to provide a simple CR-RC type pulse with a nominal peaking time of 45 ns. The shaper output is followed by a buffer which drives the signal off the chip. The figure 5.6 represents a typical output signal from the PreShape 32 chip.

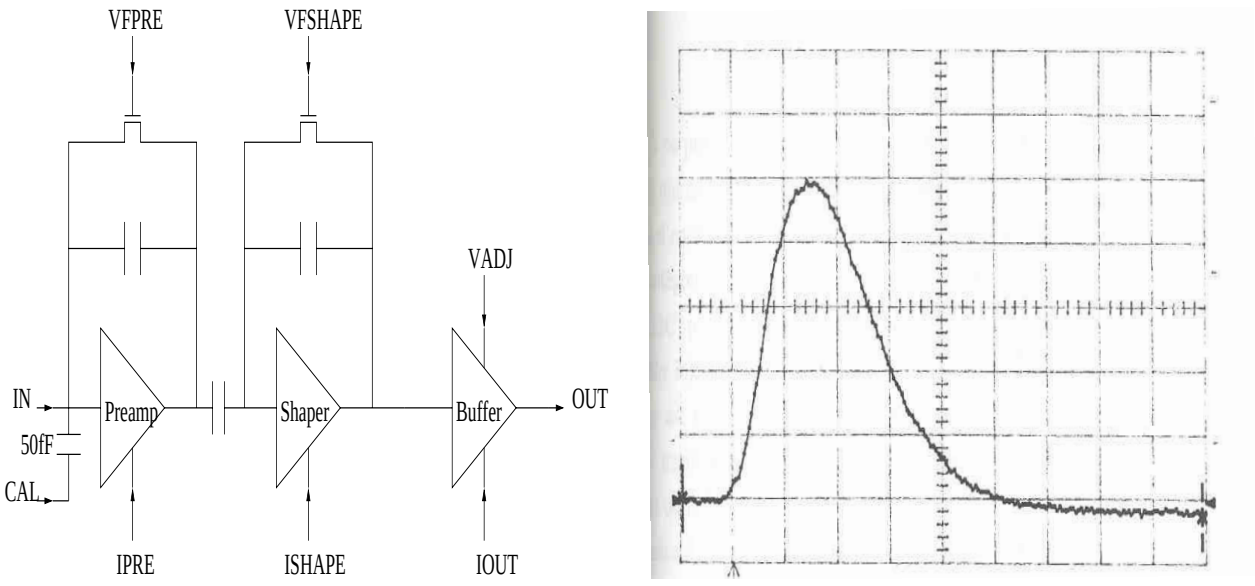

Figure 5.6: Schematic layout of one single PreShape 32 channel and typical output signal from a PreShape 32 channel. The signal is produced by the conversion of a 5.9 keV photon emitted by a ^{55}Fe source, in Ne/CO_2-70/30%. The abscissa has a unit of 50 ns/division and the ordinate has a unit of 20 mV/division. The signal has been recorded with a digitizing oscilloscope directly connected to the PreShape 32 output.

Each channel has got a 50 fF capacitor, C_{cal}, which provides the facility to calibrate the channel by injecting a known charge ($Q = C_{cal} * V$) into the preamplifier input. The amplification factor of the electronics is 12.5 mV/pC. The PreShape saturates with $\sim$ 800,000 electrons at the input, which corresponds to a gas gain of $\sim$ 4,000 for the used gas mixtures. To perform measurements at higher gains, we used the discrete electronics HY-CH-A1, built at CERN by J.C. Santiard, with an amplification factor of 1.4 mV/pC, about one order of magnitude smaller than for the PreShape.

The analogue signal coming from the readout electronics is digitized by an Analog to Digital Converter (ADC). The ADC (LeCroy 2249) housed in a CAMAC (Computer Automated Measurement And Control) crate integrates a negative signal over a time defined by a gate signal, 250 ns long, triggered when the output signal exceeds the discriminator threshold set to - 3.4 mV. The data acquisition (DAQ) is based on a PC (pentium 300) computer interfaced with a CAMAC instrumentation bus through a SCSI interface. The DAQ system is controlled by a program written with LabVIEW [106]. The software, entirely graphical programmed, allows the complete control of the instrumentation. Moreover, including analysis libraries, the program provides the online monitoring of the acquisition of charge distributions and writes the data in a file which can be later processed with PAW, an interactive utility for experimental data analyses [107].

Experimental set-up using a X-ray generator

For several measurements, as the study of the rate capability of the MICROMEGEM detector, the use of an intense source of mono-energetic radiation is required. For this purpose, we use a set-up[2] where 8.3 keV photons are generated from an X-ray tube, up to a rate of 10^6Hz/mm^2. The beam was collimated to a surface of 0.3 mm^2, ensuring the irradiation of a group of 4 strips. The set-up is presented in figure 5.7.

The X-ray generator is a conventional tube (Philips mod. PW 2217/20) with an iron target, which serves as anode for the electron beam emitted by an incandescent filament. The working principle of the X-ray generator is described in figure 5.8. The power supply for the X-ray tube, BERTAN series XR, can operate at high current, up to 3 mA. The power supply and the gas system are similar to those described in the previous section and accurate picoammeters, on the HV lines, allow to record the current on the different electrodes.

To read out the anodes we use a charge preamplifier, ORTEC 142 PC, followed by a shaping amplifier, ORTEC 450. The analogue signal is duplicated by a linear fan-in/fan-out, LeCroy 428F. A copy of the signal is sent to a discriminator to produce a gate of 600 ns long, while a second copy is sent to the ADC, LeCroy 2259B. The ADC integrates the signal over the gate when the signal exceeds the threshold set to 30 mV. For some applications, the anodes were disconnected from the readout electronics and grounded through a 10 MΩ resistor. The anode current is calculated by measuring the potential drop across the resistor with an accurate voltmeter KEITHLEY 182.

5.3.2 Transparency

The gas gain of a proportional counter is given by the ratio of the total charge created during the avalanche multiplication over the primary charge released when an ionizing

[2]Measurements performed at the Université de Mons-Hainaut, Av Maistriau, 19 b-7000 Mons.

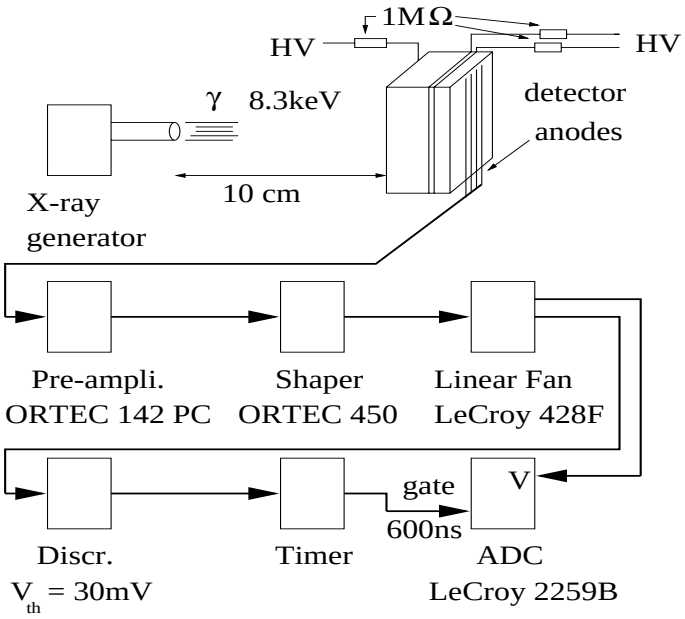

Figure 5.7: Layout of the experimental set-up using an X-ray tube.

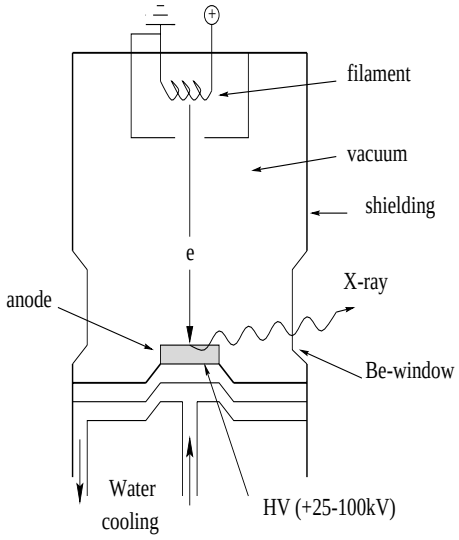

Figure 5.8: Working principle of the X-ray generator.

particle crosses the sensitive volume of the counter. Although the drift field does not participate to the gas amplification directly it influences both the measured gain and the energy resolution. Indeed, primary charges created by the incident particle in the conversion gap may not reach the amplification regions if some field lines terminate on the upper GEM electrode. This loss of primary electrons leads to a degradation of the energy resolution and to a decrease of the measured gain. The effective gain is the product of the gas gains and of the collection efficiency or transparency. The transparency is defined as the fraction of primary electrons which passe through the mesh holes, producing an avalanche. The transparency of the GEM is an important issue for applications in which the number of primary ionizations is low as in the detection of MIP's.

To measure the absolute transparency of the GEM foil, we should detect single electrons. A possible solution is to use devices equipped with solid photocathodes [108]. In these experiments, a poor transparency leads to the loss of the single electron and therefore to the loss of the event. Consequently, the transparency measurement is based on a precise evaluation of the counting rate of single-photoelectron pulses: the photoelectron counting rate of a MWPC+GEM is normalized to the counting rate of a single MWPC. In our set-up, a relatively large number of primary electrons, $\sim$ 168 with Ne/CO_2-70/30%, are released by a 5.9 keV photon, preventing an absolute measurement of the charge transfer through the GEM. For this reason we investigate the transparency in the MICROMEGEM through the dependence of the relative effective gain and of the energy resolution on the electric drift field, keeping the gas amplification constant (see references [109], [110]). Such a dependence is shown in figure 5.9 for a Ne/CO_2-70/30% gas mixture. The lower GEM electrode voltage, V_{low}, is fixed to - 100 V and the potential difference across the GEM foil, ΔV_{gem}, is 570 V. The absolute transparency and relative gain, computed with MAXWELL [94] and GARFIELD [95], are also shown. These simulations have been performed by generating a matrix of 2500 electrons uniformly distributed over an area corresponding to the MICROMEGEM cell shown in figure 4.17,

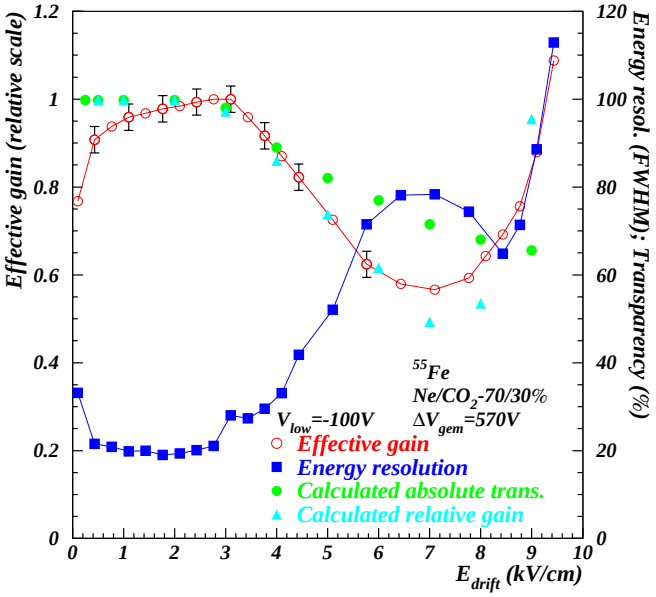

Figure 5.9: Dependence of the effective gain and of the energy resolution (FWHM) on the drift field, E_{drift}, with Ne/CO_2-70/30%. The amplification voltages applied on the bottom GEM electrode and across the GEM are fixed to - 100 V and 570 V respectively. The calculated absolute transparency and gain are also represented for the same settings.

at a distance of 200 μm above the GEM foil where the drift field is homogeneous. The drift path of each electron is computed towards the GEM foil, taking into account the diffusion. The relative gain is calculated by integrating the Townsend and the attachment coefficient along the electron drift path and by multiplying the result with the fraction of electrons that reach the GEM channel.

Between 0.5 kV/cm and 3 kV/cm, we observe a plateau region where the effective gain is maximum and the energy resolution goes through a minimum. The better energy resolution in this range suggests that only a small fraction of primary charges is lost and thus the transparency is high. This hypothesis is confirmed by the simulation which shows that the absolute transparency is close to a 100%. Below a drift field of 0.5 kV/cm, the relative effective gain decreases and the energy resolution degrades. This is attributed to the ballistic deficit because of the lower drift velocity (see section 3.5.2). The ballistic deficit is not taken into account in the simulation which gives and optimum transparency of a 100 % even below 0.5 kV/cm.

Increasing the cathode drift voltage beyond the plateau region, a deterioration of the effective gain and of the energy resolution is observed. It is due to the existence of field lines in the drift region that terminate on the upper GEM electrode leading to a loss of primary charges. Note however that beyond E_{drift} = 4 kV/cm the computed absolute transparency is higher than the relative gain. The difference is due to the dissociative attachment of electrons with the gas molecules which creates an additional loss of primary electrons (see section 3.3.3) and, therefore, increases the relative gain drop compared to the transparency loss. Beyond 6 kV/cm, the rise of the gain is explained by an enhancement of the amplification in parallel mode in the drift region counteracting the loss of transparency. In this region the agreement between the data and the calculated effective gain is at the level of 10% due to large fluctuations of this first amplification which results

from a relatively weak electric field over a large distance. It has been shown that this configuration favors large gain fluctuations (see section 3.4.2 and references [36], [37]).

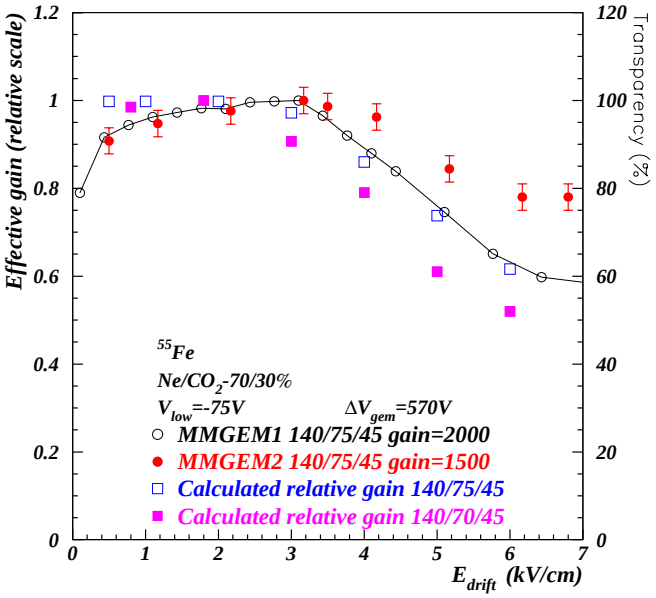

Figure 5.10: Effective gain as a function of the drift field, for two similar MICROMEGEM's filled with Ne/CO_2-70/30%. The voltage applied on the lower GEM electrode is fixed to - 75 V and the potential difference across the GEM is kept to 570 V. The calculated gain is also shown for two GEM hole diameters in the copper layers, 70 and 75 μm.

Influence of the geometry

The geometry of the GEM can also strongly influence the transparency, as smaller GEM holes may reduce the probability for the electrons to reach the GEM channel. Therefore we define the optical transparency of the GEM mesh τ as the ratio of the hole area to the total area,

$$\tau = \frac{\pi D^2}{2\sqrt{3}P^2}, \tag{5.1}$$

assuming cylindrical holes of diameter D with a pitch P.

Figure 5.10 shows the relative effective gain for two MICROMEGEM's as a function of E_{drift}, with - 75 V applied on the lower GEM electrode and with ΔV_{GEM} fixed to 570 V. Both GEM foils have been manufactured at CERN with a nominal outer diameter of 75 μm (see section 5.1), corresponding to an optical transparency of 0.26. The simulated relative gain is also shown for two different GEM hole diameters in the copper layers, 75 and 70 μm ($\tau = 0.225$). Although the simulated gain of MMGEM1 is in very good agreement with the data, we observe differences up to 20% for MMGEM2. These gain discrepancies observed beyond E_{drift} = 3 kV/cm can be explained by small variations in the GEM hole geometry; the optical inspection of the GEM foil of MMGEM2 with a microscope has shown that the holes are slightly larger, with an outer diameter of 79 μm corresponding to an optical transparency of 0.29. This is in agreement with the simulations which show

that the transparency is strongly dependent on the GEM hole dimension: a 5 μm smaller diameter, corresponding to an optical transparency loss of $\sim$ 10%, reduces the relative effective gain by 15% beyond E_{drift} = 4 kV/cm and shortens the plateau by $\sim$ 1 kV/cm. Note that hole diameter variations of few microns between different GEM foils could be the tolerance of the manufacturing procedure (see section 5.1).

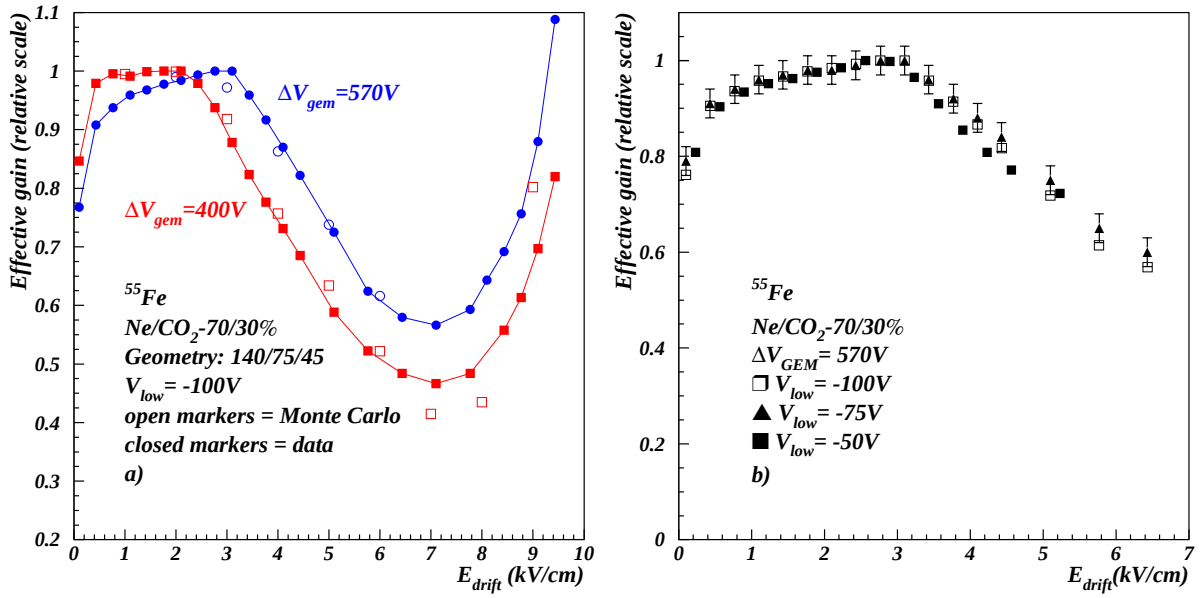

Figure 5.11: Effective gain as a function of the drift field for two different values of ΔV_{gem}, with Ne/CO_2-70/30% and with V_{low} = - 100 V (a); the open and closed markers correspond to the simulation and the data respectively. Effective gain as a function of the drift field for different voltages applied on the bottom GEM electrode, in Ne/CO_2-70/30% and with ΔV_{gem} fixed to 570 V (b).

Influence of the GEM potential difference and of the lower GEM voltage

For a given geometry, the extension of the plateau region depends on the potential difference applied in the GEM, as shown in figure 5.11 a) displaying the relative effective gain as a function of the drift field for two different values of ΔV_{gem}, with Ne/CO_2-70/30% and with V_{low} = - 100 V. The better plateau observed with ΔV_{gem} = 400 V is due to the use of the slow electronics HY-CH-A1 which has a smaller ballistic deficit coefficient. An increase of 170 V for ΔV_{gem} extends the plateau by 1 kV/cm. The electric field simulations show that at high electric field in the GEM, the lines from the drift region are better focused inside the holes. Therefore a higher drift field has to be applied before the field lines start to reach the upper GEM electrode, reducing the transparency. In figure 5.11 b), we compare the relative effective gain as a function of the drift field for different voltages applied on the lower GEM electrode keeping ΔV_{gem} fixed to 570 V, with the gas mixture Ne/CO_2-70/30%. The transparency is almost independent on V_{low}, suggesting that the drift field and the transfer field are decoupled. We will see in section 5.3.3 that although V_{low} does not affect the transparency, it strongly influences the measured gain.

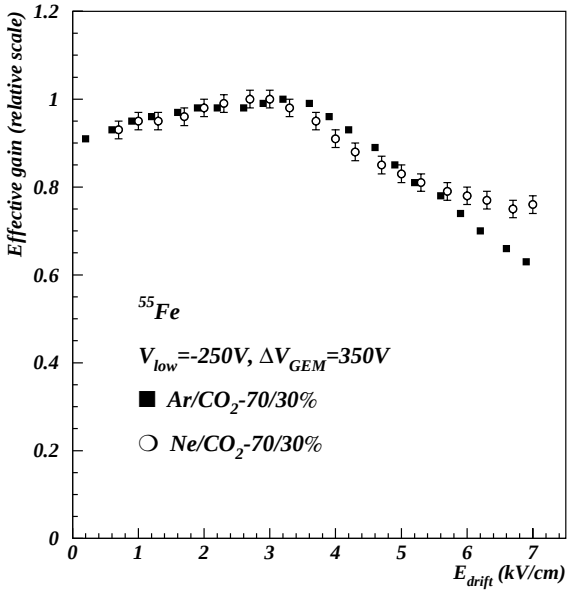

Figure 5.12: Effective gain as a function of the drift field for two different gas mixtures, Ar/CO_2-70/30% (closed marks) and Ne/CO_2-70/30% (open marks), with V_{low} = - 250 V and ΔV_{gem} = 350 V.

Influence of the gas mixture

In figure 5.12, we compare the relative effective gain of two different gas mixtures with V_{low} and ΔV_{gem} fixed to - 250 V and 350 V respectively. Up to a drift field of 5 kV/cm the behaviour of the effective gain is very similar for both gas mixtures. An equal loss of transparency can be explained by the fact that both gas mixtures have a similar transverse diffusion coefficient, within 5%, in this electric field range [111]. Beyond a drift field of 5 kV/cm, we observe that the effective gain drop is reduced with the Ne/CO_2-70/30% gas mixture. This behaviour already seen in figure 5.9 is due to the onset of electron multiplication in parallel plate-mode in the drift gap. With Ar/CO_2-70/30% the signal does not increase because of the absence of this additional amplification. Indeed the Townsend coefficient with argon is one order of magnitude smaller than with neon at this electric field value (see section 3.4).

All these studies of the transparency show that, with this GEM geometry, the drift field has to be maintained at a moderate value, around 3 kV/cm, if a maximum transparency is needed. This could be a handicap for applications with a magnetic field perpendicular to the drift field. In this case, a high drift field is required to compensate the Lorentz angle. It is also important to note that at 3 kV/cm, the electron drift velocity is close to 65 μm/ns in Ar/CO_2-70/30% and higher in Ne/CO_2-70/30% [111], which ensures a full collection time of less than 45 ns in both mixtures, for a 3 mm drift distance.

5.3.3 Gain study

To study the gain as a function of various parameters, we measure the effective gain maintaining the drift field at 3 kV/cm where the transparency is maximum and assumed to be close to a 100% (see previous section).

Gain dependence on GEM voltages and gas

The gain was first measured as a function of ΔV_{gem} for different values of V_{low} in the Ne/CO_2-70/30% gas mixture. The results are summarized in figure 5.13. Assuming a transparency close to a 100%, avalanche multiplication up to 20,000 was reached and values higher than 10,000 were obtained for several voltages on the lower GEM electrode. The maximum gains are similar to those achieved with two-stage devices like the DOUBLE GEM detector [112], the Micro-Groove+GEM detector when the GEM and the Micro-Groove layers are in contact [113] and the MSGC+GEM detector (see reference [114] and chapter 6).

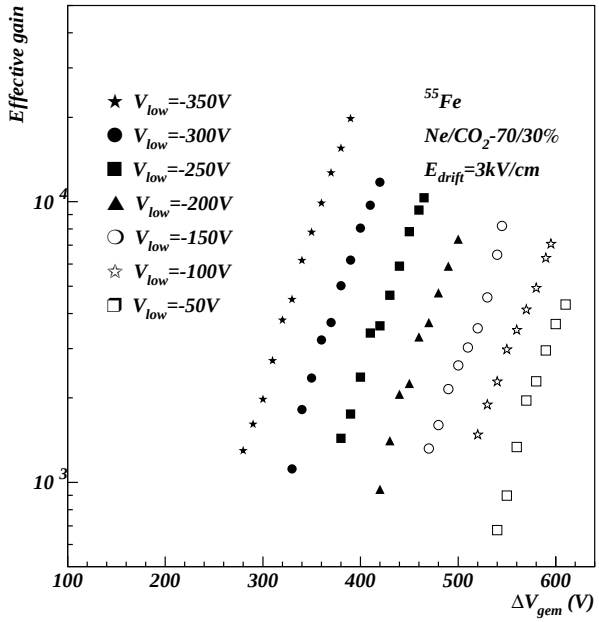

Figure 5.13: Effective gain of the MICROMEGEM filled with Ne/CO_2-70/30% as a function of the potential difference across the GEM, ΔV_{gem}, at different voltages on the lower GEM electrode, V_{low}. The open marks represent relatively low voltages on V_{low} while the closed marks show higher voltages.

The maximum gain of each curve on figure 5.13 corresponds to the highest ΔV_{gem} without sparks. In our experiment, a spark is defined as an overcurrent exceeding a threshold set to 1 μA on the high voltage power supply. When the detector is powered but not irradiated, the current drawn by the electrodes amount to few nA. It is important to note that although the whole stored charge, which is $\sim 3\ 10^{-6}$ C at the highest voltages, can be released in one spark, the discharges do not destroy neither the MICROMEGEM structure nor the PreShape 32 electronics, equipped with protection resistors of 400 Ω. It has been shown that the PreShape 32 protected by resistors above 200 Ω resists more than 500 discharges of $\sim 10^{-6}$ C at a sparking rate of $\sim$ 0.5 Hz [93]. Similar behaviour has been observed with the PreMux 128 chip [92]. Note also that the highest gains are obtained by pushing the amplification in the transfer gap i.e. using the parallel plate-mode.

Figure 5.14 compares the effective gain in Ar/CO_2-70/30% and Ne/CO_2-70/30% for two different voltages on the bottom GEM layer, V_{low} = - 250 V and V_{low} = - 300 V. The plot shows that in this geometry argon and neon both allow to reach gains higher than 10,000. We also notice that for given voltage settings, the gain in Argon is larger. This

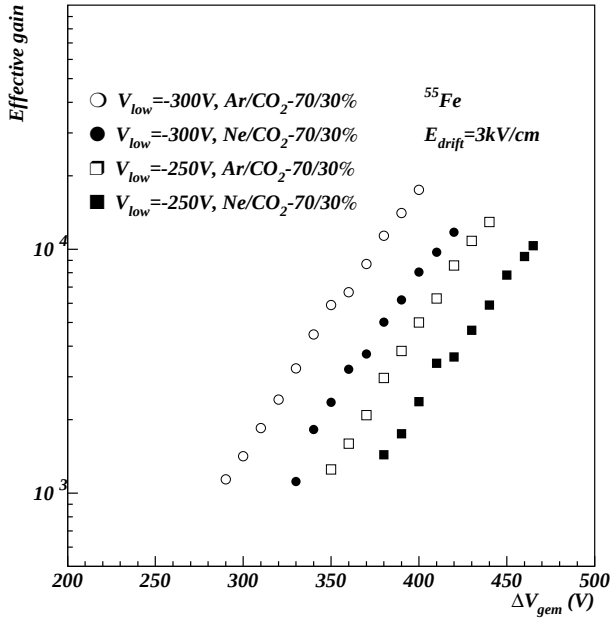

Figure 5.14: Effective gain as a function of the potential difference across the GEM, ΔV_{gem}, for Ar/CO_2-70/30% (open marks) and Ne/CO_2-70/30% (closed marks) at V_{low} = - 250 V (squares) and V_{low} = - 300 V (circles). The drift field is fixed to 3 kV/cm.

can be explained by a lower effective energy needed to produce one electron-ion pair for argon than for neon (see table 3.1).

The maximum effective gain

We already observed in figure 5.13 that the largest gains are obtained by pushing the amplification in the transfer gap, i.e. using the parallel plate-mode, although the maximum ΔV_{gem} we can apply through the GEM foil has then to be reduced to avoid the onset of sustained discharges. Figure 5.15 a) displays such a dependence of the maximum ΔV_{gem} on V_{low} in Ne/CO_2-70/30%. The decrease observed for - V_{low} above 150 V suggests a strong coupling between the electric fields existing in the two amplification regions. It can be noticed that the working voltages are different from those presented in figure 5.13; this is due to the use of another detector although of same geometry. As already mentioned in section 5.3.2, these differences can be due to small variations in the geometry. Moreover these higher voltages does not lead to gains larger than those presented in figure 5.13.

In figure 5.15 b) we show the maximum effective gain, corresponding to the maximum ΔV_{gem}, as a function of the voltage on the bottom GEM electrode. Below V_{low} = - 50 V, part of secondary electrons produced during the avalanche in the GEM holes are collected by the lower GEM electrode [110], reducing the measured gain. Beyond V_{low} = - 50 V, the maximum achievable gain saturates around 7,000, increasing up to 10,000 only at the highest V_{low}. The maximum gain seems to be limited by a critical charge of $\sim$ 0.4 pC in Ne/CO_2-70/30%. Beyond this critical avalanche size, the photon feedback induces a permanent generation of avalanches whatever the voltages on the different electrodes are.

Figure 5.16 displays the effective gain as a function of the upper GEM voltage , V_{up} = V_{low} + ΔV_{gem}, when V_{low} and ΔV_{gem} vary from - 50 V to - 350 V and from 390 V to

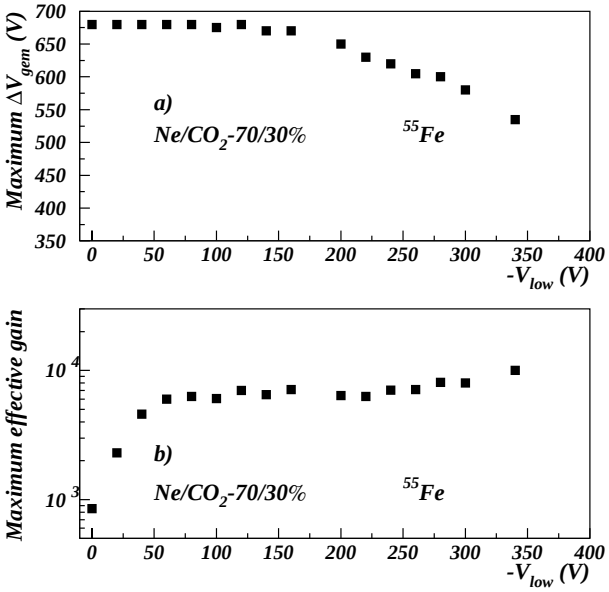

Figure 5.15: Maximum potential difference across the GEM (a) and maximum effective gain (b) as a function of the lower GEM voltage. The MICROMEGEM is filled with the Ne/CO_2-70/30% gas mixture.

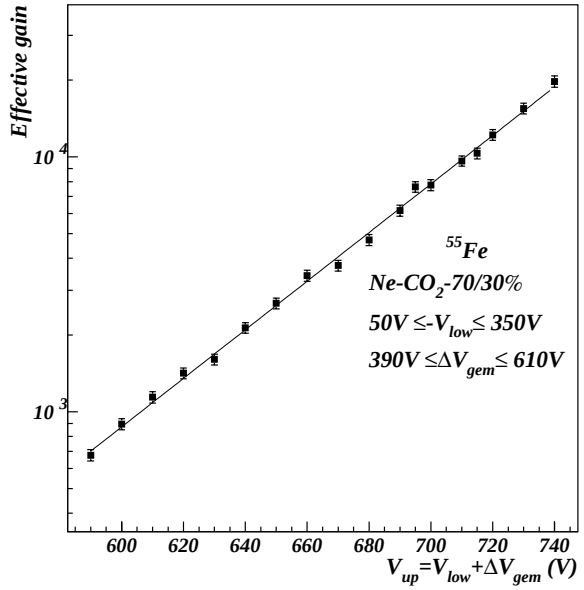

Figure 5.16: Effective gain of the MICROMEGEM in Ne/CO_2-70/30% as a function of the potential on the upper GEM electrode, V_{up}, when V_{low} and ΔV_{gem} vary from - 50 V to - 350 V and from 390 V to 610 V respectively.

610 V respectively. The exponential behaviour shows that the MICROMEGEM detector works like a one amplification stage device, working in parallel plate-mode, with a gap of 100 μm. This operation mode corresponds to the working principle of the MICROMEGAS detector (see section 4.4.2).

Gain dependence on the lower GEM voltage

The results discussed in the previous sections suggest that the MICROMEGEM detector can operate in two different modes: either with a single amplification in the GEM with charge collection by the anode strips or with amplification both in the GEM and in the transfer gap. To observe the transition between these two modes, the gain has been measured as a function of the voltage applied to the lower GEM electrode with fixed ΔV_{gem} and drift field. With the mixture Ar/CO_2-70/30%, we have investigated the repartition of the currents in all electrodes when varying the transfer field. To obtain significant currents, the chamber was irradiated with 8 keV photons from an X-ray gun, at a rate higher than 10^5Hz (see section 5.3.1). The electrode currents are reported in

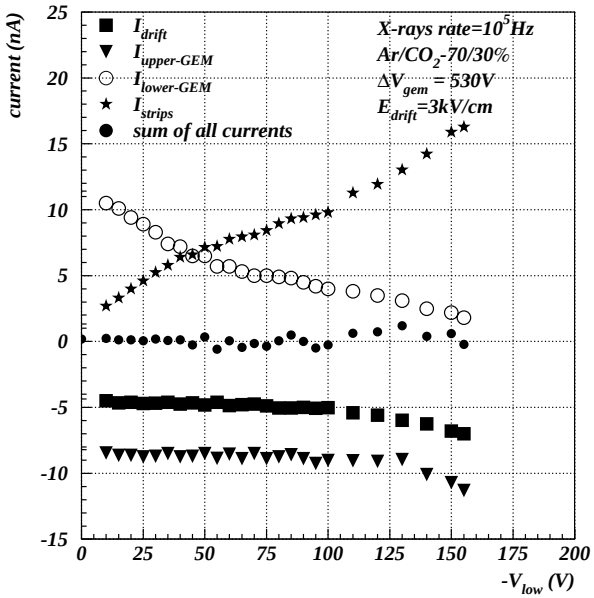

Figure 5.17: Influence of the lower GEM voltage on the currents recorded on all electrodes in Ar/CO_2-70/30%. The drift field is fixed at 3 kV/cm and the potential difference across the GEM is held to 530 V.

figure 5.17 as a function of - V_{low} for ΔV_{gem} = 530 V and E_{drift} = 3 kV/cm. Up to V_{low} = - 100 V, the ion currents, I_{drift} and $I_{upper-GEM}$, are rather constant as well as the sum of the two other currents indicating a constant gas gain. The increase of the electron current on the strips is compensated by the decrease of the current collected on the lower GEM electrode. In this way the increase of the effective gain is due to the better charge collection efficiency by the pick-up strips. The kink observed in the electron currents around V_{low} = - 50 V is probably due to the change of the electric field configuration: the electric field flux from the upper GEM electrode to the lower GEM electrode is replaced by the flux from the upper electrode to the anode strips.

Increasing the transfer field beyond V_{low} = - 100 V, the amplification in parallel plate-mode below the GEM foil is enhanced and produces a non-linear rise of the strip current. This gas gain increase is confirmed by the increase of the total ion current.

The transition from one operation mode to the other is also clearly observable by measuring the effective gain as a function of the lower GEM electrode voltage, as shown in figure 5.18 with a mixture of Ne/CO_2-70/30%, a ΔV_{gem} of 650 V and a drift field of

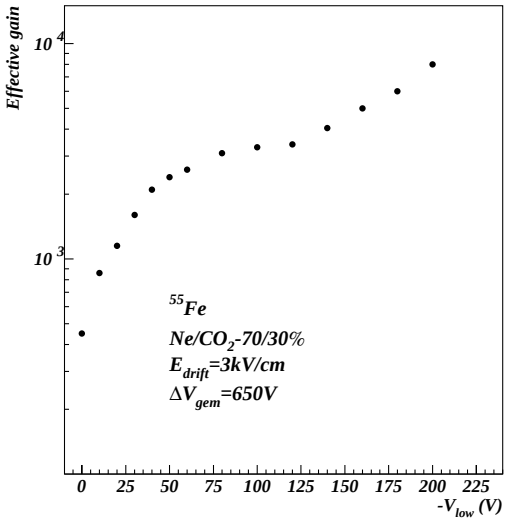

Figure 5.18: Influence of the lower GEM voltage on the effective gain with ΔV_{gem} fixed to 650 V, with E_{drift} = 3 kV/cm and with the Ne/CO_2-70/30% gas mixture.

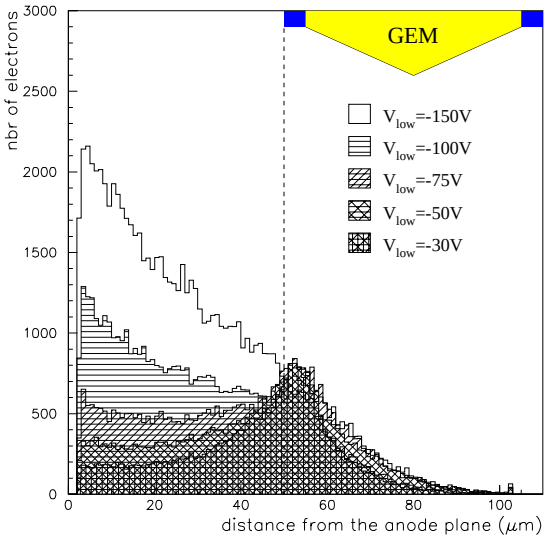

Figure 5.19: Distribution of the distance from the anode plane of the secondary electron production point for different voltages applied to the lower GEM electrode with ΔV_{gem} = 500 V and E_{drift} = 3 kV/cm.

3 kV/cm. As for the current measurements performed with Ar/CO_2-70/30%, the curve shows two kinks around V_{low} = - 50 V and - 100 V, respectively. It is important to note that with such a high GEM potential difference, the effective gain is already $\sim$ 400 without transfer field (V_{low} = 0 V) and that it increases by almost one order of magnitude when entering in the parallel plate avalanche mode.

The transition between the two operation modes has also been investigated with Monte Carlo simulated avalanches in one GEM channel. For each primary electron the coordinates of the creation point of all the secondary electrons are recorded during the avalanche process. The distribution of the distance to the anode plane of the electron production point is shown in figure 5.19 for avalanches produced with a fixed potential difference across the GEM of 500 V and various lower GEM voltages. As expected from the electrostatic simulations (see section 5.4), the amplification region extends downwards from the GEM even at voltages as low as - 30 V. We clearly see that up to V_{low} = - 75 V, the distribution has a peak around 55 μm above the substrate which corresponds to the exit of the GEM hole. The exponential shape of the distribution beyond V_{low} = - 100V shows that the parallel plate amplification starts around this value of V_{low}, confirming the experimental observations.

5.3.4 Gain uniformity

For a large experiment as CMS, a uniform gain in a given counter and from one detector to another is mandatory. In section 5.3.2 we observed hole variations of a few microns between GEM foils produced in different batches. These discrepancies, due to the etching procedure used to manufacture the foils, modify the transparency and the effective gain.

For the same potential difference across the GEM, smaller holes reduce the transparency but increase the electric field strength at the hole centre, therefore enhancing the electron amplification. On the optimum transparency plateau, gain variations up to 50% have been observed between similar MICROMEGEM counters. The strong correlation between the effective gain and the hole diameter has been reported for various GEM geometries by other authors (see reference [115]).

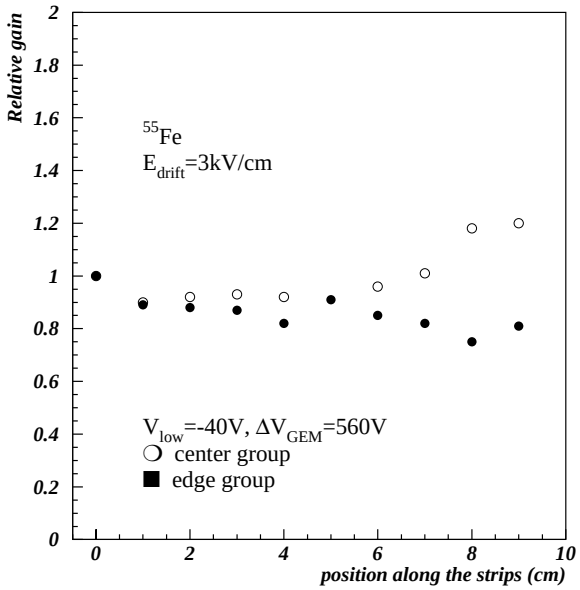

Figure 5.20: Gain uniformity along the anode strips at the center (open marks) and on the edge (closed marks) of the detector operated with V_{low} = - 40 V, ΔV_{gem} = 560 V and E_{drift} = 3 kV/cm.

Within a counter, the uniformity has been studied by performing a scan along the strips. Figure 5.20 shows the relative gain as a function of the distance along the strips in the centre and on the edge of the counter. The detector was operated with V_{low} = - 40 V, ΔV_{gem} = 560 V and E_{drift} = 3 kV/cm. We observe that the gain is uniform within 20%. Since the GEM foil is well supported by regularly located spacers (see section 5.1), the gain fluctuations are probably due to the GEM hole variations. The optical inspection of the GEM holes with a microscope has shown that the diameter fluctuations are within 1.5 μm over the all active area.

5.3.5 Energy resolution

A pulse charge spectrum obtained with a ^{55}Fe source is shown in figure 5.21 for a Ar/CO_2-70/30% gas mixture and settings V_{low} = - 300 V, ΔV_{gem} = 340 V, E_{drift} = 3 kV/cm, leading to an effective gain of 4,000. The main peak and the escape peak of argon are clearly resolved with an energy resolution (FWHM) of 22% at 5.9 keV. In the MICROMEGEM detector, the main factors which affect the energy resolution are the transparency, the gas gain fluctuations in both stages and the uniformity of the gas gain. The effect of the transparency is clearly observed in figure 5.9 and was discussed in section 5.3.2. At the optimum drift field of 3 kV/cm, the gas gain fluctuations mainly determine the energy resolution. In a multiple amplification-stages device, these fluctuations are determined by

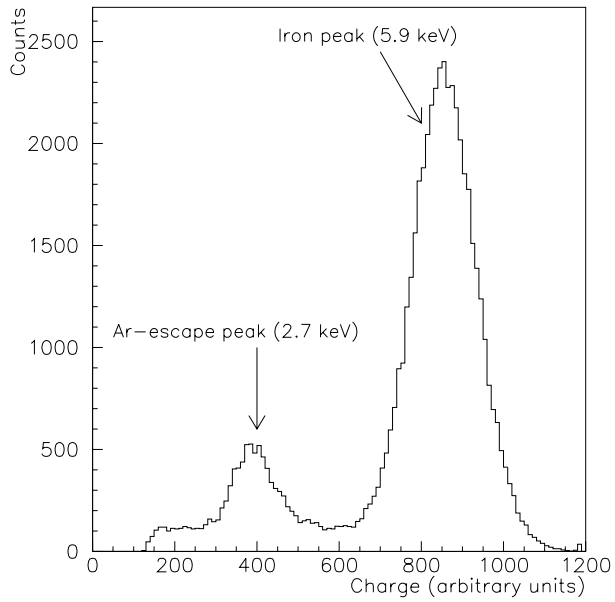

Figure 5.21: Charge spectrum in Ar/CO_2-70/30% at an effective gain of 4,000 with V_{low} = - 300 V, ΔV_{gem} = 340 V and E_{drift} = 3 kV/cm. The iron peak and the escape peak of Argon are clearly seen with an energy resolution (FWHM) of 22%.

the fluctuations of the first avalanche and are due to the non-uniformity of the GEM holes diameter. However inhomogeneities in the electric field below the GEM-foil can increase the spread of the charge distribution. These inhomogeneities are connected to the overlap between the transfer field and the GEM field in the regions located just below the GEM holes (see figure 5.4). As observed in the previous section both effects lead to 20% gain fluctuations across all active area.

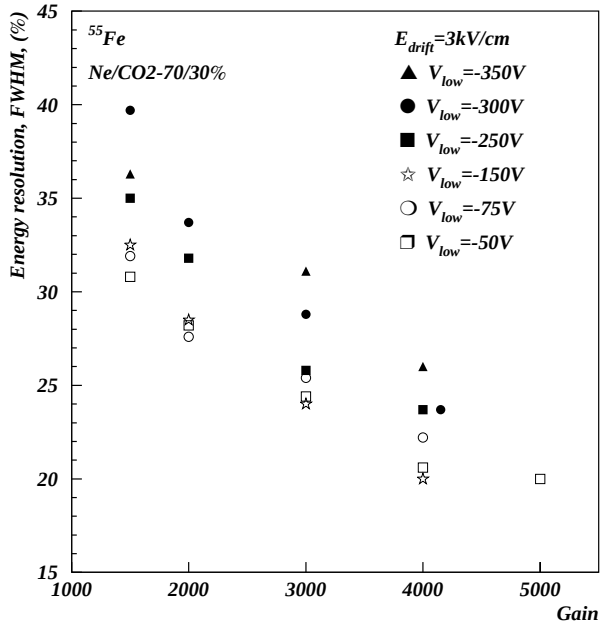

Figure 5.22: Energy resolution (FWHM) as a function of the effective gain in Ne/CO_2-70/30% for different settings on V_{low} and with E_{drift} = 3 kV/cm.

Figure 5.22 reports the energy resolution (FWHM) in the mixture Ne/CO_2-70/30% as a function of the gain for different voltages on the lower GEM electrode. The open marks correspond to relatively low voltages on this electrode while the closed marks represent settings where the parallel plate multiplication is highly enhanced. In any case, the energy resolution improves with gas multiplication, reaching between 20 and 25% at a gain of 4000. Because of the saturation of the PreShape 32 electronics, energy resolutions at gains higher than 5000 are not available. We note also that at the same gain, the energy resolution degrades at high voltages on the lower GEM electrode. Indeed, pushing the parallel plate multiplication, the high electric field is no longer confined in the central region of the GEM channels. This effect has been observed with simulations by integrating the Townsend coefficient along the drift path of electrons starting at a distance of 1 μm below the GEM foil. The multiplication factor M is shown in figure 5.23 a) as a function of the distance from the GEM hole axis for different values of V_{low}. The upper GEM voltage has been fixed to - 650 V in order to keep the overall gain constant around 3000. We observe that the amplification factor is strongly inhomogeneous due to the non-uniformity of the electric field in this region (see section 5.2). The extent of the avalanche region is defined by the region where the integral of the Townsend coefficient is larger than 2. The simulation shows that below V_{low} = - 100 V, the avalanche occurs at a distance from the hole axis smaller than $\sim$ 35 μm, i.e. the GEM hole radius. As seen in section 5.3.3, the electric field is not high enough to provide the parallel-plate amplification beyond this radius. At higher V_{low} the parallel-plate mode starts and extends the avalanche region towards the entire transfer gap. It is also important to note that keeping the upper GEM voltage to the constant value of - 650 V, the extension of the amplification region is accompanied by a reduction of the electric field in the GEM channel as observed in figure 5.23 b) which shows the calculated electric field strength as a function of the distance from the pick-up strips along the axis of the GEM hole. Consequently, at high transfer field, the overall amplification is provided by a weaker electric field applied over a broader volume. These conditions are expected to favour gain fluctuations as well as the degradation of the energy resolution (see section 3.4.2 and references [36], [37]). However the energy resolution of the MICROMEGEM obtained with moderate V_{low}, up to - 150 V, are comparable with the results of other detectors built with the PCB technology ([102], [103], [112]).

5.3.6 High rate behaviour of the MICROMEGEM

As pointed out in section 2.4, the use of gaseous detectors in the CMS Tracker, in which the particle flux can exceed 10^4Hz/mm^2, requires that the detectors have a good gain stability at these high rates.

The MSGC suffers less from space charge than the MWPC due to a smaller distance between the electrodes (see section 4.2). At high rate, however, the presence of the insulating substrate provokes the charging-up of the surface due to the accumulation of ions. This polarization causes modifications to the amplification field and to the gain. Therefore the absence of material between the GEM foil and the pick-up strips should allow the MICROMEGEM detector to maintain a good rate capability, which is one of the main properties of parallel-plate counters and of the MICROMEGAS detector [77]. However some authors have reported short terms, rate-dependent instabilities, which slightly modify the measured gain of a GEM due to the charging-up of the kapton [116].

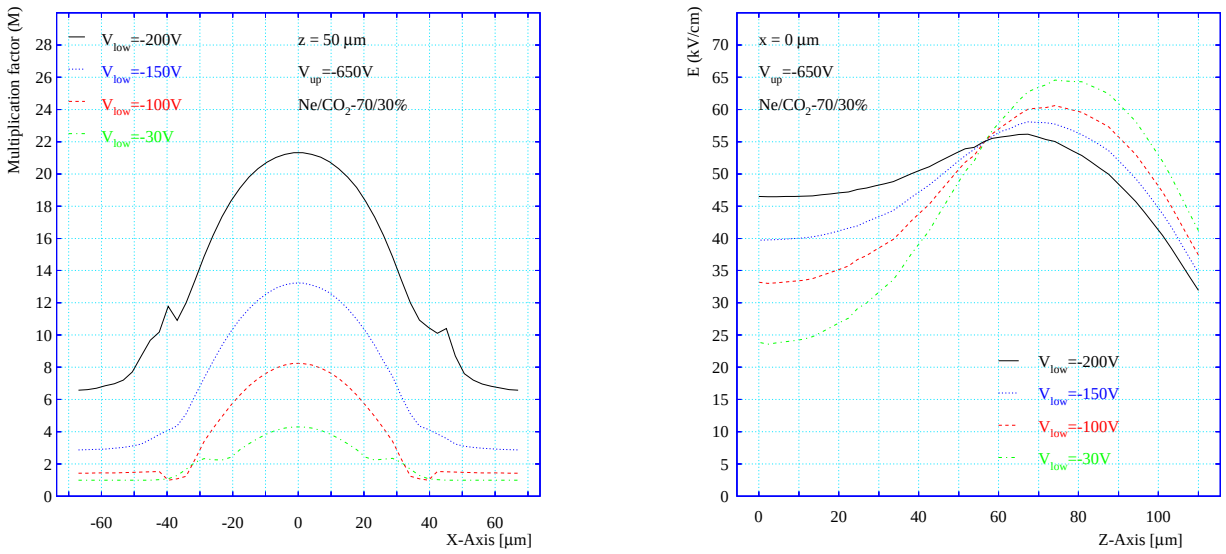

Figure 5.23: Multiplication factor of electrons released 1 μm below the GEM foil as a function of the distance from the GEM hole axis, for different values of V_{low} (a). Electric field strength as a function of the distance from the pick-up strips, along the GEM hole axis for different values of V_{low} (b). The upper GEM voltage is fixed to - 650 V in order to provide a gain of 3000.

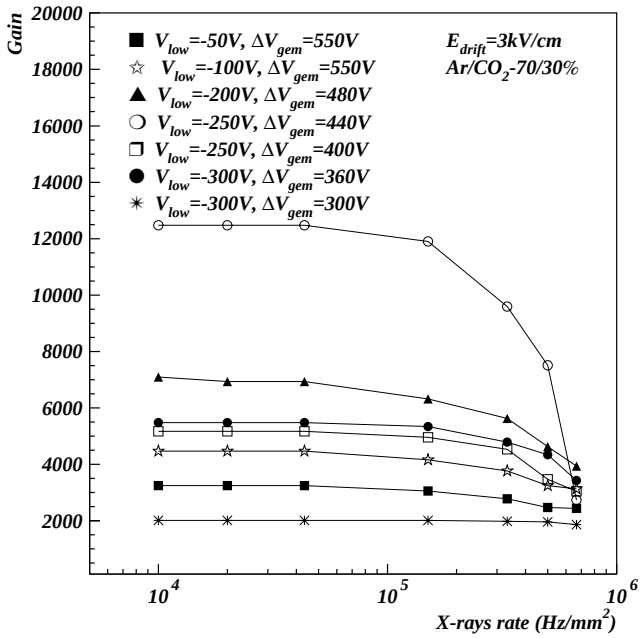

Figure 5.24: Gain as a function of X-rays rate in Ar/CO_2-70/30% for different configurations of voltages.

To study the rate capability of the MICROMEGEM, we exposed the detector to high fluxes of 8.3 keV photons from an X-ray tube, up to 10^6 Hz/mm^2 (see section 5.3.1). Figure 5.24 shows the gain as a function of the X-ray rate, for different voltage settings with an Ar/CO_2-70/30% gas mixture, at E_{drift} = 3 kV/cm; the gain is computed from the pulse height of the signal. No significant dependence of the gain on incoming flux has been

observed up to a rate of 10^5 photons/mm^{2}s. At higher rate the space charge distorts the electric field in the amplification region and limits the gas gain to a maximum of ~ 3000 at a rate close to 10^6 Hz/mm^{2}s. For an MSGC, this maximum gain is reached at a flux of 10^5Hz/mm^{2}s [85, 117]. Moreover we did not see any reduction of the maximal voltages we can apply on the different electrodes. Even high rates do not induce discharges in the detector. Given the large range of applied voltages, we also note that the detector rate behaviour is independent of the amplification-mode used. This quite promising rate capability can be explained by a fast charge collection and a fast evacuation of the ion space charge.

We did not have the opportunity to study the ageing properties of the MICROMEGEM detector. However, owing to extensive studies performed with a DOUBLE-GEM detector [118] and a TRIPLE-GEM detector [119], we do not expect large degradation of the MICROMEGEM gain under long-term exposure to radiation. Indeed the gas used, Ar/CO_2, has good aging properties and the 80 μm wide anodes should not be sensitive to any polymeric deposit.

5.4 Test in an intense hadron beam

The MICROMEGEM detector has been introduced to avoid the onset of discharges due to the presence of HIP's, by using an amplification shared between two stages (see section 4.4.1). Although this technique has shown promising features during the laboratory tests performed with X-rays (see previous sections), its feasibility had to be proven in a high intensity beam of hadrons producing HIP's with a large dynamic range of deposited energy. This section reports the test of the MICROMEGEM detector in such conditions. In section 5.4.1, we present the beam test facility as well as the experimental set-up. The data analysis is discussed in section 5.4.2. The results of the signal-to-noise ratio (SNR) at high intensity are presented in section 5.4.3 and the spark analysis is discussed in section 5.4.4.

5.4.1 The πm1 test facility at PSI and the experimental set-up

Simulation studies have shown that the charge energy deposition in the counters expected during LHC operation is best approached by 300 MeV pions [120]. The continuity of the irradiation may also have an influence on the discharge occurrence in the detector. Therefore the MICROMEGEM detector has been exposed to the πm1 beam at the Paul Scherrer Institute (PSI) cyclotron, in Villigen, Switzerland, with other gaseous detectors tested in the framework of the CMS experiment. This low energy pion beam, 350 MeV, is bunched at a frequency of 50 MHz, leading to an approximately continuous beam. The average beam intensity could be varied between 10-20 Hz/mm^2, called low intensity regime and 5 kHz/mm^2 called high intensity regime. The high intensity regime reproduces approximately the charged particles flux of LHC at a distance of 60 cm from the interaction point. The beam profile is estimated to have a Gaussian distribution in the directions orthogonal to the beam, with a standard deviation of 40 mm allowing the irradiation of the entire detector surface. In addition to the low energy pions which are MIP's, the detector is also exposed to heavily ionizing particles produced by strong interactions between the pions and the detector material. The HIP's rate is of the order of 10^{-4} per pion.

Two MICROMEGEM's have been mounted on a bench together with other gaseous counters like MSGC's with thick metal strips [121], MICROMEGAS and double GEM detectors, studied in the framework of the CMS collaboration. The bench was equipped with two pairs of scintillators at the front (F) and at the back (B); their coincidence provided the trigger for the data taking. Large scintillators, 10×10 cm^2, were used at low beam intensity (LI) and small ones, 1×5 cm^2, at high beam intensity (HI). Consequently these scintillators are called : LIF, HIF, LIB and HIB. The MICROMEGEM detectors are similar to those described in section 5.1, but the anodes are read out by the PreMux 128 chip [122].

The Readout electronics

The PreMux 128 is the successor of the PreShape 32, described in section 5.3.1; it has 128 channels. The front-end chip is based on the PreShape 32 amplifier and shaper and has been equipped with a multiplexer. This multiplexing unit allows the digitization of several strips of the substrate with a single ADC. The working principle of one channel of this chip is illustrated in figure 5.25. The strip signal is sampled twice by opening the switches S_1 and S_2. S_2 is closed at a time close to the time at which the signal is maximum and S_1 is closed when the pulse returns to the baseline. Since the time constant of the RC stages is very small (3.5 ns) compared to the rise time of the signal ($\sim$ 40 ns), the voltages of C_1 and C_2 closely follow the voltage on the input. When S_1 and S_2 are opened, these voltages are stored on the capacitors. The difference of voltages on the capacitors are amplified by external differential amplifiers. To collect the maximum charge, we have to adjust the delay between S_2 and the trigger signal. For this test, the delay has been fixed to 50 ns with respect to the trigger.

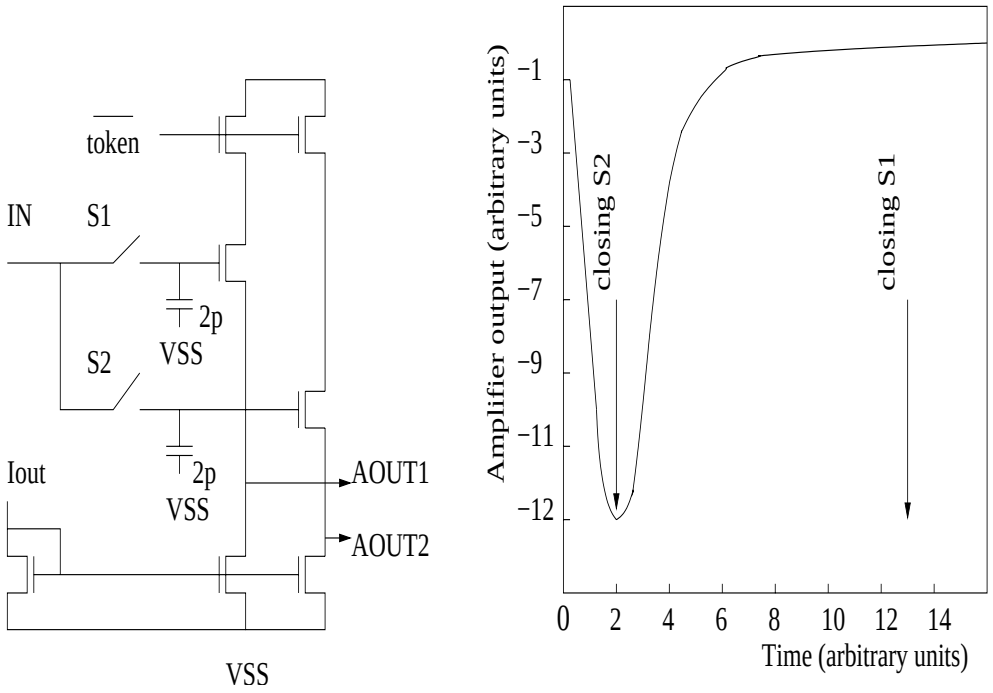

Figure 5.25: Schematic layout and working principle of a single PreMux 128 channel.

High voltage system

The high voltages are provided by CAEN high voltage power supply to the GEM electrodes and the drift plane. The electrodes are decoupled from the high voltage by protection resistors of 10 MΩ. A bad HV connection to the drift plane prevented one MICROMEGEM from operating during almost the whole period. The current drawn by the power supply has a trip level set to 1 μA

Gas system

A gas mixer built at CERN was used. To avoid gas pollution, the distribution tubes are made of stainless steel. The choice of the gas mixture was limited to Ne/DME-33/66% and Ne/DME-90/10%. Although the number of primary ionization is lower with increasing Ne content, the Ne/DME-90/10% mixture has been chosen to obtain higher gains [123].

Data acquisition system

The data acquisition system used during this test is depicted in figure 5.26. Each MICROMEGEM detector was equipped with four PreMux 128 chips, which amplify and multiplex the signals from the 512 anode strips. The readout sequence is initiated by the trigger signal from the coincidence of the two scintillators, LIF and LIB or HIF and HIB, depending on the beam intensity [124]. The trigger unit provides a fast signal to the PreMux chips, to close the switch S_2, and to the VME sequencer which synchronizes the readout of the front-end chips. The analog outputs are digitized by 12-bit Scirocco Flash ADC. Another crate holds the current monitors which consist in picoamperemeters put on the HV lines [125] recording the currents drawn by the GEM electrodes. The currents are read out every 2 ms by ADC's. The event builder combines 1024 of such measurements in one so-called slow-control event.

All raw data are finally written to DLT tapes for offline analysis. In parallel, the overall control and the online monitoring of the data acquisition was ensured by a software running on a Linux-based PC, developed at IN2P3 Lyon.

5.4.2 Data analysis

The charge generated by an ionizing particle is spread over one or several consecutive anodes, depending on the track incidence angle and on the diffusion of the electrons in the gas. To find the impact point of the ionizing particle in the counter, clusters of strips with signal have to be formed after pedestal subtraction, common mode correction and noise calibration.

Pedestal subtraction and common mode correction

The raw data $\mathrm{ADC}_i{}^j$ recorded by the Sirocco FADC for the i^{th} strip in the j^{th} event is a superposition of three contributions:

$$ADC_i^j = S_i^j + P_i + C_i^j, \tag{5.2}$$

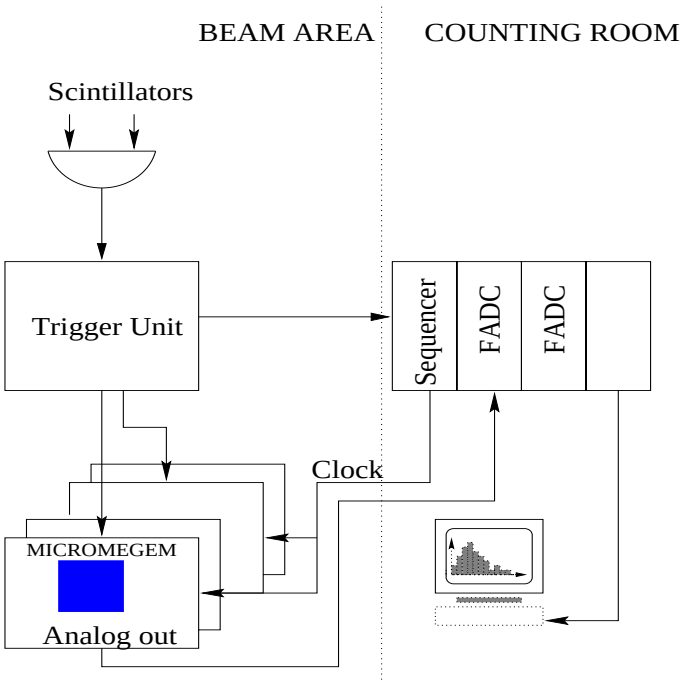

Figure 5.26: Schematic view of the data acquisition system used at PSI.

where S_i^j corresponds to a possible signal generated by an ionizing particle, P_i is the strip pedestal and C_i^j is a possible common fluctuation of the baseline of the 128 strips connected to the same readout chip. In absence of particle signals, the pulse height of each channel has a Gaussian distribution. The pedestal of a strip is defined by the average value of this distribution. The fluctuations around the pedestal are due to the noise.

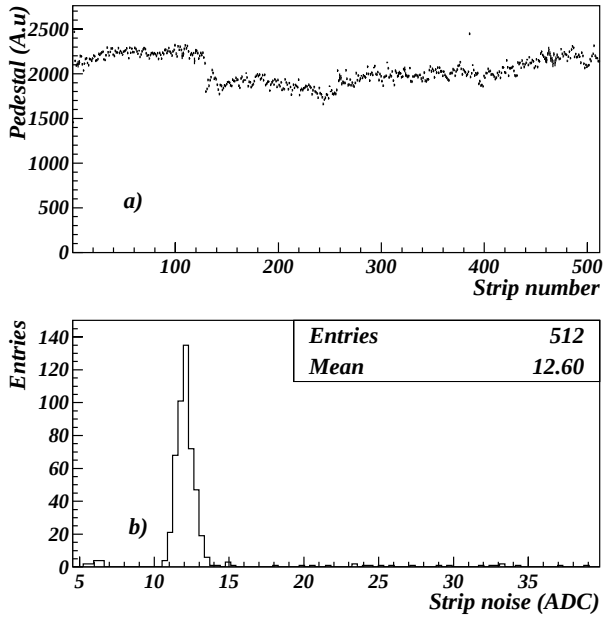

Figure 5.27: Pedestal as a function of the strip number (a) and RMS noise distribution (b) of the MICROMEGEM counter.

During these tests, once a day, dedicated runs were taken without particles for pedestal

measurements. At low intensity it is also possible to calculate the pedestal during data taking. In this case, the strips may have a particle signal, which increases the calculated mean. The pedestal subtraction has thus to be done in an iterative way in order to remove the contribution of the signals generated by ionizing particles. A first estimation of the pedestal and the RMS is computed from the first 400 events. At the second iteration, all the signals larger than three times this RMS over the pedestal value are rejected.

Once the pedestal of each strip, P_i, is known, it is subtracted from the raw data. The common mode is computed for each event from the average of the remaining signals on the 128 strips connected to the same PreMux 128 chip. To remove strips which may have a signal, this is also performed in an iterative way. After pedestal subtraction and common mode correction, this set of 400 events is used to compute the strip noise, σ_i, defined as the standard deviation of the remaining signal distribution.

Figure 5.27 a) shows the pedestal measured for each strip of a MICROMEGEM detector. We clearly observe that it depends on the chip, with a period of 128 strips. The RMS noise distribution is shown in figure 5.27 b). The average strip noise is around 13 ADC counts which is 50% higher than the noise measured with MSGC's equipped with thick metal strips and tested in the same conditions [121]. This additionnal noise can be explained by the capacitive coupling between the large anodes, 80 μm wide, and the close lower GEM electrode which results in a strip capacitance of 14 pF instead of 7 pF for the MSGC's.

Cluster characteristics

A cluster is defined by a group of adjacent strips, each having a signal larger than 3 times the strip noise of that channel. To allow for broken or dead strips, one strip with a signal below the threshold is tolerated within a cluster. The coordinate of the impact point is reconstructed by computing the barycentre of the cluster charge:

$$y_{cluster} = \frac{\sum_i S_i y_i}{\sum_i S_i}, \tag{5.3}$$

where y_i and S_i are the y-coordinate and the charge of the i-th strip of the cluster.

The cluster charge, $\sum_i S_i$, is proportional to the energy deposited in the counter by the ionizing particle. A typical cluster charge distribution, recorded at low intensity $\sim$ 10 Hz/mm^2, is shown in figure 5.28 a) for a MICROMEGEM operated with a Ne/DME-90/10% gas mixture, at V_{low} = - 320 V, ΔV_{gem} = 120 V and E_{drift} = 1 kV/cm. Note that the operation voltages are far from those commonly used with X-ray sources, where the GEM potential difference is generally well above 200 V (see figure 5.13). In this hadron beam, the potential difference across the GEM has to be lowered to a value as low as 120 V in order to avoid the onset of sparks induced by the heavily ionizing particles. With these settings, a drift field of 1 kV/cm was found to be optimum. Indeed with E_{drift} = 2 kV/cm, the cluster charge is already reduced by 20%. This optimum value, lower than those obtained during X-rays measurements (see section 5.3.2), is due to the low potential difference applied across the GEM. The cluster charge distribution has a Landau shape as discussed in section 3.1. The distribution peak not well separated from the noise distribution suggests that the detector is not fully efficient. The corresponding cluster noise distribution is shown in figure 5.28 b). The cluster noise is defined as the

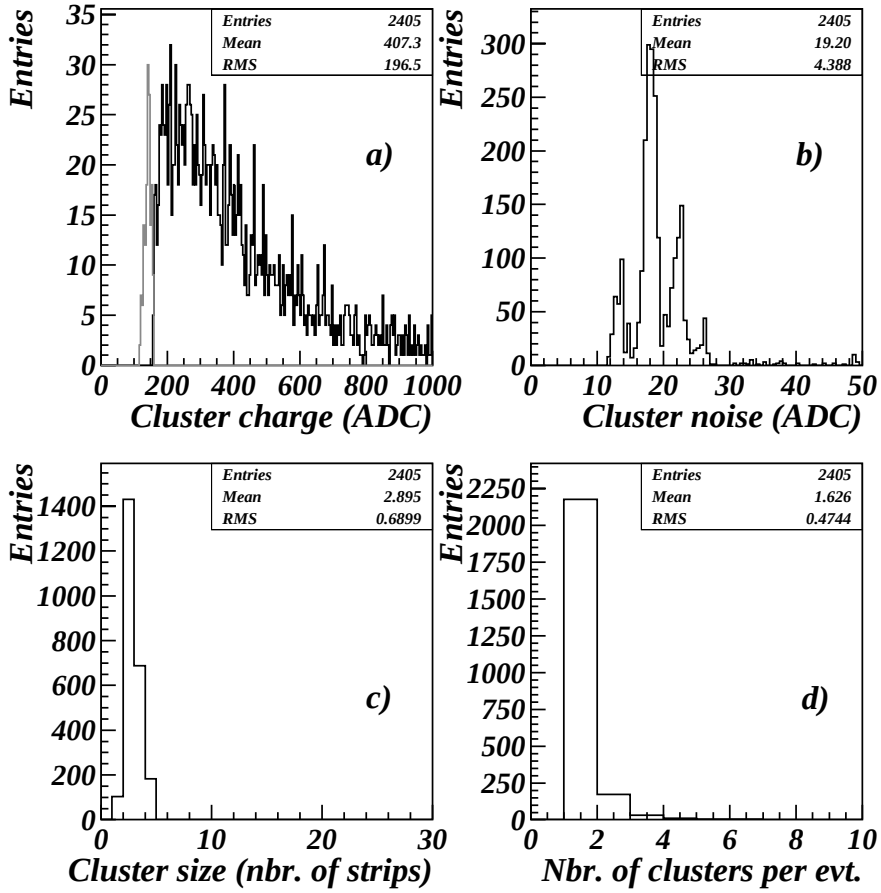

Figure 5.28: Cluster charge (a), cluster noise (b), cluster size (c) and cluster multiplicity distributions of the MICROMEGEM filled with Ne/DME-90/10% with V_{low} = - 320 V, ΔV_{gem} = 120 V and E_{drift} = 1 kV/cm at low intensity ($\sim$ 10 Hz/mm^2).

quadratic mean of the strip noise. The main peaks correspond to clusters containing one, two or three strips. Figure 5.28 c) represents the distribution of the number of strips in the clusters which is in average $\sim$ 2.9 strips per cluster. This number is larger than the cluster size of $\sim$ 2.3 strips measured during these tests with MSGC's filled with Ne/DME-33/66% and operated with E_{drift} = 10 kV/cm. The larger cluster size in Ne/DME-90/10% is due to a larger transverse diffusion coefficient, 282 $\mu m/\sqrt{cm}$ at E_{drift} = 1 kV/cm instead of 165 $\mu m/\sqrt{cm}$ at E_{drift} = 10 kV/cm in Ne/DME-33/66%. The transverse diffusion coefficients in both gas mixtures have been computed with the program MAGBOLTZ (see reference [96] and section 4.5). As shown in figure 5.28 d), at low intensity ($\sim$ 10 Hz/mm^2), 1.1 clusters are found in average per trigger.

5.4.3 Signal-to-Noise Ratio

The signal-to-noise ratio of a cluster is defined as the total charge of the cluster divided by the quadratic mean of the strip noise:

$$SNR_{cluster} = \frac{\sum_i S_i}{\sqrt{\frac{\sum_i \sigma_i^2}{N}}}, \tag{5.4}$$

Figure 5.29 shows a SNR distribution for a MICROMEGEM detector operating at low intensity with a mixture of Ne/DME-90/10%; the voltage settings are V_{low} = - 320 V, ΔV_{gem} = 120 V and E_{drift} = 1 kV/cm, as explained in section 5.4.2. The SNR of the detector is defined as the maximum of probability of this distribution. With these settings, the maximum of probability is at $\sim$ 19. Although we did not perform detection efficiency measurements, the shape of the distribution, with a sharp edge on the left, suggests that the counter is not fully efficient. Note that a MICROMEGAS detector equipped with the same readout electronics, operated with a mixture of Ne/DME-90/10% and with E_{drift} = 0.7 kV/cm, is efficient at 92% for an SNR of 19 [92].

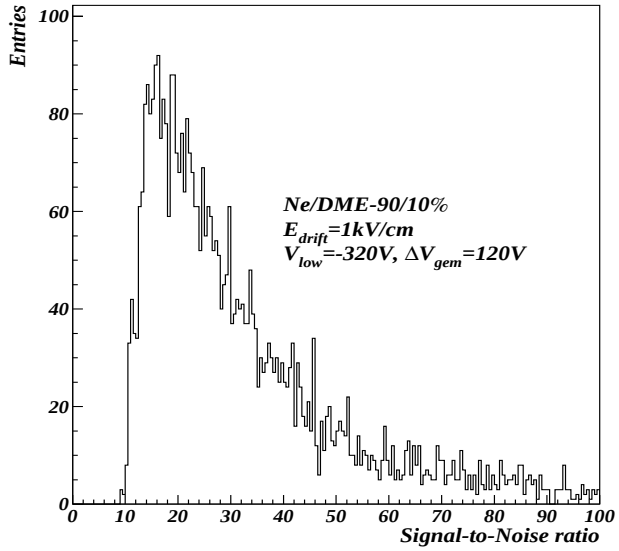

Figure 5.29: Signal-to-noise ratio distribution of the MICROMEGEM filled with Ne/DME-90/10% with V_{low} = - 320 V, ΔV_{gem} = 120 V and E_{drift} = 1 kV/cm. The beam intensity is $\sim$ 10 Hz/mm^2.

At high intensity, the presence of several particles per event renders the SNR measurement more difficult. Three particle signals per event are recorded in average at high intensity, as observed in figure 5.30 (closed line) for a MICROMEGEM filled with Ne/DME-90/10% and operating with V_{low} = - 250 V, ΔV_{gem} = 165 V and E_{drift} = 1 kV/cm. The cluster multiplicity measured at low intensity with the same setting is also represented (dashed line). Therefore tracking should be done to select the triggering particle to compute the SNR at high intensity. Unfortunately we did not have a telescope at our disposal. Moreover the multiple scattering, 300 μm between two successive detection planes, is not negligible and renders the track reconstruction difficult. Consequently the SNR at high intensity is computed by selecting the cluster with the highest charge per event. This selection artificially shifts the SNR at high intensity to larger values than at low intensity. This effect is shown in figure 5.31. Both SNR distributions have been recorded at the same voltage settings of V_{low} = - 250 V, ΔV_{gem} = 165 V and E_{drift} = 1 kV/cm but with two different beam intensities. The closed line distribution is obtained in the high intensity regime, $\sim 4\times10^3$Hz/mm^2, while the dashed distribution corresponds to the low intensity regime of $\sim 10^2$Hz/mm^2. The SNR measured at high intensity is $\sim$ 25% larger than the SNR measured at low intensity. In the following of this section, the measurements at high intensity are corrected for this artificial rate dependence: the high intensity SNR is given

by the value measured at low intensity with the same settings or by subtracting 25% of its value at the settings for which the measurement was not repeated at low intensity.

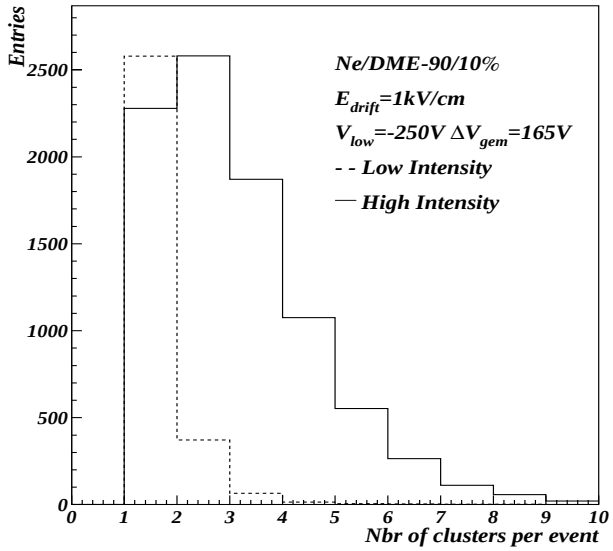

Figure 5.30: Cluster multiplicity at low ($\sim$ 10 Hz/mm^2) and high ($\sim 4\times10^3$ Hz/mm^2) beam intensity for a MICROMEGEM filled with Ne/DME-90/10% and operating at V_{low} = -250 V, ΔV_{gem} = 165 V and E_{drift} = 1 kV/cm.

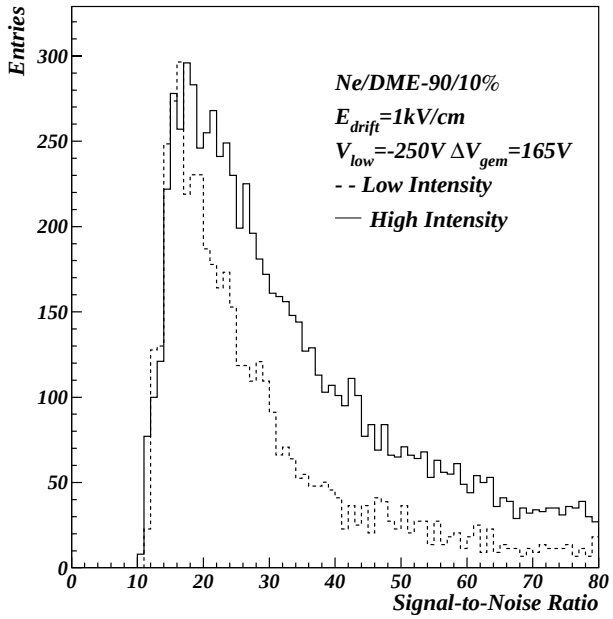

Figure 5.31: Signal-to-noise ratio distributions at low and high beam intensity for the settings V_{low} = - 250 V, ΔV_{gem} = 165 V and E_{drift} = 1 kV/cm, with Ne/DME-90/10%.

At high intensity, a voltage scan has been performed Ne/DME-90/10% in order to reach the highest stable SNR. Figure 5.32 a) shows the SNR as a function of - V_{up} at high intensity (HI) and low intensity (LI), with E_{drift} = 1 kV/cm. Note that at high intensity,

the detector could not sustain a potential difference between the bottom GEM electrode and the strips larger than 250 V because of sparks. Therefore - V_{low} has been reduced to 250 V at high intensity instead of 300 V at low intensity. The last point of each curve corresponds to the highest sustainable SNR without sparks. We observe that although this highest SNR is 19 at low intensity, it is reduced to 15 at high intensity.

Figure 5.32 b) shows the highest sustainable SNR as a function of the lower GEM electrode voltage, at high intensity. The SNR of each value of V_{low} corresponds to the highest sustainable ΔV_{gem} with this V_{low}. We observe that at high intensity the maximum SNR is rather constant, ~ 14, whatever the voltage on the lower electrode is. Consequently this shows also that ΔV_{gem} has to be reduced when -V_{low} is increased to avoid the onset of discharges. Therefore the maximum voltage applied on the upper GEM, - V_{up}, seems to be limited to 410-415 V at high intensity, 30 volts less than at low intensity. This behaviour is similar to the limitation of the avalanche size shown in figure 5.15 which is due to the strong coupling between the two amplification stages. As pointed out in the sections 5.2 and 5.3.3 the MICROMEGEM detector behaves like a single-stage device and its gain has to be reduced at high intensity in order to avoid discharges induced by HIP's, like with the MICROMEGAS detector. But at this reduced gain, the detector is most probably not fully efficient.

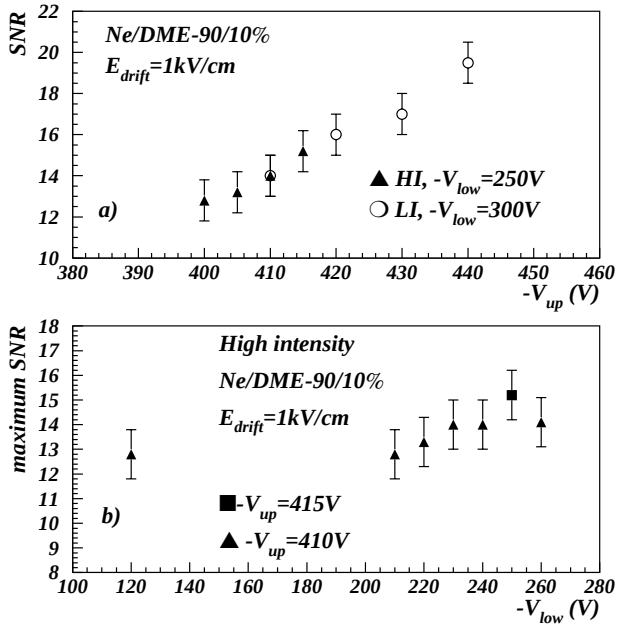

Figure 5.32: Signal-to-noise ratio as a function of the upper GEM electrode voltage, - V_{up}, at low intensity (open marks) and at high intensity (closed marks) (a). Maximum sustainable SNR at high intensity as a function of V_{low} (b). E_{drift} is 1 kV/cm and the gas mixture is Ne/DME-90/10%.

5.4.4 Spark analysis

In a powered but not irradiated detector, the current recorded on the electrodes is expected to be less than 10 nA. Under high radiation rate, the drawn current can reach up to a 100 nA on the bottom GEM electrode, depending on the beam intensity and on the

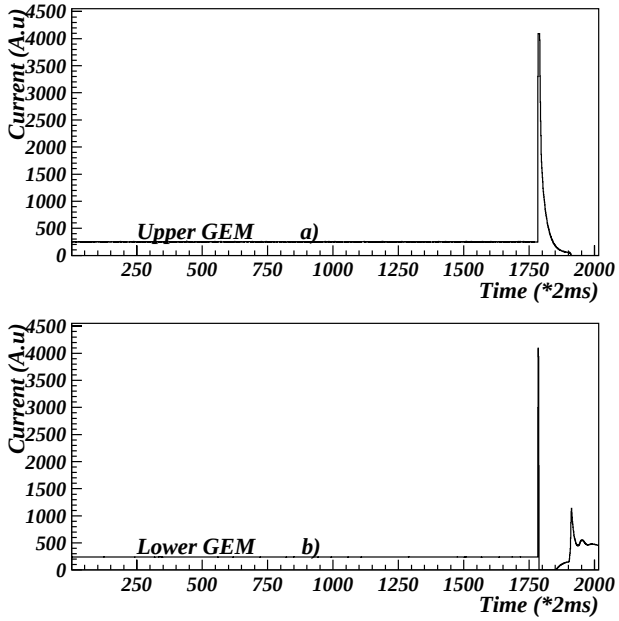

Figure 5.33: Current measured as a function of time on the upper GEM electrode (a) and on the lower GEM electrode (b) when a discharge occurs in a MICROMEGEM filled with Ne/DME-90/10% and operated with V_{low} = - 250 V, ΔV_{gem} = 150 V and E_{drift} = 1 kV/cm.

detector gain. The occurrence of a spark in the counter produces a short (few ns) but large (above 1 μA) fluctuation on the recorded electrode currents. Figure 5.33 displays the current simultaneously recorded on both GEM electrodes as a function of time, for V_{low} = - 250 V, ΔV_{gem} = 150 V and E_{drift} = 1 kV/cm. Because of the protection resistors on the HV lines (see section 5.4.1), we observe the re-charge of the GEM foil over several tens of milliseconds. The current peak is so high that it provoques the saturation of the picoammeters. Consequently only the lower limit on the released charge can be estimated; it is around 250 nC which is more than 5 times the released charge during a spark in a MSGC counter [121]. The current drawn often overcomes the trip level set to 1 μA and provoques the shut-down of the power supply.

After more than 50 sparks, the MICROMEGEM detector does not show any damage to its structure or short-circuit; the GEM foil is robust and can withstand repeated sparks [126]. Moreover the large anode strips, 80 μm wide and 5 μm thick, are much more robust than the delicate MSGC anodes, 7 μm large. However we have to take care that the discharges do not destroy the unprotected readout electronics as dead channels can lead to local inefficiencies. Consequently we have checked the number of active strips in the counter before and after irradiation, using the strip RMS noise. As an example, figures 5.34 a) and 5.34 b) show the RMS noise of each strip at the beginning and after a period of 35 hours at high intensity, respectively. During this period, 15 sparks have been recorded. Figure 5.34 c) represents the difference of the RMS noise after and before this period. On this figure we clearly identify 15 dips corresponding to new dead channels. Although the spark rate is low, $\sim 10^{-4}$ Hz, the destruction of the unprotected electronics prevents to operate at a higher SNR with a moderate spark rate. Indeed, studies performed during these tests with a MICROMEGAS counter have shown that a protection resistor of 400 Ω (ENC $\sim$ 1000 e^-) is sufficient to protect the PreMux 128 channels against more than 10^5 sparks with a maximum charge of $\sim$ 0.7 μC [92]. Even if discharges are to

be avoided in a large scale experiment like CMS, a protected electronics would probably permit to reach the full detection efficiency still with an acceptable sparking rate. As comparison, the maximum SNR achieved for MSGC's with thick metal strips is ~ 13 when limiting the sparking rate to 3×10^{-2} Hz [121], at high beam intensity. Note also that the spark rate of the MICROMEGAS detector is already as high as 0.15 Hz with a SNR of 12, at low intensity.

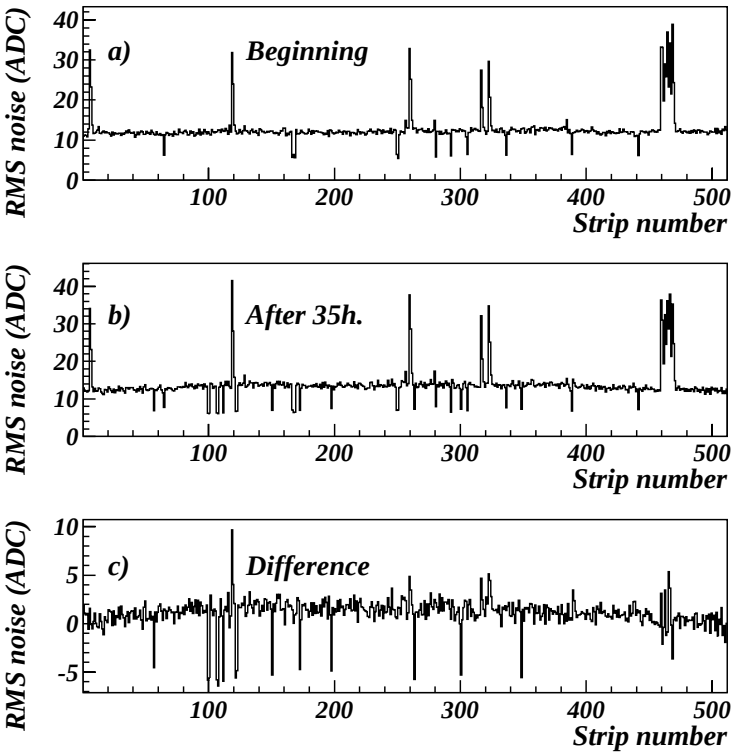

Figure 5.34: RMS noise as a function of the strip number before (a) and after (b) a high intensity period of 35 hours. In (c) the difference between the second and the first histogram is shown.

5.5 Conclusions

We have developed and tested a new micro-pattern detector with two regions of gas amplification, the MICROMEGEM. This detector is built with the advanced Printed Circuit Board technology. Our experimental investigations indicate that the device offers most of the qualities required for a modern position sensitive detector: a large gain (up to 20,000), a good energy resolution (around 20% at a gain of 4,000), a high rate capability (close to 10^5 photons/mm^{2}s) and a fast signal (collection time $\sim$ 45 ns). For X-ray detection and as tracking device, the MICROMEGEM competes well with other comparable devices like the MSGC, the Micro-Groove+GEM and the MICROMEGAS detectors. In addition to the experimental measurements, we have also performed numerous Monte Carlo simulations, which give a clear understanding of the operation modes of the MICROMEGEM detector.

We have shown that although the drift field does not directly participate to the gas gain, it strongly influences the measured gain through the transparency. A moderate drift field, below 3 kV/cm, is required to optimize the gain and the energy resolution with this GEM hole geometry. Beyond this drift field value, some primary electrons do not reach the GEM holes because some field lines directly connect the upper GEM electrode and the cathode drift plane. The primary charge loss induces a gain drop and an energy resolution degradation. The maximum drift field at which the GEM transparency remains maximum and the transparency above this value increase with the amplification field in the GEM holes. On the contrary the transfer field below the GEM and the nature of the gas have no or little influence on the transparency up to a drift field of 7 kV/cm.

The gain studies have shown that there is an interaction between the avalanche development in the GEM holes and below the GEM : the gain does not depend on the lower GEM potential but only on the upper GEM potential; the dependence is exponential as in a single stage counter. Monte Carlo simulations have confirmed that in a MICROMEGEM detector, although there are two distinct amplification mechanisms, there is a single continuous region of amplification including the GEM holes and part of the transfer gap. At V_{low} = - 100 V the amplification region extends over the entire transfer gap on a total length of 100 μm. The MICROMEGEM behaves thus like a single stage detector, as the MICROMEGAS.

We have observed gain variations of up to 20% along the strips of the MICROMEGEM. Since the GEM foil is regularly supported by pilars, these inhomogeneities are attributed to small variations in the GEM hole diameter and to fluctuations of the electric field in the transfer field.

The MICROMEGEM has also been exposed to an intense beam of pions of 350 Mev/c at the Paul Scherrer Institute (PSI). With a Ne/DME-90/10% gas mixture, the maximum signal-to-noise ratio is 14 in the high intensity beam of $\sim 4 \times 10^3$Hz/mm^2; it increases up to 19 in the low intensity beam of $\sim 10^2$Hz/mm^2. At this value, the detector starts to be efficient. Although the sparking rate is lower than a spark per hour, higher signal-to-noise ratios were not achieved because of the destruction of the unprotected readout electronics.

The poor behaviour of the MICROMEGEM in presence of HIP's, is most probably due to the fact that the detector behaves like a single-stage device. However the use of PCB technology in the construction of the detector, in contrast to the more delicate micro-electronics procedure used for MSGC, leads to lower cost and higher electrical and mechanical robustness. The geometry of the strip is free, so any pattern generating 2-D information can be used. The MICROMEGEM can also be produced with larger sizes without changing the technology. Moreover the use of non-flammable and fast gas mixtures as Ne/CO_2-70/30% and Ar/CO_2-70/30% is also an advantage for the integration of the detectors in a large scale experiment.

Chapter 6

The MSGC+GEM detector

The MSGC+GEM detector is another alternative to the MSGC, using the principle of two amplification stages. This structure combines the robustness and the simplicity of the GEM with the good spatial resolution of the MSGC, typically 40 μm. This detector has been adopted by the HERA-B experiment [127] and has been envisaged by the CMS collaboration to equip the forward outer tracker.

The structure of the MSGC+GEM is different from that of the MICROMEGEM detector studied in chapter 5. Indeed, in the MSGC+GEM detector, the two amplification stages are physically well separated; the GEM foil is stretched 2 mm above the MSGC substrate. This chapter is devoted to the study of the different operation modes of the MSGC+GEM detector.

Section 6.1 describes the MSGC+GEM modules designed for the CMS experiment. In section 6.2 we report the performance of the detector in terms of gain and energy resolution. To optimize the detector response, the study of the different operation modes, depending on the electric fields, the readout electronics, the gas mixture and the geometry, is presented in section 6.3. Section 6.4 discusses the uniformity of the detector response.

6.1 Description of the MSGC+GEM modules

Eighteen MSGC+GEM modules have been assembled following the layout of the second innermost detection ring of the CMS forward tracker. An expanded view of one of these modules is represented in figure 6.1.

Each module consists of four trapezoidal MSGC substrates mounted side by side in a common gas volume. A GEM foil is stretched 2 mm above the four substrates. A gold-plated Ferrozell[1], 300 μm thick, cathode drift plane is placed 3 mm above the GEM foil. The region between the GEM and the drift plane is called the drift gap and the region below the GEM is referred to as the transfer gap.

[1]Ferrozell from Helmut Zeder Elektronik Kuchengrund 20 D-71522 Backnang, Germany

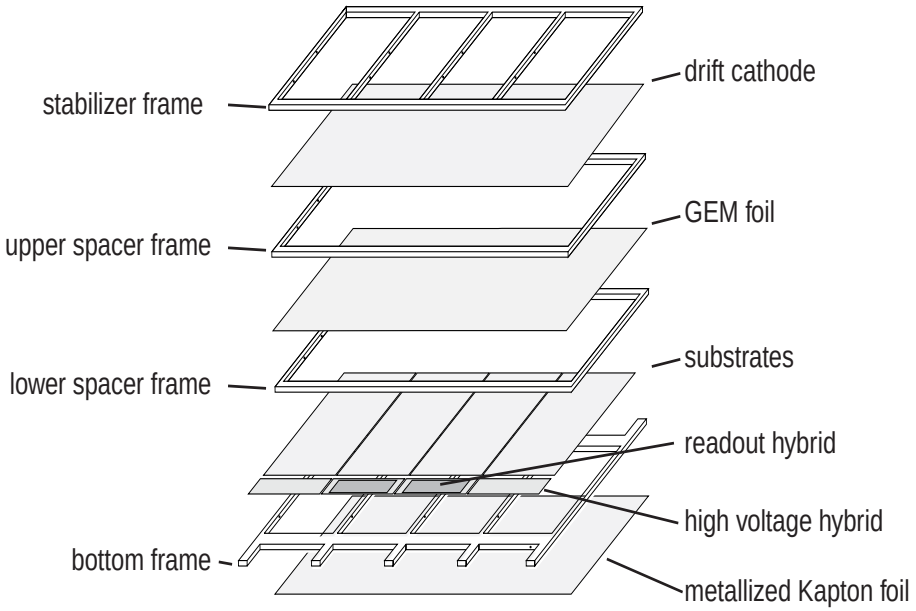

Figure 6.1: Expanded view of an MSGC+GEM detector. The trapezoidal shape of the module is not shown.

6.1.1 The Substrates

Each MSGC substrate consists of a DESAG D-263 glass plate, 300 μm thick, which carries 512 gold strips, 7 μm wide and 9.75 cm long. The anode pitch is ranging from 181 μm at the short base of the substrate to 204 μm at the large base, to account for the trapezoidal shape of the substrate; the cathode width varies from 89 μm to 106 μm to keep a constant gain along the strips, according to the homothetic rule suggested by the NIKHEF group (see eq. 4.3) [128].

A total of 91 uncoated and unpassivated MSGC substrates have been produced by three different companies. From this production, 72 substrates have been used to build the 18 modules: 60 substrates built by IMT[2], 8 by Optimask[3] and 4 at IMEC[4].

6.1.2 The GEM foils

Seventeen GEM foils have been produced at CERN in the way presented in section 5.1. The hole diameters are 72 μm in the copper and 38 μm in the middle of the Kapton layer, giving them a 'diabolo' shape (see figure 5.3). The holes form an hexagonal matrix with a distance of 120 μm between centres. The foils are segmented into four segments, each having the size of one MSGC substrate.

One unsegmented GEM foil has been manufactured by Würth Electronik[5] using a plasma etching process to create the GEM holes. The distance between the holes is 130 μm and the diameter in the copper layers is 80 μm. During the manufacturing procedure, the copper layers are etched as described in section 5.1. Afterwards, the copper surfaces act as a mask for the plasma etching: the GEM is placed in a box filled with a low

[2]IMT Masken und Teilungen AG, Greifensee, Switzerland
[3]Optimask, Morangis, France
[4]Interuniverstitaire Micro Electronika Centrum, Leuven, Belgium
[5]Würth Electronik GmbH, Roth and See, Germany

pressure, 0.2 mbar, gas mixture composed of CF4, oxygen and nitrogen. A plasma is then generated by microwave induction. The gas molecules are ionized and radicals are formed which interact with the polyimide, not affecting the copper. The duration of the process is controlled to avoid the shrinking of the kapton in the centre of the hole and to obtain a diameter in the middle of the kapton close to the diameter in the copper layers. In doing so, some polyimide is removed beneath the copper. This effect, called 'under etching', could favour the onset of sparks between the copper layers facing each other without kapton in between.

6.1.3 High voltage supply and readout electronics

All the counters were equipped with a high voltage ceramic hybrid located on their large size. These hybrids connect the cathode strips of the four substrates, in group of 16, to the high voltage bus via a 10 MΩ bias resistor.

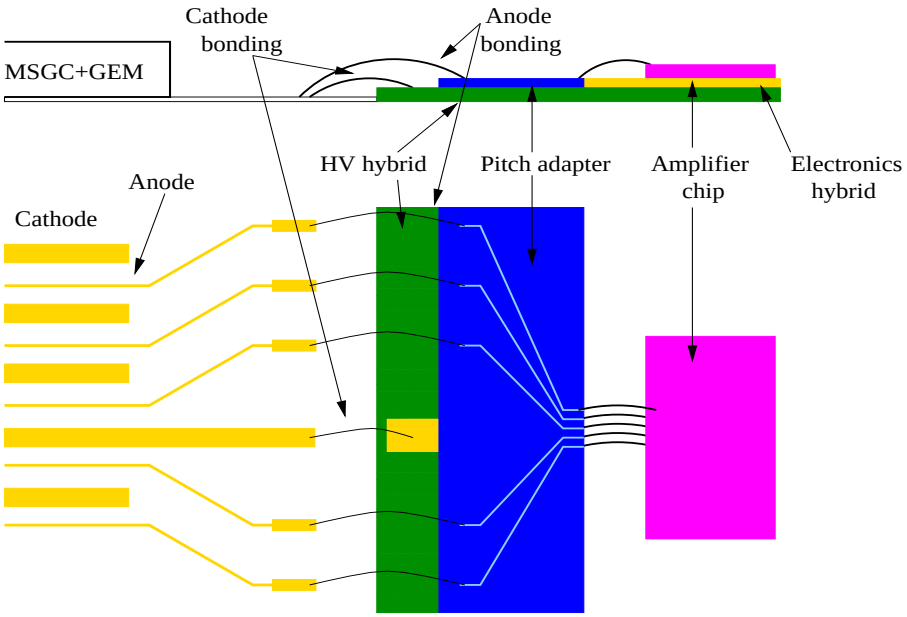

Figure 6.2: Layout of electronics and high voltage hybrids.

Only the two central substrates of each module were equipped with a ceramic electronics hybrid. Each electronics hybrid is equipped with four PreMux 128 chips. These chips hold 128 preamplifiers and shapers with 45 ns shaping time combined with a multiplexer (see section 5.4.1). As the pitch of the PreMux channels is 44 μm only, the wire bonding between the anodes and the preamplifier is performed via a pitch adapter. As shown in figure 6.2, the electronics hybrid is glued on the high voltage hybrid behind the pitch adapter. The anodes of the lateral substrates are bonded to a grounded bus.

The GEM electrodes are powered independently through a 5 MΩ resistor and equipped with a RC filter.

6.1.4 Assembling

The assembling of the MSGC+GEM modules follows the design adopted in 1998 by the CMS collaboration [129]. The main feature of this design is that the electronics and

high voltage hybrids are located outside the gas volume to avoid undesired materials released during the bonding procedure as well as during the detector functioning. A fully assembled module is shown in figure 6.3.

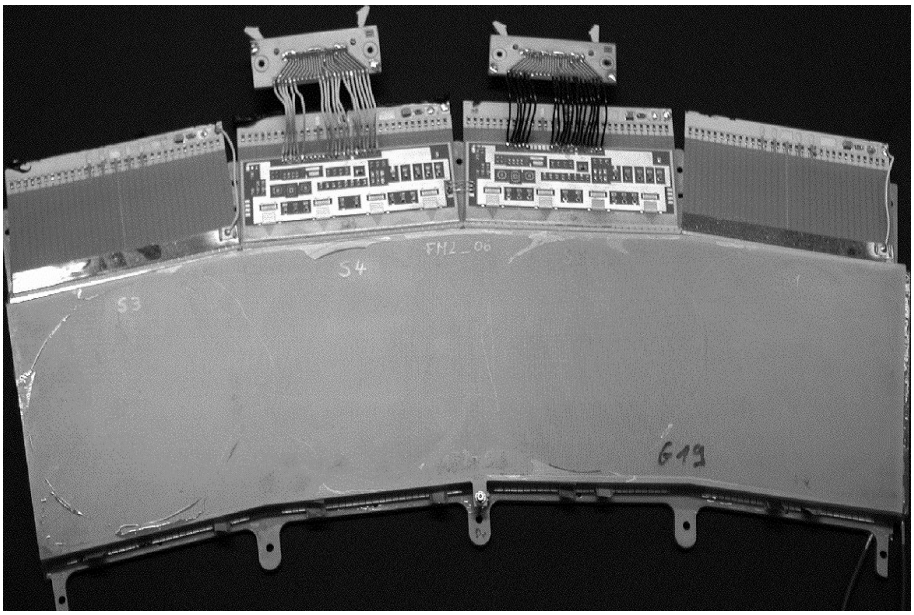

Figure 6.3: A fully assembled MSGC+GEM module with four trapezoidal counters equipped with their HV hybrid and an electronic hybrid for the two central ones.

The assembling of one module requires up to six or seven days and consists of various steps briefly described here. First, each substrate is cut to the required shape with a diamond scriber. Along the edge of the outer cathode strip, the cut is performed at a distance of only 20 μm from this cathode. To eliminate dust, the substrates are rinsed with isopropanol and cleaned with deionised water in an ultrasonic bath. After cleaning the substrates are inspected optically with a microscope and every anode is probed in order to detect anode interruptions and short circuits. In the 72 substrates less than 1% of the strips presented defects in the artwork.

The substrates are then glued on a PEEK[6] frame using precision jigs for substrate alignment under a 3D measuring device or using an optic fiber system. Two neighbouring substrates are aligned with an accuracy better than 5 μm in a way that the anodes on the edges are separated by a distance corresponding to twice the pitch elsewhere on the substrate. With this design, no detection efficiency loss is expected [123]. In parallel, a stabilizing frame is glued onto the drift plane to minimize the sagging.

Before assembling, every GEM foil is tested in a dry atmosphere with a potential difference of 500 V. Afterwards the GEM foil is stretched and glued on the lower frame of 2 mm. Then the drift plane and the GEM foil are glued onto the upper frame. Finally the module is closed by glueing the upper part (lower frame, GEM foil, upper frame, drift plane and stabilizer) to the substrates.

The different frames used to assemble the modules are made of PEEK or Ferrozel and all parts in contact with the counting gas are glued with EPO93L. The choice of materials was dictated by the requirement to be compatible with DME, which is a solvent, and to withstand LHC-like irradiation conditions [34].

[6]Poly-Ethet-Ether-Keton

6.2 Gain and energy resolution of the MSGC+GEM detector

In order to study the performance of the MSGC+GEM detectors in terms of gain and energy resolution, we have carried-out various measurements with a ^{55}Fe source. Further in this work each module will be labelled with a number corresponding to its location along the beam during the test performed at PSI which is described in chapter 7. The different measurements presented in this section have been carried out with module 12 unless mentioned otherwise.

6.2.1 Experimental set-up

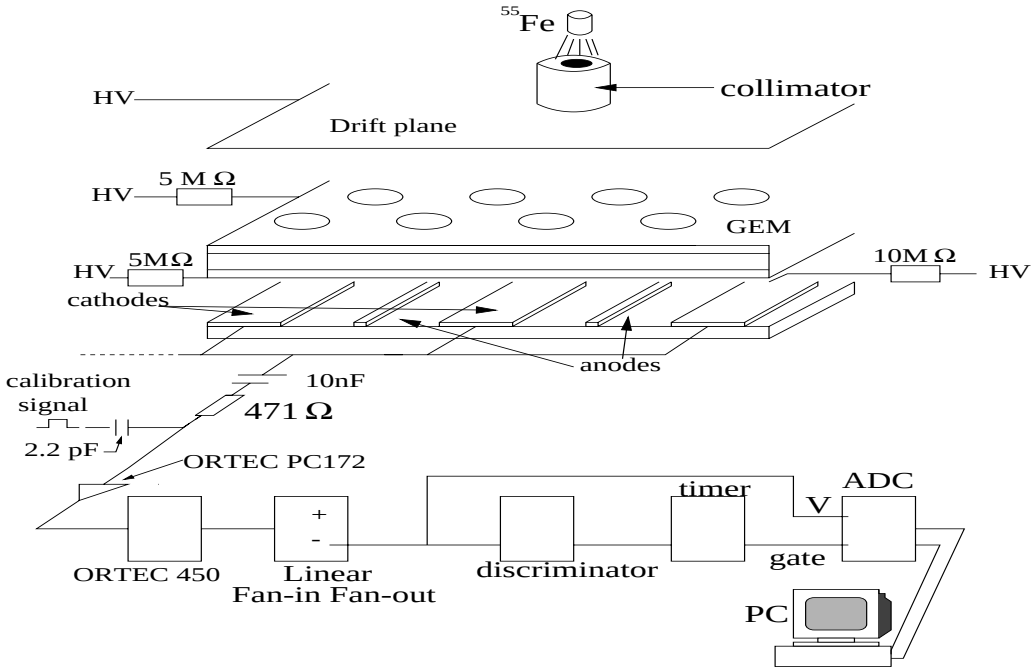

Figure 6.4: Layout of the experimental set-up used for the study of the gain and of the energy resolution, using a ^{55}Fe source.

The gain and energy resolution measurements have been performed with the experimental set-up schematically represented in figure 6.4, using a ^{55}Fe source. The 5.9 keV photons emitted from the source at a rate of $\sim$ 10 Hz/mm^2 irradiate a group of 16 strips of one MSGC substrate in one module. As the PreMux 128 electronics that equips the modules described in section 6.1 requires a trigger that can not be provided with a ^{55}Fe source, the discrete electronics ORTEC PC 172 is used to read-out the photon signals. Since the anodes are already connected to the PreMux electronics, the ORTEC PC 172 preamplifier is connected to one group of 16 cathodes through a decoupling high voltage capacitor of 10 nF.

A four channels programmable CAEN power supply delivers the high voltages independently to the drift cathode plane, the GEM electrodes and the MSGC cathodes. The applied voltages are typically - 3000 V on the drift plane, - 1000 V on the bottom GEM electrode, a potential difference of 400 V across the GEM and - 450 V on the MSGC cathodes. The anodes are grounded through the PreMux electronics. To avoid damages

in case of sustained discharges the high voltages are automatically switched off as soon as the drawn current exceeds a certain threshold set to 1 μA. When the module is powered but not irradiated, the drawn current amounts to a few nA. In this set-up, the detector is filled with a Ar/CO_2-70/30% gas mixture. The gas coming from a premixed bottle is flushed through a flowmeter to reduce the gas flow to 1 l/h, which corresponds to $\sim$ 0.5 renewals per hour.

Data acquisition

The output of the ORTEC PC 172 preamplifier is sent to a shaper amplifier, ORTEC 450. The analogue signal is then duplicated with a linear fan-in/fan-out, LeCroy 428F. A copy of the signal is sent to a discriminator to produce a gate, while a second copy is sent to an ADC (LeCroy 2249), housed in a CAMAC crate. The ADC integrates the negative signal during a time defined by the gate length, 600 ns. The data acquisition is triggered when the pulse height exceeds the discriminator threshold set to 30 mV. The data acquisition is controlled by a program written with LabVIEW [106], running on a PC computer, interfaced with the CAMAC crate through a SCSI bus. The software displays online the charge spectrum of the ^{55}Fe and simultaneously writes the data to a file.

Electronics chain calibration

The calibration of the electronics chain is performed by sending square pulses of known amplitude to a 2.2 pF capacitor put at the preamplifier input. For each amplitude, the charge spectrum is recorded, which gives a correspondence between the input charge and the ADC channel number. Afterwards, knowing the average number of primary electrons released by a 5.9 keV photon in the gas mixture, $\sim$ 200 in Ar/CO_2-70/30% (see section 3.1.2), we obtain a correspondence between the gain of the detector and the ADC channel. The amplification factor of the electronics is 120 mV/pC.

6.2.2 Results

As for the MICROMEGEM detector, the charge transfer process through the GEM foil of an MSGC+GEM, called transparency, is an important parameter to optimize and will be discussed first. After the transparency optimization, the performance in terms of gain and energy resolution will be presented.

Transparency optimization

As explained in section 5.3.2, it is not possible to measure directly the absolute transparency. Therefore we study the transparency by measuring the relative effective gain and the energy resolution as a function of the drift field. The effective gain is defined as the product of the gas gain with the GEM transparency; the relative effective gain is obtained by dividing by its maximum value.

Figure 6.5 shows the variation of the relative effective gain and of the energy resolution with the drift field, for an MSGC+GEM detector equipped with a CERN GEM, operated

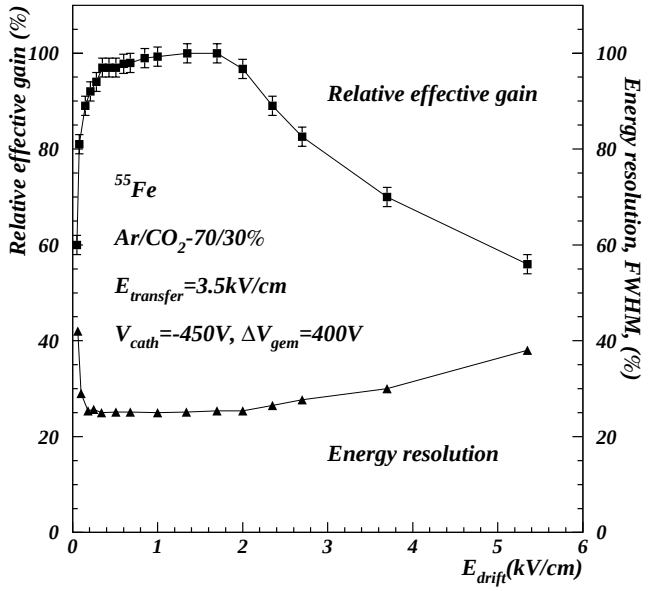

Figure 6.5: Dependence of the relative effective gain and the energy resolution (FWHM) on the drift field, E_{drift}, in Ar/CO_2-70/30%. The voltages applied on the cathodes and across the GEM are fixed to - 450 V and 400 V respectively; the transfer field is fixed to 3.5 kV/cm.

with V_{cath} = - 450 V, ΔV_{gem} = 400 V, with a transfer field of 3.5 kV/cm and filled with Ar/CO_2-70/30%. We observe a plateau ranging from 0.5 kV/cm to 2 kV/cm where the effective gain goes through a maximum and the energy resolution goes through a minimum. The better energy resolution, $\sim$ 25%, suggests that only a small fraction of the primary electrons is lost. At higher drift fields the loss of transparency reduces the effective gain and deteriorates the energy resolution. Note that the transparency loss is similar to the one measured with the MICROMEGEM equipped with a similar GEM foil and operated with the same potential difference (see figure 5.11). The signal loss below 0.5 kV/cm is attributed to the ballistic deficit of the readout electronics, resulting from the difference between the signal duration and the amplifier shaping time (see section 3.5).

Effective gain

The effective gain of an MSGC+GEM detector, has been measured as a function of the MSGC cathode voltage, V_{cath}, for several potential differences across the GEM, ΔV_{gem}. Figure 6.6 shows such a dependence for an MSGC+GEM filled with a Ar/CO_2-70/30% gas mixture and operated with E_{drift} and $E_{transfer}$ fixed to 2 kV/cm and 3.5 kV/cm respectively, leading to a transparency near to a 100% for the GEM as seen previously. We observe that gains higher than 10^4 are reached with a moderate voltage, $\sim$ - 420 V, applied on the MSGC cathodes and with an equal potential difference across the GEM. Note also that a ΔV_{gem} rise of 50 V increases the effective gain by almost a factor three. The additional amplification provided by the GEM allows to reduce the voltages applied to the MSGC cathodes, compared to an MSGC without GEM, and thus increases the safety margin before the onset of discharges. It is also important to notice that the use of a GEM allows to operate the detector with the non-flammable gas mixture Ar/CO_2-70/30%. With this mixture, the highest gain reached by an MSGC without GEM is

$\sim$ 1500 with - V_{cath} as high as 600 V [130], which does not allow to reach full MIP detection efficiency.

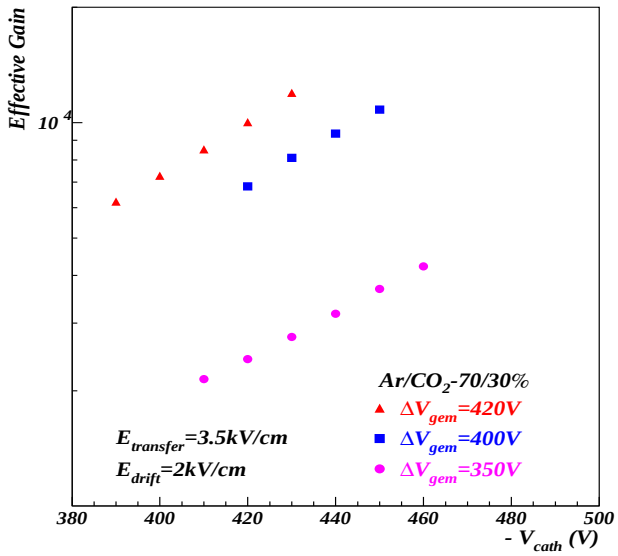

Figure 6.6: Effective gain of an MSGC+GEM detector as a function of the cathode voltage, V_{cath}, for different potential differences through the GEM, with a Ar/CO_2-70/30% gas mixture. E_{drift} and $E_{transfer}$ are fixed to 2 kV/cm and 3.5 kV/cm respectively.

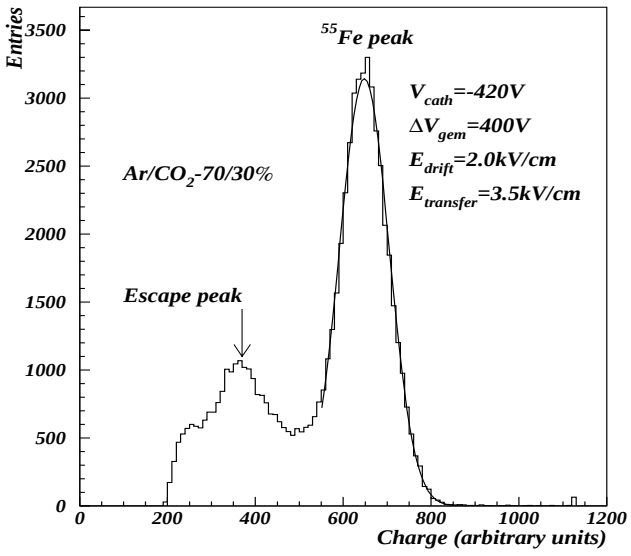

Figure 6.7: Charge spectrum of the ^{55}Fe in Ar/CO_2-70/30%, for an MSGC+GEM detector operated with V_{cath} = - 420 V, ΔV_{gem} = 400 V, E_{drift} =2 kV/cm and $E_{transfer}$ = 3.5 kV/cm.

Energy resolution

Figure 6.7 shows a typical charge spectrum of the iron source in the gas mixture Ar/CO_2-70/30%, obtained with an MSGC+GEM detector operated with V_{cath} = - 420 V, ΔV_{gem} = 400 V, E_{drift} = 2 kV/cm and $E_{transfer}$ = 3.5 kV/cm. The iron peak at 5.9 keV and the argon escape peak at 3.2 keV are clearly resolved; the energy resolution is 23% at 5.9 keV. This value is similar to the value obtained with the MICROMEGEM detector (see section 5.3.5) or with other proportional counters built with the Printed Circuit Board technology ([102, 103]); however it is lower than the energy resolution of 13% obtained with a single MSGC counter. The difference is due to the additional fluctuations during the avalanche in the GEM because of small variations in the GEM hole geometry (see section 5.3.4).

6.3 Study of the MSGC+GEM operation modes

The various voltages applied to the MSGC+GEM electrodes determine not only the gain in the two amplification regions but also the electric field configuration in the drift and the transfer gaps. We have observed in section 6.2 how the drift field strongly affects the

detector response. In this section the influences of the transfer field, the GEM geometry and the gas mixture are also reported. To avoid the influence of the ballistic deficit introduced by the readout electronics, current measurements, rather than signal-to-noise measurements, are used when available. The current measurements are performed with an X-ray beam. To interpret the signal-to-noise data and to understand the influence of a fast electronics to be used in a hadron collider experiment, data have been taken with the PreMux electronics, in a cosmic ray hodoscope in Aachen by A. Zander [133]. The results from these tests are compared to our measurements performed with X-rays.

6.3.1 Experimental set-up using an X-ray beam

To perform current measurements, a high rate of X-rays is required. For these studies[7], we have exposed the module to a beam of 8.3 keV photons, emitted by an X-ray generator (Philips mod. PW 2217/20) with a rate up to 10^6 Hz/mm^2. Using different collimators, the photon beam can irradiate an MSGC over an area from a few mm^2 up to several cm^2. A picture of the experimental set-up is represented in figure 6.8; it is similar to the set-up used with the MICROMEGEM detector (see figure 5.7).

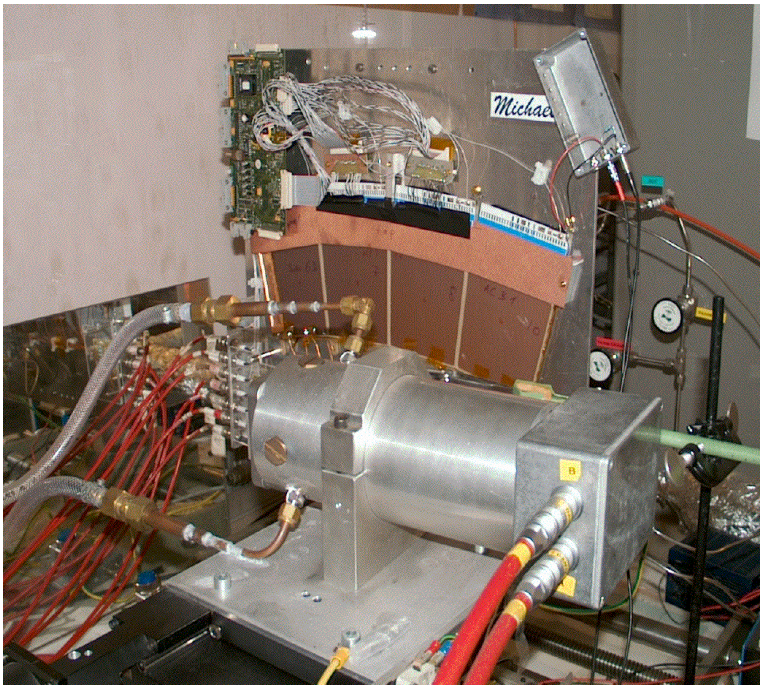

Figure 6.8: Picture of the experimental set-up using an X-ray tube, located at the Université Mons-Hainaut, UMH.

The currents drawn by the different electrodes are monitored with precise picoamperemeters [125]. When a detection area of a few cm^2 is irradiated with a flux of 10^4 Hz/mm^2, the current recorded on all the cathode strips of the irradiated counter amounts to several hundred of nA. The currents drawn by the drift plane, the upper and lower GEM are typically 50, 50, and 30 nA respectively. As the anodes of the central

[7]Measurements carried out at the Université Mons-Hainaut (UMH), Service de Physique des Particules Elémentaires.

MSGC substrates are grounded through the PreMux front-end chips (see section 6.1), only the anode current of one of the lateral substrates can be recorded. This monitoring is performed by connecting all the anodes to the ground through a 10 MΩ resistor and by measuring the potential drop across it.

6.3.2 Influence of the gas mixture on the transparency

The influence of the drift field on the transparency and on the effective gain was discussed in section 6.2. In the present section, the influence of the gas mixture on the transparency has been investigated by measuring the current drawn by the strips instead of recording the anode pulse height with an amplifier, in order to be insensitive to any ballistic deficit. Figure 6.9 shows the relative anode strip current as a function of the drift field for the Ar/CO_2-70/30% and Ne/DME-40/60% gas mixtures. For both gas mixtures, the MSGC+GEM module has been operated with $E_{transfer}$ = 3.5 kV/cm, ΔV_{gem} = 400 V and V_{cath} = - 450 V. We observe that the transparency curves are similar in both gas mixtures and both present a maximum current at $E_{drift} \simeq$ 2.0 kV/cm as observed in figure 6.5 for pulse height measurements. Beyond the optimum drift field, the relative current is 5% higher with Ne/DME-40/60% than with Ar/CO_2-70/30%. This difference can be explained by a higher attachment coefficient of Ar/CO_2-70/30% than this of Ne/DME-40/60% (see section 3.3.3). The electron attachment reduces the number of primary electrons which reach the GEM foil but does not affect the transparency.

It is important to note that although this method is not affected by any electronic ballistic deficit, an important current drop is observed at drift field below 1 kV/cm although with the ORTEC PC 172 preamplifier the drop appears only at 0.4 kV/cm (see figure 6.5). This current drop is due to a charging-up effect that will be discussed in section 6.3.5.

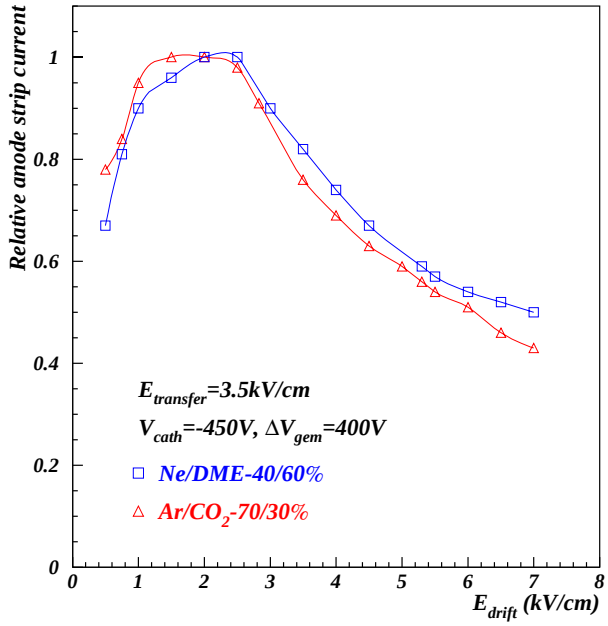

Figure 6.9: Relative anode strip current as a function of the drift field, with Ar/CO_2-70/30% and Ne/DME-40/60%. The voltage applied across the GEM is fixed to 400 V. The cathode voltage is held to - 450 V and the transfer field to 3.5 kV/cm.

6.3.3 Influence of the readout electronics

As explained in section 3.5.2, the use of a fast electronics introduces a signal reduction called ballistic deficit; it depends namely on the drift velocity and consequently on the drift field and on the gas mixture. The ballistic deficit is defined as $1 - N_{el}/N_a$, where N_{el} is the number of electrons corresponding to the signal charge, as seen through the readout electronics, and N_a is the number of electrons reaching the MSGC anode strips. Figure 6.10 shows the calculated ballistic deficit of the Premux electronics as a function of the drift field for Ar/CO_2-70/30% and Ne/DME-40/60% gas mixtures. This Monte Carlo simulation has been performed by T. Beckers [131]. The ballistic deficit reaches a plateau at a value of $\sim$ 30% for both gas mixtures. This behaviour is due to the saturation of the drift velocity when one increases the drift field. The drift velocity levels-off at a drift field as small as 1.5 kV/cm in Ar/CO_2-70/30% instead of 4.5 kV/cm in Ne/DME-40/60%. Therefore at low drift field, the ballistic deficit is more important in Ne/DME-40/60% than in Ar/CO_2-70/30%. On the plateau, the ballistic deficit is 2% smaller with Ar/CO_2-70/30% than with Ne/DME-40/60% because the drift velocity saturates at a value of 70 μm/ns in Ar/CO_2-70/30% instead of 55 μm/ns in Ne/DME-40/60%.

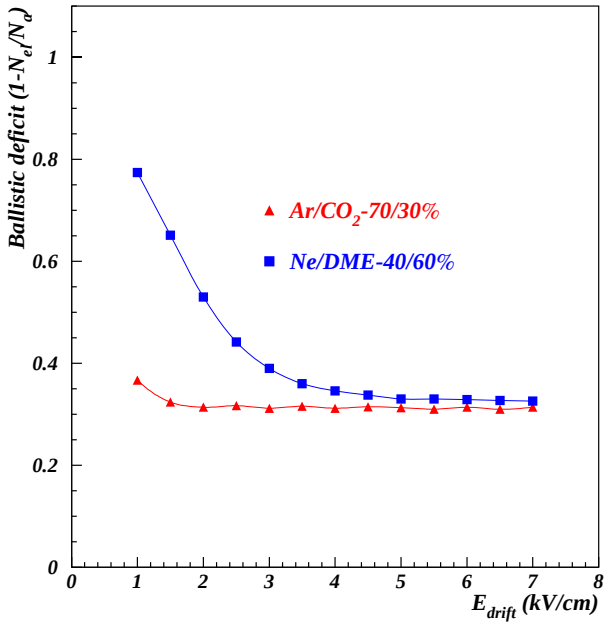

Figure 6.10: Computed ballistic deficit of the PreMux electronics as a function of the drift field for Ar/CO_2-70/30% and Ne/DME-40/60% gas mixtures [131].

The ballistic deficit behaviour, different for both gas mixtures at low E_{drift}, modifies the optimum value of the drift field determined from the transparency measurement ($\sim$ 2 kV/cm). Indeed at E_{drift} = 2 kV/cm, the ballistic deficit is 20% larger in Ne/DME-40/60% than in Ar/CO_2-70/30%. The combination of the ballistic deficit and the transparency will result in a shift of the optimum drift field towards a higher value. This effect is shown in figure 6.11 displaying the relative signal-to-noise ratio measured with the PreMux 128 and the relative current (see previous section) as a function of the drift field for an MSGC+GEM filled with Ar/CO_2-70/30% (a) and Ne/DME-40/60% (b). The value of the maximum absolute SNR is also given for each gas mixture. The module, equipped with a CERN GEM, was operated with ΔV_{gem} = 400 V, V_{cath} = - 450 V and

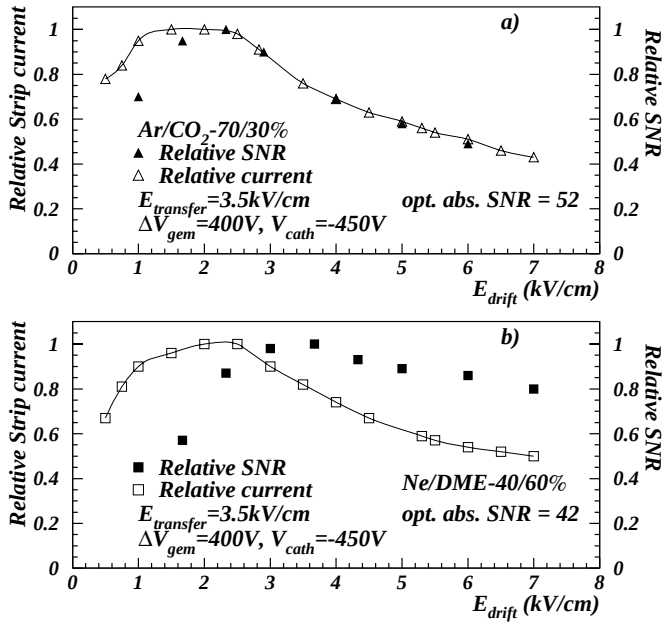

Figure 6.11: Relative SNR measured with the PreMux electronics and relative anode strip current as a function of the drift field, with Ar/CO_2-70/30% and Ne/DME-40/60%. The voltages applied to the cathodes and across the GEM are fixed to - 450 V and 400 V respectively. The transfer field is equal to 3.5 kV/cm. The value of the maximum absolute SNR is 52 and 42 for Ar/CO_2 and Ne/DME, respectively.

$E_{transfer}$ = 3.5 kV/cm. First we observe that although the transparency is hardly affected by the gas (see figure 6.9), the SNR curve obtained with the Ne/DME-40/60% gas mixture is very different from the one obtained by recording the current and from the curves measured with the Ar/CO_2-70/30% gas mixture. With Ar/CO_2-70/30%, the increase of the ballistic deficit starting only at $E_{drift} \leq$ 1.5 kV/cm, the E_{drift} value optimizing the signal-to-noise remains 2 kV/cm, where the signal-to-noise ratio is equal to 52. For Ne/DME-40/60%, this value is shifted up to 4 kV/cm, where the signal-to-noise ratio is equal to 42. In both cases the presence of the ballistic deficit hides the transparency plateau.

Consequently it may be thought that with the PreMux electronics the fast Ar/CO_2-70/30% gas mixture is more suited than Ne/DME-40/60%. However it is important to note that the optimum absolute SNR, measured at E_{drift} = 2 kV/cm with Ar/CO_2-70/30% (SNR = 52) and at E_{drift} = 3.5 kV/cm with Ne/DME-40/60% (SNR = 42), is only 20% higher with Ar/CO_2-70/30% than with Ne/DME-40/60%, although the transparency is reduced by almost 30% at E_{drift} = 3.5 kV/cm. Moreover T. Beckers has shown with Monte Carlo simulations that with a drift field of 4 kV/cm, the ballistic deficit difference between both gas mixtures is equal to 4% (see figure 6.10). This difference does not compensate the lower primary ionization density of Ar/CO_2-70/30%, 93 pairs/cm, compared to this of Ne/DME-40/60%, 122 - 136 pairs/cm (see section 3.1.2). Consequently, an 80% higher gain is needed to reach 98% detection efficiency with Ar/CO_2-70/30% than with Ne/DME-40/60% at a drift field of 4 kV/cm. However Ar/CO_2-70/30% has the advantage of being cheap, non-flammable as well as non-corrosive and was tried successfully by the HERA-B collaboration [127].

6.3.4 Influence of the GEM geometry

The transparency has already been extensively studied for CERN GEM's (see sections 6.2.2, 6.3.3 and 5.3.2). In this section we present the study of the transparency for the Würth GEM. Indeed, the different shape of the holes (see section 6.1.2) might influence the transparency.

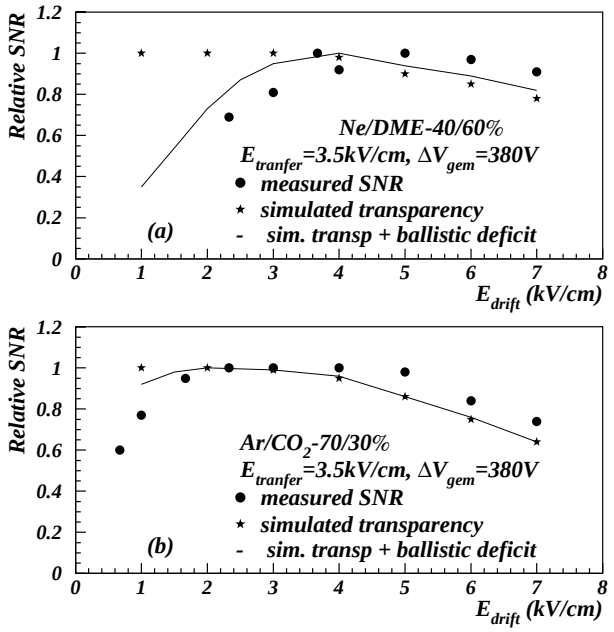

Figure 6.12: Relative SNR as a function of the drift field in Ne/DME-40/60% (a) and Ar/CO_2-70/30% (b). The MSGC+GEM was operated with $E_{transfer}$ = 3.5 kV/cm and ΔV_{gem} = 380 V. The absolute simulated transparency is also represented with and without taking into account the ballistic deficit of the PreMux 128 preamplifier.

Figure 6.12 shows the relative SNR, measured with the PreMux 128 preamplifier, as a function of the drift field for the MSGC+GEM detector equipped with the Würth GEM, for the Ne/DME-40/60% (a) and Ar/CO_2-70/30% (b) gas mixtures. The transfer field is fixed to 3.5 kV/cm and the potential difference across the GEM is equal to 380 V. For both gas mixtures, we compare the measurements with the absolute transparency simulated with a three dimensional model using the MAXWELL and GARFIELD programs (see section 4.5), with and without taking into account the ballistic deficit. The ballistic deficit of the PreMux 128, shown in figure 6.10, has been computed with a separate Monte Carlo simulation performed by T. Beckers [131]. We observe that the data and the simulation including the ballistic deficit both show a larger signal drop at low drift field, for the Ne/DME-40/60% than for the Ar/CO_2-70/30%, as expected from the measurements performed with the CERN foil (see figure 6.11). The agreement between the data and the simulation is at the level of 15%. It is to be noted that with the Würth GEM, the SNR measurements still show a plateau in both gases; this is due to a longer plateau of maximum transparency. This is likely to be due to the GEM hole geometry.

To underline the influence of the GEM hole geometry on the transparency, figure 6.13 shows the measured relative SNR as a function of the drift field for a CERN GEM and for the Würth GEM. A larger transparency degradation is observed for the foil produced at CERN for drift fields above 2 kV/cm. If only the outer diameter of the CERN GEM holes

is taken into account, both foils have approximately the same optical transparency. This quantity, defined as the ratio of the hole area over the total area (see Eq. 5.1), amounts to 0.32 and 0.34 for the CERN and the Würth GEM respectively. Therefore the larger transparency loss observed for the CERN GEM beyond E_{drift} = 2.0 kV/cm is likely to be due to either the size or the biconical shape of the CERN GEM holes.

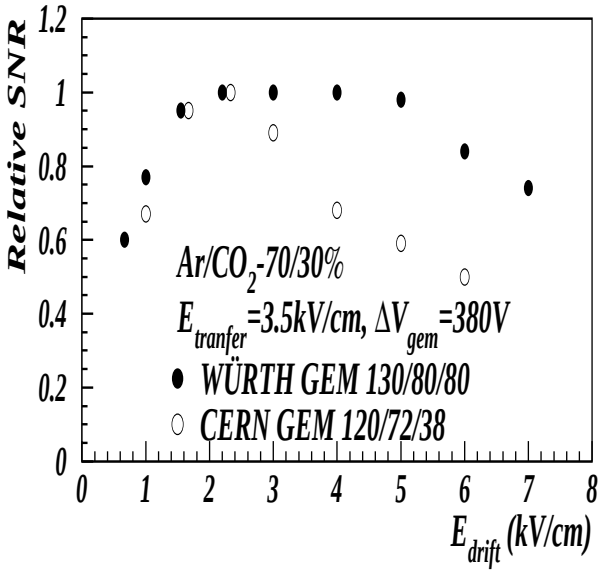

Figure 6.13: Relative SNR as a function of the drift field for a CERN and the Würth GEM.

6.3.5 Charging-up effects

We have seen in section 6.2, using a slow electronics, that the GEM transparency presents a plateau region below E_{drift} = 2.0 kV/cm, where the transparency is supposed to be close to a 100% and the effective gain is maximum. This is confirmed by the electrostatic field simulation of the GEM, presented in section 5.3.2, that shows that all the field lines from the drift gap enter in the GEM channels and that the optimum plateau extends down to electric fields lower than 1 kV/cm.

As seen in section 6.3.2, we have also investigated the transparency by exposing an MSGC+GEM detector to a high photon rate of 10^3 Hz/mm^2 and by recording the current drawn by the anodes as a function of the drift field (see figure 6.9). This approach was used in order to avoid the effect of the increasing ballistic deficit at low drift field when using a fast electronics. We observe a current drop at drift fields as high as 1 kV/cm with both the Ne/DME-40/60% and Ar/CO_2-70/30% gas mixtures, which is in contradiction with our measurements performed with the slow front-end electronics, ORTEC PC 172. To underline the discrepancy both measurements are presented together in figure 6.14 for the Ar/CO_2-70/30% gas mixture. During both measurements the MSGC cathodes were operated with - 450 V and a potential difference of 400 V was applied across the GEM foil; the transfer field was fixed to 3.5 kV/cm.

Several authors have reported significant gain drops at drift fields lower than 2 kV/cm with DME-based gas mixtures ([110], [134]). The measurements performed by these

authors have been carried out with a high rate of X-rays, above 10^5 Hz. Although these authors attribute the gain loss to e^--ion recombinations or to a pollution related to the use of DME in the gas mixture, we will show here that the gain drop is due to another effect.

We want to point out first that electron-ion recombinations are not expected with drift field above a few hundred V/cm (see Ref. [135] and section 3.3.3). In our case, the current measurements have been performed using a clean gas system [136], used for aging measurements, which ensures the absence of electronegative pollutants in the gas mixture. Moreover this drop is not observed for the signal measurements taken with a slow electronics. What was different during this two sets of measurements displayed in figure 6.14 is the particle rate. We have thus studied the radiation rate and the time dependence of this drop at low drift field.

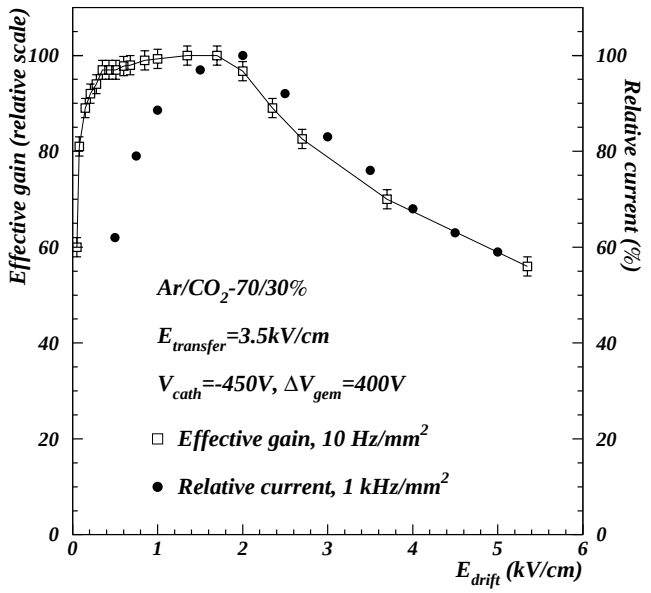

Figure 6.14: Effective gain measured with a slow electronics and relative strip current as a function of the drift field in Ar/CO_2-70/30%. The voltages applied to the MSGC cathodes and across the GEM are fixed to -450 and 400 V respectively. The transfer field is equal to 3.5 kV/cm.

Various transparency curves such as the one shown in figure 6.14 have first been recorded in various conditions of radiation rate and gain, with the Ar/CO_2-70/30% gas mixture. The rate was varied from 10^3 Hz/mm^2 to 10^4 Hz/mm^2 and the gain from 1000 to 5000. All the curves present a maximum current at $E_{drift} \simeq 2$ kV/cm and the same current decrease above this optimum value because of the transparency loss, in agreement with the measurements performed with the ORTEC PC 172 electronics. To summarize the results for drift fields below 2 kV/cm, figure 6.15 shows the current loss at $E_{drift} = 0.5$ and 0.75 kV/cm relative to the maximum current recorded at $E_{drift} = 2$ kV/cm as a function of the cathode current which is affected by the detector gain and the radiation rate. We clearly observe the influence of the total charge created in the detector on the measured current. With a drift field of 0.5 kV/cm, a 50% signal drop is observed at a photon rate of 10^4 Hz/mm^2 and a gain of $\sim$ 5000. At 0.75 kV/cm, this current drop is already reduced by a factor of about two. To investigate the origin of this effect, we have also recorded the time development of the current drop.

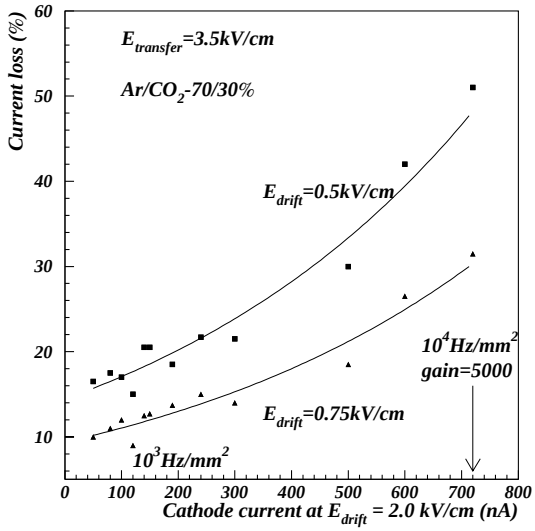

Figure 6.15: Current loss relative to the maximum current recorded at E_{drift} = 2 kV/cm as a function of this maximum current for E_{drift} = 0.5 and 0.75 kV/cm with Ar/CO_2-70/30%. The rate has been varied from 10^3 Hz/mm^2 to 10^4 Hz/mm^2 and the gain from 1000 to 5000. The transfer field has been fixed to 3.5 kV/cm.

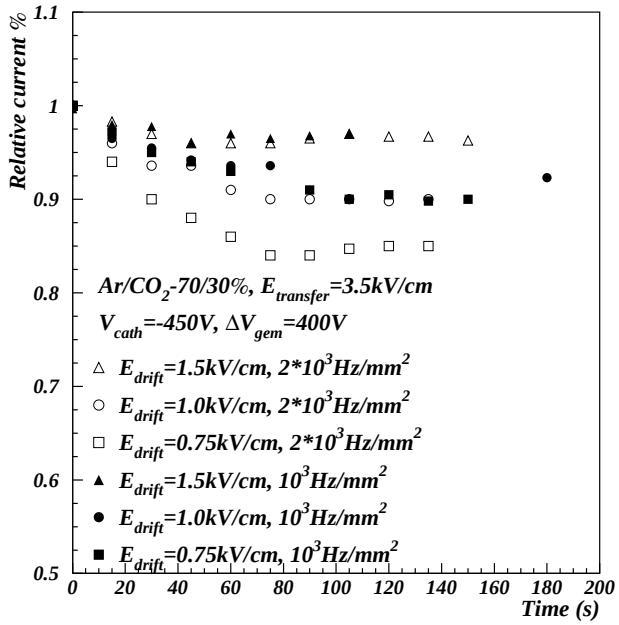

Figure 6.16: Relative current recorded as a function of time for different drift fields and with irradiation rates of either 10^3 Hz/mm^2 (closed marks) or 2×10^3 Hz/mm^2 (open marks). The MSGC+GEM is operated with V_{cath} = - 4.5 kV/cm, ΔV_{gem} = 400 V and $E_{transfer}$ = 3.5 kV/cm. The counter is filled with Ar/CO_2-70/30%.

Figure 6.16 shows the relative current as a function of time, for different drift field values with an X-ray rate of either 10^3 Hz/mm^2 or 2×10^3 Hz/mm^2. The reference current of each curve corresponds to the stabilized current recorded at E_{drift} + 0.25 kV/cm. The measurements sequence starts immediately after a drift field reduction of 0.25 kV/cm occurring at time zero. We observe first that the time constant is long, several minutes, and

that the current drop at the equilibrium depends both on the irradiation rate and on the drift field: a factor two in rate increases the drop by more than 5% at E_{drift} = 0.75 kV/cm, and a decrease of the drift field by 0.25 kV/cm increase the current drop by 5% at an irradiation rate of 2×10^3 Hz/mm^2. The dependence on the irradiation rate and the long time constant suggest the charging-up of an insulating layer. As this charging-up strongly depends on the drift field that can hardly influence a possible charging-up of the MSGC substrate, it is likely to occur on the Kapton of the GEM foil. That the major part of this effect is not due to the MSGC substrate is confirmed in figure 6.17 which shows the relative current drop as a function of time for different cathode voltages, with E_{drift} = 0.5 kV/cm, $E_{transfer}$ = 3.5 kV/cm, ΔV_{gem} = 450 V and the rate equal to 10^3 Hz/mm^2. We observe that although the MSGC gain rises by almost a factor 3 when one increases - V_{cath} from 400 to 470 V (see figure 6.6 and reference [114]), the time constant is unchanged and the current drop remains of the order of $\sim$ 17%.

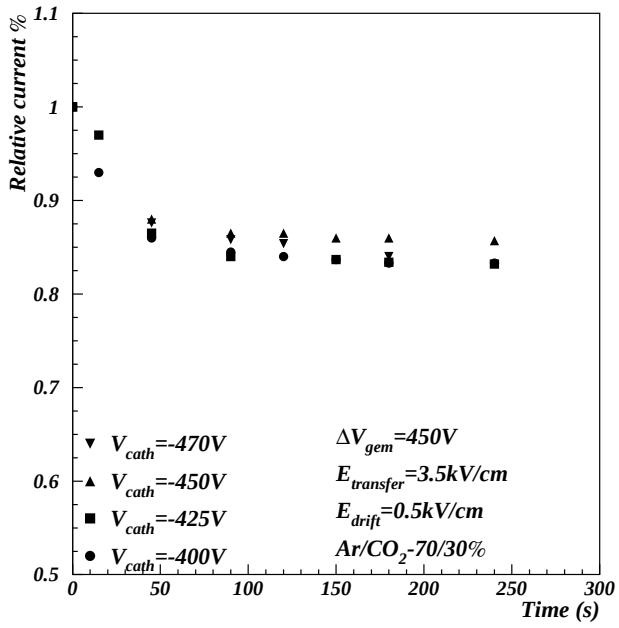

Figure 6.17: Relative current measured as a function of the time for different MSGC cathode voltages. The voltage applied across the GEM is equal to 400 V, E_{drift} and $E_{transfer}$ are fixed to 0.5 and 3.5 kV/cm respectively. The detector is filled with the Ar/CO_2-70/30% gas mixture

It is important to mention that a similar behaviour reported in reference [110] has been observed with a detector equipped with a GEM and pick-up strips. Although the authors attribute this drop to e^--ion recombinations, it is most probably due to the charging-up of the GEM which is the only amplification stage in that detector. The charging-up of the GEM can be a drawback for the use of a GEM as readout for a Time Projection Chamber (TPC) in a high rate experiment. In these applications drift fields as low as 0.5 kV/cm are commonly used [139].

Although it has been shown in figure 6.16 that the current drop is reduced when the drift field increases and vanishes at drift field higher than 2 kV/cm, the charging-up effect has been observed also at drift fields as high as 2 kV/cm in different conditions. These observations have been made with the set-up using the iron source and the ORTEC PC 172 readout electronics (see section 6.2.1). Figure 6.18 shows the relative effective gain

as a function of the time for different sharings of the gain between the two amplification stages, keeping an overall effective gain of the order of 4000. The potential difference across the GEM ranges from 380 to 400 V, the cathode voltage varies from - 455 V to - 400 V and the drift field is fixed to 2 kV/cm. The X-ray rate is $\sim$ 10 Hz/mm^2. After an effective gain loss of about 17%, whatever the voltages on the different electrodes are, the effective gain remains stable until the radiation source or the power is switched off. As for the previous effect, the long time constant, several tens of minutes, indicates the

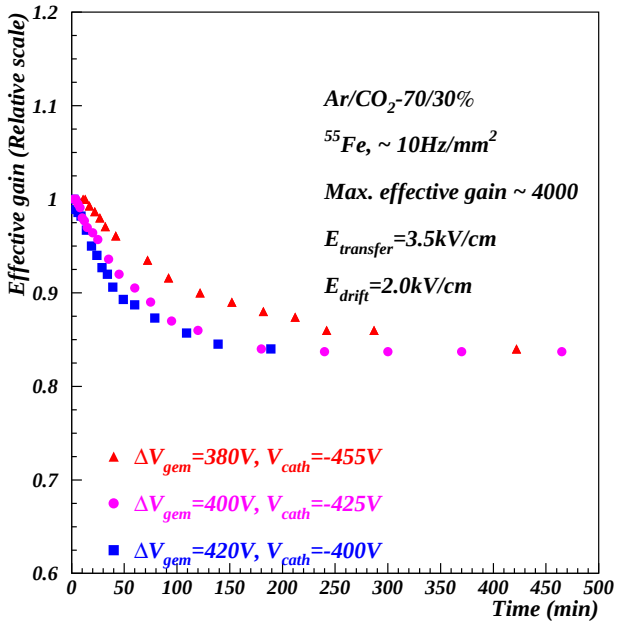

Figure 6.18: Relative effective gain as a function of time, for different gain sharings between the two amplification stages, with the Ar/CO_2-70/30% gas mixture. The transfer field and the drift field are fixed to 3.5 and 2.0 kV/cm respectively.

charging-up of an insulator. We also observe that the time constant depends on the gain sharing between the two amplification stages. A shorter time constant correlated with a larger GEM gain suggests that the charging-up takes place on the kapton of the GEM rather than on the MSGC substrate.

6.3.6 Influence of the transfer field

As for the drift field, the transfer field does not directly participate to the gas amplification. However this field may influence the effective gain and the general behaviour of the detector. Indeed, we have seen with the MICROMEGEM counter, see section 5.3.3, that the strong coupling between the transfer field and the field in the GEM may limit the maximum sustainable gain in presence of HIP's. However the transfer field in an MSGC+GEM module is typically one order of magnitude smaller than in a MICROMEGEM detector and the transfer gap is 40 times larger.

The influence of the transfer field has been investigated with the set-up equipped with the X-ray generator by recording the ion current drawn by the drift plane (I_{drift}), the cathode (I_{cath}), the lower (I_{gemdwn}) and the upper GEM (I_{gemup}) electrodes. The anodes are grounded through the PreMux electronics.

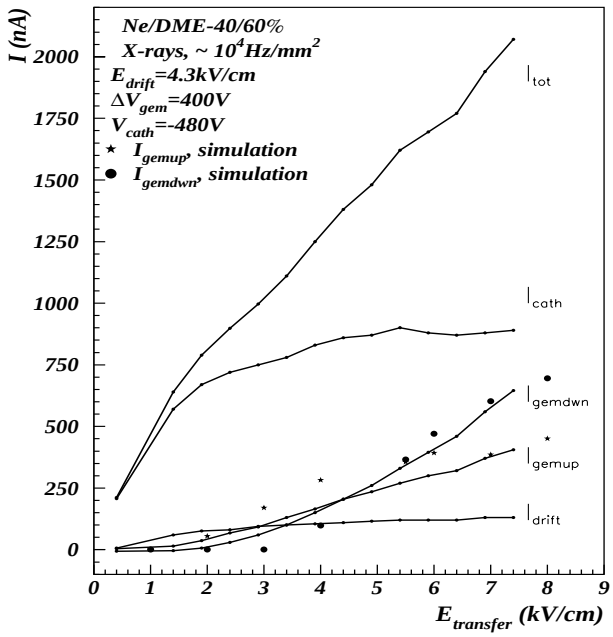

Figure 6.19: The different ion currents, I_{cath}, I_{gemdwn}, I_{gemup}, I_{drift} and I_{tot} as a function of the transfer field with Ne/DME-40/60%. V_{cath} and ΔV_{gem} are fixed to -480 V and 400 V respectively and the drift field is kept at 4.3 kV/cm. The detector is irradiated with a rate of X-rays of $\sim 10^4$Hz/mm^2.

Figure 6.19 shows the ion currents measured on the MSGC detector electrodes as a function of the transfer field. The MSGC module was operated with E_{drift} = 4.3 kV/cm, V_{cath} = - 480 V, ΔV_{gem} = 400 V and with a Ne/DME-40/60% gas mixture. The total ion current, I_{tot}, is also represented as well as the GEM electrode currents simulated with GARFIELD. The Monte Carlo simulation used for the results displayed in figure 6.19 is performed by recording the end point of the drift path of ions coming from the avalanche developed near the MSGC strips. Indeed the number of ions coming from the GEM avalanche is negligible. For example, with an overall gain of 10,000 and with an equal sharing of the gain between the two amplification stages, the ions produced in the GEM holes represent only 1% of the ions produced near the MSGC substrate. Moreover it has been shown that up to 30% of the ions created during the avalanche in the GEM are absorbed on the kapton edges [138]. Therefore this contribution has been neglected for this analysis.

The data show first that I_{tot} linearly increases with the transfer field, which shows an enhancement of the gain at the MSGC anodes. This gain rise is similar to the one measured with an MSGC without GEM when the drift field is increased [137]. Secondly the data and the current simulation show that the lower GEM current starts to increase at a value as low as 2 - 3 kV/cm, showing a change of operation mode when the ions, produced by the avalanche around the MSGC anodes, start to be collected by the lower GEM electrode instead of by neighbouring cathodes strips. As the ion diffusion at atmospheric pressure is about 250 smaller than usual values for electron, ions can be considered as traveling along the electric field lines. Therefore the rise of I_{gemup} at E_{drift} = 2 - 3 kV/cm suggests a modification of the electric field configuration which has been investigated with electrostatic field simulations.

Figure 6.20 shows the electric field lines coming from the MSGC substrate in a GEM

hole operated with a potential difference of 400 V and a drift field of 2 kV/cm, for a transfer field of 2 kV/cm (a) and 3 kV/cm (b). We clearly observe the change of operation mode: the electrostatic field simulation at the level of the MSGC substrate shows that beyond $E_{transfer}$ = 2 kV/cm, some electric field lines starting from the MSGC anodes are collected on the lower GEM electrode instead of the neighbouring cathode strips. Since the ions follow these field lines, this also explains the saturation of the cathode current although the overall amplification increases. Although the overall amplification is enhanced at large transfer field, such configuration could be unsafe in presence of HIP's as discharges onset in the GEM can directly reach the delicate MSGC anodes. This effect is discussed in chapter 7. Note also that at $E_{transfer}$ = 4 kV/cm still a large fraction of the ions liberated in the MSGC avalanche are collected by the cathode strips ($\sim$ 60%), the three other electrodes collecting each around 10% of the ions. At higher transfer field, only the currents recorded on the GEM electrodes increase; the drift cathode current remains constant, showing the decoupling between the transfer and the drift fields. The combination of a GEM with an MSGC permits to reduce the ion feedback into the drift volume to less than 10% for an MSGC+GEM instead of $\sim$ 40% for an MSGC without GEM. This feature can be exploited for the readout of high rate projection chambers to avoid space charge effects in the large drift volume [139].

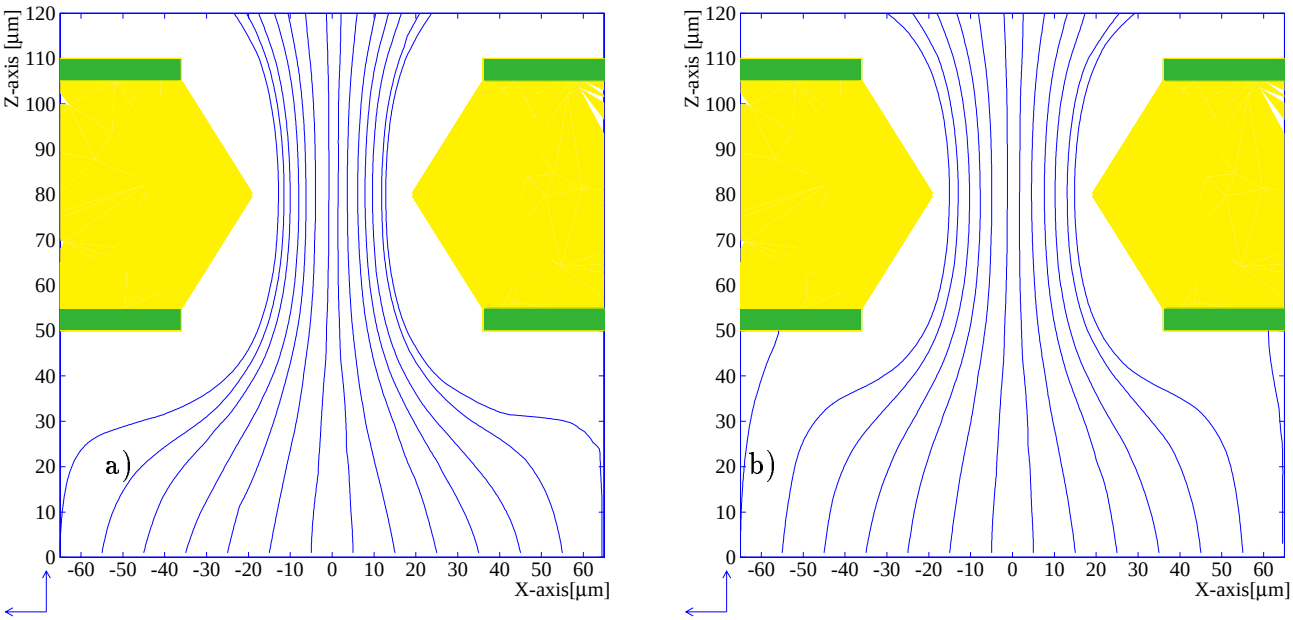

Figure 6.20: Computed electric field lines coming from the MSGC anodes in a GEM hole operated with a potential difference of 400 V, for a transfer field of 2 kV/cm (a) and 3 kV/cm (b). The drift field if fixed to 2 kV/cm.

6.4 Uniformity of the detector response

Each MSGC+GEM module studied in this work is equipped with a GEM foil in one piece stretched over four wedge shaped MSGC substrates (see section 6.1). The absence of additional pillars placed in the detection area could result in the sagging of the GEM foil, modifying the electric field configuration and therefore the detector response. The

uniformity of the detector response has been investigated by measuring with a ^{55}Fe source, the relative effective gain as a function of the position along the MSGC strips for two modules (9, 12) as shown in figure 6.21. Both counters were operated with V_{cath} = - 450 V, ΔV_{gem} = 400 V, $E_{transfer}$ = 3.5 kV/cm and with E_{drift} = 2 kV/cm. For both counters we observe up to 25% gain variations in the centre with respect to the edges of the detector. This value is comparable with the fluctuations reported with the MICROMEGEM counter where the GEM foil is regularly supported by pillars (see section 5.3.4). We can also observe a systematic gain variation in opposite directions for both detectors suggesting an upwards GEM sagging for module 9 and a downwards one for module 12. Indeed, for a given set of voltages, an upwards sagging reduces the drift gap and increases the drift field which results in a larger transparency loss. In addition, it extends the transfer gap which reduces the transfer field and the gain at the MSGC anodes. Although we will see in chapter 7 that a sagging as high as 1.5 mm has been observed in some counters, we will show that, here, the gain variations have to be attributed to another effect.

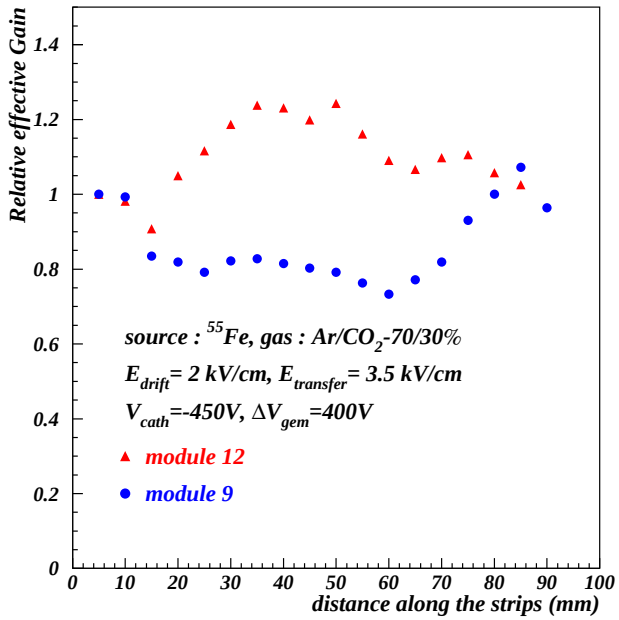

Figure 6.21: Relative effective gain as a function of the position along the strips for modules 9 and 12 filled with Ar/CO_2-70/30%. Both counters were operated with V_{cath} = - 450 V, ΔV_{gem} = 400 V, $E_{transfer}$ = 3.5 kV/cm and with E_{drift} = 2 kV/cm. The measurements have been performed with a ^{55}Fe source.

After the tests, module 12 has been opened and visually inspected with a microscope. Figure 6.22 shows the height variations of the GEM foil as a function of the position along the strips. Even if some correlations may be seen between the variations of the relative effective gain (see figure 6.21) and those of the relative height over the first half of the detector, they are less obvious in the second half; especially same gain values do not correspond to same heights. In addition the upwards height variation observed between 20 and 55 mm should lead to a gain decrease, as discussed in the preceding paragraph, contrary to what is observed and the large gain variations observed can not be explained by such small height variations. Figures 6.5 and 6.19 have shown that to obtain gain variations of 25%, electric field variations of more than 30% are needed; the maximum height variation of 110 μm represents only 5% of the nominal height.

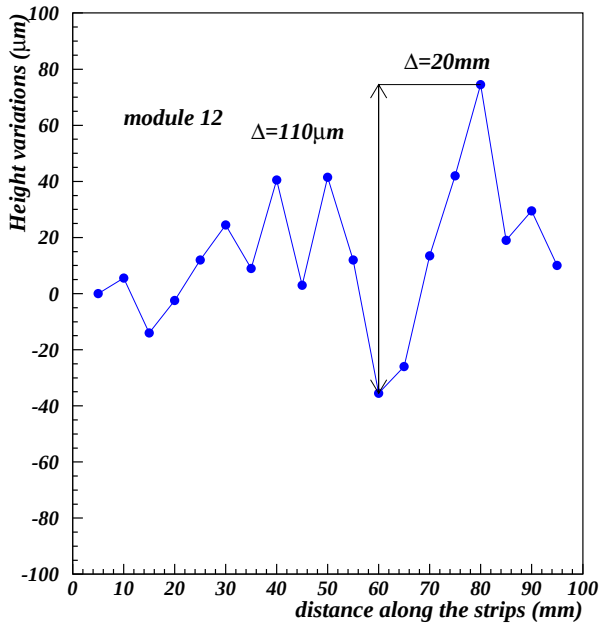

Figure 6.22: Height variations of the GEM foil as a function of the distance along the strips for module 12.

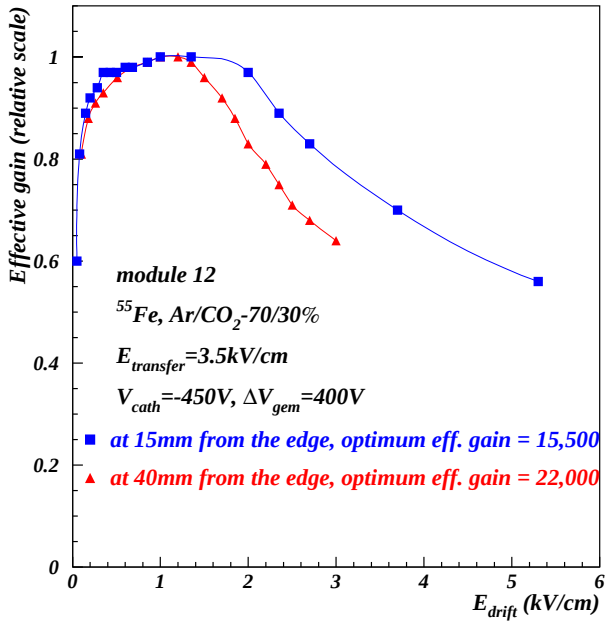

Figure 6.23: Effective gain as a function of the drift field at two different positions in module 12 filled with Ar/CO_2-70/30%. The voltages applied to the cathodes and across the GEM are fixed to -450V and 400V respectively; the transfer field is equal to 3.5 kV/cm.

The effective gain variations observed on figure 6.21 must thus be attributed to another effect. We are going to show that it is most probably due to GEM hole diameter variations. Larger holes are expected to lead to a better optical transparency but a lower gain as the electric field lines are less focused. Therefore we have investigated the transparency in the regions of minimum and maximum effective gain for module 12, at 15 and 40 mm from the detector edge, where the effective gain is respectively $\sim$ 15,500 and $\sim$ 22,000. Figure 6.23 shows the effective gain as a function the drift field at these positions, with

$E_{transfer}$ = 3.5 kV/cm, ΔV_{gem} = 400 V, V_{cath} = - 450 V and with Ar/CO_2-70/30%. A better transparency is observed at 15 mm: the plateau is longer and beyond the plateau it is almost 30% higher than at 40 mm. This suggests that at 15 mm, the GEM hole aperture might be larger. As, at this position, the effective gain is lower with a better transparency, it means that the absolute gain is smaller, in agreement with the hypothesis of larger holes. The optical inspection of the hole diameter in the upper copper layer confirms this hypothesis. Indeed, in that region the holes are 2 μm larger on average.

6.5 Conclusions

The aim of this chapter was to study the performance of the MSGC+GEM detectors and to understand their various operation modes. This study covered various subjects as the performance in terms of gain and energy resolution, the influence of the GEM geometry on the transparency, the influence of the readout electronics, etc.

We have shown that the combination of an MSGC with a GEM allows to reach very high gains, up to 10,000, with moderate voltages, $\sim$ 420 V, applied on the MSGC cathodes and across the GEM. A cathode voltage of 650 V is needed to reach such gains with an MSGC without GEM. The energy resolution of the MSGC+GEM is of the order of 23% FWHM, that is similar to the results obtain with other micro-pattern gaseous detectors using the PCB technology. The energy resolution is about 10% worse than for an MSGC without GEM. The large gain fluctuations are due to the PCB technology used to manufacture the GEM foil. With this technology the size of the smallest structures is almost 10 times larger than those obtained with micro-electronics technique. The transparency of the GEM foil has also been extensively studied. We have shown that with CERN GEM's, an optimum transparency is obtained with a drift field of $\sim$ 2 kV/cm. Although the optical transparency is similar for the Würth GEM, the transparency plateau is $\sim$ 2.5 kV/cm longer for the Würth than for the CERN GEM's. This can be explained by the larger hole inner diameter of the Würth GEM, 80 μm instead of 38 μm for the CERN GEM's. We have also shown that the gas mixture hardly affects the transparency.

The influence of the fast readout electronics PreMux 128 has also been studied with the Ar/CO_2-70/30% and Ne/DME-40/60% gas mixtures. Simulations show that the ballistic deficit is similar, around 30%, for both gas mixtures at high drift field ($E_{drift} > 5$ kV/cm). However at lower drift field, the ballistic deficit is strongly affected by the electron drift velocity of the gas mixture. Consequently the combination of a fast electronics with a small plateau of optimum transparency shifts the optimum drift field to higher values at which the transparency is lowered. For the CERN GEM's the optimum drift field is shifted by almost 2 kV/cm, which leads to a transparency loss of $\sim$ 30%. This behaviour shows the importance to use an appropriate readout electronics and GEM foils with a high optical transparency.

We also observed signal losses dependent on the incident particle rate and on the drift field, for drift field values lower than 2 kV/cm. We have shown that this effect is due to the charging-up of the GEM foil. This could be a drawback if one foresees to use an MSGC+GEM detector in a high rate experiment with a low drift field, like for the readout of a large Time Projection Chamber.

We have studied the influence of the transfer field on the detector response and found that above a transfer field value of 2 - 3 kV/cm, the current drawn by the lower GEM

electrode rapidly increases with the transfer field. The simulations show that field lines originating on the MSGC anodes end on the lower GEM electrode at transfer fields above 2.5 kV/cm. This might cause instabilities in presence of a high rate of highly ionizing particles, when a GEM discharge propagate to the MSGC substrate, damaging the strips.

We have observed gain variations of up to 25% along the strips for two MSGC+GEM modules. This value is comparable to the gain non-uniformity obtained with the MICROMEGEM detector where the GEM foil is regularly supported by pillars. In addition the optical inspection of one of them has shown a negligible GEM sagging of the order of a 100 μm, indicating that the gain inhomogeneities are due to GEM hole diameter variations of a few microns, which can be the tolerance of the manufacturing procedure.

Chapter 7

The MF2 milestone

The MSGC detectors have first been considered to equip the outer part of the CMS Tracker (see section 2.4.4). In 1997 it was reported that similar detectors exposed to an intense pion beam of relatively low momentum, 350 MeV/c, [140] or to alpha particles [78], showed frequent destructive discharges, questioning the robustness of these detectors in the LHC environment [140]. Triggered by these observations, different studies have been performed to improve the stability of the MSGC in presence of Heavily Ionizing Particles. A first alternative introduced by R. Bellazzini [141] is the advanced passivation technique (see section 4.3.4). Although MSGC's with advanced passivation have shown that they can be operated at gains higher than 10,000 without sparks, the CMS collaboration has also investigated the possibility to use MSGC+GEM detectors for the endcap parts of the tracker. Consequently a large scale test of passivated MSGC and MSGC+GEM detectors of final design has been required by the CMS collaboration. The main objectives of this test was to investigate the robustness of such detectors when exposed to experimental conditions close to what is expected at the LHC. Eighteen detector modules have been operated at voltage settings corresponding to a 98% detection efficiency for minimum ionizing particles during a period of five weeks. The rate of discharges and the number of dead strips have been recorded throughout the exposure.

We describe the experimental set-up at PSI and the data acquisition system and we define the milestone in section 7.1. Section 7.2 describes the data analysis procedure and provides the cluster characteristics. In sections 7.3 and 7.4 we discuss the signal-to-noise ratio of the MSGC+GEM modules at low and high intensity respectively. In section 7.5 we present the procedure for the spark analysis. In sections 7.6 and 7.7 results on the detector stability and the robustness are presented. Finally section 7.8 reports on the study of the safety margins.

7.1 The experimental set-up at PSI

The modules were mounted back-to-back on nine support plates on an optical bench installed in the πM1 pion beam of momentum 350 MeV/c at PSI. One of these forward MSGC+GEM modules equipped with the electronic readout and the power supply board was shown in figure 6.3. The 18 forward MSGC+GEM modules were placed between two boxes, each containing 16 barrel MSGC's as shown in figure 7.1. Each MSGC+GEM module is labelled with a number corresponding to its position along the beam line.

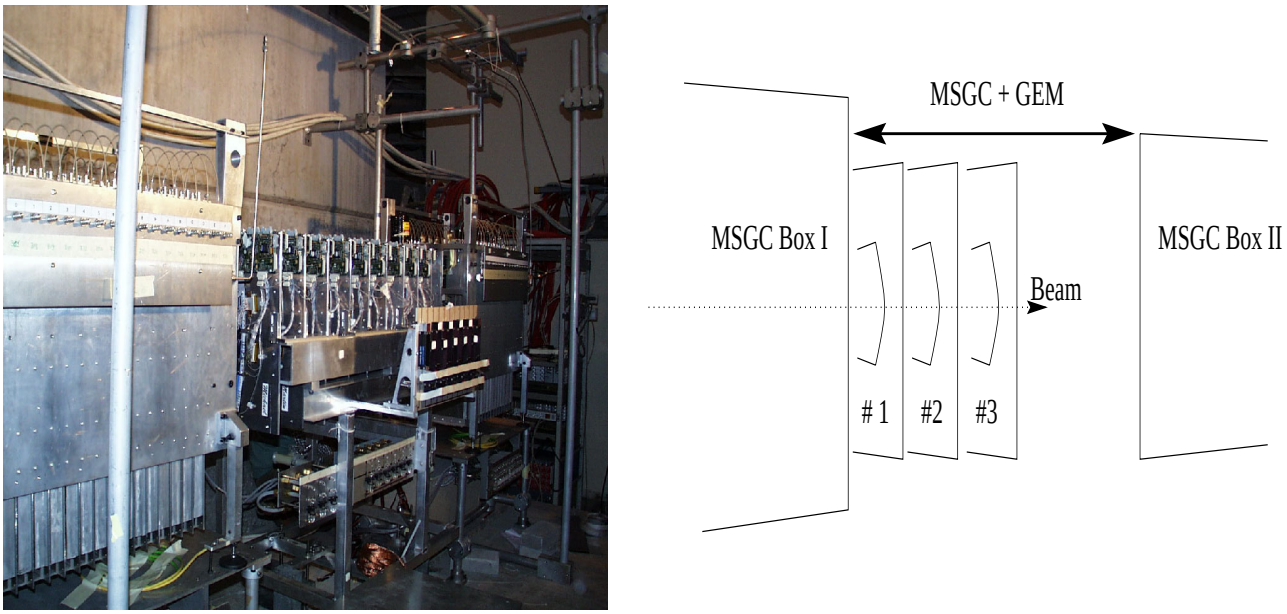

Figure 7.1: Picture and schematic view of the MSGC+GEM bench at PSI, sandwiched between two boxes, each containing 16 MSGC detectors participating to the barrel part of the CMS milestone [142].

The beam is a 350 MeV pion beam whose intensity can be varied between ~ 200 Hz/mm^2, called low intensity, and 10 kHz/mm^2, called high intensity, at the exit of the collimators. At high intensity, the rate exceeds the expected rate at LHC at the innermost MSGC layers of the CMS Tracker. Along the bench, 2.5 m long, the rate decreases because of the beam divergence. Consequently, at the position of the first forward modules, the particle rate is down to 4 kHz/mm^2 at high intensity which is still close to the LHC conditions. The beam profile is rather large and covers the two central substrates of a module; the rate drops by about a factor 2 outside an area of 10×10 cm^2. In addition to the 350 MeV/c pions which are MIP's, the detectors were also exposed to HIP's produced by strong interactions between the low momentum pions and the detector material. The probability to produce a HIP in an MSGC+GEM module is of the order of 10^{-4} per pion. The particle rate and the trigger are provided by the coincidence of two scintillators, LIF and LIB or HIF and HIB, depending on the beam intensity (see section 5.4.1), located in front and behind the three sets of chambers.

The chosen gas mixture is Ne/DME-40/60%; it is flushed in parallel to the nine pairs of modules with a rate of 1 l/h, yielding to two gas volume renewals per hour.

The milestone definition is the following: 12 MSGC+GEM modules have to be operated at high intensity with a signal-to-noise ratio that would ensure a 98% detection efficiency in CMS with the final electronics. During this period, the number of interrupted anode strips is limited to a value corresponding to a strip loss of less than 10% over 10 years of operation at the LHC (5×10^7 s) at full luminosity. Therefore for the milestone period less than 0.27% of the anode strips could be lost which corresponds to a maximal strip loss of 33 for the 24 MSGC substrates. All detector modules, except module 2 equipped with MSGC substrates produced at IMEC, were found adequate to be considered for the milestone. The IMEC substrates have shown instabilities at low voltages as well as shorts and are discarded from further analysis. Consequently, taking

into account all the modules except the IMEC module, the maximal allowed strip loss amounts to 45.

The entire period has been subdivided in four phases: the setting-up period of about one week, the hardening phase of one week where the loss of weak strips or electronic channels was allowed. These two first phases were followed by the milestone period of 376 hours and by one week which was devoted to the investigation of the operation margins. In this work only the results about the forward-backward MSGC+GEM system are reported for the milestone period and the margin week. This official CMS milestone is called Milestone Forward number 2 (MF2). The results concerning the MSGC's of the barrel milestone can be found in reference [142].

The data acquisition system used for the MF2 milestone is depicted in figure 7.2. It

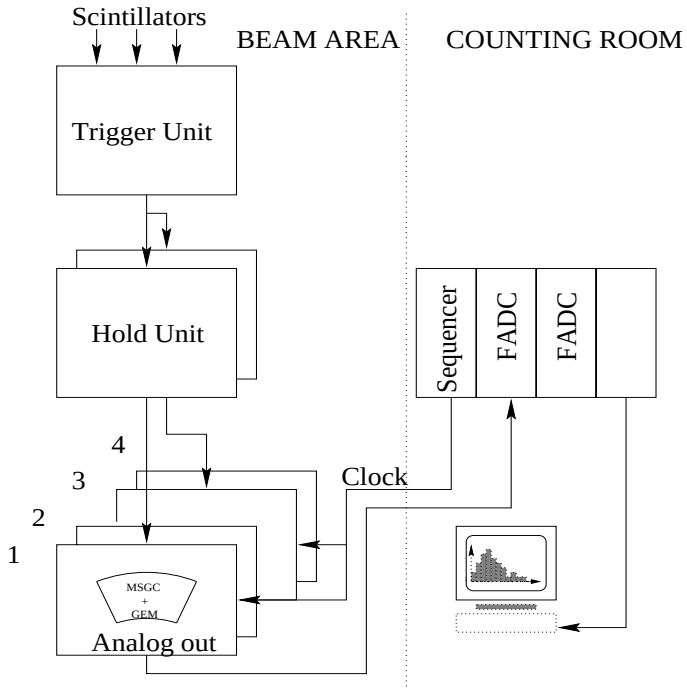

Figure 7.2: Schematic view of the data acquisition system used during the MF2 Milestone at PSI.

is similar to the system described in section 5.4.1 but the number of channels is four times greater; the number of strips to read out for the forward system alone was $18 \times 2 \times 512 = 18{,}432$. A VME sequencer is used to synchronize the readout of the front-end chips. The trigger which is described in details in reference [124] starts all the sequencers and waits for the end of the readout of all ADC's before a new cycle. The analog outputs are digitized by Scirocco FADC. The currents drawn by the substrates and the upper GEM electrodes are monitored by picoamperemeters put on the HV lines [125]. The currents are read out every 2 ms by ADC's, housed in a second crate. The event builder combines 1024 of such measurements in one so-called slow-control event. The overall control and the online monitoring of the data acquisition were ensured by a software running on a Linux-based PC, developed at IN2P3 Lyon.

7.2 Data Analysis

The Data Analysis procedure is similar to the procedure described in section 5.4.2. To extract the particle signal from the raw data, we have to compute the pedestal and the common mode shift. During this test, once a day, dedicated runs were taken without

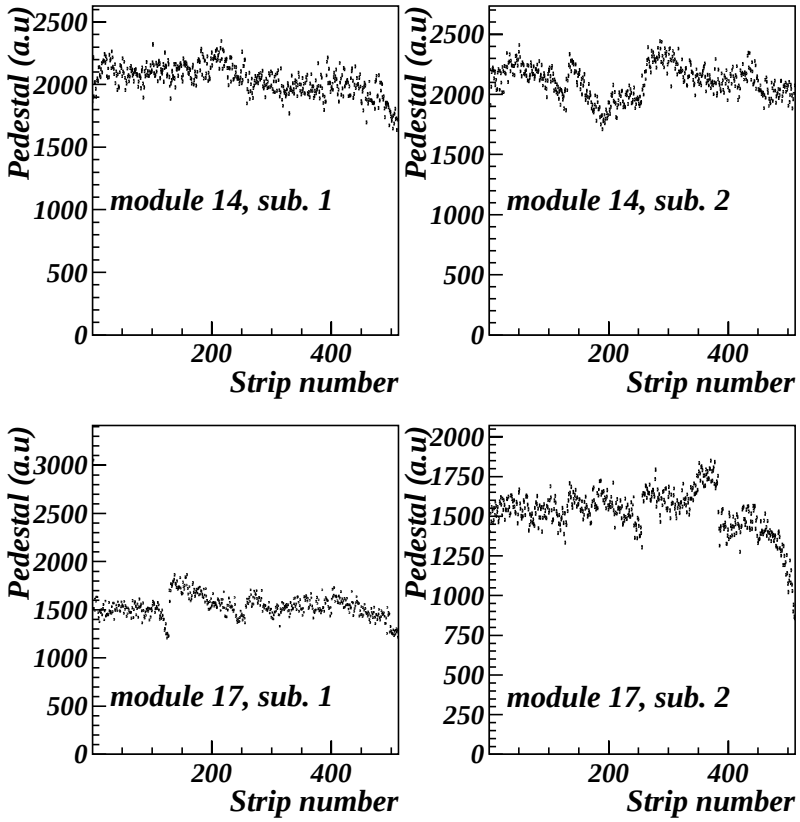

Figure 7.3: Pedestal as a function of the strip number for the two central substrates of the MSGC+GEM modules 14 and 17.

beam particles, with a random trigger, for pedestal calculation. The pedestal of each strip is defined as the average of the corresponding ADC count distribution. Figure 7.3 shows the pedestal as a function of the strip number for the two central substrates of the MSGC+GEM modules 14 and 17. In both cases we clearly observe the common shifts of the eight PreMux chips which equip one module. After subtraction of the pedestal from the raw data, the common mode is calculated for each event from the average of the remaining signals for sets of 128 strips connected to the same readout chip. After pedestal and common mode corrections, the noise of each strip, σ_i, is computed from the standard deviation of the remaining signal distribution. The RMS noise per strip is shown in figure 7.4 for the same modules. The RMS noise per strip ranges from 10 to 12 ADC counts. Some dips, corresponding to dead or broken strips, are also observed. The strips were identified as dead or noisy if their noise is less than 0.66 times the average noise or more than 10 times that average respectively. They are therefore excluded from further analysis. Clusters of adjacent strips having a signal are then formed. To be included in a cluster the strip must have a signal larger than 3 times the strip noise of that strip. To allow for broken or dead strips, the algorithm tolerates one strip having a signal lower than the threshold within a cluster. A cluster is accepted for further analysis if its charge exceeds 3.4 times the RMS value of the cluster noise. With a threshold of 3.4 the noise cluster rate reaches a value of 0.8% per substrate.

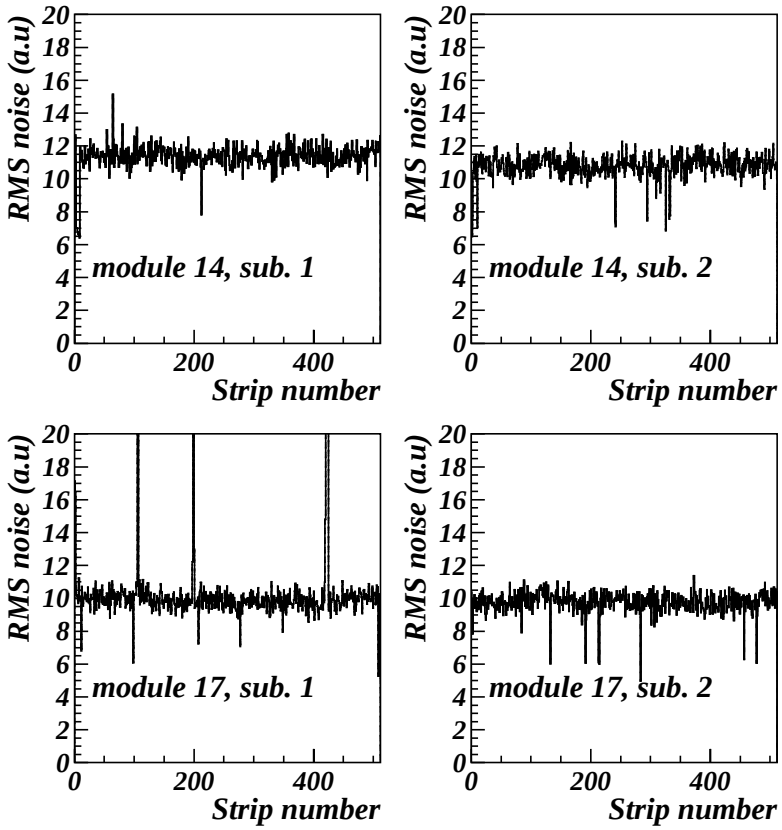

Figure 7.4: RMS noise as a function of the strip number for the two central substrates of the MSGC+GEM modules 14 and 17.

Before starting any measurements, the timing of the signal sampling has to be adjusted in order to record the maximum possible charge. For this purpose a delay box has been inserted in the trigger line between the arrival of the trigger and the opening of the PreMux 128 channel switch S_2 (see figure 5.25). Figure 7.5 shows the cluster charge as a function of this delay for one MSGC+GEM module. A delay value of 50 ns with respect to the trigger has been chosen to collect the maximum charge. Fixing this delay, we can now study the cluster characteristics.

Figure 7.6 represents the distributions of the cluster charge (a), the cluster noise (b), the cluster size (c) and the event multiplicity for counter 3, in a low intensity run. The module is operated with V_{cath} = - 450 V, ΔV_{gem} = 335 V, $E_{transfer}$ = 3.5 kV/cm and $E_{drift} \simeq$ 5 kV/cm. First we observe that unlike the MICROMEGEM detector, the cluster charge distribution is well separated from the noise distribution, which suggests a higher detection efficiency. The cluster size of 3.1 is 25% larger than the value obtained with an MSGC without GEM, filled with Ne/DME gas mixture [55]. The difference can be explained by the additional diffusion resulting from a longer drift path in the MSGC+GEM module. The average number of clusters per trigger is 1.6 for one module; this is 50% higher than the value measured with the MICROMEGEM detector in the same beam conditions. A possible explanation is that even at the low beam intensity of 200 Hz/mm^2, an additional out-of-time particle may be detected on the second substrate of the module in more than 40% of the events.

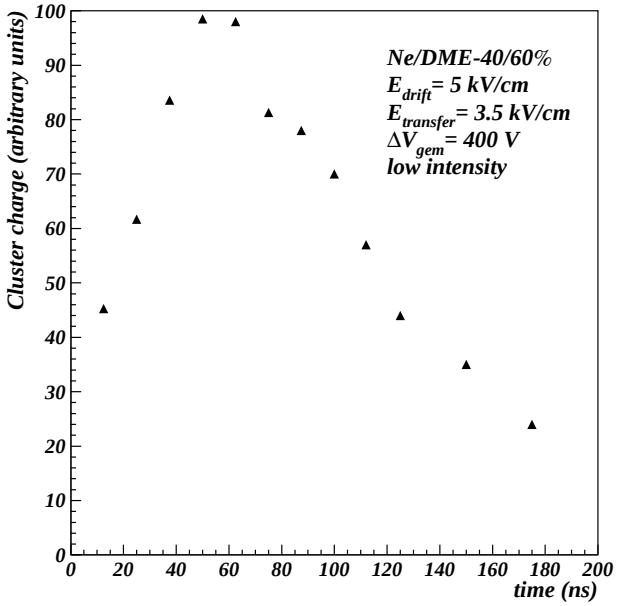

Figure 7.5: Cluster charge as a function of the trigger delay for an MSGC+GEM operated with ΔV_{gem} = 400 V, $E_{transfer}$ = 3.5 kV/cm and E_{drift} = 5 kV/cm, at low intensity. The detector is filled with a Ne/DME-40/60% gas mixture.

7.3 Signal-to-noise ratio at low intensity

The signal-to-noise ratio, SNR, is defined as the maximum of probability of the Landau distribution of the largest cluster detected for a given trigger divided by the quadratic mean of the noise for all strips contributing to the cluster (see equation 5.4). The first week of this test, called the setting-up phase, was dedicated to find the working point of the different modules by performing high voltage scans with a low intensity beam and by monitoring in parallel the onset of discharges or sparks with the picoamperemeters located on the HV lines (see section 7.1). A spark is identified by a large current excursion during a short time: one order of magnitude above the nominal value in less than 2 ms. Figure 7.7 shows the signal-to-noise ratio as a function of the cathode strip voltage for module 5 operated at low beam intensity with ΔV_{gem} = 335 V, $E_{transfer}$ = 3.5 kV/cm and with E_{drift} fixed to 5 kV/cm. The curve shows the expected exponential dependence of the signal-to-noise ratio on the cathode voltage. For the safety of the counters, the measurements were not pushed to cathode strip voltages higher than 500 V for which the SNR is as high as 80 with a moderate spark rate of the order of 5×10^{-3} Hz. It is important to mention that for each - V_{cath} lower than 480 V no sparks have been recorded during a run of 1 hour, which gives an upper limit of 0.27×10^{-3} Hz on the spark rate. At low intensity the highest SNR reached with the MSGC+GEM is 4 times larger than the highest SNR obtained with the MICROMEGEM (see figure 5.32) and with the MICROMEGAS [92] counters.

The working point is defined as the voltage setting at which the SNR is sufficient to guarantee a 98% detection efficiency for MIP's with the final readout electronics foreseen for the CMS collaboration, APV [105]. This minimal SNR has been measured during

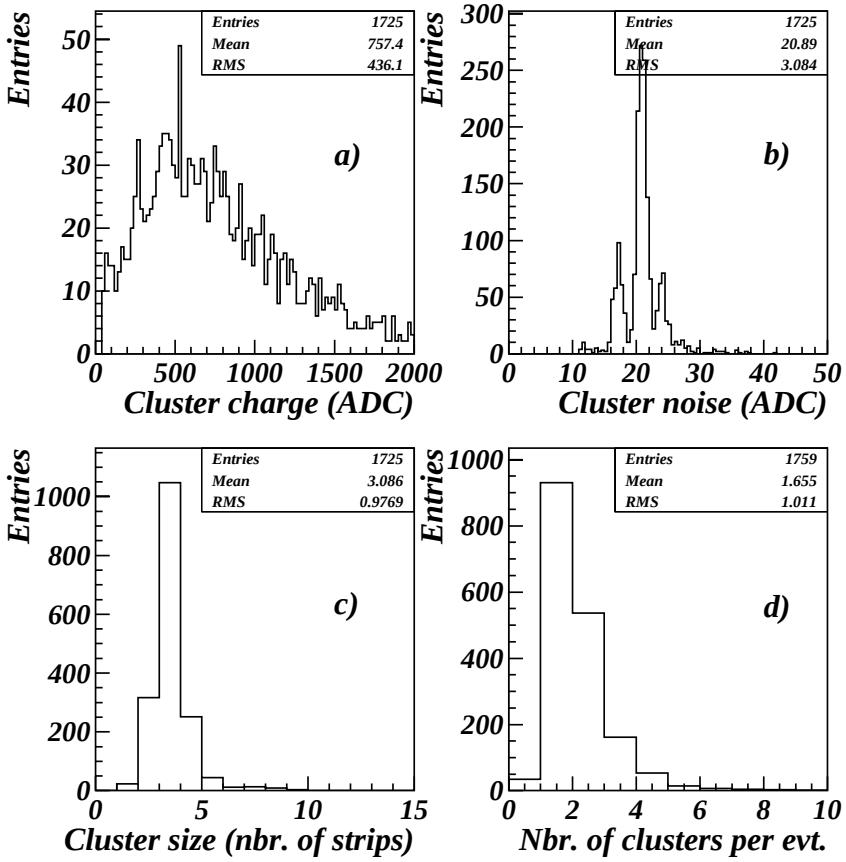

Figure 7.6: Distribution of the cluster charge (a), the cluster noise (b), the cluster size (c) and the event multiplicity for counter 3, at low intensity. The module is operated with V_{cath} = - 450 V, ΔV_{gem} = 335 V, $E_{transfer}$ = 3.5 kV/cm and $E_{drift} \simeq$ 5 kV/cm.

previous beam tests performed at CERN [114] but was also determined at PSI during runs at low intensity. To determine the working point at PSI, the efficiency of two modules, situated in the middle of the bench, has been measured as a function of the SNR, as shown in figure 7.8. For this purpose, tracking has been done using 7 detection planes, 3 upstream and 4 downstream, of the two central modules. Each cluster reconstructed in the first module is considered as a possible starting point, called seed, for a particle track. In the next module, a cluster will be added to the track if its centre of gravity position is at less than 5 mm from the track impact point prediction; in case of ambiguity only the largest cluster is retained. The prediction assumes perpendicular tracks. A track is accepted if the selection algorithm finds seven aligned clusters. The detection efficiency of the central modules is defined by the number of tracks detected by these modules. In figure 7.8, we observe that a detection efficiency of 98% is reached at an SNR value of 17, confirming the results given in reference [114]. However all MSGC+GEM modules have been operated during the milestone at an SNR of the order of 37 (see figure 7.9). Indeed, the PreMux 128 front-end chip was used for this tests instead of the final APV chip [144]. The APV uses a deconvolution algorithm, based on a weighted average of three time samples, taken at 25 ns intervals, and optimized for optimal LHC-bunch crossing identification. This algorithm introduces an additional noise of $\sim$ 1000 electrons [145]. Moreover the ballistic deficit increases from 32 to 55% with the Ne/DME-40/60% gas mixture according to the Monte Carlo simulation performed by T. Beckers [131]. Consequently, these contributions require an increase of a factor 2.2 in SNR to reach 98% detection efficiency with an APV

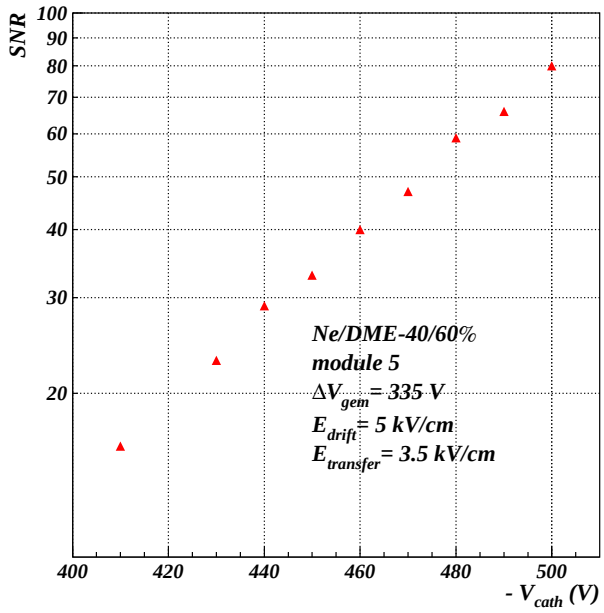

Figure 7.7: Dependence of the signal-to-noise ratio of the MSGC+GEM module 5 on the cathode strip voltage at low intensity ($\sim$ 200 Hz/mm^2). The detector is operated with a transfer and a drift field of 3.5 and 5 kV/cm respectively. The potential difference across the GEM is fixed to 335 V.

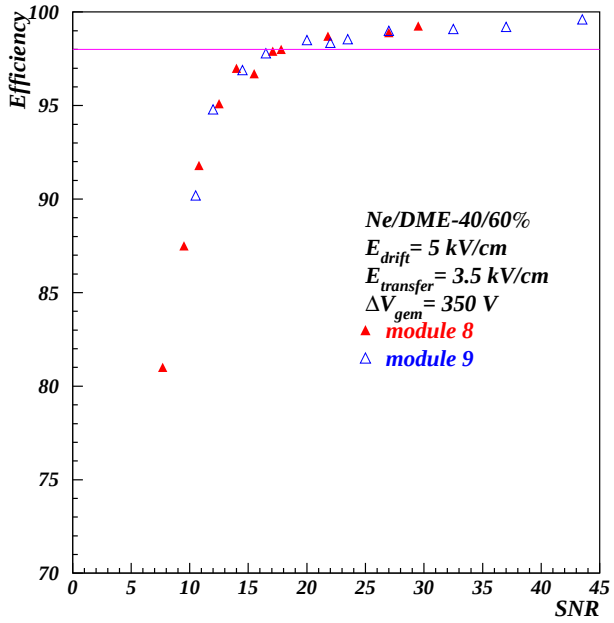

Figure 7.8: Detection efficiency of two modules as a function of the signal-to-noise ratio with ΔV_{gem} = 350 V, with Ne/DME-40/60% gas mixture. E_{drift} and $E_{transfer}$ are fixed to 5 and 3.5 kV/cm respectively.

chip.

From these measurements, the voltages applied on the MSGC cathodes and across the GEM have been individually tuned for each substrate, in order to reach an SNR of at least 37, taking care of minimizing the spark rate. The drift field was fixed around 5 kV/cm in order to ensure a drift velocity above 45 μm/ns (see figure 4.7). The transfer field was

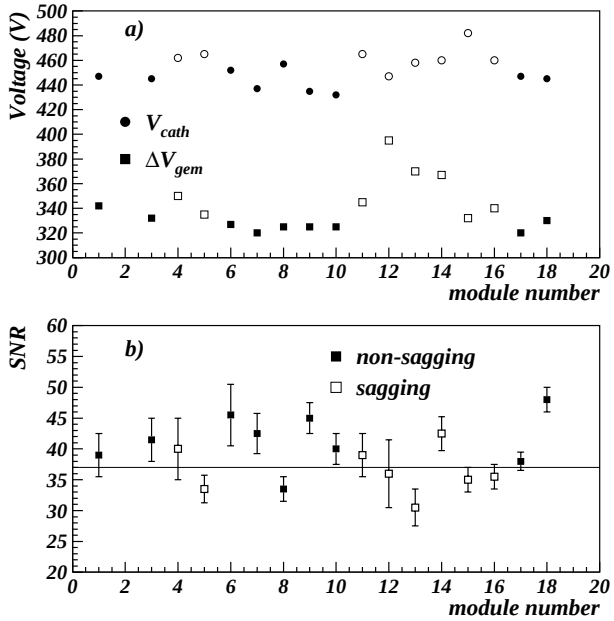

Figure 7.9: MSGC cathode voltage and GEM potential difference used to operate each module (a) and the corresponding SNR (b). The open and closed marks identify the sagging and the non-sagging GEM's respectively, according to their delay.

fixed to 3.5 kV/cm in order to avoid the possible propagation of sparks onset in the GEM foil towards the delicate MSGC anodes (see section 6.3.6). The voltage settings of all modules and the corresponding SNR are reported in figure 7.9 (a) and (b) respectively. The cathode voltages range from 430 to 480 V and the GEM potential differences vary between 320 and 400 V. With these settings, the SNR may vary by up to 50% from one module to another. These large fluctuations are probably due to variations of the GEM hole geometry and to assembling problems which created a large saggitta for some GEM foils.

Detectors with a significant saggitta have been identified because of their abnormal delay time with respect to the trigger. For example, module 14 has a $\sim$ 60 ns longer delay as compared to that shown in figure 7.5; it has revealed a sagging towards the cathode drift plane of up to 1 mm in the centre of the GEM foil, during an optical inspection. Indeed for a given potential difference between the upper GEM electrode and the cathode drift plane, an upwards sagging will result in a larger transfer gap and consequently to a longer delay. The detectors identified as sagging are indicated in figure 7.9 by open marks. It is not possible to give the exact field configuration for these detectors since the electric fields vary along the strips. Therefore one has applied a potential difference between the upper GEM electrode and the cathode drift plane similar to that of the counters with a normal delay, providing a drift field of 5kV/cm for a drift gap of 3 mm. However a higher voltage, - 1200 V instead of - 1000 V, has been applied to the lower GEM electrode for these detectors. We observe from figure 7.9 that almost all the sagging detectors were operated with amplification voltages slightly higher than for the non-sagging modules. Note that SNR variations are also observed between modules identified as non-sagging and operated with the same settings. With V_{cath} = - 445 V and with ΔV_{gem} = 335 V, the SNR of module 3 and 18 are 41 $\pm$ 3 and 49 $\pm$ 2 respectively. The 20% difference is attributed to fluctuations in the GEM hole geometry from one foil to another. Indeed we have seen in section 6.4 that the effective gain of a module with a negligible saggita may

vary by up to 25% along the strips because of a few microns difference in the GEM hole aperture, which could be the tolerance of the manufacturing procedure.

We will see in section 7.6, that even large GEM saggings do not prevent the MSGC+GEM detectors to be stably operated at the working point, during more than 360 hours at high intensity. However the GEM mounting should be improved, for uniformity purpose, by inserting pillars in the detection area like in the MICROMEGEM or the triple GEM detector [143].

7.4 Signal-to-noise ratio at high intensity

The detectors have been operated at high intensity throughout the entire milestone period at their working point determined during low intensity runs (see previous section). Figure 7.10 shows the distributions of the cluster multiplicity (a) and of the SNR (b) for

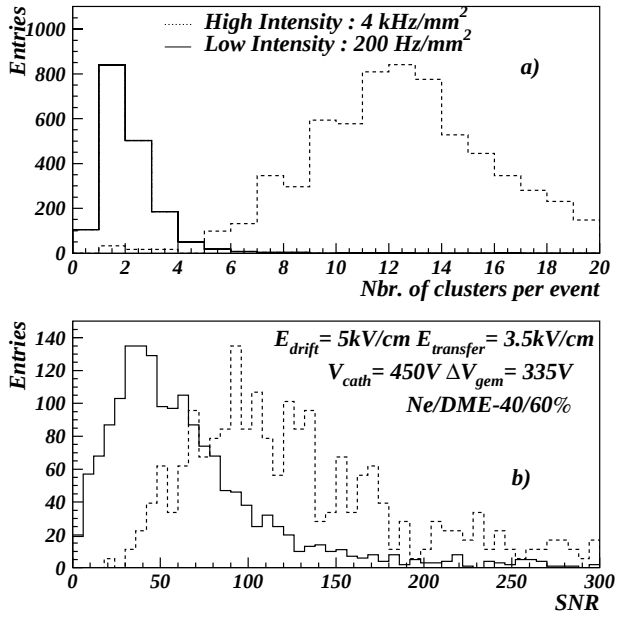

Figure 7.10: Distributions of the cluster multiplicity (a) and of the SNR for module 3 at low (200 Hz/mm^2) and high (4 kHz/mm^2) beam intensity.

one module at low (200 Hz/mm^2) and high (4 kHz/mm^2) intensity. The cluster multiplicity increases from $\sim$1.6 at low intensity to 12, on average, at high beam intensity.

To obtain the correct SNR distribution at high intensity is difficult, if not impossible, because of the high multiplicity of particles (see figure 7.10 a) and of the important multiple scattering of low momentum pions. In absence of a telescope, track reconstruction would require a complex algorithm. In addition, the absence of timing information would not allow to identify the triggering particle. Assuming that out of time particles give smaller signals, on average, than the triggering particle, the SNR distribution is built by selecting the cluster with the highest SNR. This approach clearly detects the triggering particle at low intensity, as observed in figure 7.11 that shows the strip number corresponding to the barycenter of the cluster with the highest SNR as a function of the module number for one event. However at high intensity, the cluster with the highest

SNR does not always correspond to the triggering particle. A typical event is represented in figure 7.12. In this figure, the strip number corresponding to the barycenter of all the detected clusters are shown as a function of the module number. The cluster with the highest SNR in each module is identified by closed marks. We clearly observe that all the clusters with the highest SNR do not necessarily belong to the same particle track. The rest of the clusters identified with open marks corresponds to off-time particles superposed to the triggering particle. Therefore the selection algorithm induces an artificial shift of the SNR distribution towards larger value. At the highest intensity of 4 kHz/mm^2, the maximum of probability of the SNR distribution is almost a factor 2.5 higher than the maximum value at low intensity (see figure 7.10 b).

7.5 Spark Analysis

As seen in section 4.3.4, discharges can damage and destroy the delicate MSGC anodes but may also destroy the electronics channels if a discharge from the GEM reaches the substrate (see section 5.4.4). To investigate these effects, the currents drawn by the MSGC cathodes and by the upper GEM electrode of each module have been monitored during the entire test period. At the SNR value of $\sim$ 37 and at high intensity, the currents drawn by 512 cathodes and the GEM electrode amount to $\sim$ 200 nA and 50 nA respectively.

Figure 7.13 shows the cathode current variation with time when a discharge occurs in one group of 16 strips. The total charge amounts to $\sim$ 35 nC, corresponding to the charge stored in the capacitance of one cathode group. This capacitance is measured to be $\sim$ 80 pF. With a typical V_{cath} of - 450 V, the stored charge can be estimated to 36 nC. Figure 7.14 shows the charge distribution of the cathode current excursions recorded during the test. Two types of events can be clearly identified. The first peak, with a charge smaller than 5 nC, corresponds to streamers. The streamers are probably induced by HIP's which produce avalanches large enough to be detected by the picoamperemeters. Despite the large number of this kind of events, they do not seem to destroy the MSGC anodes. The second peak with an average charge of 30 nC corresponds to sparks between anodes and cathodes of the substrates.

Another type of destructive discharges may occur in the module: a spark onset in the GEM may propagate towards the substrate. Such sparks are considered particularly dangerous as the whole charge stored in the GEM capacitance may reach the MSGC anodes. We have seen in section 6.3.6 that the probability of such events may increase with the transfer field as more electric field lines connect the MSGC anodes to the GEM electrodes. With the moderate transfer field used, $\sim$ 3.5 kV/cm, none of these sparks have been observed throughout the entire test period.

7.6 Detector stability

The detector stability has been controlled over 20 days by looking at the evolution of the sparking rate and the signal-to-noise ratio with time. Such evolution is shown in figures 7.15 and 7.16 for the SNR and the spark rate of module 3, respectively. The MSGC+GEM module was operated during the whole period with V_{cath} = - 450 V,

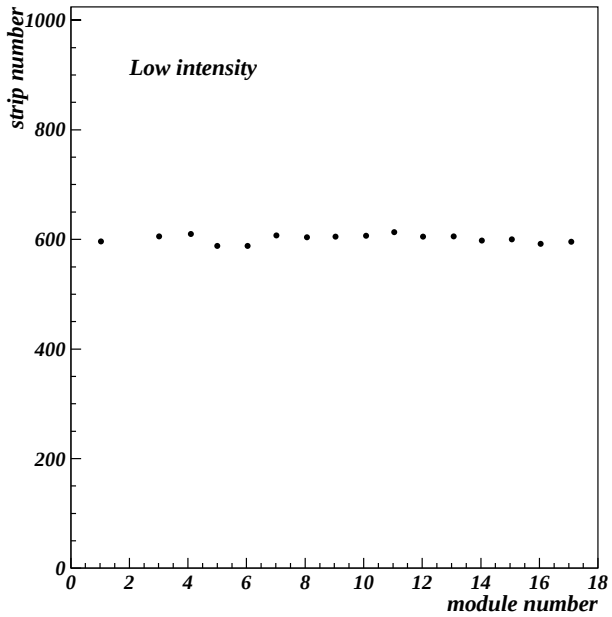

Figure 7.11: Strip number corresponding to the barycenter of the cluster with the highest SNR as a function of the module number for an event taken at low beam intensity (200 Hz/mm^2).

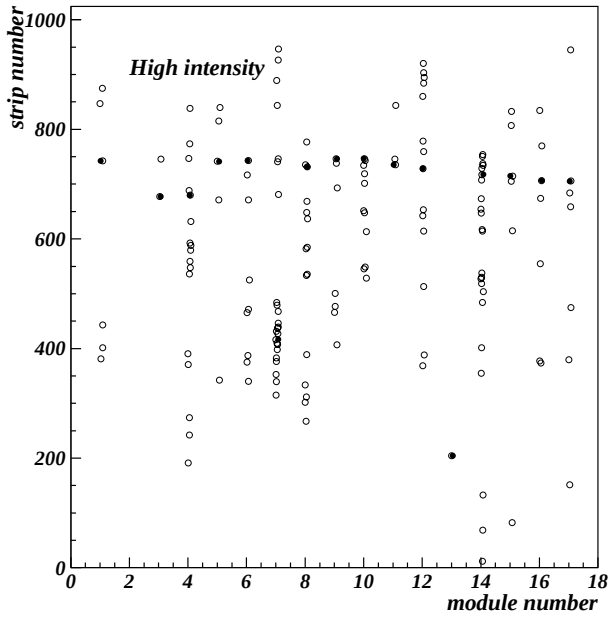

Figure 7.12: Strip number corresponding to the barycenter of all the detected clusters as a function of the module number for an event taken at high beam intensity (4 kHz/mm^2). The closed marks correspond to the clusters with the highest SNR of each module; the open marks correspond to clusters produced by off-time particles.

ΔV_{gem} = 350 V, $E_{transfer}$ = 3.5 kV/cm and $E_{drift} \simeq$ 5 kV/cm. We observe in figure 7.15 that most of the time, the SNR is larger than the required value of 37 (see section 7.3), with a negligible sparking rate of less than 10^{-3} Hz as shown in figure 7.16 for the two substrates. Although the voltages of this module were constant during the whole period, the SNR was not constant. SNR variations up to 35% have been observed in different

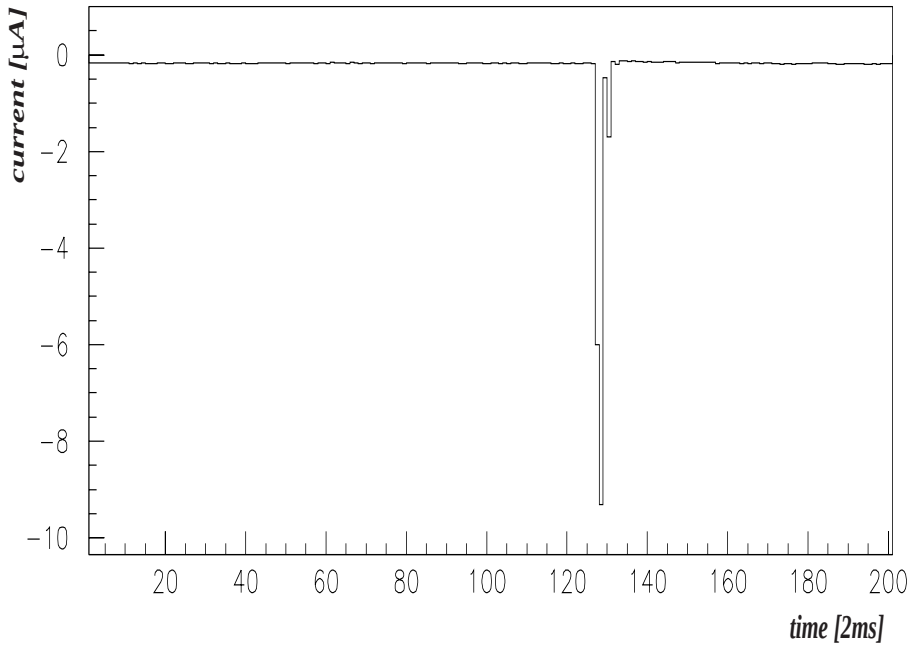

Figure 7.13: Cathode current as a function of the time when a discharge occurs in one group of 16 strips.

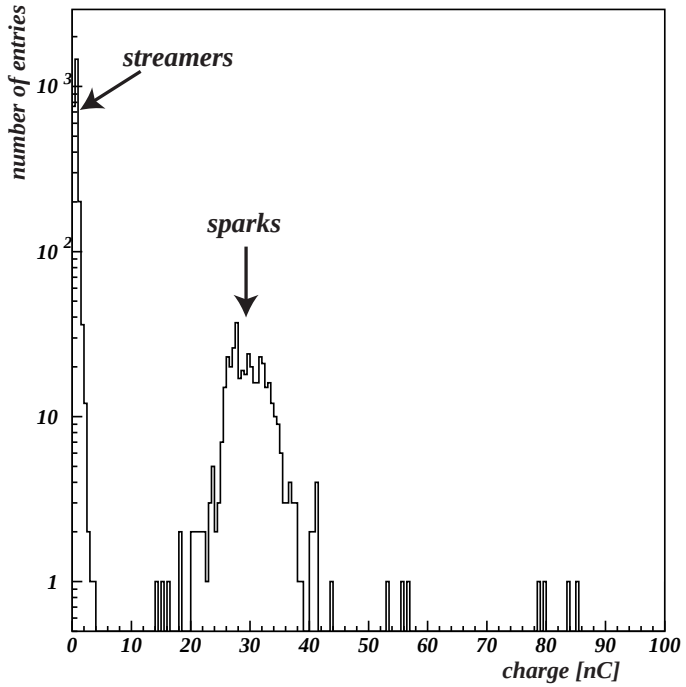

Figure 7.14: Charge distribution of all the sparks recorded during the MF2 milestone period on the MSGC cathodes.

modules. To understand the origin of these fluctuations we have first studied independently the cluster charge and cluster noise variations as shown in figure 7.17 for module 5 at high and low intensity.

We clearly observe that the noise slightly increases with an almost constant rate resulting in an increase of less than 0.5 ADC counts, after a period of 21 days. This effect is observed at low intensity as well as at high intensity. The increase has been registered

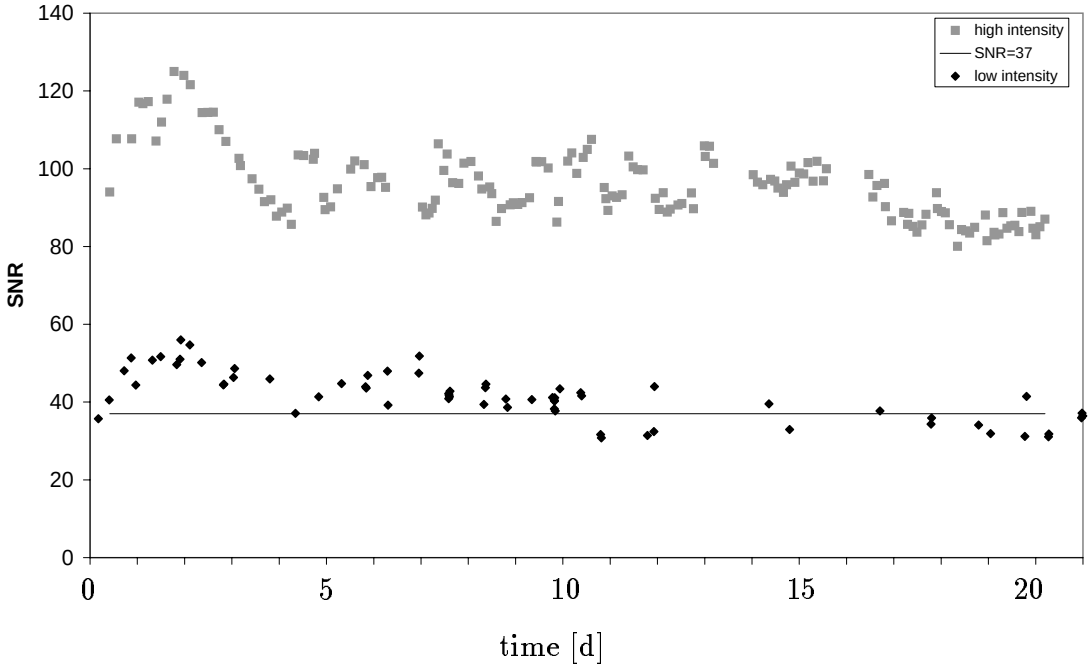

Figure 7.15: SNR of module 3 as a function of time (during the milestone period), at low and high beam intensity.

for all modules but seems slightly less important for some detectors located downstream on the bench. A possible explanation could be the non radiation hard preamplifier electronics which is damaged by the particle flux. This increase of noise induces an SNR drop of $\sim 2.5\%$ over the milestone period but does not explain all the SNR fluctuations.

At the beginning, each detector shows a signal increase of up to 35% after the first two days. As the milestone part followed a one week period of high intensity running, this effect can not be attributed to a kind of charging-up related to the beginning of the tests. Figure 7.18 shows the daily mean of the SNR at high intensity and the atmospheric pressure, as a function of time during the milestone period. The large increase registered during the first two days may be related to a pressure drop and the 10% decrease of the SNR observed during the last five days could correspond to a pressure rise. However for the rest of the period, it is difficult to see a clear correlation between the pressure variations and the SNR fluctuations.

As no record of the temperature was available, the temperature dependency has been investigated by looking to day-night variations. Indeed the temperature in the experimental hall was not regulated but varied with the external temperature. An analysis performed by T. Beckers [131], using a special type of Fourier transform allowing for non-equidistant spread of times [132], shows that variations above a level of 2.1% could be excluded.

As the SNR is rate dependent (see section 7.4), we have also investigated the correlation between the SNR fluctuations and the particle rate at high intensity, which is shown in figure 7.19 as a function of time. We observe that the intensity has been raised

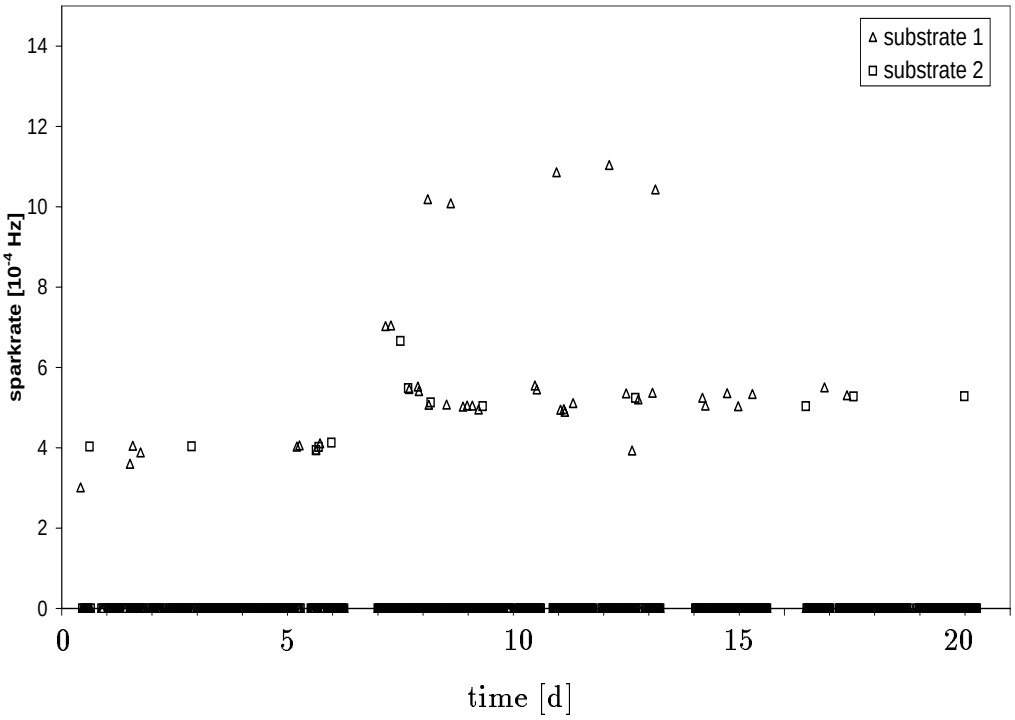

Figure 7.16: Spark rate for both substrates of module 3, as a function of time at high intensity.

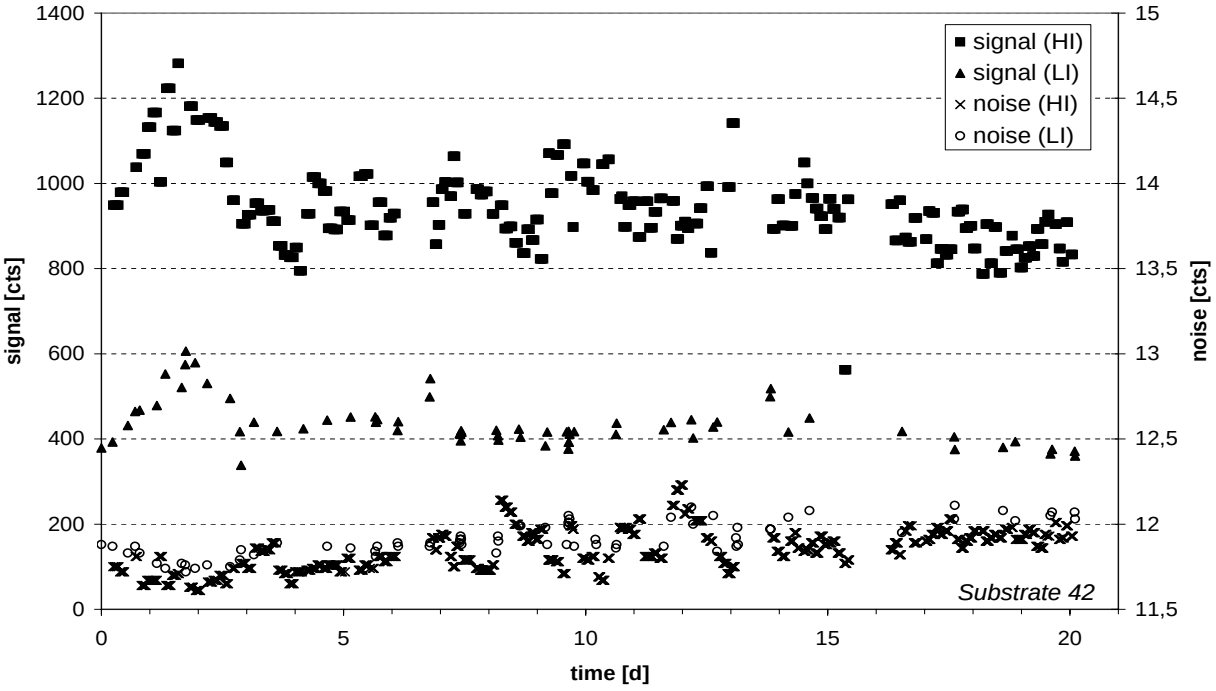

Figure 7.17: Cluster charge and cluster noise as a function of time, at low and high beam intensity.

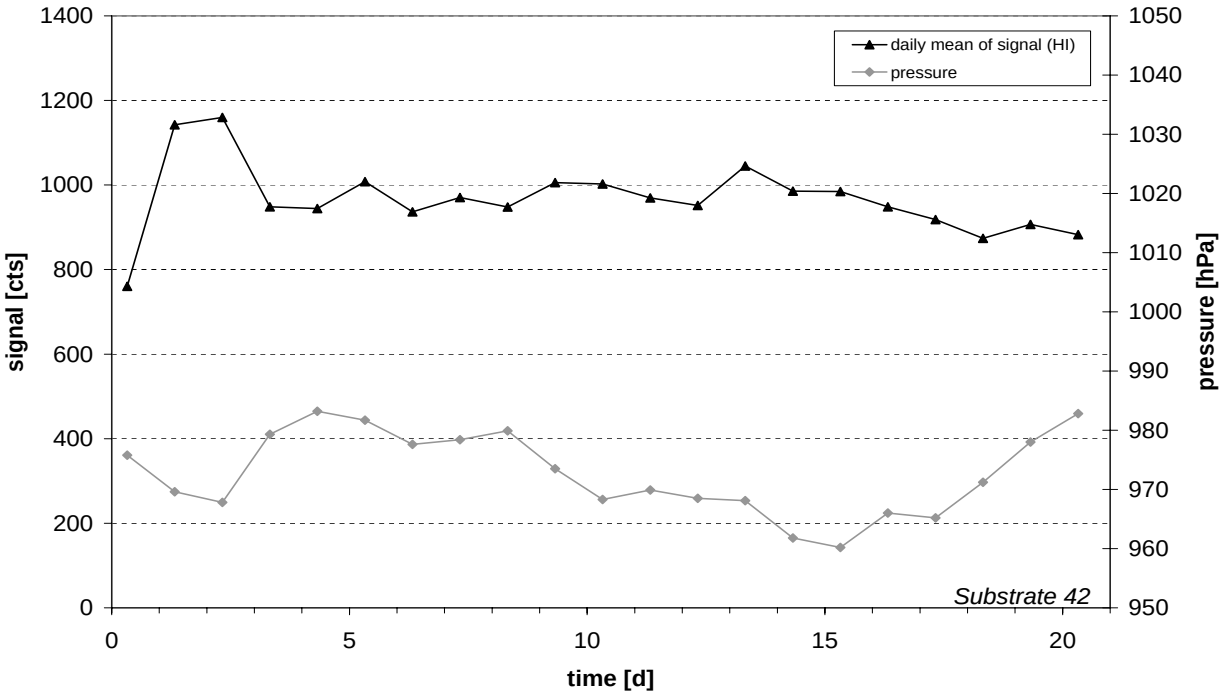

Figure 7.18: Daily mean of the SNR at high intensity and atmospheric pressure as a function of time.

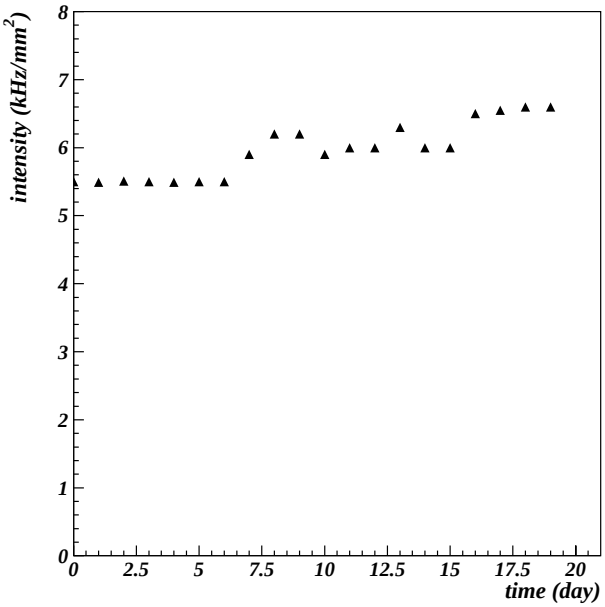

Figure 7.19: Particle rate measured by the HI scintillators as a function of time.

after 7 days by 10% and gradually increased after nine days, at the end of this period. Again no obvious correlation can be seen between these intensity variations and the SNR fluctuations.

Recapitulating this extensive study of the environmental parameters like, the pressure, the temperature, the beam intensity, ..., no clear correlation between the signal variations and one of these parameters can be established and none of them can explain all the SNR variations observed during the milestone period. However the increase of noise resulting

of the use of non-radiation hard preamplifier could be an explanation of the slow SNR decrease observed in figure 7.15.

7.7 Detector robustness

The robustness of the MSGC+GEM's was controlled by monitoring the spark rate and by counting the number of dead strips. To investigate possible strip damages or strip losses, we have used three different approaches. The first method is based on the monitoring of the beam profiles. An interrupted or dead strip can be identified by a local inefficiency of this strip accompanied by an enhancement of the counting rate on the neighbouring strips, since the electrons released above the damaged strips are deviated towards the neighbouring ones by the electric field. The second method injects a signal capacitively coupled to the readout channels and the last one measures the RMS noise of each strip determined from the daily pedestal runs. This approach is illustrated in figure 7.20 for the two central substrates of module 8. The RMS noise is shown as a function of the strip number before (a) and after (b) the milestone period of 376 hours at high intensity. The difference between the RMS noise after and before is also represented in the plot (c) of the figure. The strip noise depends on the strip capacitance that is linearly dependent

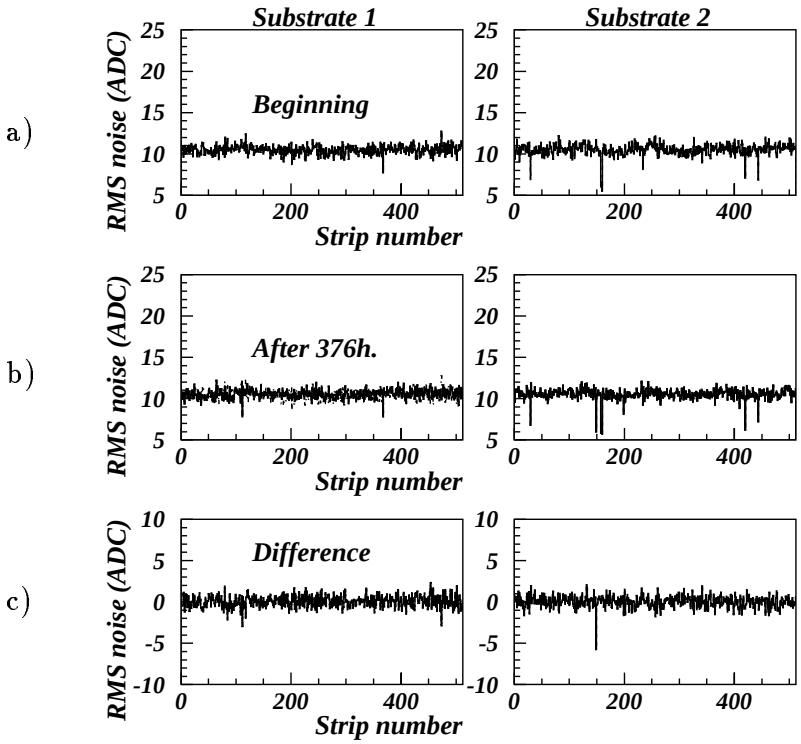

Figure 7.20: RMS noise as a function of the strip number before (a) and after (b) the milestone period for the two central substrates of module 8. The difference is also represented (c).

on the strip length. Therefore an interrupted or broken strip is revealed by a reduced RMS noise. A strip will be definitely considered as dead if it is confirmed by the three methods. After 376 hours at high intensity (figure 7.20 (b)), two new dips corresponding to dead strips are clearly visible around strip 110 of substrate 1 and around strip 150 of

substrate 2. The other dips observed in figure 7.20 (c) for substrate 1 are due to strips having different noise levels before and after the milestone, as it can be seen in the upper plots.

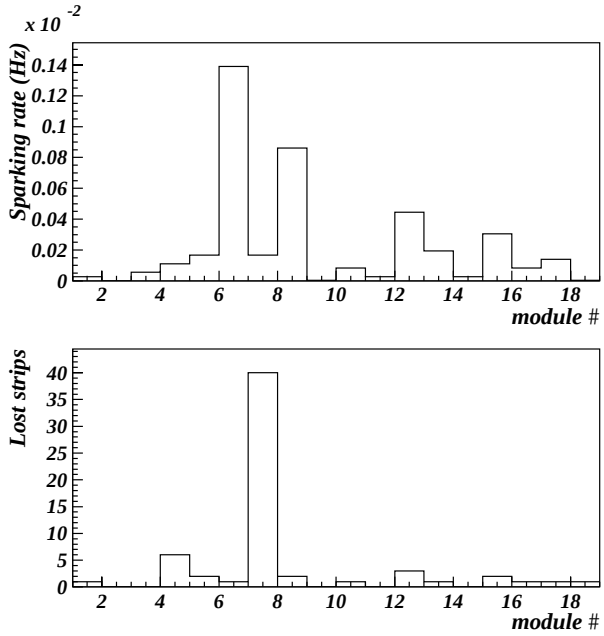

Figure 7.21: Average number of sparks and number of dead strips for each module for the milestone period.

Figure 7.21 shows the average sparking rate (a) and the total number of strips lost (b) for each module during the milestone period. The sparking rate ranges from 10^{-4} to 10^{-3}Hz which corresponds to less than 4 sparks per hour and per module. The number of lost strips is, on average, one per module over the 20 days, except for modules 4 and 7 which were badly assembled. The GEM of module 4 was ripped off during the assembly. A possible explanation for the large number of dead strips is that chips of dried glue were left inside the module when repairing the damages during the assembly. One substrate of module 7, the substrate 45, lost more than 40 strips during the milestone period; the cutting along one edge was performed inside the metallization, leaving gold chips on the substrate surface. In the framework of mass production these counters would have been discarded during the assembly. The strip loss of module 7 is not considered for the dead strip counting.

Figure 7.22 b) shows the position of the lost strips accumulated during the milestone period; a typical beam profile is shown in figure 7.22 a). Although the statistics of lost strips is small, it seems that there is no correlation between the strip loss and the beam intensity. It is also important to note that the number of dead strips is not higher in groups which were previously damaged. This is shown in figure 7.23 which presents the distribution of the distance between the strips broken during the milestone period and the nearest previously broken strip. If we take into account the fact that three of the four strips lost at a distance of one strip belong to module 4, badly assembled, the average number of strips between broken strips is larger than 42. This shows that the neighbouring strips of a broken strip are not fragilized.

To summarize the history of the strip loss throughout the milestone period, figure 7.24 displays the accumulated number of dead strips as a function of time for all the counters

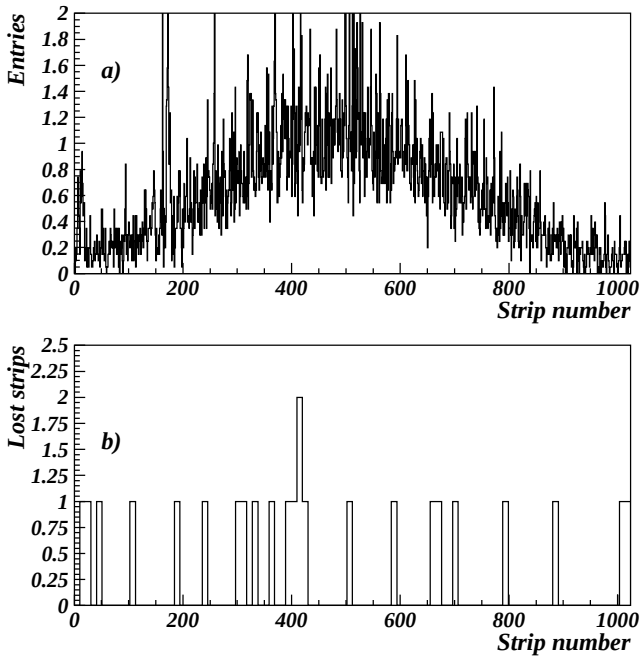

Figure 7.22: Beam profile of a counter in the middle of the bench (a) and distribution of the accumulated dead strips during the milestone period.

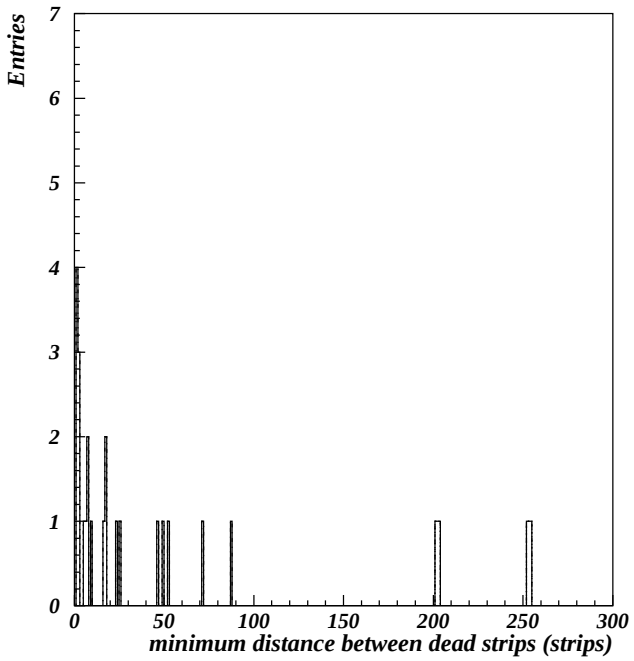

Figure 7.23: Distribution of the distance, expressed in number of strips, between the strips lost during the milestone period and the nearest previous broken strip.

except substrate 45, badly cut, and the two IMEC substrates discarded since the beginning of this analysis. The line corresponds to the maximal strip loss allowed for the 33 other substrates. For the 33 substrates considered, 24 anodes out of 16896 exposed were damaged, which corresponds to an anode loss of 0.14%. This value is almost a factor two below the limit of 0.27% imposed by the CMS collaboration which corresponds to less than 10% of strips when extrapolated to 10 years of operation at LHC. Considering the 12 milestone modules, 18 strips were lost, that is 45% below the limit of 33 imposed by the CMS collaboration. Extrapolation to 10 years of operation at LHC indicates that the

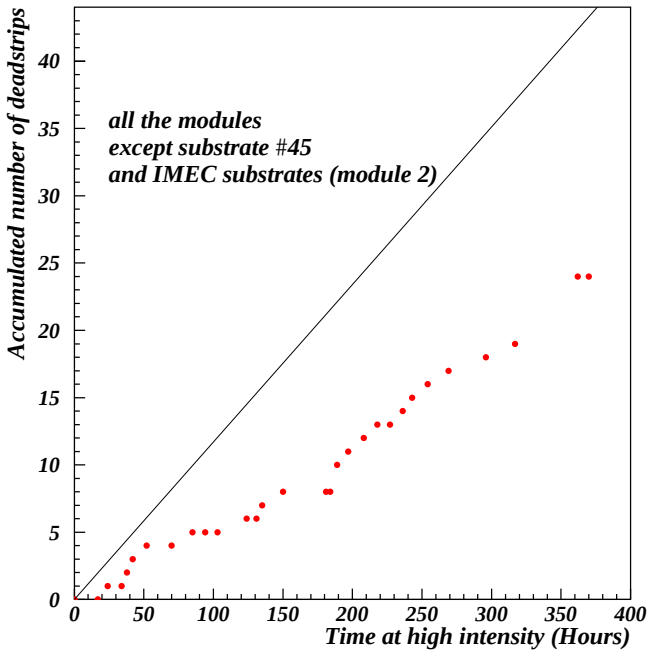

Figure 7.24: Accumulated number of dead strips as a function of the time at high intensity for all detectors, except one badly cut substrate (substrate 45) and the IMEC module, during the milestone period.

strip loss would result in a negligible loss of detection efficiency and a slight degradation of the spatial resolution in less than 4% of the covered area.

7.8 Study of the margins

During the milestone period the modules were operated with an SNR value around 37, ensuring a 98% detection efficiency with the final readout chip. This period has been followed by a week during which the detector voltages have been raised in order to explore the margins beyond the working point, in a LHC-like environment. However it is essential to note that an SNR of 37 already corresponds to a margin of a factor 2.2 if the detector is equipped with an adapted electronics (see section 7.3).

Not all the modules participated to this part of the test: the modules 2, 4 and 7 were discarded because they encountered problems during the assembly and some of the counters were also used to perform other measurements in parallel. The spark rate and the strips loss were monitored during this last part of the PSI test.

Figure 7.25 shows the SNR of detector module 17 as a function of time at low and high beam intensity, during the margin period. After one day of slowly increasing the SNR, the module has run with an SNR of almost a factor two above the working point. During the last days, the module has been pushed to an SNR close to three times the required one and worked at this value for about 17 hours without substantial increase of the spark rate, as observed in figure 7.26 which shows the spark rate as a function of time for module 17, during the same period. Each mark corresponds to a run of about one hour duration. We observe that no spark has been observed on substrate 1. For substrate 2 a few runs recorded two or up to four sparks per hour but for most of the runs no

sparks were observed. Table 6.1 summarizes the sparking rate and the maximum SNR reached by different counters during the exploration of the margins. It can be seen that the counters can be operated safely well beyond the working point during more than 50 hours at high intensity and, the last day, three detectors worked at an SNR around a 100, corresponding to a gain of $\sim 10^4$, during 17 hours.

detector	SNR	spark rate ($*10^{-4}$Hz)	Hours of operation	SNR	spark rate ($*10^{-4}$Hz)	Hours of operation
1	61	2.7	55			
8	48	1.6	46	72	0.5	17
9	65	0.03	46	106	$\leq$0.1	17
10	63	1.1	65			
17	58	0.3	34	94	2.0	17
18	68	$\leq$0.03	46	96	$\leq$0.1	17

Table 7.1: Summary of the maximum SNR, the average sparking rate and the time of exposure during the exploration of the margins.

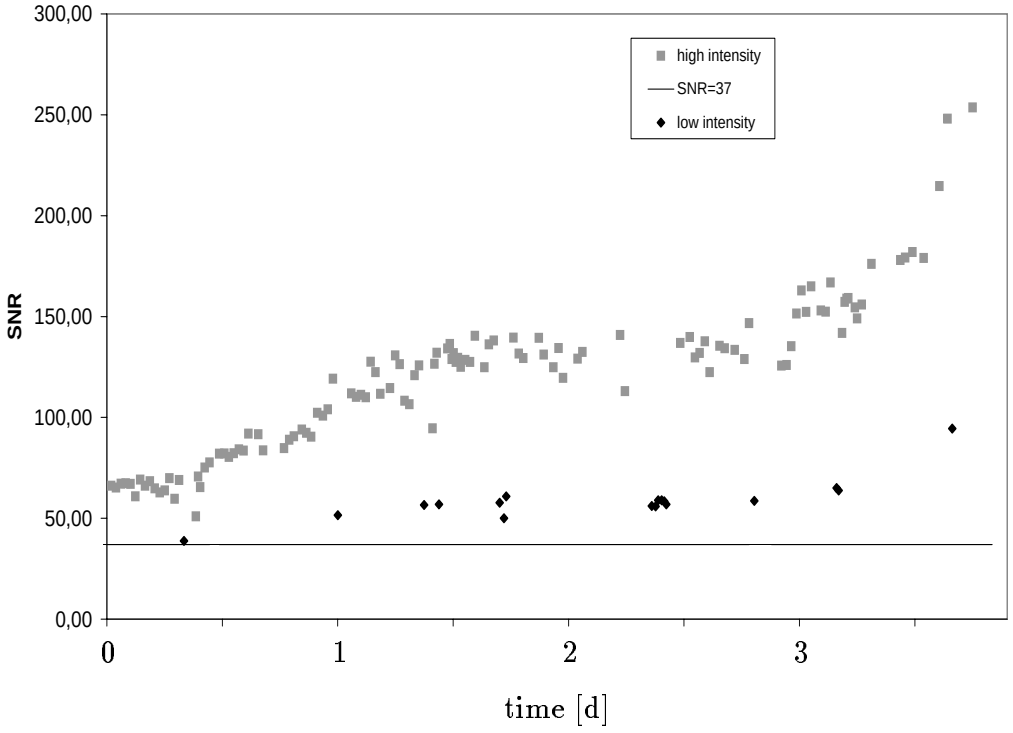

Figure 7.25: SNR as a function of time during the margin period for module 17, at high and low beam intensity.

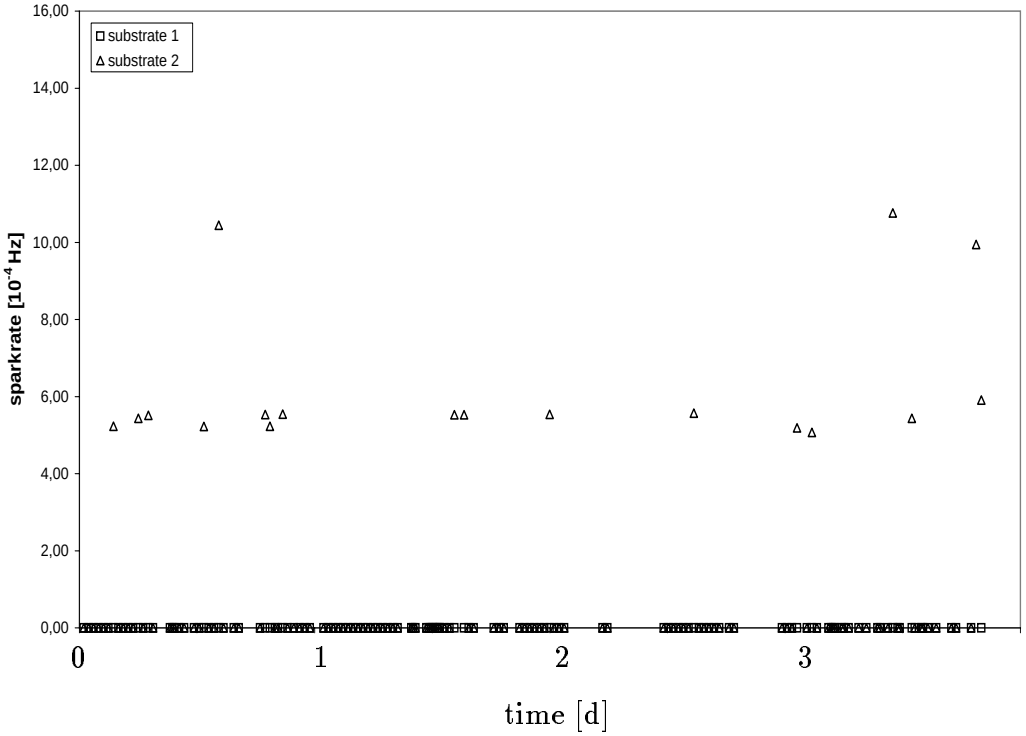

Figure 7.26: Sparking rate as a function of time during the margin period for module 17, at high and low intensity.

7.9 Conclusions

The aim of this chapter was to study the MSGC+GEM detector, foreseen to equip the CMS forward tracker and to demonstrate the reliability of this technology in LHC-like irradiation conditions.

The robustness of 18 MSGC+GEM modules has been investigated in experimental conditions close to what is expected at the Large Hadron Collider. We have proven the stability of operation of these counters by studying their behaviour during five weeks in a high intensity pion beam of momentum 350 MeV/c. The counters were operated at their working point, that is an SNR of 37, which would lead to a detection efficiency of 98% when using an electronics working in deconvolution mode. The rate of sparks induced by heavily ionizing particles was modest, less than 10^{-3} Hz, and the accumulated strip loss remained well below the limit imposed by the CMS collaboration. Extrapolation to 10 years of operation at LHC shows that this strip loss would result in a negligible loss of detection efficiency and to a slight degradation of the spatial resolution in less than 4% of the total covered area.

We have shown that the MSGC+GEM counters equipped with a fast front-end electronics working in peak mode reach 98% of detection efficiency at an SNR of 17. This working point already gives a factor 2.2 for the safety margin. This also shows that fast filtering as deconvolution is not suited for a detector for which the signal induction on the anode is so slow. Moreover it has been shown that MSGC+GEM modules could safely be

operated up to three times the working point without noticeable increase of the sparking rate.

Over the milestone period, up to 35% SNR variations have been observed in several modules. No clear correlations have been seen with either the atmospheric pressure, the temperature or the beam intensity. However a constant increase of noise is observed. This noise increase could be attributed to the use of non radiation hard preamplifiers.

Gain variations up to 20% have been observed between counters working at the same settings. They are attributed to a large sagitta of the GEM foil for a few counters that was measured to be as large as 1.0 mm. Although these large sagitta did not prevent the modules to be operated at the working point during 376 hours at high intensity, the GEM mounting should be improved for uniformity purpose.

We have also proven that the low transparency ($\sim 60\%$) of the CERN GEM's, operated with a drift field of ~ 5 kV/cm, did not prevent the MSGC+GEM to be operated at an SNR of 37 during the entire test period.

To conclude is has been demonstrated that the MSGC+GEM is a valid technology for tracking detectors at high rate of highly ionizing particles. The mechanical assembly has to be improved to minimize the GEM sagging and to obtain a better uniformity of the detector response. It is also important to invest a fast electronics minimizing the ballistic deficit. Finally the eighteen modules, representing 0.72 m^2 or about 1% of the forward MSGC tracker, have been built in only 2.5 months, confirming the readiness of such counters for mass production.

Chapter 8

The muon High Level Trigger

Event selection is one of the key issues at the LHC, as the events which reveal new physics are flooded by soft interactions occurring typically 10^{10} times more frequently. To select interesting events, the experiments rely on signatures which are present only in interesting physics and which can be easily detected. Muons with a high transverse momentum p_T provide one of these signatures.

This chapter describes a study of the CMS muon trigger performed with Monte Carlo simulations. We focus on the later stages of the trigger decision. In particular we have developed a tracking algorithm combining the central tracker and the muon chambers for the level-3 muon trigger.

In section 8.1 we first describe the constraints in which the CMS trigger system has to operate and the main sources of background to high p_T muons. The detailed simulation of the CMS detector used for the present work is described in section 8.2. Section 8.3 presents the different samples of simulated events used for these studies. Since the performance of the level-3 muon trigger strongly depends on those of the previous levels, some time is spent in section 8.4 to study the performance of the level-1 and level-2 muon triggers. In section 8.5 we describe in details the reconstruction algorithm that we propose for the level-3 muon trigger and we discuss its performance. In section 8.6 we study the background rates, at the level-1, 2 and 3, for an important event topology, i.e. one single muon in the final state.

8.1 Constraints on the trigger system

8.1.1 Constraints from the Data Acquisition system

The CMS trigger, described in section 2.5, consists of two main steps: the level-1 which is hardware-based and the High Level Trigger, HLT, which is software based. The level-1 trigger is designed to accept a maximum event rate of 100 kHz. To account for uncertainties in the estimates of the cross sections at high energies and in the knowledge of branching ratios, a large safety factor on the simulation of trigger rates is included. The level-1 trigger rate is thus limited to an average output rate of 25 kHz for the design of the level-1 trigger algorithms. This 25 kHz output rate has to be shared among both muon

and calorimeter triggers. Consequently we consider the muon level-1 trigger rate to be limited to $\sim$ 6 kHz.

The constraints on the HLT are less stringent. The output rate is limited by the amount of data that can be stored on disk and reprocessed offline. The limit is set to 100 Hz in CMS, equally shared between the muons, electrons/photons, jets and mixed objects streams. The HLT is further subdivided into the level-2, the level-3 and the level-4. Each level should provide a factor 10 of rate reduction. The main difference between the levels is the processing time. The level-2 should confirm the level-1 decision within 40 ms of CPU time. This time holds for processors of the year 2007. Assuming a factor 2 increase in CPU speed every 1.5 year, this is equivalent to $\sim$ 300 ms on a present Pentium III 1 GHz CPU. The level-3 decision should be taken in 60 ms ($\sim$ 500 ms on present CPU's) and the maximum HLT latency is one second.

The speed constraint is met by analyzing only a part of the detector data, and by running fast and approximate reconstruction algorithms. At level-2, only the data of the calorimeters and of the muon chambers are processed. At level-3, the data from the calorimeters and the muon chambers can be combined with tracks reconstructed in the central tracker.

8.1.2 Muon sources

The trigger is the start of the physics event selection process. In order to select the interesting phenomena and to reject a maximum of background, we have to look to event characteristics like the muon transverse momentum p_T. For this purpose, figures 8.1 and 8.2 show the muon rate as a function of the muon transverse momentum for different muon sources [146].

One of the main sources of high p_T muons is the high p_T tail of muons coming from soft interactions, called the minimum bias (M.B.), represented by closed marks in figure 8.1. Beyond $p_T = 30$ GeV/c the contributions from the minimum bias and the leptonic decay of the W boson are comparable. As an example, figure 8.2 shows the rate of the two muons coming from the Higgs decay channel $H \rightarrow WW \rightarrow \mu\nu\mu\nu$. Note that the rate of this interesting signal is 10^{-5} times smaller than the rate of muons coming from the minimum bias at a p_T value of 40 GeV/c. For this signal, the highest rate amounts to $\sim 10^{-5}$ Hz at high p_T values, 30 and 40 GeV/c for the two muons respectively. Comparing the muon p_T distributions, a high p_T threshold, above 20 GeV/c, would be adequate to have the highest possible trigger efficiency for muons coming from interesting signals together with the highest possible background reduction. With this threshold, the total background muon rate amounts to 100 Hz, as seen in figure 8.3 which shows the rate of muons above threshold as a function of the threshold on the muon transverse momentum for the minimum bias and the $W \rightarrow \mu + \nu$ channel at low luminosity (2×10^{33} cm^{-2}s^{-1}). The parent particle is also indicated for muons coming from the minimum bias. For muons with $p_T > 20$ GeV/c, the contributions from heavy quarks b/c and from the leptonic decay of the W boson are comparable, and the contribution from π/K decays is 10 times smaller.

Although the total background muon rate for $p_T > 20$ GeV/c is of the order of 100 Hz, the signal muon rate is negligible, $<10^{-4}$ Hz for $H \rightarrow WW \rightarrow \mu\nu\mu\nu$ [146]. Assuming that the level-1 muon trigger selects all muons with a $p_T > 20$ GeV/c and only these, it

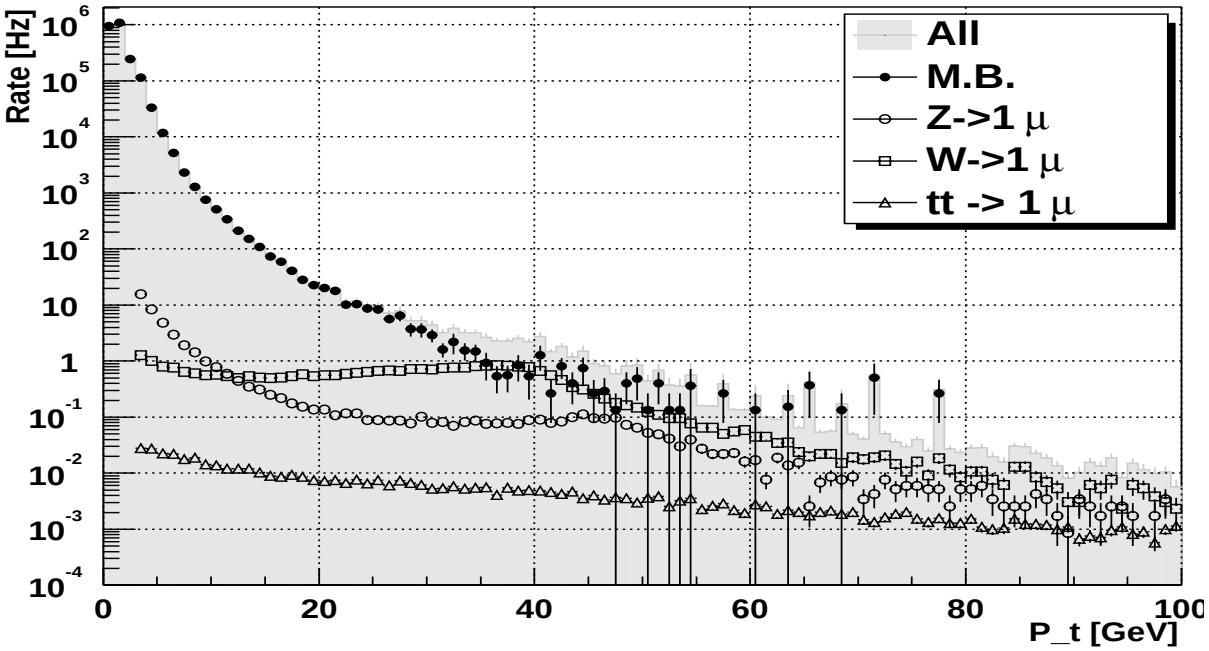

Figure 8.1: Muon rate as a function of the muon transverse momentum for muons coming from different sources at low luminosity (2×10^{33} cm^{-2}s^{-1}). The muon rate coming from the minimum bias (M.B.) is represented by closed marks [146].

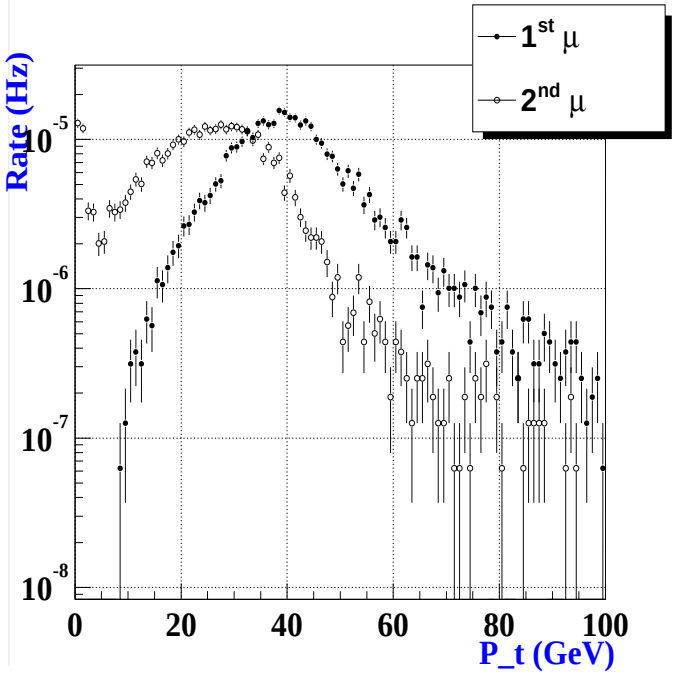

Figure 8.2: Muon rate as a function of the muon transverse momentum for muons coming from the Higgs decay channel $H \rightarrow WW \rightarrow \mu\nu\mu\nu$ at low luminosity (2×10^{33} cm^{-2}s^{-1})[146].

means that the HLT has to provide a rate reduction factor of 4 to reach an output rate of 25 Hz. In addition, due to the coarse p_T measurement at level-1, low p_T muons are also selected. At level-1, the p_T resolution is about 20% (see section 8.4) leading to a non zero

trigger efficiency for muons with a transverse momentum below the p_T threshold. This effect is shown in figure 8.4 which displays the level-1 trigger efficiency as a function of the muon transverse momentum for a p_T threshold of 30 GeV/c. The convolution of this

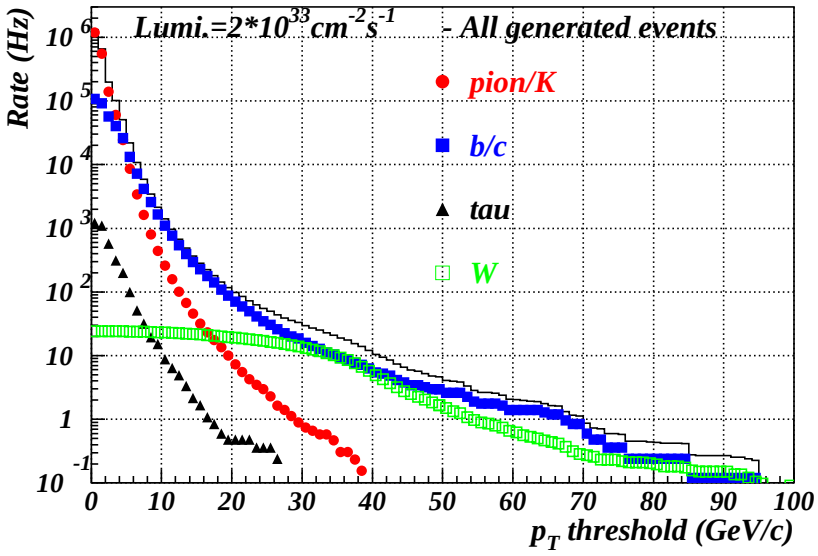

Figure 8.3: Rate of muons above threshold as a function of the p_T threshold for the minimum bias and the leptonic decay of the W boson at low luminosity (2×10^{33} cm^{-2}s^{-1}). The sum of both contributions is also shown (solid line).

trigger efficiency curve with the muon spectrum gives the cumulative rate of the level-1 trigger as a function of p_T for a threshold of 30 GeV/c, leading to a total muon trigger rate at level-1 of $\sim$ 1 kHz.

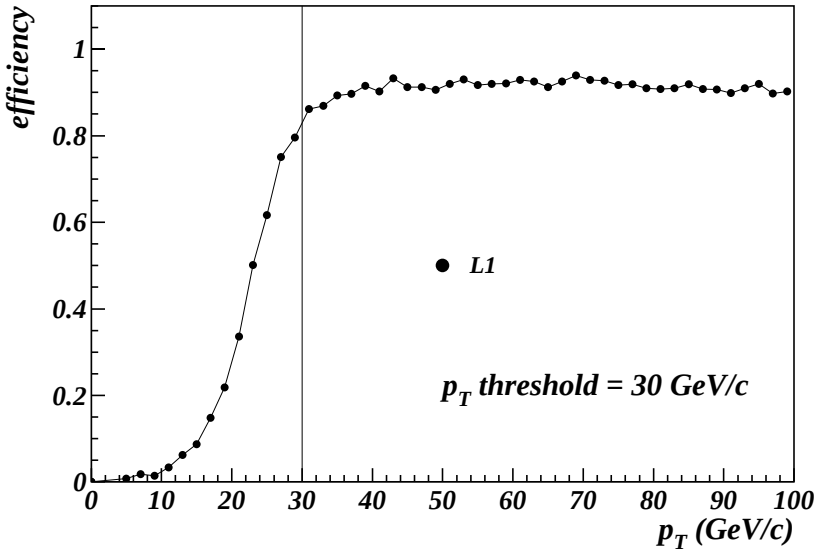

Figure 8.4: Efficiency at the level-1 muon trigger as a function of the muon transverse momentum for a p_T threshold of 30 GeV/c.

8.2 The CMS detector simulation

The performance of the CMS detector with an entire silicon inner tracker as described in section 2.4 is evaluated by means of simulation studies using CMSIM, the simulation program of the CMS detector and ORCA, the Object-oriented Reconstruction program for CMS Analysis [147]. The simulation program CMSIM is based on the GEANT simulation package [148]. This software is commonly used in high energy physics to describe the geometry of a detector and to simulate the interactions of particles with the detector material. The detector structure and sensitive elements being defined, the program follows the particles step by step, taking into account the energy lost by interactions with the detector material, and simulates the possible particle decays. For these studies, the energy cuts in GEANT are set to trace particles down to relatively low energies, for instance 10 MeV for muons in the inner tracker. Below these cuts, the particle range is considered as negligible and all the remaining energy is supposed to be deposited at the stopping point. The GCALOR hadronic package [149] has been used for a realistic simulation of hadronic interactions down to 1 MeV. In addition, in front of all muon chambers, over the latest 10 cm of material, multiple scattering, bremsstrahlung, Compton scattering and pair production processes are activated in the GEANT simulation with a low energy cut-off, 100 keV for muons, in order to have a realistic simulation of δ-rays and shower processes, which can produce spurious hits in the muon chambers.

After simulation of the particle trajectory through the CMS apparatus, the signal specific to each detector is simulated in all counters hit by the incident particle. The particle signals and the electronic noise are generated on the detector channels and neighbouring channels above threshold are grouped into clusters. The coordinates of the particle crossing points are then computed from these clusters. This step, called the digitization, corresponds to the generation of the raw data in the real experimental environment. The digitization is performed within the ORCA program [1].

In the digitization of the solid state detectors of the tracker, the signal is taken to be proportional to the energy deposited by the particle in the semiconducting material, computed by GEANT. In the muon system the digitization is different for the drift tube (DT), the Cathode Strip Chamber (CSC) and the Resistive Plate Chamber (RPC) (see section 2.4.1). In the DT chambers, the relation between the impact point position and the drift time is parametrized, according to beam tests of DT prototypes and simulation studies with the GARFIELD program (see reference [95] and section 4.5). The drift time is then converted into Time-to-Digital-Converter (TDC) counts. In the CSC digitization, we use the GEANT thin-layer approximation to model the energy loss in the gas: electrons produced in the gas by ionizing collisions along the muon trajectory or by δ-rays are transported to the neighbouring anode wire according to the local magnetic and electric fields. The electron attachment by $Ar/CO_2/CF_4$ gas molecules is taken into account. The avalanche multiplication in the vicinity of the anode is simulated by a Polya distribution. The analog signal is then computed using parameterizations of the amplifier and shaper response. For the RPC digitization, after the computation of the energy deposited by the incident particle, the avalanche growth is simulated as well as the signal formation taking into account the time response fluctuation coming from the front-end electronics.

[1] Unless mentioned otherwise the ORCA.6.1.1 release has been used for this work

8.3 The Monte Carlo data samples

All the studies presented in this work have been performed with several samples of events with at least one muon in the final state with a transverse momentum, p_T, high enough to reach the muon system, i.e. 3 and 1.5 GeV/c in the barrel and in the endcap regions respectively. These samples are further denoted as generated single muon samples. All the samples have been generated with the PYTHIA generator program [150]. The event kinematics (muon p_T and η distributions, characteristics of the underlying event) is defined by the PYTHIA input parameters.

A large part of these samples is devoted to the main source of muon background which are the muons coming from the minimum bias events having at least one muon in the final state. Although the single muon triggers will have rather high p_T thresholds, typically above 10 GeV/c, it is important to simulate muons with lower transverse momentum, produced at high rate (a few MHz), which leave signals in the muon chambers and can potentially trigger the muon data acquisition system of CMS. A sample of $\sim$ 200,000 minimum bias events has thus been used.

Another source of muons, particularly important in the high p_T region, $p_T \geq 30$ GeV/c, is the muons originating from W's, either directly from $W \rightarrow \mu + \nu$, or in the decay chain of $\tau's$ or hadrons. Therefore a sample of 10,000 leptonic W boson decay events has been used to measure the acceptance of the HLT muon trigger (see figure 8.3).

To estimate the performance of the muon trigger in terms of efficiency, resolution and pulls, we have used a sample of 60,000 events with one muon generated from the interaction point, distributed uniformly over the transverse momentum range, $5 < p_T < 100$ GeV/c, over the pseudo-rapidity range, $|\eta| < 2.4$, and over the azimuthal angle ϕ.

The trigger efficiency of true muons may be affected by the presence of other events occurring in the same or nearby bunch crossings. Indeed the average number of minimum bias events for each bunch crossing will amount to 3.4 and 17.3 at low (2×10^{33} cm^{-2}s^{-1}) and high (10^{34} cm^{-2}s^{-1}) luminosity respectively. To evaluate this effect, minimum bias events, with no muon in the final state and randomly chosen, are added to the event with a muon at the digitization level; this procedure is further called pile-up. In the trigger rate studies presented in this work, only the low luminosity phase has been investigated. For the evaluation of the processing time of the algorithms, a sample of 2,000 $W \rightarrow \mu + \nu$ events at high luminosity has been used.

8.4 The level-1 and level-2 muon triggers

Before discussing in detail the performance of the third muon trigger level, it is important to summarize the main features of the levels 1 and 2, which can affect the results of the level-3. Therefore we give an overview of the reconstruction algorithms as well as of the performance in terms of efficiency, resolution on the muon track parameters and pulls, for both levels.

8.4.1 The level-1 muon trigger

The level-1 muon trigger system of the CMS experiment will be implemented using specially designed hardware. It is based on the three independent muon detectors (see section 2.4.1): the Drift Tubes in the barrel region ($|\eta| < 1.15$), the Cathode Strip Chambers in the endcap region ($1.04 < |\eta| < 2.4$) and the Resistive Plate Chambers in almost the whole acceptance region of the muon system ($|\eta|$ <2.1). The complementary features of the three subsystems provide a muon selection with an efficiency of 95%, and an unambiguous bunch crossing identification. Indeed the muon system combines the good spatial resolution of the DT's and CSC's, $\sim 200\mu$m, and the very good time resolution, ~ 3 ns, of the RPC's which are dedicated trigger detectors. Note also that the multilayer structure of the DT's and CSC's provides the possibility of an effective noise rejection.

The two subsystems made of DT + RPC detectors in the barrel part and CSC + RPC detectors in the forward are processed in parallel and deliver independently the information about the detected particles to the Global Muon Trigger, GMT (see figure 2.13). Up to four muon candidates are selected by each subsystem. The GMT combines the four highest p_T muons from the barrel and the forward. The GMT performs a matching based on the proximity of the candidates in (η,ϕ) space. If two candidates are matched, their parameters are combined to give optimum precision. Finally the muon candidates are sorted with respect to their momentum and the four highest p_T muons in the entire CMS detector in every bunch crossing are transmitted to the Global Trigger, GT. The two extreme cases of such combination would be to apply a logical .OR., maximizing the efficiency, and the logical .AND., maximizing the background rejection. In the current simulation, the final GMT selection applies a more sophisticated algorithm, using the quality information associated to the tracks from the regional triggers. The quality of a detected muon corresponds to the number of hits in coincidence. So a muon candidate is accepted if it is confirmed independently by the Drift Tube or the Cathode Strip Chamber and the Resistive Plate Chambers, regardless of the quality of the muon track. If the muon candidate is detected by only one type of muon detectors, a η dependent quality criterion is applied.

Figure 8.5 shows the level-1 muon trigger efficiency as a function of the pseudo-rapidity, η, for the Global Muon Trigger. The efficiency is defined as the probability to find at least one muon of any transverse momentum for events in which one muon is generated. For this study we have used the Monte Carlo data sample of 60,000 single muons described in section 8.3. The level-1 efficiency is above 97% in a large part of the η range. The efficiency dips observed at $|\eta| \simeq 0.25$ and in the range $0.75 < |\eta| < 1$ are due to the geometric acceptance of the muon system. For $\eta > 2.1$ the efficiency is slightly lower because the CSC's are the only detectors present at this pseudo-rapidity. Figure 8.6 shows the level-1 muon trigger efficiency as a function of the muon transverse momentum p_T. The level-1 efficiency, above 97%, is uniform over the entire range $5 < p_T < 100$ GeV/c. The number of duplicate tracks is of the order of 0.2%. Since in this sample there is only one muon, the duplicate track can be produced by the hit multiplicity which can be due to Bremsstrahlung. The trigger reconstructs two tracks, close to each other, and with identical parameters.

Since the muon transverse momentum resolution determines the sharpness of the p_T cut, it is important to study the resolution on this parameter. However the reconstruction procedure leads to a Gaussian residual distribution for $1/p_T$ and not p_T. Therefore the

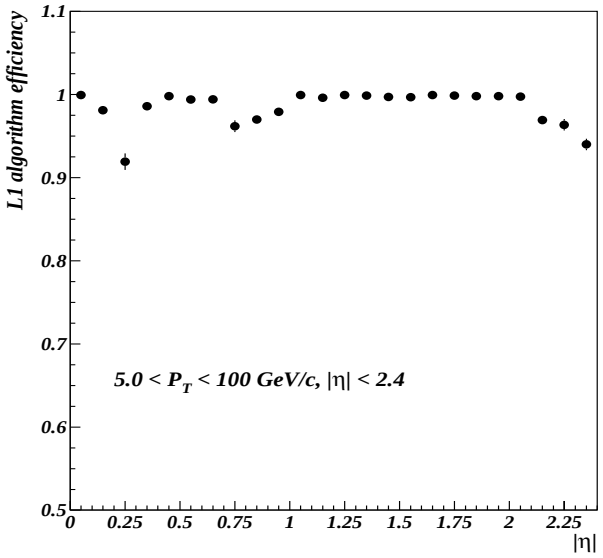

Figure 8.5: Level-1 muon trigger efficiency as a function of η for single muons generated with uniform p_T, η and ϕ distributions.

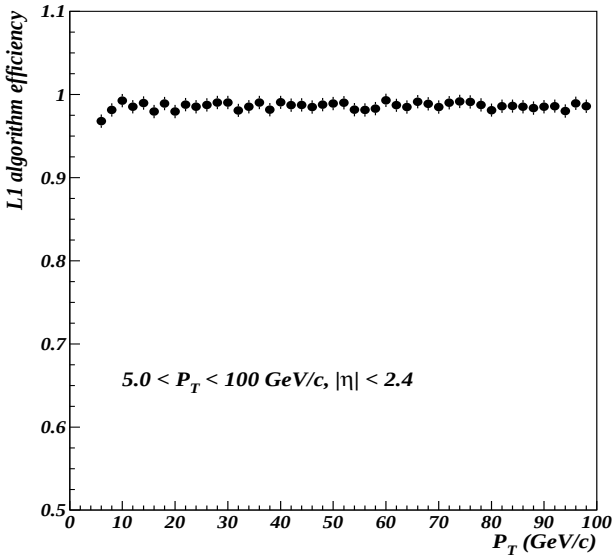

Figure 8.6: Level-1 muon trigger efficiency as a function of the muon transverse momentum for single muons generated with uniform p_T, η and ϕ distributions.

transverse momentum resolution is calculated from the distribution of the $1/p_T$ residual:

$$\frac{\Delta p_T}{p_T} = \frac{1/p_T^{rec} - 1/p_T^{gen}}{1/p_T^{gen}}, \tag{8.1}$$

where p_T^{rec} and p_T^{gen} represent the muon transverse momentum at the trigger reconstruction and at the generation level respectively. For muons generated at a single transverse momentum, this distribution should be Gaussian.

Figures 8.7 a), b) and c) show the $1/p_T$ residual for different pseudo-rapidity ranges, $|\eta| < 0.8$ (a), $0.8 < |\eta| < 1.2$ (b) and $|\eta| > 1.2$ (c), corresponding to muons detected in the barrel (a), in the transition region (b) and in the endcap (c). This study is performed using the single muon sample (see section 8.3). The $1/p_T$ resolution at level-1 amounts to 14.7%, 22.9% and 23.0% in the barrel, the transition and the endcap region respectively. The degradation of the resolution with η is due to the larger amount of material traversed by the incident muon. Note that the distributions are not peaked at zero. This is due to the fact that the level-1 output is biased because it is defined at 90% efficiency. This means that the p_T estimate is increased by $2.5 \times \sigma$ in order to achieve 90% efficiency for any given threshold. In the $1/p_T$ residual distribution 90% of the events have a Δp_T value smaller than zero. Note also the presence of non-Gaussian tails especially in the overlap and in the endcap regions, because of the increase of the amount of material. The presence of non-Gaussian tails are due to events suffering from large scattering collisions, from large energy loss in the iron or from hard bremsstrahlung, which can skew the momentum measurement towards lower p_T. The $1/p_T$ resolution and the presence of non-Gaussian tails is also responsible for the selection of a large fraction of low p_T muons by the level-1 muon trigger. This effect, called feed-through, is illustrated in figure 8.8, which shows the p_T spectrum of the generated muons (shaded area) and of the muons selected by the level-1 muon trigger for a p_T threshold set to 20 GeV/c. We clearly observe that a large

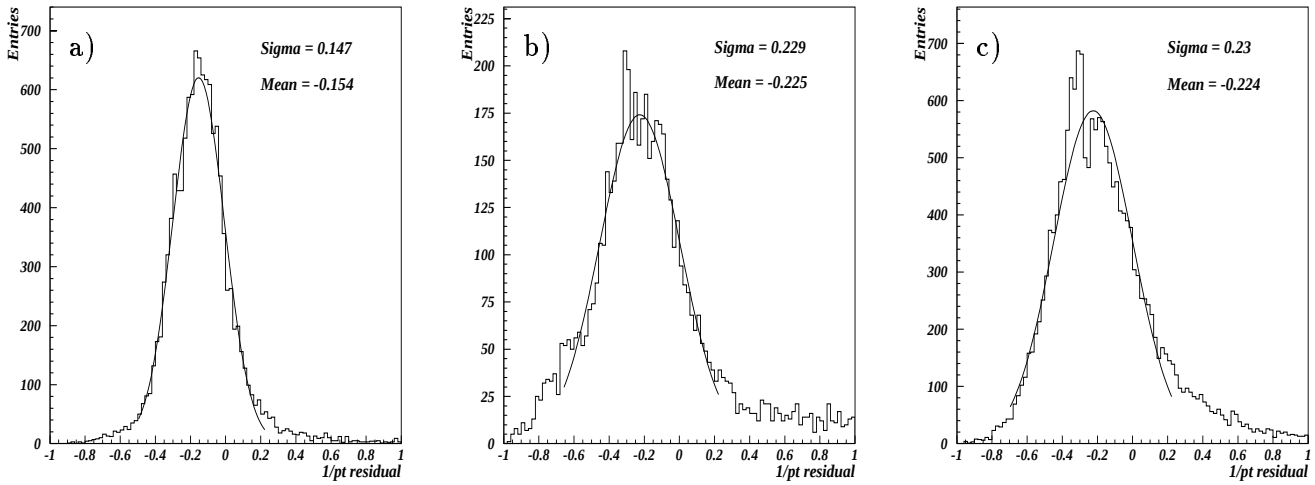

Figure 8.7: Inverse transverse momentum residual for single muons detected in the barrel (a), the transition (b) and the endcap (c) regions.

fraction of the muons selected by the level-1 is given by muons with $p_T < 5$ GeV/c. Due to the high rate of low p_T muons, up to 1 MHz (see figure 8.1), this contribution will dominate the rate of muons selected by the level-1.

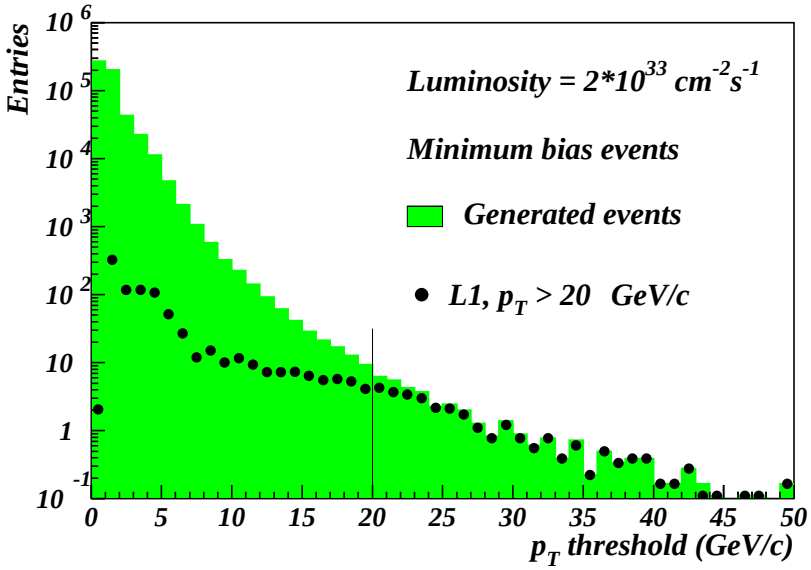

Figure 8.8: Transverse momentum spectrum for the generated muons (shaded area) and for the muons selected by the level-1 muon trigger with a p_T threshold of 20 GeV/c.

8.4.2 The level-2 muon trigger

The level-2 is the first step of the High Level Trigger. As the level-1, the level-2 muon trigger uses only the data from the muon chambers to confirm the muon candidates but it is software-based and will be implemented on commercial processors. Given the longer time allowed for the level-2 trigger, 40 ms instead of 3.2 μs for the level-1, the level-2 can perform a complete track fitting using all the muon detector data. This complete track fitting should therefore improve the p_T estimation with respect to the level-1. However to limit the CPU time, the reconstruction is localized in the region of interest where the level-1 has found a muon candidate. The level-2 muon reconstruction, briefly described in the next section, is performed according to a general procedure, adopted for tracking in the silicon inner tracker of CMS.

Level-2 muon reconstruction

The level-2 algorithm uses the reconstructed hits built from the digitized signals in the muon system, and builds tracks using the Kalman filtering technique [151] [152]. The Kalman Filter is an iterative procedure which allows to estimate the parameters describing the state of a system from a set of measurements. The filter proceeds iteratively from a coarse estimate of the track parameters and updates these parameters by including the information of the successive detection layers, one by one. At a given detection layer, the track parameters are propagated to the next layer according to the equations of motion for charged particles in a magnetic field, taking into account the energy loss in the detector material. On this layer, the coordinates of the hits compatible with the propagated track parameters are combined to these parameters to provide a new estimate with a better accuracy than at the previous detection layers. Therefore the track parameters are known with optimal precision only after the last measurement has been included in the fit.

The muon track reconstruction algorithm for the level-2 trigger starts with the results of the level-1 Global Muon Trigger. The starting point, called seed, consists of a state vector composed of the position, the direction and the momentum of the muon at the second muon station, either in the barrel or in the endcap. After the seeding the algorithm progresses detection layer per detection layer going outwards and collecting the detector hits. Note that for the DT's and CSC's the hits consist in track segments. Indeed, since the muon chambers are assembled to form super-layers (see section 2.4.1) a fast local pattern recognition using the reconstructed hits from digitized signals in the DT's and CSC's is performed. This local pattern recognition estimates the muon position and direction in two or three dimensions. At the outermost muon station, the propagation is reversed and the trajectory is filtered by rejecting bad hits according to tighter cuts. Finally the level-2 delivers the track parameters and their errors, with optimal precision, at the innermost muon station. These parameters can be used for extrapolation, matching or global fitting with the inner tracker, in the subsequent trigger stage. To improve the transverse momentum resolution, a constrained fit assuming that the muon candidate originates from the interaction region is performed, using the muon system alone. The beam spot size, with a transverse and longitudinal dimension RMS of 15 μm and 5.3 cm respectively, is assumed as the uncertainty on the primary vertex position. If this extrapolation fails, the muon candidate is discarded from further processing.

The level-2 performance

We first study the algorithm efficiency of the level-2 muon reconstruction with respect to the level-1. The algorithm efficiency is defined as the probability to reconstruct a muon of any transverse momentum at the level-2 for simulated events which have been accepted by the Global Muon Trigger. Figures 8.9 and 8.10 show the level-2 algorithm efficiency as a function of η and as a function of p_T respectively. These studies have been performed with the Monte Carlo sample of single muons, described in section 8.3. The algorithm efficiency is very high, close to a 100% over the whole η range. This value is $\sim 4\%$ larger than the efficiency reported in reference [153]; this is due to the addition of the RPC data in the current version of the level-2 muon reconstruction algorithm. In figure 8.10 we can also observe the very high efficiency, close to a 100%, for muons with a transverse momentum larger than 7 GeV/c.

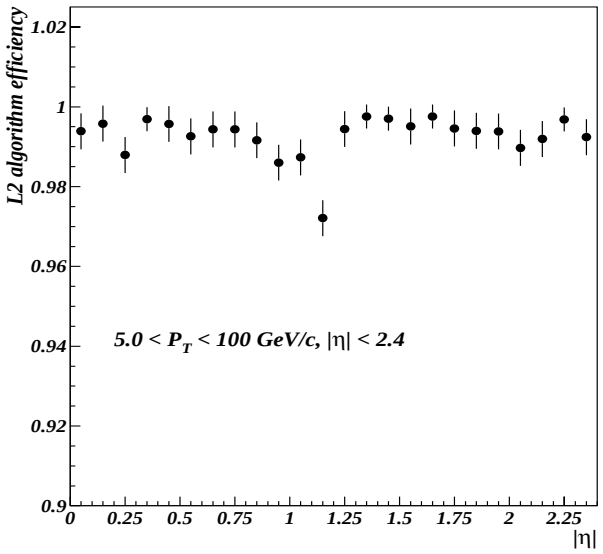

Figure 8.9: Level-2 muon trigger algorithm efficiency as a function of η for single muons generated with uniform p_T, η and ϕ distributions.

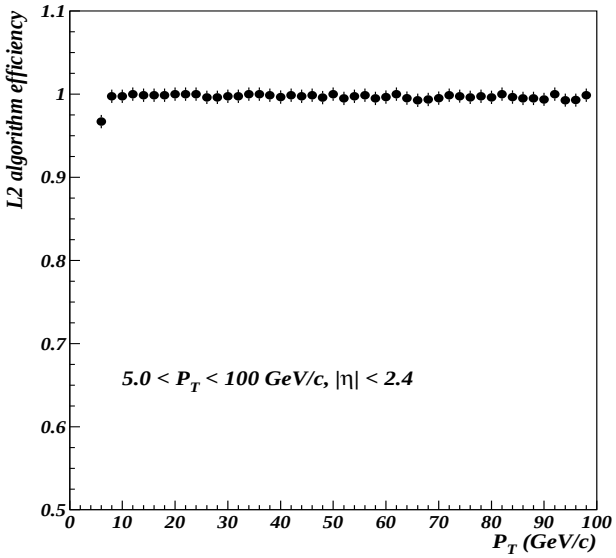

Figure 8.10: Level-2 muon trigger algorithm efficiency as a function of p_T for single muons generated with uniform p_T, η and ϕ distributions.

The resolution on the transverse momentum is expected to improve at the level-2 with respect to the level-1, since the muon reconstruction is based on a more elaborated algorithm with a complete track fitting using all the information of the muon chambers. The $1/p_T$ residual, defined according to Eq. 8.1, is shown in figures 8.11 for different pseudo-rapidity ranges, $|\eta| < 0.8$ (a), $0.8 < |\eta| < 1.2$ (b) and $|\eta| > 1.2$ (c), corresponding to muons detected in the barrel (a), the transition (b) and the endcap (c). The $1/p_T$ resolution is 17.5%, 23.2% and 24.8% for the barrel, the transition and the endcap region respectively to be compared with the results of the level-1, 14.7%, 22.9% and 23.0% respectively (see section 8.4.1). These results are not satisfactory and are not in agreement with the $1/p_T$ resolution obtained with previous ORCA releases which provide a $1/p_T$ resolution of 12.5%, 16.3% and 20% for the barrel, the transition and the endcap regions respectively at level-2. The difference is attributed to reconstruction errors in this version of the level-2 algorithm. Although on average the level-2 $1/p_T$ resolution is worse than at

level-1, it improves at low transverse momentum. For $p_T < 10$ GeV/c, the $1/p_T$ resolution is 2% better at level-2 than at level-1, as shown in figure 8.12 which displays the inverse transverse momentum residual at the level-1 (a) and at the level-2 (b) muon trigger. As observed for the level-1, the degradation of the $1/p_T$ resolution with η is due to the combined effect of the presence of material in front of the CSC's, with respect to the barrel chambers and of the smaller integrated magnetic field.

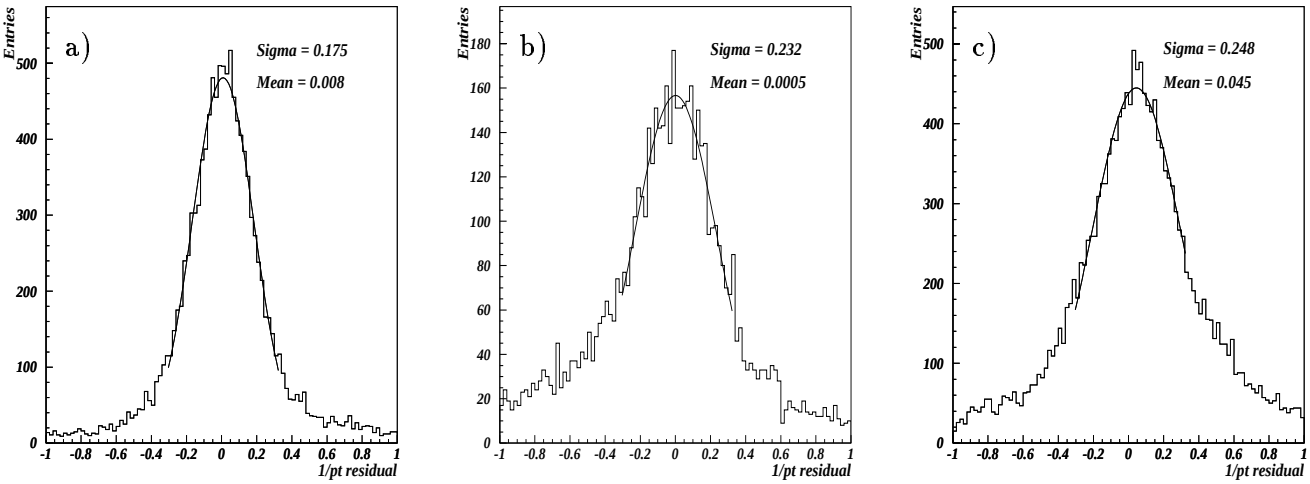

Figure 8.11: Inverse transverse momentum residual for single muons accepted by the level-2 trigger, in the barrel (a), the overlap (b) and the endcap (c) regions.

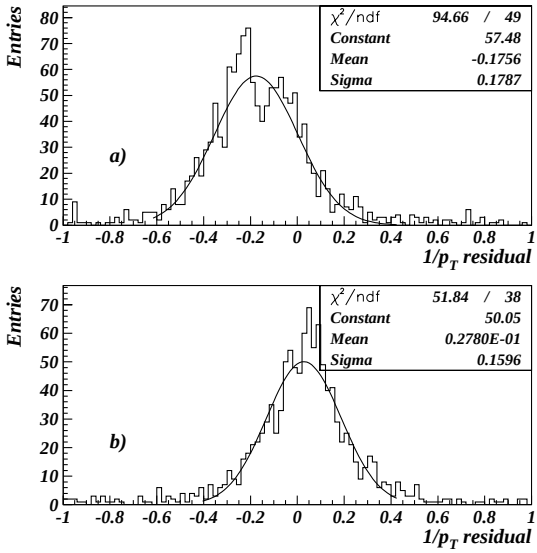

Figure 8.12: Inverse transverse momentum residual at level-1 (a) and level-2 (b) for muons with a transverse momentum smaller than 10 GeV/c.

The quality of the reconstructed muon tracks is checked with the pulls on the different

track parameters, $1/p_T$, η, and ϕ. The pulls are defined as

$$Pull(x_i) = \frac{x_i^{rec} - x_i^{gen}}{\sigma(x_i^{rec})}, \tag{8.2}$$

where x_i^{rec} and x_i^{gen} represent the reconstructed and generated values of the i^{th} track parameter respectively and $\sigma(x_i^{rec})$ is the error on the reconstructed parameter, i.e. the square root of the corresponding diagonal element of the parameters covariance matrix. Figure 8.13 shows the distribution of the $1/p_T$ pulls for muon tracks reconstructed at the

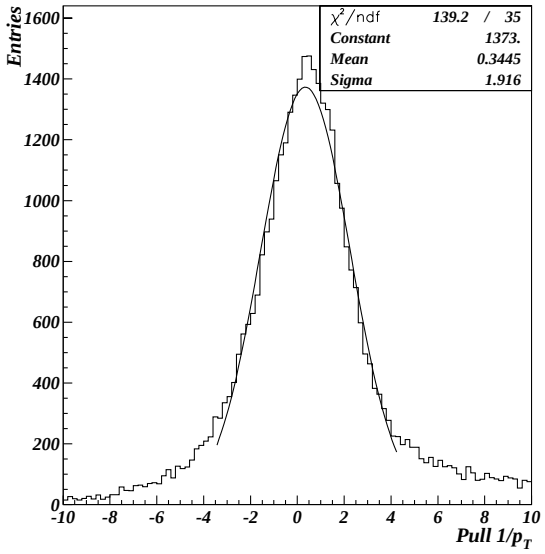

Figure 8.13: Distribution of the $1/p_T$ pulls for muon tracks reconstructed at the level-2 with the ORCA.6.1.1 release.

level-2 with the ORCA.6.1.1 release. The average value of $\sim 0.33 \pm 0.02$ is not compatible with zero. For an ideal reconstruction the mean and the standard deviation of the pull distribution should be equal to 0.0 and 1.0 respectively. Clearly this is not the case; the standard deviation of the Gaussian curve fitted to the central part of the $1/p_T$ pull distribution is close to 2, indicating that the covariance matrix is not correctly estimated. Moreover the distribution exhibits large non-Gaussian tails. The large tails indicate unsolved reconstruction errors, like the presence of outliers in the reconstructed tracks, or that physical effects are not properly taken into account in the estimation of the track parameter errors.

8.5 The level-3 muon trigger

The level-3 muon trigger is based on the combination of the data from the muon chambers and from the silicon tracker. The better spatial resolution of the silicon detectors should improve the resolution on the track parameters and should provide sharper cuts with respect to the previous trigger levels. The transverse momentum resolution achieved by combining the muon system with the inner tracker is expected to improve by a factor 10 for $p_T < 1$ TeV. In this range, the precision is determined by the tracker; the muon chambers

performance being spoiled by multiple scattering in the iron yoke. The reconstruction algorithm that we have implemented is based on the code developed by the CMS tracker group to reconstruct particle trajectories in a high hit multiplicity environment. This code is adequate for detectors arranged in detection layers, like the tracker and the muon systems, and has shown good tracking performance [154].

The algorithm that we have developed is based on the idea that the muon system and the tracker are similar detectors. This similarity is already exploited at large in the ORCA reconstruction software[2].

A part of the tracker code which was optimized with great care is the search for measurements, called hits, compatible with a trajectory. This pattern recognition is affected by the high hit multiplicity at LHC and dominates the time spent in the track reconstruction. We have used a powerful tracker pattern recognition code to perform the combined muon reconstruction in the tracker and in the muon system. This approach differs from the existing level-3 algorithm described in reference [157]. We will thus first describe our algorithm in some details with special emphasis on the differences with the existing code, before discussing its performance in terms of efficiency, track parameter resolutions and computing time.

8.5.1 The level-3 muon reconstruction

The reconstruction algorithm that we propose relies on the interface common to the tracker and the muon chambers, in order to treat both systems as a whole. This present the advantage to avoid code duplication, to guarantee a common interface as well as an easier code maintenance. The main idea is to start the muon trajectory at the innermost muon chamber, according to the level-2 output. This starting point, called seed, is obtained after a complete track fitting in the muon chambers performed at the level-2. Our level-3 algorithm carries on the Kalman filtering towards the interaction point, inside the central tracker. This approach is equivalent to make a complete fit in the tracker and the muon systems.

The track reconstruction consists in four steps:

- the seed generation provides initial estimates of the track parameters;
- the trajectory building grows each seed, detection layer by detection layer into one or more trajectory candidates;
- the trajectory cleaning removes duplicate tracks;
- the trajectory smoothing performs a refitting of the remaining tracks in order to get the optimal track parameters all along the trajectory.

The seed generation

For each muon candidate delivered by the level-2 muon trigger, the algorithm creates a seed in the innermost muon chamber hit by the muon. The seed consists of a set of starting parameters which define the position, the direction, the estimation of the momentum of the muon candidate as well as the covariance matrix of these parameters in this innermost muon chamber.

[2]The use of Object-Oriented programming in C++ renders this more effective

The trajectory building

The trajectory building is based on a Kalman filtering. The principle is the following. Starting from a coarse estimate of the track parameters in the innermost muon layer, provided by the level-2 muon trigger, the filter proceeds iteratively and includes the hits of the successive tracker detection layers one by one. From the current layer of a growing trajectory candidate, the trajectory builder first asks for the next possible detection layers. For each of these layers, it asks for the hits that are compatible with the current trajectory state extrapolated onto this layer. The algorithm creates one trajectory candidate per compatible hit found plus one candidate which does not include any hit in this layer to account for possible detection inefficiencies. For each compatible hit, the trajectory is updated and the builder proceeds with the next compatible layers.

As the number of trajectory candidates grows exponentially as the trajectory builder proceeds, only the candidates with the smallest χ^2 are kept at each layer, a penalty being added to the χ^2 for each missing hit. In the current implementation of the level-3 muon reconstruction algorithm, the number of trajectory candidates allowed at each layer is limited to 30. Moreover a trajectory with more than one missing hit is also discarded from the reconstruction. Note that since duplicate tracks are only removed after the trajectory building, at the trajectory cleaning step, this could lead to some waste of time. It has been shown [154] that with a reconstruction algorithm using all compatible hits found in a layer[3] to update the trajectory state, the CPU time consumption per track is about three times smaller. In this algorithm, called Deterministic Annealing Filter (DAF) [155], only one trajectory candidate is grown per seed.

A crucial step in the trajectory building is the transition from one detection layer to another and especially between the innermost muon detection layer and the first outer tracker layer. Indeed these layers are separated by the CMS coil and the calorimeters. The innermost muon detection layer and the outermost tracker layer are separated by a distance of 3 m at $\eta = 0$ and up to 5.5 m at $\eta = 1.2$, which corresponds to 120 and 160 radiation lengths respectively. The propagation of the track parameters between two layers is performed by a propagator which extrapolates the trajectory state taking into account the magnetic field and the material in the CMS apparatus. The first propagation between the muon and the tracker system is performed with the GEANE numerical algorithm [156], which takes into account accurately the magnetic field non-uniformities and the material. This propagator is also used by the level-2 muon reconstruction code. For all the propagation of track parameters between different layers inside the CMS inner tracker, the level-3 trajectory builder uses a very fast, reasonably precise implementation optimized for the tracker. It is based on the approximation that the magnetic field is almost uniform inside the tracker and that all the material is concentrated on the detection surfaces.

The trajectory cleaning

More than one track candidate can be reconstructed for each level-2 muon candidate. In this case the algorithm will keep the trajectory with the larger number of hits found in the tracker.

[3]The weight of each hit is given by an assignment probability depending on the distance between the hit and the trajectory state.

The trajectory smoothing

In the filtering process, the track parameters are known with optimal precision after the last measurement has been included in the fit. Therefore, after the trajectory building, the parameters of the reconstructed tracks are re-computed all along the track. This step, called smoothing, provides optimal track parameters at any detection layer.

8.5.2 Comparison with the existing level-3 algorithm

The existing reconstruction algorithm written for the level-3 muon trigger is based on the same steps but differs from the one presented in this work in the seed generation step. In the existing level-3 algorithm the seed generation is not automatic and does not use in an optimal way the level-2 fit. The existing algorithm starts from the innermost muon chamber and propagates the track parameters of the level-2 muon candidate towards the tracker volume, using the GEANE propagator. This extrapolation provides the track parameters on a virtual cylindrical surface corresponding to the tracker outer surface. The seeding consists first in finding the detection layers of the tracker compatible with this extrapolated measurement. The number of compatible layers is limited to three for each level-2 muon candidate. Afterwards, the algorithm finds the compatible hits in each compatible layer. Each compatible hit is considered as seed for the muon trajectory to be built in the tracker. For each seed the trajectory builder proceeds in an iterative way as previously described. After the trajectory building, the smoothing performs a refitting including also the hits from the muon detectors. In addition, after the smoothing, a trajectory cleaning is required in order to reduce the number of duplicate tracks since more than one track may be found for a given level-2 muon candidate. The number of candidates growing exponentially as the trajectory builder proceeds, this could result in a waste of time compared to our algorithm in which exactly one seed is generated per level-2 candidate.

8.5.3 The level-3 performance

Track parameter resolutions

Figure 8.14 shows the inverse momentum residual distribution obtained with the proposed level-3 muon reconstruction algorithm for different pseudo-rapidity ranges, $|\eta| < 0.8$ (a), $0.8 < |\eta| < 1.2$ (b) and $|\eta| > 1.2$ (c). The $1/p_T$ resolution of $\sim 1.2\%$, 1.9% and 2.3% for the barrel (a), transition (b) and endcap region (c) respectively is about one order of magnitude better than the resolution reached at level-2. The $1/p_T$ resolution obtained with the existing level-3 code on the same muon sample is 1.8%, 2.0% and 2.4% for the barrel, transition and endcap regions respectively. The slight improvement of the $1/p_T$ resolution obtained with the algorithm presented in this work is attributed to the fact that 15% of the reconstructed tracks have one additional measurement in the tracker. This is illustrated in figure 8.15 which shows the distribution of the number of hits found in the inner tracker for the existing algorithm (a) and the algorithm proposed in this work (b).

Figure 8.16 shows the inverse transverse momentum resolution as a function of the muon transverse momentum for the barrel ($|\eta| < 0.8$) and endcap ($|\eta| > 1.2$) regions.

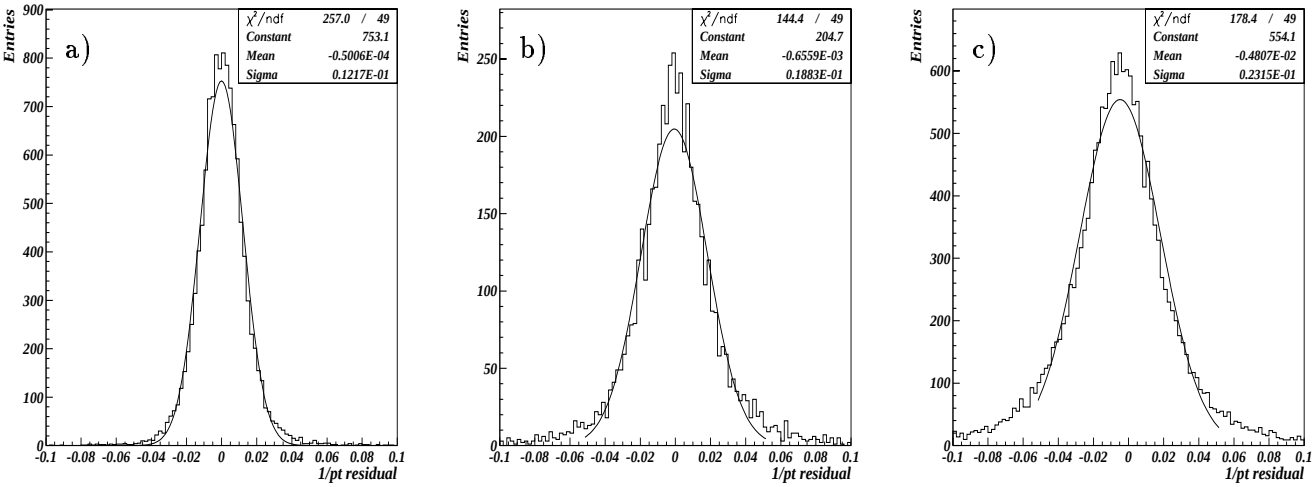

Figure 8.14: Inverse transverse momentum resolution for muons accepted by the level-3 trigger, in the barrel (a), the overlap (b) and the endcap (c) regions.

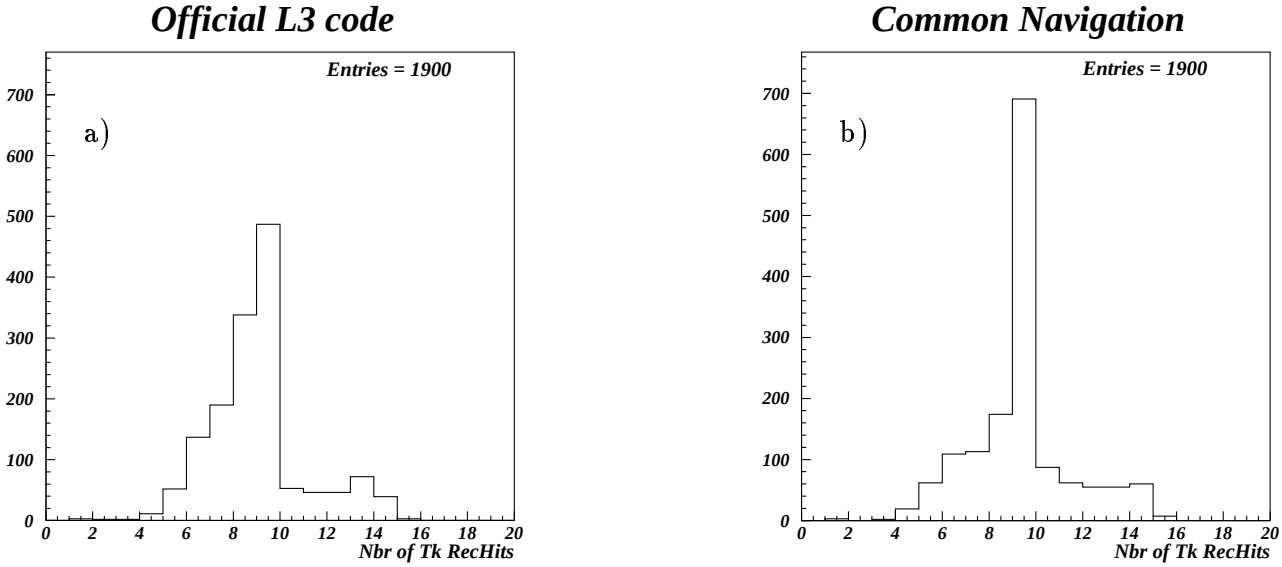

Figure 8.15: Distribution of the number of hits found in the inner tracker for the existing algorithm (a) and the algorithm presented in this work (b).

The resolution degrades almost linearly with p_T since the intrinsic momentum error of the tracker detectors increases with the particle transverse momentum (see section 2.4.4). The resolution is also systematically worse in the endcap region because of the larger thickness of material traversed and of the smallest length of the trajectory projected in the tracker transverse plane. This is illustrated in figure 8.17 which shows the $1/p_T$ resolution as a function of the pseudo-rapidity. The number of reconstructed hits associated to the simulated track is also shown. The best $1/p_T$ resolution is reached in the barrel region ($|\eta| < 0.8$) where the $1/p_T$ resolution is rather constant with a value of $\sim 1.2\%$. This

behaviour is due to the fact that the particle trajectory has a maximum projected path in the tracker transverse plane and traverses a small amount of material. The thickness of the CMS tracker amounts to ~ 0.3 and ~ 1.0 radiation lengths at $|\eta| < 0.2$ and $|\eta| = 1.5$ respectively (see figure 2.11).

The $1/p_T$ resolution degradation at $\eta > 1.5$ is due to the fact that the muons exit the tracker before reaching the maximum tracker radius of 1.1 m. The degradation of the $1/p_T$ resolution at $\eta = 1.2$, which corresponds to the transition region between the barrel and the endcap parts of the tracker, is due to the smaller number of reconstructed hits found to reconstruct the muon trajectory in the tracker, 7.5 instead of 11 in the barrel. The lower number of reconstructed hits is due to the smaller number of detection layers crossed by the muon, 11.6 on average at $\eta = 1.2$ instead of 13.3 for $\eta < 0.8$. In addition the reconstruction in the transition region is more problematic since the track reconstruction combines measurements from barrel detectors and from endcap detectors. However these results are close to the performance obtained with the CMS tracker alone reported in the Technical Proposal [18]: the $1/p_T$ resolution amounts to $\sim 0.66\%$ and 1.5% at $\eta = 0.1$ and 2.0 respectively for muons with a transverse momentum of 10 GeV/c.

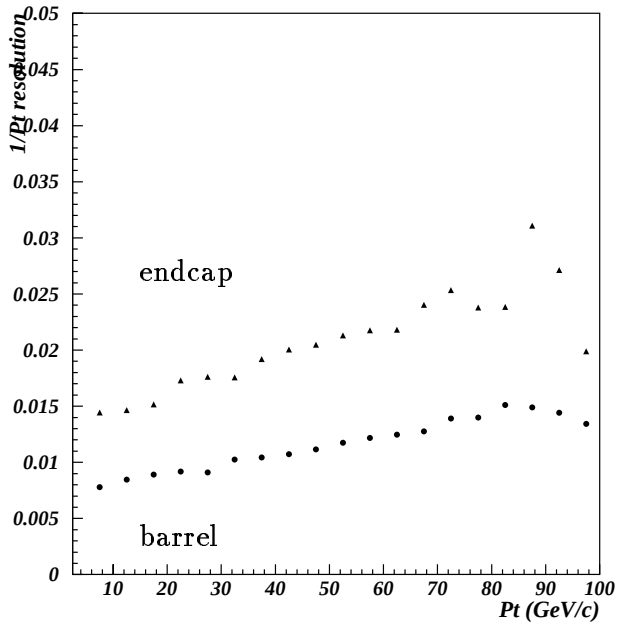

Figure 8.16: Inverse transverse momentum resolution as a function of the muon transverse momentum for muons accepted by the level-3 muon trigger.

As for the level-2, it is important to check the error estimation on the different track parameters. Figure 8.18 shows the pull distributions of the track parameters $1/p_T$, ϕ and θ for muon tracks reconstructed at the level-3. The standard deviation of the Gaussian curves fitted to the ϕ and θ pull distributions is of the order of 1.2, showing that the errors on these parameters are correctly estimated. The standard deviation of the $1/p_T$ pull distribution is worst ~ 1.5 but closer to 1 than the value obtained at the level-2 (see figure 8.13), which shows an improvement in the estimation of the covariance error matrix. The standard deviations of the pull distributions different from 1 are due to the approximations that the magnetic field is uniform in the tracker and that the dead material is concentrated in detection surfaces. It has been shown in reference [123] that standard deviations close to 1 can be obtained with the GEANE numerical algorithm.

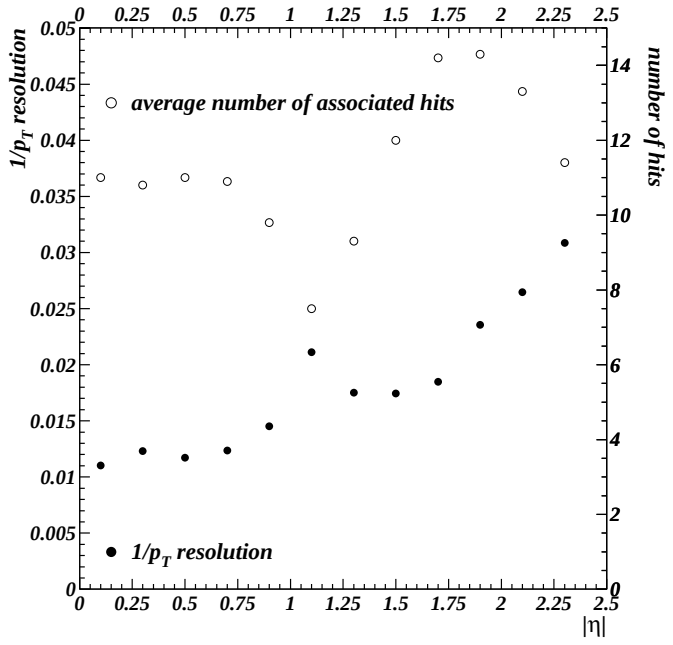

Figure 8.17: Number of reconstructed hits associated to the muon track and $1/p_T$ resolution as a function of the pseudo-rapidity for muon tracks reconstructed by the level-3 muon trigger.

It is also important to note the reduction of the non-Gaussian tails with respect to the level-2 muon trigger.

All these results are in agreement with the performance obtained with the existing level-3 muon reconstruction algorithm [146]. The combination of the very good transverse momentum, less than 2%, and the reduction of the non-Gaussian tails, should result in the reduction of the efficiency to select a muon with a p_T smaller than a given threshold and should therefore lead to a large suppression of the low transverse momentum background. This topic will be studied in some details in section 8.6.

Algorithm efficiency

We will now study the algorithm efficiency of the code developed in this work for the level-3 muon trigger, using the Monte Carlo data sample of 60,000 single muons with uniform p_T, η and ϕ distributions (see section 8.3). Figures 8.19 and 8.20 show the level-3 muon trigger efficiency with respect to the level-2, as a function of the pseudo-rapidity and of the muon transverse momentum, respectively. The efficiency over the entire η range is on average equal to 92%. The dip observed for $0.75 < \eta < 1.2$ corresponds to the critical transition region. Indeed in this η range, the level-3 reconstruction code is more delicate since it combines measurements from the barrel and the forward tracker detectors. To check that the inefficiencies observed at level-3 are strongly related to badly reconstructed muons at level-2, we have looked at the χ^2 distributions obtained at the level-2 muon trigger. Figure 8.21 displays the χ^2 distributions for all the muons reconstructed at level-2 and for those which are not reconstructed at level-3. We observe that the fraction of muons not reconstructed at level-3 increases with the χ^2 obtained at the level-2 reconstruction. Beyond $\chi^2 = 60$, the algorithm efficiency at level-3 is below 50%; these muons contribute to more than 25% of the level-3 efficiency loss.

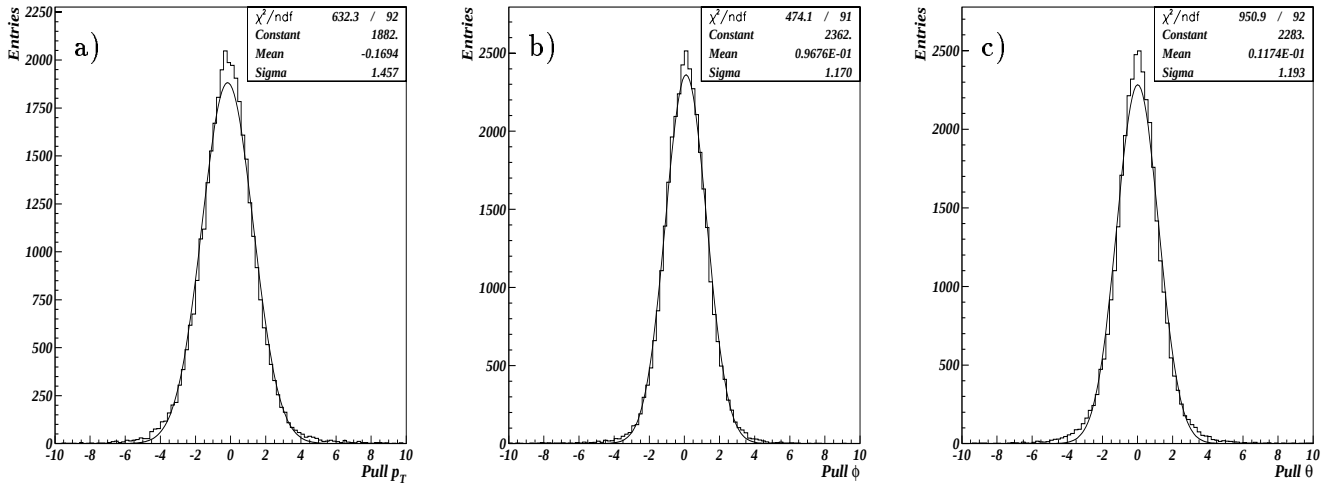

Figure 8.18: Distribution of the pulls of the track parameters $1/p_T$ (a), ϕ (b) and θ (c) for muon tracks reconstructed at the level-3 muon trigger.

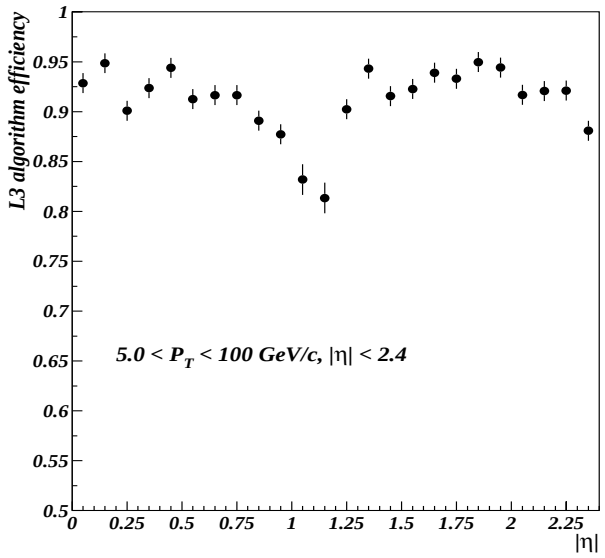

Figure 8.19: Level-3 muon trigger algorithm efficiency as a function of η for single muons generated with uniform p_T, η and ϕ distributions.

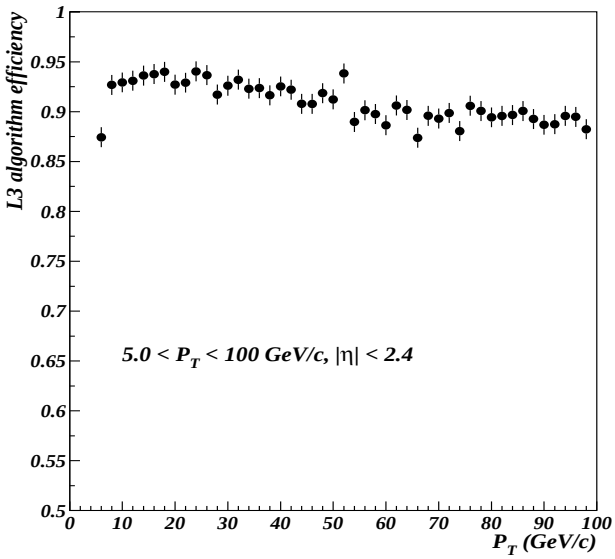

Figure 8.20: Level-3 muon trigger algorithm efficiency as a function of p_T for single muons generated with uniform p_T, η and ϕ distributions.

In figure 8.20, we observe that beyond $p_T = 10$ GeV/c, the algorithm efficiency reaches a plateau around 93% and for $p_T > 30$ GeV/c, the algorithm efficiency slowly decreases with p_T. This effect is due to the increasing probability that a muon suffers from hard bremsstrahlung along its trajectory. On one hand if the bremsstrahlung occurs in the muon system, it renders the level-2 muon reconstruction problematic and deteriorates the precision of the track parameters for the level-3 seeding. On the other hand if the bremsstrahlung occurs between the inner tracker and the muon system, the muon trajec-

tory is difficult to extrapolate from the muon station to the tracker. Indeed the momentum estimate at the innermost muon station will be much smaller than the momentum of the particle at the exit of the tracker since part of the muon energy has been given to the irradiated photons. To investigate this effect we have looked at the difference between the reconstructed and generated transverse momentum. Figure 8.22 shows the p_T^{rec} - p_T^{gen}/p_T^{gen} distributions, obtained at the level-2 for all the muons reconstructed at this level and for the muons which are not reconstructed at the level-3 (shaded area). This distribution is also displayed for muons of $p_T^{gen} > 50$ GeV/c, which are not reconstructed at the level-3. We observe that a large fraction of the tracks which are not reconstructed by the level-3 corresponds to muons with a transverse momentum underestimated by the level-2. This fraction increases with the muon transverse momentum, as expected from the increase of the probability that a muon suffers from bremsstrahlung. It has been shown that the bremsstrahlung probability is of the order of 4% for each muon station for muons with a momentum of 100 GeV/c [158].

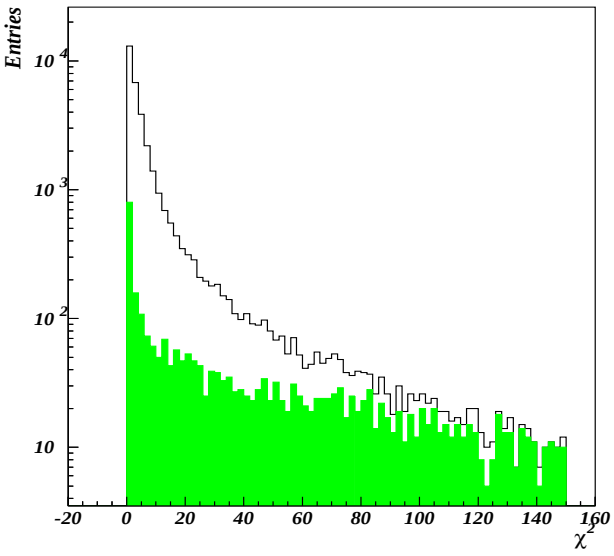

Figure 8.21: Distribution of χ^2 at the level-2 muon trigger for all the muons reconstructed at this level and for those which are not reconstructed at level-3 (shaded area).

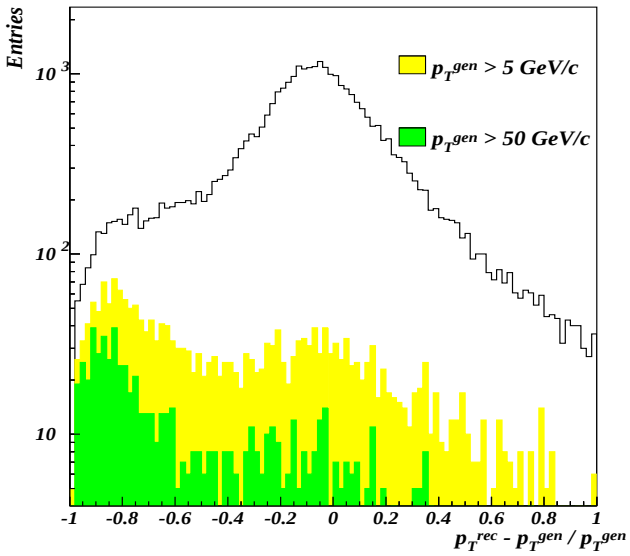

Figure 8.22: Distribution of $\frac{p_T^{rec}-p_T^{gen}}{p_T^{gen}}$ at level-2 for all the muons reconstructed at this level and for those which are not reconstructed at the level-3 ($p_T^{gen} >$ 5 GeV/c). The distribution is also shown for muons with $p_T^{gen} > 50 GeV/c$

It has been shown in reference [159] that the existing algorithm has an efficiency of 95% on average over the range $|\eta| < 2.4$, with a p_T resolution at the level-2 muon trigger better than the one obtained for the present studies (see section 8.4.2). Moreover we have demonstrated that the level-3 inefficiencies are strongly correlated to the quality and the resolution of the track parameters provided by the level-2 reconstruction algorithm and which are used to generate the seed of the muon trajectory at the level-3. Therefore we expect an increase of the level-3 muon reconstruction efficiency with the advent of an improved level-2 reconstruction code. In addition the implementation of a Kalman filter taking into account the radiation energy loss should also improve the level-3 algorithm efficiency for high p_T muons [160].

Threshold resolution

We have already seen in figure 8.4 that at level-1, even for a threshold on the p_T as high as 30 GeV/c, a fraction of muons with low transverse momentum ($p_T < 10$ GeV/c) is selected by the level-1 muon trigger. To understand how the acceptance of muons with a transverse momentum below threshold can be reduced with an improved transverse momentum resolution and the reduction of the non-Gaussian tails of the $1/p_T$ residual distribution, it is interesting to look at the efficiency as a function of the generated muon transverse momentum, at the different trigger levels for different p_T thresholds. The sharpness of such curves at the threshold value is related to the $1/p_T$ resolution and to the non-Gaussian tails of the $1/p_T$ distribution of the corresponding trigger level. These efficiency curves are shown in figures 8.23 for the level-1, -2 and -3 and with a p_T threshold of 10 (a), 20 (b), 30 (c) and 40 GeV/c (d). In these figures, the efficiency of the levels

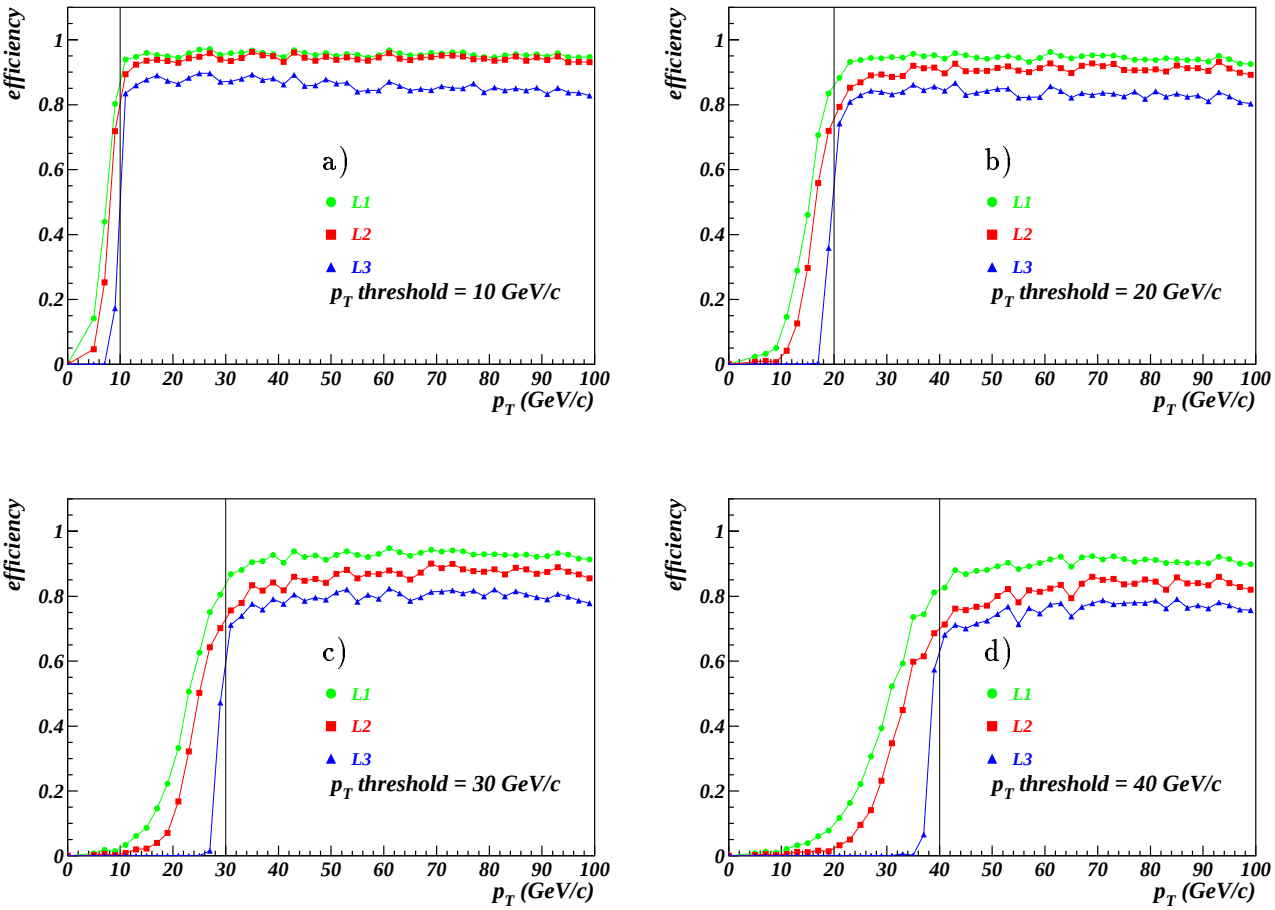

Figure 8.23: Efficiency curves as a function of the muon transverse momentum for the level-1, -2 and -3, with a threshold of 10 (a), 20 (b), 30 (c) and 40 GeV/c (d).

2 and 3 does not correspond to the algorithm efficiency, but it is calculated with respect to the muon spectrum at the generator level. Note also that the reconstructed muon momentum is increased by one sigma in order to provide a p_T cut with an efficiency of

90% at each level (see section 8.4.1). We clearly observe that the efficiency for muons with a p_T lower than the threshold is reduced at higher trigger levels: for a p_T threshold of 40 GeV/c, the fraction of muons of transverse momentum below threshold goes from $\sim$ 20% at level-1, to $\sim$ 13% at level-2 and to $\sim$ 2% at level-3. Since the convolution of the efficiency curves with the rate of generated muons gives the rate contribution of each trigger level for a given threshold, the sharp cuts observed at level-3 suggest a significant reduction of the muon background rate at this level, as we will see in section 8.6.

Timing

The CPU time consumption is an important issue for an algorithm which is foreseen to reconstruct muon tracks online. We discuss in this section the time sharing between the different steps of the muon reconstruction. These studies have been performed with the sample of $W \rightarrow \mu + X$ events at high luminosity (10^{34} cm^{-2}s^{-1}). Table 8.1 shows the average time of the muon reconstruction and the contribution of the different steps of the track reconstruction, the seeding, the trajectory building and the smoothing, for the algorithm studied in this work as well as for the existing level-3 code. The timing is also given for the level-2 algorithm, in which the smoothing is replaced by a vertex constrained fit (see section 8.4.2). All the times are given for a processor Intel P-III with a 1 GHz CPU. The total reconstruction time of our algorithm is about 810 ms per muon, which is similar to the reconstruction time taken by the level-2 and 40% faster than the existing level-3 code. The difference with respect to the existing level-3 code is mainly due to the seed generation which is almost 6 times faster with our algorithm than with the existing one. Indeed, as described in section 8.5.1, the seeding of the existing code is more complex. In addition, the 25% longer trajectory building for the existing code is due to the fact that for one muon candidate provided by the level-2 more than one seed can be generated. Consequently more than one trajectory candidate have to be grown inside the tracker, which increases the combinatorics (see section 8.5.1).

However note that we do not take into account the time consumption needed by both level-3 algorithms for the first propagation of the track parameters between the innermost muon detector and the outermost tracker detector. Indeed as seen in section 8.5.1 this propagation uses the GEANE numerical algorithm which takes into account with excessive precision the inhomogeneities of the CMS magnetic field and the presence of material. Therefore this propagation may be up to 100 times slower than a propagation performed between two tracker layers with the fast propagator used inside the tracker and can be as long as 1 s. The speed-up of this propagation should be achieved with the development of a fast propagator, similar to the one used for the tracker, with a suitable approximation of the dead material and the magnetic field inhomogeneities.

Finally it is also important to note that the reconstruction time of the level-3 algorithm presented in this work, $\sim$ 810 ms on today's 1 GHz CPU, is close to the timing requirements for the HLT trigger when extrapolated to the future CPU's which would be available at the LHC turn-on (see section 2.5). However the level-2 reconstruction is 2.5 times too slow compared to the HLT requirements. For the level-2 reconstruction algorithm, it has been shown that up to 95% of the total time is spent in the propagation between the muon layers which uses the GEANE numerical algorithm [161]. This result shows the importance to implement a fast propagator taking into account the magnetic field inhomogeneities and the dead material.

step	Level-2 (ms)	Level-3 (ms)	Existing L3 (ms)
seeding	25	70	400
trajectory building	700	732	900
smoothing/vertex constr. fit	75	8	8
Total time	800	810	1308

Table 8.1: Time consumption of the different steps of the muon trajectory building for the level-3 algorithm presented in this work, for the existing code and for the level-2.

8.6 Muon trigger rate for the single muon topology

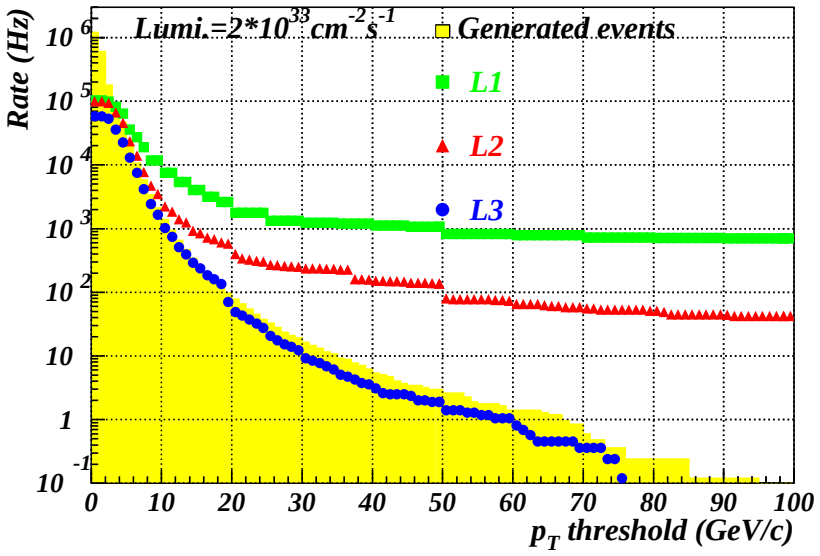

Figure 8.24: Minimum bias rates for the level-1, 2 and 3 single muon triggers at low luminosity, 2×10^{33} cm^{-2}s^{-1}, as a function of the threshold on the reconstructed muon transverse momentum. The generated rate corresponds to the shaded area.

As we have seen in section 2.3, some interesting physics channels can only be efficiently selected by a single muon trigger. In this section we will discuss the background rate acceptance of such a trigger at various levels as a function of the transverse momentum threshold.

As seen in section 8.1, at low transverse momentum, the background rate is dominated by the minimum bias events. These events will flood the single muon trigger if either the transverse momentum threshold is too low or if the resolution on its determination is too poor. Figure 8.24 shows the output rate of the levels 1, 2 and 3 of the single muon trigger at low luminosity (2×10^{33} cm^{-2}s^{-1}) as a function of the threshold applied on the muon transverse momentum for the minimum bias events. The rate of the generated events is also represented (shaded area). The maximum trigger rate that can be accepted at each level by the muon trigger are 6 kHz, 2.5 kH, 250 Hz and 25 Hz for the level-1, 2, 3 and 4 respectively (see section 8.1). We observe that the level-1 output rate is above the generated one, beyond a p_T threshold of $\sim$ 4 GeV/c and that beyond 30 GeV/c, the level-1 rate is almost constant. These effects are due to the poor resolution on the transverse

momentum. As the muon p_T spectrum decreases exponentially, the overestimation of the p_T for only a few percents of the muons leads to a large output rate even for large p_T thresholds. To stay below the allowed trigger rate of 6 kHz, the level-1 single muon p_T threshold could easily be put at 20 GeV/c, leading to a rate of $\sim$ 2 kHz only, but surely not at 10 GeV/c, which would result in a trigger rate of about 10 kHz. Increasing the threshold beyond 20 GeV/c, one can only reduce the trigger rate down to $\sim$ 1 kHz with the drawback of reducing the trigger acceptance still further for signal events (see figure 8.23).

In figure 8.24 we also observe how the successive trigger levels reduce the rate. Although we have seen in section 8.4.2 that the level-2 $1/p_T$ resolution is on average similar to the resolution of the level-1, the improvement of the $1/p_T$ resolution for low p_T muons, $p_T < 20$ GeV/c (see figure 8.12), reduces the muon rate. Beyond a p_T threshold of 50 GeV/c the level-2 muon trigger provides more than a factor 10 in the rate reduction. A transverse momentum threshold of 20 GeV/c can be maintained at level-2 as it leads to a trigger rate of $\sim$ 400 Hz, well below the allowed limit of 2500 Hz. Maintaining this threshold at level-3 leads to a trigger rate of 50 Hz, below the allowed limit of 250 Hz for level-3, but implies further reduction at level-4 to reach the maximum HLT trigger rate of 25 Hz for the muon stream. If no further reduction is applied at level-4, the level-3 single muon trigger threshold has to be increased up to about 25 GeV/c.

Note that at level-3, the output rate is very close to the generated rate because of the reduction of the efficiency to select muons with a transverse momentum lower than the threshold (see figure 8.23). This behaviour is due to the very good transverse momentum resolution, $\sim$ 2%, and the reduction of the non-Gaussian tails in the $1/p_T$ distribution at the level-3 reconstruction (see figure 8.14).

Given the rates allowed for the single muon stream at the different trigger levels, a possible scenario is the following: a p_T threshold of 12 GeV/c could be applied to the Global Muon Trigger, which reduces the rate to 5.4 kHz. The same cut applied at the level-2 reduces the minimum bias rate to $\sim$ 1 kHz. At level-3, this cut leads to a background rate of 500 Hz, two times the maximum rate allowed. A cut above 14 GeV/c is required at level-3 to reduce the rate below 250 Hz.

Let us now study the effect of the threshold on the single muon trigger acceptance for one example of signal event. For this study, we have chosen the leptonic decay of the W boson. Although this channel is a background for the single muon stream, it has been chosen because the muon p_T spectrum is close to the muon spectrum expected for the $H \rightarrow WW \rightarrow \mu\nu\mu\nu$, for Higgs masses ranging from 120 to 160 GeV/c^2 (see section 8.1). The trigger acceptance for $W \rightarrow \mu\nu$ events is shown in figure 8.25 as a function of the threshold on the muon transverse momentum for the muon trigger at the level-1, 2 and 3. The solid line shows the integrated muon transverse momentum distribution for the generated events, multiplied by the level-1 efficiency with a p_T threshold equal to zero. So, this histogram represents the acceptance as a function of the p_T threshold for a trigger with an infinite transverse momentum resolution. The apparent higher efficiency of the level-1 and the level-2 with respect to the generated distribution is due to the efficiency to select muons with a transverse momentum below threshold at the early trigger levels. The improved transverse momentum resolution at the level-3 muon trigger with respect to the previous stages clearly reduces this behaviour.

Table 8.2 shows the generated rate, the level-3 output rate for the minimum bias events as well as the rate and the trigger acceptance for the $W \rightarrow \mu\nu$ channel at low

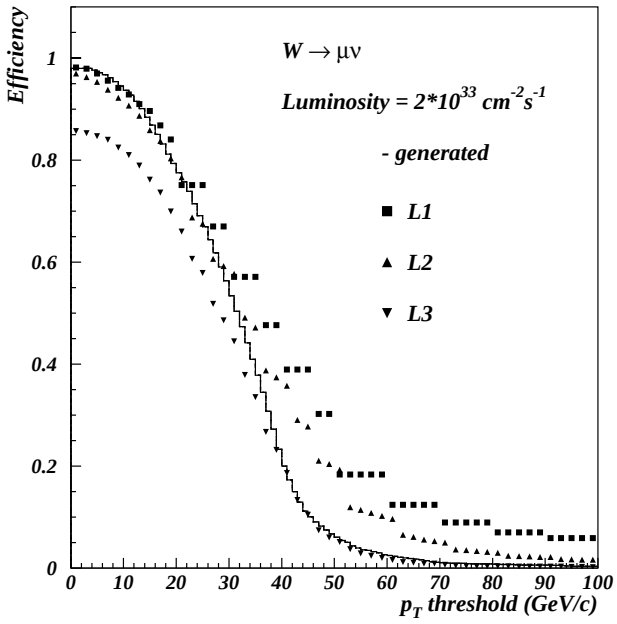

Figure 8.25: Trigger acceptance for the $W \rightarrow \mu\nu$ channel as a function of the p_T threshold for the different levels of the muon trigger. The solid line corresponds to the integrated p_T distribution of the generated events, multiplied by the level-1 acceptance with a p_T threshold equal to zero.

luminosity. With a p_T threshold of 20 GeV/c at level-3 the trigger acceptance for $W \rightarrow \mu\nu$ amounts to 66% with a background and a signal rate of 50 and 14.7 Hz respectively, far below the limit of 250 Hz for the level-3, assuming a further rate reduction of a factor 10 at the level-4. Without further reduction at level-4, a p_T threshold of 28 GeV/c is needed to reduce the rate from the minimum bias and the W leptonic decay below 25 Hz as seen in table 8.3, which shows the contribution to the level-3 output rate of the different muon origins for this p_T threshold value. With a threshold of 28 GeV/c, the acceptance for the $W \rightarrow \mu\nu$ channel drops to $\sim$ 50.0%. In table 8.3 we also observe that the rate of muons coming from the minimum bias background is similar to the $W \rightarrow \mu\nu$ contribution. Since the background rate at the level-3 muon trigger is close to the generated one, this shows the importance to select the muons not only according to their transverse momentum but also according to additional event characteristics in order to obtain a further background rejection but keeping the signal efficiency as high as possible. A single criterion applicable at level-2 is the isolation criterion using the calorimeters. Indeed we have seen in section 8.3 that the muon rate is dominated by muons coming from b/c quarks up to a muon transverse momentum of $\sim$ 30 GeV/c. The non-prompt muons coming from pion or kaon decays are dominant in the low p_T region, decreasing from 80% to 10% in the p_T range from 2 to 20 GeV/c. The contribution from the W boson becomes important only at very high transverse momentum, above 30 GeV/c. Consequently, to reduce the HLT output rate, it is necessary to reduce the b/c component and eventually also the π/K component if the p_T threshold chosen at the level-3 is low. The isolation criterion could be based on the fact that muons coming from the W leptonic decay are isolated, which means that only a small energy deposit in the calorimeters is expected within a cone surrounding the muon track. Instead, the muons

coming from b/c cascades are produced in jets. The isolation criterion can be applied at any trigger level. At level-2, isolation algorithms using the calorimeters data to perform the isolation criteria have already been studied [153] and it has been shown that a rate reduction factor of about 2 can be achieved with a p_T threshold of 15 to 30 GeV/c. At level-3, isolation algorithms using the pixel detector are still under study [162].

p_T thr. (GeV/c)	Gener. rate (Hz)	L3 M.B. rate (Hz)	$W \to \mu\nu$ L3 rate (Hz)	W acc. %
0	1.5×10^6	7.0×10^4	19.0	86.0
5	2.3×10^4	1.5×10^4	18.7	85.0
8	3.5×10^3	2.5×10^3	18.4	82.5
10	1.5×10^3	1.0×10^3	18.3	81.0
12	700	500	18.1	79.0
14	350	300	17.8	74.0
16	200	180	17.3	76.0
18	130	120	16.3	70.0
20	90	50	14.7	66.0
25	33	20	14.0	57.5
30	15	9.5	11.0	45.0

Table 8.2: Summary of the generated rate and the level-3 output rate for the minimum bias events (M.B.) for various p_T thresholds, at low luminosity (2×10^{33} cm^{-2}s^{-1}). The rate and the level-3 muon trigger acceptance for the $W \to \mu\nu$ channel is also given.

muon origin	rate (Hz)
$b/c \to \mu X$	13.0
$W \to \mu\nu$	10.3
$\pi/K \to \mu X$	1.3
Total	24.6

Table 8.3: Contribution to the level-3 output rate of the different muon origins, for a p_T threshold of 28 GeV/c.

8.7 Conclusions

This chapter was dedicated to the study of a new algorithm for the muon reconstruction at the level-3 muon trigger and to the study of the output rate as well as of the efficiency for the single muon topology with this algorithm. The presented algorithm, based on the Kalman filtering approach, exploits at maximum the common interface between the muon and the tracker systems. This allows to avoid code duplication and also improves the code maintenance.

We have demonstrated that the performance of this algorithm in terms of track parameter resolution is close to those obtained with the existing code. The algorithm efficiency is of the order of 93% for single muons with a transverse momentum ranging from 10

to 30 GeV/c. These results are very encouraging since they have been obtained after a level-2 muon trigger which suffers from reconstruction errors. For high p_T muons the efficiency could also be improved by taking into account at the level-2 reconstruction the energy loss by bremsstrahlung.

We have also shown that the CPU time consumption of this algorithm, $\sim$ 800 ms, is about a factor 2 faster than the official code since our algorithm creates exactly one seed for each level-2 muon candidate. These results do not take into account the time spent for the propagation of the track parameters from the innermost muon chamber towards the tracker. The implementation of a fast algorithm to propagate the track parameters from the innermost muon layer to the outermost tracker layer, like the one actually used for the central tracker, should improve the timing performance at level-3 as well as level-2 to match with the HLT timing requirements.

We have also studied the background rates expected with a single muon trigger. To stay below the maximum allowed rate at each level, the transverse momentum threshold can be as low as 12 GeV/c at level-1 and level-2. At level-3, if no further reduction is applied at level-4, the p_T threshold has to be raised to 28 GeV/c to maintain the single muon trigger rate below 25 Hz. We have also shown that with such a high p_T threshold, the trigger acceptance for signal events is already significantly reduced to $\sim$ 50%, pointing to the need of using other criteria like an isolation criterion to reject the b/c quarks contribution.

Although the efficiency and the time consumption can still be improved, we have shown that the algorithm proposed in this work is a good alternative to the actual code used for the level-3 muon reconstruction.

Chapter 9

Conclusions

This thesis is a contribution to the research and development program that preceded the construction of the central tracker of the Compact Muon Solenoid (CMS) and to the elaboration of its High Level Trigger. The CMS experiment is one of the two general purpose experiments being installed at the Large Hadron Collider (LHC), the future proton-proton collider of CERN. The LHC is designed for a wide range of physics studies, in particular for the discovery of the Higgs boson and of new physics beyond the Standard Model. These studies will be made possible by the unprecedented proton interaction energy and the high luminosity of the LHC, 14 TeV and 10^{34} $cm^{-2}s^{-1}$ respectively. This results in a very high event rate of 10^9 Hz. This harsh irradiation environment put stringent constraints on the performances of the detectors and on the trigger of the data acquisition system of the experiment.

We have first participated in the development of alternatives to the Micro-Strip Gas Counter (MSGC), which was envisaged by the CMS collaboration to equip the outer parts of the CMS tracker. These alternatives are the MICROMEGEM and the MSGC+GEM detectors. Both use the principle of two amplification stages and both are equipped with a Gas Electron Multiplier (GEM) which provides the first amplification. This principle allows to share the total gas gain of the detector between two amplification structures in cascade. The voltage on both structures can be considerably reduced which reduce the discharge probability as well as the risk of damages in case of sparks.

In the MICROMEGEM, the GEM foil is sustained 50 μm above an array of pick-up strips. The GEM amplification is extended below the GEM foil by applying an intense electric field between the strips and the GEM foil. Since this detector has been developed in Brussels, we have first studied its performance in terms of gain, energy resolution and rate capability with X-ray sources. High gains, above 10,000 are easily reached with an energy resolution of about 23%. These results are similar to the performance of other micro-pattern gaseous detectors equipped with a GEM. Although the maximum gain competes well with that of the MSGC, which is around 10,000, the energy resolution of the MICROMEGEM is 10% worse than for the MSGC. The difference is due to the Printed Circuit Board technology, instead of the micro-electronics technology, used to produce the electrode structure. With the Printed Circuit Board technology, the size of the smallest electrode is almost ten times larger than those obtained with the micro-electronics technology. High gains of up to 10,000 are also reached at high X-ray fluxes of 10^5 Hz/mm^2.

With the MICROMEGEM we have also studied experimentally and with simulations the electrical transparency of the GEM foil in two gas mixtures, for different electric field configurations. The simulations have been performed with a three dimensional model of the GEM foil and are in good agreement with the experimental data. The results give a clear understanding of the operation modes of the MICROMEGEM detector. A maximum transparency, close to a 100% is obtained for drift fields lower than $\sim$ 3 kV/cm. Indeed beyond this value, some primary electrons do not reach the amplification region of the GEM because some drift lines directly connect the upper GEM electrode and the cathode drift plane. This effect results in a loss of the measured gain and in a degradation of the energy resolution. The transparency is not affected by the transfer field, which confirms that the transfer field and the drift field are decoupled. However the transparency strongly depends on the potential difference applied across the GEM. We have also shown that the gas mixture has almost no influence on the transparency.

The behaviour of the MICROMEGEM detector in presence of heavily ionizing particles has been studied by exposing the detector to a 350 MeV/c pion beam of intensity $\sim$ 4×10^3 Hz/mm^2. In this irradiation conditions the maximum signal-to-noise amounts to 14 and the detector is not efficient. This behaviour is due to the coupling between the intense electric fields in the GEM and below the GEM which provide the gas gains. Since the detector structure is not damaged by the occurrence of sparks, the use of a protected electronics should allow to increase the maximum signal-to-noise in presence of HIP's.

We have shown experimentally and with simulations that in the MICROMEGEM detector, although there are two distinct amplification mechanisms, there is a single continuous region of amplification. Consequently, the MICROMEGEM behaves like a one stage amplification device with an amplification gap of 100 μm, like the MICROMEGAS detector. The poor behaviour in presence of heavily ionizing particles shows that the MICROMEGEM is not adapted for the LHC. However its mechanical robustness and its low price render this detector very attractive for X-rays applications with high radiation fluxes.

We have then studied the MSGC+GEM detector envisaged for the CMS forward tracker. In this detector, a single GEM foil is stretched 2 mm above four MSGC substrates. The gain and the energy resolution are comparable to other two-stage amplification devices and the MICROMEGEM: gains above 10,000 are easily obtained with an energy resolution of about 23%. The degradation of the energy resolution with respect to the one obtained with an MSGC without GEM, is due to the addition of the GEM, which is manufactured by Printed Circuit Board technology instead of micro-electronics technique for the MSGC electrodes.

In contrary to the MICROMEGEM detector, we have shown that the MSGC+GEM detector is really a two-stage amplification device in which the amplification structures are well separated. This geometry allows the MSGC+GEM to be operated stably in presence of heavily ionizing particles. Eighteen MSGC+GEM modules have been exposed during 360 hours in a 350 MeV/c pion beam at high intensity, up to 4 kHz/mm^2, in presence of heavily ionizing particles. This irradiation conditions are close to the LHC environment. The detectors were operated during this period at a signal-to-noise ratio of 37 that would lead to a detection efficiency of 98% when using the final electronics foreseen for the CMS tracker. The rate of discharges was modest, less than 10^{-3} Hz, an the accumulated number of strips amounted to 24 out of 16896 strips exposed. This number would result in a negligible loss of detection efficiency and to a slight degradation of the spatial resolution

in less than 4% of the total covered area. Finally we have shown that several detectors can be operated with a signal-to-noise ratio of the order of 100, which provides a safety margin of more than a factor two. It is also important to note that with an appropriate front-end electronics the MSGC+GEM detector reach 98% of detection efficiency with a signal-to-noise ratio of 17.

The study of the MSGC+GEM detectors has been completed by investigating its different operation modes. At LHC, the tracking detector will be equipped with a fast electronics, having a shaping time of 45 ns. The use of such a fast electronics with the Ne/DME gas mixture, commonly used with MSGC's, results in some signal loss at low drift fields because of the ballistic deficit of the electronics. A high drift field, up to 10 kV/cm, is therefore preferable. Consequently it is essential to optimize the GEM foil geometry in order to extend the plateau of the optimum transparency at such high drift fields.

For a large scale experiment a uniform response within a counter and between different counters is mandatory. Care has to be taken in the GEM foil production to minimize the GEM hole variations which can lead to 25% of gain fluctuations along the MSGC strips. It is also important to improve the mounting procedure of the GEM foil to avoid large GEM saggita.

We have also shown that the MSGC+GEM detector can be operated with fast gas mixtures like Ar/CO_2 which can not be used with the MSGC. However the higher drift velocity does not compensate the loss of primary ionization compared to Ne/DME. Ar/CO_2 is also very attractive because it is non-flammable, which is also an advantage for safety reason in a large scale experiment like CMS.

We have also observed a charging-up at drift field lower than 2 kV/cm. We have demonstrated that this charging-up effect occurs in the GEM foil and not on the MSGC substrate. This effect also depends on the radiation rate and the signal loss amounts to 50% with a radiation rate of 10^4 Hz/mm^2 and with a drift field as low as 0.5 kV/cm. This charging-up should not prevent the use of MSGC+GEM detectors at LHC since a drift field of a few kV/cm is required in order to collect all the charge in less than 50 ns. However this effect could be an important drawback for the use of a gaseous detector equipped with a GEM as readout for a large Time Projection Chamber (TPC).

The MSGC+GEM detector is a good alternative to the MSGC counter, combining the the robustness of the GEM and the performance of the MSGC. We have shown that the MSGC+GEM device is adequate to be used at LHC.

The last part of this work is devoted to the development of a new algorithm for the level-3 muon trigger. This level is the first which can combine the data from the tracker and from the muon chambers. The use of the tracker data should allow to measure the transverse momentum of the muons with an accuracy of the order of 1% compared to 15% for the muon chambers only. This good resolution should allow to reduce the trigger efficiency for muons of transverse momentum below the threshold and, therefore, to reduce the background of low p_T muons. This algorithm, based on the Kalman filter, fully exploits the similarities and the common interface between the tracker and the muon system; it considers both systems as a unique tracker. The performance of the proposed algorithm was evaluated with the help of a detailed simulation of the CMS experiment. The efficiency for single muons is presently around 92% over the entire pseudo-rapidity range but it is expected to increase with the improvement of the track reconstruction

code at the level-2, which provides the starting parameters for the level-3 trajectory. The proposed algorithm lead to a very good accuracy on the track parameters; the transverse momentum resolution if equal to 1 and 2% in the barrel and the endcap region respectively. The main advantage of this algorithm is the CPU time reduction due to the fast seeding with respect to the existing code. On average the muon reconstruction takes 800 ms, about a factor two faster than the existing code. The implementation of a fast propagation of the track parameters and their errors, like the one used inside the tracker, should improve the timing performance of the level-3 and the level-2 muon trigger to match with the CMS requirements. Finally we have estimated the trigger rate for the single muon trigger at low LHC luminosity. We have shown that maintaining a transverse momentum threshold of 20 GeV/c at each trigger level, the trigger rates are well below the allowed limit. At this threshold the acceptance for the $W \rightarrow \mu\nu$ channel is of the order of 66%. Without further rate reduction at the level-4, a threshold of 28 GeV/c is required, reducing the acceptance for the $W \rightarrow \mu\nu$ channel to $\sim 50\%$. Thanks to the good transverse momentum resolution of the level-3 muon trigger, the minimum bias rate is close to the generated rate. Therefore other selection criteria, like isolation cuts, have to be applied in order to further reduce the background rate and to maintain a good signal acceptance.

In this work we have had the opportunity to study different aspects of the CMS experiment. On one hand we have shown that, contrary to the MICROMEGEM, the MSGC+GEM is an adequate counter which fulfills all the requirements to be used in the CMS tracker. On the other hand we have proposed an algorithm for the level-3 muon trigger that is almost a factor two faster than the existing code.

Bibliography

[1] The LHC study group, The Large Hadron Collider, Conceptual Design, CERN/AC/95-05, 1995.

[2] D. Denegri, Standard Model physics at the LHC (pp collisions), Proc. ECFA workshop for LHC, Aachen 1990, CERN 90-10, Eds. G. Jarlskog and D. Rein, vol. I, p. 56.

[3] F. Englert and R. Brout Broken symmetry and the mass of gauge vector mesons, Phys. Rev. Letters **13** (1964) 321.

[4] P. W. Higgs Spontaneous Symmetry Breakdown without Massless Bosons, Phys. Rev **145** (1966) 1156.

[5] M. Spira QCD effects in Higgs physics, CERN-TH/97-68, 1997.

[6] S. Abdullin Discovery potential for supersymmetry in CMS, CMS-NOTE 1998/006.

[7] F. Abe et al. (CDF collaboration), Phys. Rev. D **50** (1994) 2966; F. Abe et al. (CDF collaboration), Phys. Rev. Lett. **73** (1994) 225.

[8] F. Abe et al. (CDF collaboration), Phys. Rev. Lett. **74** (1995) 2626.

[9] L. Wolfenstein, Parametrization of the Kobayashi-Maskawa matrix, Phys. Rev. Lett. **51** (1983) 1945.

[10] BABAR collaboration, Observation of CP violation in the B^0 meson system, SLAC-PUB-8904, hep-ex/0107013, and submitted to Phys. Rev. Lett., July 2001.

[11] Belle collaboration, Observation of large CP violation in the neutral B meson system, Phys. Rev. Lett. **87** (2001) 091902.

[12] CMS Collaboration, The Compact Muon Solenoid, CERN/LHCC 94-38.

[13] D.H. Perkins, Introduction to High Energy Physics, Third edition, Addison-Wesley, 1987.

[14] CMS Collaboration, The Muon Project, CERN/LHCC 97-32.

[15] CMS Collaboration, The Electromagnetic Calorimeter Project, CERN/LHCC 97-33.

[16] CMS Collaboration, The Hadron Calorimeter Project, CERN/LHCC 97-31.

[17] CMS Collaboration, The Tracker Project, CERN/LHCC 98-6.

[18] CMS Collaboration, The Tracker Project Addendum, 2000.

[19] CMS Collaboration, The Trigger and Data Acquisition Project, Volume I, The Level-1 Trigger, CERN/LHCC 2000-038.

[20] CMS Collaboration, The Trigger/DAQ project, CERN/LHCC, to be published.

[21] C. Grupen, Physics of Particle Detection, AIP Conference Proceedings 536 VIII ICFA School (1999) 3.

[22] U. Fano, Annual Review of Nuclear Science vol. 13 (1963).

[23] J. E. Moyal, Theory of ionization fluctuations, Phil Mag. **46** (1955) 263.

[24] L. Landau, J. Phys., 4, (1944) 201.

[25] J. H. Cobb et al., The ionisation loss of relativistic charged particles in thin gas samples ans its use for particle detcetion Nucl. Instr. and Meth. **A 133** (1976) 315.

[26] A. V. Zarubin, Properties of wire chamber gases, Nucl. Instr. and Meth. **A 283** (1989) 409.

[27] R. Bouclier et al., Recent developments of the multidrift tube, Nucl. Instr. and Meth. **A 283** (1989) 509.

[28] Particle Data Group: Phys. Rev.**54 (1996) 1**.

[29] S.E. Baru et al., X-ray detectors based on multiwire proportional chambers Nucl. Instr. and Meth. **A 392** (1997) 12.

[30] R.D. Evans, Compton effect, Handbuch der Physics (Ed. J. Flugge) Springer-Verlag, Berlin **34** (1958) 218.

[31] J. H. Parker et al., Phys. Rev. 181 (1969) 290.

[32] E.B. Wagner et al., Time-of-flight investigations of electron transport in some atomic and molecular gases, J. Chem. Phys. **47** (1967) 3138.

[33] F. Bloch and N.E. Bradbury, On the mecanism of unimolecular electron capture, Phys. Rev. **48** (1935) 689.

[34] R. Bouclier et al., Nucl. Instr. and Meth. A 350 (1994) 464.

[35] Basic processes of gaseous electronics, University of California Press, Berkeley (1955).

[36] G.D. Alkhazov, Nucl. Instr. and Meth. **A 89** (1970) 155.

[37] H. Sakurai Dependence of the energy resolution on anode diameter in xenon proportional counters, Nucl. Instr. and Meth. **A 313** (1992) 155.

[38] R. Bellazzini, M. A. Spezziga, La Rivista del Nuovo Cimento vol.17 (1994) n^o 12.

[39] W. Blum and L. Rolandi, Particle detection with drift chambers.

[40] G. Charpak et al., The use of multiwire proportional counters to select and localize charged particles, Nucl. Instr. and Meth. **A 62** (1968) 262.

[41] A. Oed et al., Position sensitive detector with microstrip anode for electron multiplication with gases, Nucl. Instr. and Meth. **A 263** (1988) 351.

[42] T. Beckers et al., Optimisation of MSGC design and operation conditions, Nucl. Instr. and Meth. **A 346** (1994) 95.

[43] R. Bouclier et al;, Performance of Gas MicroStrip Chambers on glass substrates with electron conductivity, Nucl. Instr. and Meth. **A 332** (1993) 100.

[44] Angelini et al., IEEE Trans. Nucl. Sci. **37 (no 2)** (1990) 112.

[45] Angelinini et al., Nucl. Phys. **B 23A** (1991)

[46] R. Bouclier et al., Nucl. Instr. and Meth. **A 381** (1996) 289.

[47] K. Ackerstaff et al., The HERMES Spectrometer Nucl. Instr. and Meth. **A 417** (1998) 230.

[48] F. Angelini et al., Results from the first use of MSGC's in a high energy physics experiment, Nucl. Instr. and Meth. **A 315** (1992) 21.

[49] M.K. Ballintijn et al., Results from the MSGC tracker at SMC, Nucl. Phys. **B 44** (1995) 268 (Proc. Suppl.).

[50] The RD28 collaboration, Develoment of MSGC's for radiation detection and tracking at high rates, CERN/LHCC 96-18, LDRB Status Report/RD-28 (1996).

[51] J. Scmitz, Results on Monte Carlo simulations of a microstrip gas counter, Nucl. Instr. and Meth. **A 323** (1992) 638.

[52] T. Lohse et al., An experiment to Study CP Violation in the B System Using an Internal Target at the HERA Proton Ring, DESY-PRC 94/02 (1994).

[53] O.Bouhali et al., Operation of microstrip gas counters with Ne/DME gas mixtures, Nucl. Instr. and Meth. **A 378** (1996) 432.

[54] M. Ackermann et al., Large scale test of wedge shaped Micro Strip Gas Counters, Nucl. Instr. and Meth. **A 436** (1999) 313.

[55] O. Bouhali et al., Contribution to the study of the MSGC tracker of the CMS detector, at the future proton collider LHC, PhD. Thesis, Université Libre de Bruxelles, Belgium, December 1999.

[56] ATLAS MSGC, ATLAS internal note INDET-NO-076 (1994).

[57] R. Bouclier et al., Results of wire chamber ageing tests with CH_4- and DME-based gas mixtures, Nucl. Instr. and Meth. **A 346** (1994) 114.

[58] J.E. Bateman et al., The experimental characterisation of gas microstrip detectors; III: Lifetime characteristics, RAL-94-114 (1994).

[59] R. Bouclier et al., Development of MSGC's for high rate application, Nucl. Instr. and Meth. **A 367** (1995) 168.

[60] R. Bouclier et al., High rate operation of micro-strip gas chambers, Proc. IEEE Nuclear Science Symposium, San Fransisco, Oct. 21-28, 1995.

[61] F. Angelini et al., A large area, hig gain micro-gap counter, Nucl. Instr. and Meth. **A 362** (1995) 273.

[62] R. Bouclier et al., Study of materials outgassing and their effect on gaseous detector lifetime, CMS-TN 96-038.

[63] M. Jilbaly et al., Nucl. Instr. and Meth. **A 283** (1989) 692.

[64] I. Boulogne, Etude des détecteurs gazeux a micro-pistes MSGC en vue de leur exploitation sous haut flux de radiations, PhD. Thesis, Université de Mons-Hainaut, Belgium, June 2002.

[65] O.Bouhali et al., Operation of microstrip gas counters with DME-based gas mixtures, Nucl. Instr. and Meth. **A 413** (1998) 105.

[66] J.T.M. Baines et al., Work at RAL on the ageing properties of gas microstrip detectors, Proc. Int. Workshop on MSGC's, Lyon, 1995, Eds D. Contardo and F. Sauli.

[67] R. Bouclier et al., Some factors affecting the lifetime of Micro Strip Gas Chambers operated at high rates in laboratoty conditions, Proc. Int. Workshop on MSGC's, Lyon, 1995, Eds D. Contardo and F. Sauli.

[68] I.P. Duerdoth et al., Lifetime characteristics of an MSGC with thin, high resitivity substrate, Proc. Int. Workshop on MSGC's, Lyon, 1995, Eds D. Contardo and F. Sauli.

[69] Y. Pestov and L. Shekhtman, Influence of the bulk resistivity of glass with electronic conductivity on the performance of microstrip gas chamber, Nucl. Instr. and Meth. **A 338** (1994) 368.

[70] R. Bouclier et al., Development of microstrip gas chambers on thin plastic supports, Nucl. Instr. and Meth. **A 315** (1992) 521.

[71] A. Barr et al., Diamond over coated Microstrip Gas Chambers for high rate operation CERN-PPE/97-21.

[72] F. Angelini et al., Operation of MSGCs with gold strips built on surface treated thin glasses, Proc. Int. Workshop on MSGC's, Lyon, 1995, Eds D. Contardo and F. Sauli.

[73] W.G. Gong et al., Nucl. Instr. and Meth. **A 374** (1996) 144.

[74] J.J. FLORENT et al., The electrostatic field in microstrip chambers and its influence on detector performance, , Nucl. Instr. and Meth. **A 329** (1993) 125.

[75] V. Peskov et al., Feedback and breakdowns in microstrip gas counters, Nucl. Instr. and Meth. **A 397** (1997) 243.

[76] H. Raether, Electron avalanches and breakdown in gases, Butterworths, Washington, 1964.

[77] Y. Ivaniouchenkov et al., Breakdown limit studies in high rate gaseous detectors, Nucl. Instr. and Meth. **A 422** (1999) 300.

[78] A. Bressan et al. , High rate behavior and discharge limits in micro-pattern detectors, Nucl. Instr. and Meth. **A 424** (1999) 321.

[79] R. Bouclier et al., The Gas Electron Multiplier, Nucl. Instr. and Meth. **A 381** (1996) 289.

[80] I. Duerdoth et al., A study of breakdown in microstrip gas chambers, Nucl. Instr. and Meth. **A 348** (1994) 356.

[81] R. Bellazzini et al., Technique for characterization of discharges in micro-strip gas chambers, Nucl. Instr. and Meth. **A 398** (1997) 426.

[82] R. Bellazzini et al., The CMS Micro-strip Gas Chamber project - Development of a high rate resolution tracking detector for harsh radiation environments, Nucl. Instr. and Meth. **A 457** (2001) 22.

[83] R. Bouclier et al., The Gas Electron Multiplier, IEEE Nuclear Science Symposium and Medical Imaging Conference, Anaheim, CA, 3-9 Nov 1996.

[84] T. Zeuner et al., Nucl. Instr. and Meth. **A 446** (2000) 324.

[85] R. Bouclier et al., New observations with the gas electron multiplier (GEM), Nucl. Instr. and Meth. **A 396** (1997) 50.

[86] J. Benlloch et al., Further developments of the Gas Electron Multiplier, Nucl. Instr. and Meth. **A 419** (1998) 410.

[87] A. Bressan et al., Beam tests of the Gas Electron Multiplier, Nucl. Instr. and Meth. **A 425** (1999) 262.

[88] R. Bellazzini et al., Nucl. Instr. and Meth. A 424 (1999) 444.

[89] R. Bellazzini et al., Nucl. Instr. and Meth. A 423 (1999) 125.

[90] B. Adeva et al., Nucl. Instr. and Meth. A 435 (1999) 402.

[91] Y. Giomataris et al., MICROMEGAS: a high granularity position sensitive gaseous detector for high particle flux environments, Nucl. Instr. and Meth. **A 376** (1996) 29.

[92] F. Jeanneau, Etude des détecteurs MICROMEGAS et GEM. Recherche du Boson de Higgs dans le canal $H^0 \to WW \to qql^{\pm}\nu$ avec l'expérience CMS. Thèse de doctorat, Université de Haute Alsace, Mulhouse, France, 1999.

[93] G. De Lentdecker, Etude d'un compteur a gaz a grille microscopique (MICROMEGAS) pour un traceur au LHC. Mémoire, Université Libre de Bruxelles, Belgium (june 1998).

[94] MAXWELL, Ansoft Co, Pittsburg, PA, USA.

[95] R. Veenhof, GARFIELD, recent developments, Nucl. Instr. and Meth. A 419 (1998) 726.

[96] S. Biagi, A Multiterm Boltzmann Analysis of drift velocity, diffusion, gain and magnetic-field effects in argon-methane-water-vapour mixtures, Nucl. Instr. and Meth. **A 283** (1989) 716.

[97] V. Palladino and B. Sadoulet, Application of classical theory of electrons in gases to drift proportional chambers, Nucl. Instr. and Meth. **A 128** (1975) 323.

[98] W. Beaumont et al., Studies of an MSGC equipped with a GEM grid as tracking device, Nucl. Instr. and Meth. **A 419** (1998) 394.

[99] J.M. Brom et al., Comparative studies of MSGC and MSGC+GEM detectors, Nucl. Instr. and Meth. **A 419** (1998) 400.

[100] T. Hott, MSGC development for the Inner Tracker of HERA-B, Nucl. Instr. and Meth. **A 408** (1998) 258.

[101] F. Angelini et al., Nucl. Instr. and Meth. A 355 (1993) 69.

[102] R. Bellazzini et al.,The micro-groove detector, Nucl. Instr. and Meth. **A 424** (1999) 444.

[103] R. Bellazzini et al., The WELL detector, Nucl. Instr. and Meth. **A 423** (1999) 125.

[104] L.L. Jones, RD20 PreShape32 User Manual Version 1.0, Rutherford Appleton Laboratory (1993).

[105] L.L. Jones, APVM Specification, Rutherford Appleton Laboratory, June 1998.

[106] National Instruments Corporation

[107] CN/ADS Group, PAW user's guide, Program Library Q100, CERN 1993.

[108] C. Richter et al., presented at the 8^{th} Pisa Meeting on Advanced Detectors, May 21-27, 2000.

[109] S. Bachmann et al., Charge amplification and transfer processes in the gas electron multiplier, Nucl. Instr. and Meth. A 438 (1999) 376.

[110] R. Bellazzini et al., What is the real gas gain of a standard GEM, Nucl. Instr. and Meth. **A 419** (1998) 429.

[111] W. Beaumont et al., Operation of Micro Strip Gas Counter equipped with a Gas Electron Multiplier, Nuclear Physics B proc. 78 (1999) 395.

[112] A. Bressan et al., Beam tests of the gas electron multiplier, Nucl. Instr. and Meth.

[113] R. Bellazzini et al., A two-stage high gain micro-strip detector, Nucl. Instr. and Meth. **A 425** (1999) 218.

[114] D. Macke, Micro Strips Chamber with Gas Electron Multipliers and their Application in the CMS Experiment, PhD. Thesis, III. Physikalisches Institut B, University of Technology Aachen, Germany, 2000.

[115] J. Benlloch et al., IEEE Trans. Nucl. Sci. NS-45 (1998) 234.

[116] J. Benlloch et al., Further developments and beam tests of the gas electron multiplier (GEM), Nucl. Instr. and Meth. **A 419** (1998) 410.

[117] P. Fonte et al., Rate and gain limitations of MSGC's combined with GEM and other preamplification structures, Nucl. Instr. and Meth. **A 419** (1998) 405.

[118] S. Bachmann et al., presented at the IEEE Nuclear Science Symposium and Medical Imaging Conference, Seattle, 1999.

[119] M.C. Altunbas et al., Aging Measurements with the Gas Electron Multiplier (GEM), to be published in Nucl. Instr. and Meth.

[120] M. Huhtinen, CMS NOTE-1997/073.

[121] W. Beaumont et al, Beam test results of MSGC's with thick metal strips, CMS NOTE 1999-059.

[122] L. Jones, PreMux 128 Specifications 2.3, Rutherford Appleton Laboratory (1995).

[123] P. Vanlaer, Contribution to the study of the central tracking system of the CMS detector, at the future proton collider LHC, PhD. Thesis, Université Libre de Bruxelles, Belgium, september 1998.

[124] B. Schwaller et al., The trigger system of the CMS barrel and forward milestones, CMS NOTE 1998/029.

[125] K. Bernier, Etude du comportement des détecteurs gazeux à micro-pistes MSGC sous irradiation intense de neutrons rapides, PhD. Thesis, Université Catholique de Louvain, Belgium, May 2001.

[126] S. Bachmann et al., Discharge studies and prevention in the Gas Electron Multiplier , Nucl. Instr. and Meth. **A 479** (2002) 294.

[127] T. Zeuner et al., Nucl. Instr. and Meth. A 413 (1998) 105.

[128] CMS The Compact Muon Solenoid, Technical Proposal, CERN/LHCC 94-38 (1994).

[129] CMS Collaboration, The Tracker Project, CERN/LHCC 98-6, 1998.

[130] F. Sauli, Gas detectors: recent developments and future perspectives, Nucl. Instr. and Meth. **A 419** (1998) 189.

[131] T. Beckers, MSGC based tracking detectors for high energy physics experiments, PhD. Thesis, Universitaire Instellingen Antwerpen, Belgium, 2002.

[132] J.D. Scargle Studies in astronomical time series analysis. II - Statistical aspects of spectral analysis of unevenly spaced data, ApJ **263** (1982) 835

[133] A. Zander, Experiences with a pre-series of Micro Strip Gas Counters with Gas Electron Multipliers for high rate applications, PhD. Thesis, III. Physikalisches Institut B, University of Technology Aachen, Germany, 2001.

[134] V. Zhukov, private communication.

[135] W. Blum and L. Rolandi, Particle detection with drift chambers, Accelerator Physics, Springer-Verlag, 1994.

[136] I. Boulogne et al., Aging tests of MSGC for the CMS Forward Tracker at Mons University, proceedings of the International Workshop on Ageing phenomena in Gaseous Detectors, Hamburg, October 2001, to be published in Nucl. Instr. and Meth. A.

[137] O. Bouhali et al., Operation of microstrip gas counters with DME gas mixtures, Nucl. Instr. and Meth. A 446 (2000) 324.

[138] U. Moosbrugger, 3d-Simulation of Avalanche Processes in a GEM, http://consult.cern.ch/writeup/garfield/examples/gem/report/report.html

[139] , F. Sauli, GEM readout of the time projection chamber, CERN-EP-TA1 Internal Report, July 29, 1999.

[140] B. Schmidt, Proceedings of the 36th Workshop of the INFN Eloisatron Project on New Detectors, Erice, 1997.

[141] R. Bellazzini et al., Substrate-less, spark free micro-strip gas counters, Proceedings of the VII Pisa Meeting on Advance Detectors 'Frontiers Detectors for Frontier Physics', Isola d'Elba, Italy 1997.

[142] R. Bellazzini et al., The CMS Micro-strip Gas Chamber project - Development of a high resolution tracking detector for harsh radiation environments, Nucl. Instr. and Meth. **A 457** (2001) 22.

[143] S. Bachmann et al., Performance of GEM in high intensity particle beams, Nucl. Instr. and Meth. **A 470** (2001) 548.

[144] L.L. Jones et al., A 128 channel Analogue Pipeline Chip for MSGC readout at LHC, Proceedings of the Fourth Workshop on Electronics for LHC experiments, September 1998.

[145] F.G. Sciaccia, Definition of the Front-end Signal Processing Algorithm for MSGCs in CMS, CMS IN-1997/021.

[146] S. Lacaprara, Development of High Level Trigger algorithm for the CMS experiment for events with muons in the final state, Ph-D thesis, Universita degli studi di Padova, Padova, Italy, December 2001.

[147] S. Wyhnoff, ORCA.6.1.1, User Guide, May 29, 2002.

[148] R. Brun et al., GEANT, Detector description and simulation tool, CERN program library W5013 (1994).

[149] C. Zeitniz, T.A. Gabriel, The GEANT-CALOR interface and benchmark calculation of Zeus test calorimeters, Nucl. Instr. and Meth. **A 349** (1994) 106.

[150] T. Sjöstrand et al, PYTHIA.6.152 Comp. Phys. Comm., **135** (2001) 238.

[151] R. Früwirth, Application of Kalman filtering to track and vertex fitting, Nucl. Instr. and Meth. **A 262** (1987) 444.

[152] E.J. Wolin et al., Covariance matrices for track fitting with the Kalman Filter, Nucl. Instr. and Meth. **A 329** (1993) 493.

[153] D. Acosta et al., Results on L2 trigger reconstruction in single and di-muon topologies, CMS NOTE 2001/011.

[154] A. Khanov, et al., Tracking in CMS: software framework and tracker performance, Nucl. Instr. and Meth. **A 478** (2002) 460.

[155] R. Früwirth, A. Strandlie, Comput. Phys. Commun. 120 (1999) 197.

[156] V. Innocente et al., GEANE-Average Tracking and Error Propagation Package, CERN writeup W5013, 1994.

[157] N. Neumeister, Muon Reconstruction, CMS Workshop on Track reconstruction, January 30, 2001.

[158] C. Albajar, Status report of the RD5 Expriment, CERN/DRDR/93-49 (1994).

[159] N. Neumeister, Updates on L2 and L3 muon reconstruction, CMS week, CERN, December 2001.

[160] W. Adam, Inclusion of radiative energy loss in the standard track reconstruction, PRS/b-tau meeting, July 9, 2002.

[161] S. Lacaprara, CPU Analysis of L2-L3 HLT muons, PRS/muon meeting, February 28, 2002.

[162] N. Amapane High Level Trigger Algorithms for Muon Isolation, to be published as CMS-NOTE.

Acknowledgements

J'aimerais tout d'abord remercier Madame Catherine Vander Velde qui, après avoir dirigé mon mémoire, a accepté de superviser mon travail de thèse pendant ces quatre années. Je dois beaucoup à son expérience, son esprit critique et ses encouragements. Je lui suis également très reconnaissant d'avoir lu et relu, avec attention, le texte de cette thèse.

Je tiens ensuite à exprimer ma gratitude au Professeur Jean Sacton pour m'avoir accueilli dans le service de Physique des Particules Elémentaires qu'il dirigeait aux débuts de mes travaux, ainsi qu'au Professeur Daniel Bertrand qui lui a succédé.

I am also indebted to Professeur Fred Udo who has read my thesis and who always has provided precious suggestions and remarks. Je voudrais également remercier le Professeur Walter Van Doninck dont la bonne humeur et la joie de vivre ont égaillé les tests en faisceau au PSI. Je lui suis très redevable de sa confiance et de son soutien.

Je suis très reconnaissant envers Pascal Vanlaer, sans qui la partie de ce travail dédiée à l'étude du système de déclenchement de CMS n'aurait pas pu être menée à bien. Merci aussi à Othmane Bouhali pour m'avoir initié à la simulation des détecteurs à gaz. I would like to thank Valery Zhukov for his priceless support during the experimental part of this work and for his fruitful suggestions.

D'autre part, j'ai eu le plaisir de travailler avec Evelyne Daubie et Isabelle Boulogne à l'Université de Mons Hainaut. Merci également à Francis Defontaine pour son aide précieuse lors de l'installation des dispositifs expérimentaux.

Je tiens aussi à remercier vivement le Professeur Fabio Sauli de m'avoir accueilli dans son laboratoire au CERN pour me permettre d'effectuer des mesures avec des particules hautement ionisantes.

Je voudrais ensuite saluer mes collègues Tom Beckers, Stéphanie Moreau, Andreas Nowack et Anette Zander pour les nombreuses et souvent très longues, mais toujours enrichissantes discussions concernant les résultats des tests menés au PSI. Merci tout particulièrement à Olivier Devroede qui, grâce à son aide et son humour, a rendu la chasse aux bugs dans les dédales du C++ moins pénible.

Mes remerciements s'adressent également à tous les membres de l'IIHE pour leur accueil chaleureux. Ils ont su, par leur motivation et leur sympathie, favoriser un travail agréable et fructueux. Je salue mes collègues physiciens: Caroline, Xavier, Steven, Roel, Sophie, Philippe, Peter, Jorgen et tous les autres, jeunes ou moins jeunes.

Merci aussi à Rolande et Myriam Pins pour avoir passé plusieurs heures à mesurer la taille des trous des GEMs. Je serais impardonnable si j'oubliais l'aide de Monique Garnier, Danielle Peymans ainsi que celle de Josée. Je remercie également Denis Johnson pour ses nombreuses corrections d'anglais.

Je voudrais saluer et remercier chaleureusement et tendrement ma famille, en particulier mon frère à qui je souhaite bonne chance pour la thèse qu'il a finalement décidé de commencer. Merci enfin à Isabelle, pour son aide, son soutien, sa patience et toutes les raisons qu'il n'est pas nécessaire d'expliquer.